Universität der Bundeswehr München

VALIDATION OF PASSIVE TEMPERATURE STABILISATION OF ADDITIVELY MANUFACTURED INTEGRAL STRUCTURES WITH INFUSED PHASE CHANGE MATERIAL

Dominik Wild

Vollständiger Abdruck der von der Fakultät für Luft- und Raumfahrttechnik der Universität der Bundeswehr München zur Erlangung des akademischen Grades eines

Doktor-Ingenieurs (Dr.-Ing.)

angenommenen Dissertation.

Gutachter/Gutachterin:

1. Prof. Dr.-Ing. Markus Czupalla
2. Univ.-Prof. Dr.-Ing. Roger Förstner
3. Univ.-Prof. Dr.-Ing. habil. Lars Zigan

Die Dissertation wurde am 19.03.2024 bei der Universität der Bundeswehr München eingereicht und durch die Fakultät für Luft- und Raumfahrttechnik am 01.08.2024 angenommen. Die mündliche Prüfung fand am 11.09.2024 statt.

KURZFASSUNG

Infused Thermal Solutions (ITS) stellt eine monolithische Integralbauweise mit eingebetteter passiver Thermalkontrolle zur thermalen Stabilisierung von Raumfahrt-Komponenten, ohne aktive Heiz- und Kühlsysteme dar. Die passive Thermalkontrolle wird durch die Einbettung von Phasenwechselmaterial (engl.: Phase Change Material; kurz PCM) in zuvor additiv gefertigte Komponenten erreicht, die auf einem doppelwandigen Design mit integrierter Gitterstruktur (engl.: lattice) basieren. Das PCM wird zwischen den Doppelwänden als Makro-Verkapselung für die thermale Energiespeicherung (engl.: Thermal Energy Storage; kurz TES) eingebettet. Auf diese Weise resultiert das ITS-Technologie Design Konzept zu einer additiv gefertigten monolithischen integralen Komponente mit integrierter Gitterstruktur und eingebettetem PCM. [WIL-21]

Die in der ITS-Forschung für TES verwendeten PCMs sind aufgrund ihrer hohen spezifischen latenten Schmelzwärme in Kombination mit dem breiten Schmelztemperaturbereich, der eine hohe Flexibilität des ITS-Designs ermöglicht, auf organische PCM (Paraffine) beschränkt. Dieser nutzbare Effekt von PCM flacht Temperaturspitzen ab, reduziert Temperaturgradienten und dämpft Abkühlphasen, wodurch weniger Heizleistung erforderlich wird. [WIL-21]

In dieser Dissertation wird die grundlegende Validierung der passiven Temperaturstabilisierung von additiv gefertigten integralen Strukturen mit eingebettetem PCM durch thermale Analysen unterstützt. Zusätzlich werden Hardwaretests mit Prüfkörpern und einem skalierten ITS-Demonstrator durchgeführt, dessen Struktur auf dem Infrared Sounder Instrument (IRS) basiert, welches eine Nutzlast des Meteosat Third Generation (MTG) Satelliten ist. Die MTG spezifischen thermalen Orbit-Anwendungsfälle werden aus den vorliegenden thermalen Orbit-Daten abgeleitet. Mit diesem Hardware-Demonstrator wird die ITS-Technologie thermal validiert.

Die thermalen Vorhersagen für alle Prüfkörper und das Demonstrator Modell werden in ESATAN modelliert. Die Vorhersagen der thermalen Modelle basieren auf der bereits veröffentlichten Subroutine für die thermo-physikalische Modellierung des PCM-Verhaltens. Diese PCM-Subroutine ist generisch und vollständig parametrisiert. Die numerische Simulation des PCM-Verhaltens basiert auf der Latentwärmespeicher-Methode (LHS) in Kombination mit Hysterese-Modellen, um das Verhalten von PCM in technischer Qualität mit nicht unterbrochenen und unvollständigen Phasenwechselzyklen zu simulieren.

Alle thermalen Prüfkörper sowie der ITS-Demonstrator werden additiv durch das (engl.: laser powder bed fusion; kurz LPBF) Verfahren unter Verwendung der hoch wärmeleitfähigen Aluminiumlegierung AlSi10Mg gefertigt. Die Kombination der Synergieeffekte einer integrierten Gittermatrix zwischen Doppelwänden trägt wesentlich zur Verbesserung der effektiven Wärmeleitfähigkeit sowie zur Versteifung des doppelwandigen ITS-Bauteils als Ganzes bei. Es wird weiterhin gezeigt, dass das integrierte BCC2-Gitter die effektive Wärmeleitfähigkeit deutlich erhöht und somit die Auswirkungen des typischerweise schlecht wärmeleitenden Paraffins minimiert. [WIL-21]

Weiterhin werden sowohl die konduktive als auch die konvektive Wärmeübertragung innerhalb von ITS-Strukturen analysiert und mit experimentellen Daten korreliert. Konvektive Wärmeübertragung kann unter bestimmten Umständen auftreten. Jedoch im Vergleich zur konduktiven Wärmeübertragung innerhalb von ITS-Strukturen ist Konvektion bei den durchgeführten Messungen weder dominant noch führt Konvektion zu signifikanten Modellabweichungen.

Durch systematische steady-state TVC-Tests wird das konduktive ITS Wärmeübertragungs-Modell validiert. Die Validierung erfolgt sowohl mit als auch ohne PCM, um die thermalen Eigenschaften des lattice und des PCMs entkoppelt voneinander zu ermitteln. Das konduktive Wärmeübertragungs-Modell ist darüber hinaus vollständig parametrisiert.

Die Ergebnisse der TVC-Zyklen-Tests im Vergleich zu den Vorhersagen zeigen und bestätigen für alle Prüfkörper und den ITS-Demonstrator die prognostizierten Hauptmerkmale der passiven thermalen Temperatur-Stabilisierung, nämlich die Dämpfung von Extremtemperaturen, die Verengung des Temperaturbands und die Minimierung von Unterkühlungs-Phasen, was wiederum die Heizleistung minimiert.

Die Skalierbarkeit der ITS-Technologie wird am Demonstrator-Modell validiert. Die vorhergesagten und gemessenen Temperaturkurven mit eingebettetem PCM des Demonstrators können mit guter Genauigkeit korreliert und die erreichte Temperaturstabilisierung quantifiziert werden.

Die Quantifizierung der erreichten Temperaturstabilisierung erfolgt durch Metriken, die in die entwickelten Softwaretools zur Daten-Nachbearbeitung integriert sind und größtenteils auf MATLAB-Code basieren.

Das ITS-Konzept wurde bereits 2018 im Rahmen der deutschen nationalen Initiative INNOSpace Masters (Link) des Deutschen Zentrums für Luft- und Raumfahrt (DLR) zum Sieger für die innovativste Technologie im Bereich Mobilität und Raumfahrtanwendungen gekürt.

Darüber hinaus wurde das ITS-Konzept mit dem Forschungspreis der Fachhochschule Aachen im Jahr 2020 ausgezeichnet (Link).

Die Erkenntnisse und Ergebnisse aus dem ITS-Forschungsprojekt (Förderkennzeichen: 50RP1975, gefördert durch das Bundesministerium für Wirtschaft und Energie, Deutschland) sind bereits sowohl in wissenschaftlichen Abhandlungen als auch umfänglich im wissenschaftlich-technischen Erfolgskontrollbericht veröffentlicht worden. [WIL-23]

Die Veröffentlichung des Erfolgskontrollberichts musste auf Anweisung des Deutschen Zentrums für Luft- und Raumfahrt (DLR) als Zuwendungsgeber bereits im Januar 2023 und somit vor Fertigstellung dieser vorliegenden Arbeit erfolgen. Des Weiteren sind alle Veröffentlichungen im Zusammenhang mit der ITS-Forschung und dem Autor Hr. Wild in dieser Arbeit gelistet. [WIL-21]

ABSTRACT

Infused Thermal Solutions (ITS) introduces a monolithic integral design with embedded passive thermal control for temperature stabilisation of functional structures, without active heating and cooling systems. Passive thermal control is achieved by embedding phase change material (PCM) in additive manufactured components, which relate on a double-wall design with integrated intermediate lattice. The PCM is embedded between the double walls as macro-encapsulation for thermal energy storage (TES), which yields the ITS technology. Hence the integral design is attributed to additive manufactured monolithic integral structures with integrated lattice and embedded PCM. [WIL-21]

The PCMs used for TES in the ITS research are limited to organic PCMs (paraffins) due to their high specific latent heat of fusion in combination with the available broad melting temperatures range, which enables ITS model flexibility. This useable effect of the PCM flattens temperature peaks, reduces temperature gradients and damps cooling phases, which then requires less heating power. [WIL-21]

In this doctoral thesis, the fundamental validation of the passive temperature stabilisation of additively manufactured integral structures with infused PCM is supported by thermal analyses. Additionally, hardware tests are performed with specimen test series and a scaled ITS demonstrator, which is related on the Entrance Baffling Assembly (EBA) instrument structure of the Meteosat Third Generation (MTG) satellite. The MTG use cases are derived from orbit thermal data.

The thermal predictions of all test specimens and demonstrator models are modelled in ESATAN and relate on a developed subroutine for thermo-physical modelling of PCM behaviour. This PCM subroutine is generic and fully parametrised. The numeric to simulate PCM behaviour is based on the latent heat storage (LHS) method in combination with hysteresis models to consider technical-grade PCM behaviour with non-interrupted and incomplete phase change cycles.

All thermal test specimens, breadboards and the ITS demonstrator are additively manufactured by applying laser powder bed fusion (LPBF), using the highly thermally conductive additive manufacturable aluminium alloy AlSi10Mg. The combination of the synergistic effects of an integrated lattice matrix in between double walls, contributes significantly to the improvement of the effective thermal conductance as well as to stiffen the double walled ITS component as a whole. It is therefore approved that the integrated BCC2 lattice significantly enhances the effective thermal conductivity and thus minimizes the impact of typically very low conductive paraffin. [WIL-21]

Both the conductive and convective heat transfer modes are analysed and correlated with experimental data. Convective heat transfer can occur under certain circumstances, but compared to conductive heat transfer within ITS structures, it is neither dominant in the measurements made nor does convection lead to unacceptable model deviations.

Through systematic TVC steady-state tests the conductive heat transfer model and its thermal modelling concept are validated, both with and without PCM in order to yield the thermal properties of the lattice and PCM. The conductive heat transfer model is fully parameterised.

The results of the TVC cycling tests compared to the predictions demonstrate and confirm throughout all specimens and the ITS demonstrator the proposed key features of the ITS passive thermal control capability, which are to damp peak heat loads, to narrow the temperature band and to minimize subcooling phases, which in turn minimizes heater power.

The scalability of the ITS technology is validated on the demonstrator model. The predicted and measured temperature curves with embedded PCM of the demonstrator can be correlated with good accuracy and the achieved temperature stabilisation is quantified.

The quantification of the achieved temperature stabilisation is provided by metrics, which are integrated in developed software tools for data post-processing, based mostly on MATLAB code.

The ITS concept was already awarded to the winner in 2018 for the most innovative technology in the field of mobility and space applications as part of the national INNOSpace Masters initiative (link) of the German Aerospace Centre (DLR).

In addition, the ITS concept was awarded the Research Prise of the Aachen University of Applied Sciences in 2020 (link).

The findings and results from the ITS research project (funding code: 50RP1975, funded by the Federal Ministry for Economic Affairs and Energy, Germany) have already been published both in scientific papers and extensively in the final scientific-technical success-control-report. [WIL-23]

The publication of the success-control-report had to be taken place already in January 2023 on the instructions of the German Aerospace Center (DLR) as the funding body, and thus before the completion of this thesis. Furthermore, all publications related to the ITS research and the author Mr. Wild are listed in this thesis. [WIL-21]

ACKNOWLEDGEMENT

I would like to thank my supervising professors Prof. Dr.-Ing. M. Czupalla and Univ.-Prof. Dr.-Ing. R. Förstner for giving me the opportunity and support to realise this doctoral thesis.

I would also like to thank my former colleague M.Sc. J. Schrezenmeier for his work and contribution in the structural-mechanical field and the excellent as well as goal-orientated cooperation during the ITS research. Mr. Schrezenmeier was as mechanical lead in charge for the mechanical designs, tests and preparation of the CAD models for additive manufacturing. He also coordinated the additive manufacturing of all ITS parts. The structural-mechanical and thermal findings are documented in the final ITS performance review report.

Another thank must be addressed as part of the ITS research to the GoetheLab of the FH Aachen, which provided the additive manufacturing equipment and fabricated the ITS components.

Thanks also go to OHB System in Munich for providing the MTG thermal model. Without this approval, the additive manufacturing of the ITS demonstrator hardware and the associated analyses, predictions and thermal vacuum chamber tests would not have been possible.

The very first considerations on the working principle of how to apply and simulate latent heat storage as phase change material within infused structures and components in ESATAN was given by Prof. Dr.-Ing. M. Czupalla [CZU-17] in 2017. This fundamental approach has been continued with this thesis.

Furthermore, the graduates of the FH Aachen J. B. M. Gräbener, K. Bergmann, M. Reiswich, H. Brandt, V.J. Ramin, J. F. Dommann, D. S. Kohlberger and J. S. Schäfers should also be mentioned. As part of their student internship semesters or final theses in the field of thermal or structural modelling at the FH Aachen SpaceLab they have supported the ITS research by working on various topics and issues.

Among others the graduates carried out feasibility studies, thermal predictions and thermal vacuum chamber tests to prove the feasibility and effectiveness of passive thermal control using PCM embedded in additively manufactured components. The results and findings were published partial in their theses and concluding papers.

CONTENTS

LIST OF FIGURES

LIST OF TABLES

NOMENCLATURE

Acronym	Description
AIT	Assembly, Integration and Test
ANSYS	ANalysis SYStem
BCC2	Body-Centered Cubic cell strut lattice type
BOL	Begin of Life
C&DH	Command & Data Handling system
CAS	Chemical Abstract Service registry number
CCD	Charge Coupled Device
CFD	Computational Fluid Dynamics
CFRP	Carbon Fibre Reinforced Plastic
COM	Centre of Mass
CT	Computer Tomography scans
D56	Day 56 orbit case in GEO orbit, MTG use cases
DIN	German Institute for Standardisation
DLR	German Aerospace Centre
DSC	Differential Scanning Calorimetry
EBA	Entrance Baffling Assembly
ECSS	European Cooperation for Space Standardisation
EN	European Norm
EOL	End of Life
EQ	Equinox EQ orbit case in GEO orbit, MTG use cases
ESATAN-TMS	ESA Thermal Analysis Network – Thermal Modelling Suite
ExoMars	Exobiology on Mars
FDM	Finite Difference Method
FEM	Finite Element Method
FH Aachen	University of Applied Sciences, in Aachen (Germany)
GEO	Geostationary Orbit
GL	Linear conductor in ESATAN
GR	Radiative contactor in ESATAN
GSE	Ground Support Equipment
ICES	International Conference on Environmental Systems
IP	In-plane
IR	Infrared
IRS	Infrared Sounder Instrument
ISO	International Organisation for Standardisation
ISS	International Space Station
ITS	Infused Thermal Solutions
JAXA	Japan Aerospace Exploration Agency
LAT	Lattice
LEO	Low Earth Orbit

LHS	Latent Heat Storage
LPBF	Laser Powder Bed Fusion
LRV	Lunar Rover Vehicle, used during Apollo 15-17 missions
MAIT	Manufacturing, Assembly, Integration and Test
MATLAB	Matrix Laboratory
MDI	Mercury Dual Imaging system
MESSENGER	Mercury Surface, Space Environment, Geochemistry and Ranging probe
MLI	Multi-Layer Insulation
MPS	Metallic Pressurised Structure
MTG	Meteosat Third Generation
NASA	National Aeronautics and Space Administration
NBR	Nitril-Butadien-Rubber
NICER	Neutron Star Interior Composition Explorer Experiment Payload
OP	Out-of-plane
PCM	Phase Change Material
PTFE	Polytetrafluoroethylene
QI	Internal heat load in ESATAN
QS	Total solar heat load in ESATAN
RWTH	Rheinisch Westfälische Technische Hochschule, in Aachen (Germany)
SLM	Selective Laser Melting
SSH	Sun Shield
STL	Stockage Latent
TCS	Thermal Control System
TMD	Thermal Model Data
TMM	Thermal Mathematical Model
TRL	Technology Readiness Level
TVC	Thermal Vacuum Chamber
USB	Universal Serial Bus
w/o	Without

SYMBOL DIRECTORY

Symbols & latin letters	Unit	Definition
	$\%$	Percentage
Δ	$[\ ]$	Delta, difference
ΔT	K	Temperature difference
Δt	s	Time difference
a	ms^{-2}	Acceleration
A	$[-]$	Aspect ratio $A = H/W$
A, A_X	m^2	Area
A_{Edge}	m^2	Thermal node edge area
A_{Shell}	m^2	Thermal node area
c_p	$kJkg^{-1}K^{-1}$	Specific isobaric heat capacity
C	JK^{-1}	Capacitance
d	m	Diameter
d	m	Plate thickness
D	m	Depth
D_S	m	Layer thickness
d_S	m	Beam diameter
d_{Strut}	m	Strut diameter
$f_{A\ LAT}$	m^2m^{-2}	Effective area ratio of lattice
$f_{A\ PCM}$	m^2m^{-2}	Effective area ratio of PCM
$f_{L\ LAT}$	m/m	Effective heat path length through the lattice
$f_{L\ PCM}$	m/m	Effective heat path length through PCM mass
f_{PCM}	$[-]$	PCM liquid fraction (porosity)
$f_{V\ LAT}$	m^3m^{-3}	Effective lattice cell porosity
$f_{V\ PCM}$	m^3m^{-3}	Effective PCM cell porosity
g	ms^{-2}	Gravitational acceleration
h	Jkg^{-1}	Mass specific enthalpy
H	J	Enthalpy
H	m	Height
i	deg	Inclination
I	Wt^{-1}	Integral gain for PI control
I	A	Electrical current
L, L_{PCM}	$kJkg^{-1}$	Latent heat of fusion
l	m	Length
l, L	m	Length (horizontal and vertical direction)
l_1, l_2	m	Length walls side 1 and side 2
l_{Cell}	m	Lattice cell cubical side length
m_{PCM}	kg	PCM mass

Ma_{CR}	*[-]*	Critical Marangoni number
m	*kg*	Mass
p	*Nm^{-2}*	Pressure
P	*W*	Electrical power
P	*W*	Proportional gain for PI control
P_L	*W*	Laser power
q_{latent}	*kJ/kg*	Latent heat flow
$q_{sensible}$	*kJ/kg*	Sensible heat flow
Q_{cond}	*W*	Conductive heat flow
$Q, Q(t)$	*W*	Heat
R	*Ω*	Electrical resistance
Ra_{CR}	*[-]*	Critical Rayleigh number
Ra_T	*[-]*	Rayleigh number of onset of turbulence flow
Ra, Ra_H	*[-]*	Rayleigh number
Ste	*[-]*	Stefan number
t	*s*	Time
T	*°C*	Temperature
T	*K*	Absolute temperature
t_1, t_2	*m*	Wall thickness side 1 and side 2
t_{Cell}	*m*	Effective thickness
t_{PCM}	*m*	PCM layer thickness
t_w	*m*	Wall thickness
T_{PCM}	*°C*	Characteristic PCM melting temperature
U	*V*	Voltage
v	*ms^{-1}*	Velocity
v_S	*ms^{-1}*	Scan speed
W	*m*	Width
Δy_S	*m*	Track spacing

$CQUAD4$	First order rectangular shell
$CTRIA3$	First order triangular shell

Greek letters	**Unit**	**Definition**
a	m^2s^{-1}	Thermal diffusivity
a	*[-]*	Phase fraction
k, λ	$Wm^{-1}K^{-1}$	Thermal conductivity
α	*deg*	Right ascension
α	*[-]*	Solar absorptivity (*ALP)*
β	*deg*	Beta angle
β	K^{-1}	Thermal expansion coefficient
$\varepsilon, \varepsilon_H, \varepsilon_N$	*[-]*	Infrared emissivity (*EPS)*
η	$Nm^{-2}s^{-1}$	Dynamic viscosity
ν	m^2s^{-1}	Kinematic viscosity
ρ	kgm^{-3}	Density
σ	*[-]*	Measured error (thermo-optical)
σ	$Wm^{-2}K^{-4}$	Stefan-Boltzmann constant
φ	*deg*	Inclination compared to horizon

Subscripts & superscripts	**Description**
c	Solidus limit
eff	Effective
f	Final
i	Initial
i	First index of thermal network node 1
IP	In-plane
j	Second index of thermal network node 2
l	Liquidus limit
LAT	Lattice
$liquid$	Liquid phase
m	Melting
max	Maximum
$mean$	Average
min	Minimum
net	Net value
old	Old value (previous step)
OP	Out-of-plane
PCM	Phase change material
$PCM\&LAT$	PCM and lattice fractions (node)
s	Solidification
$solid$	Solid phase
tot	Total
x	Exact

ESATAN specific syntax (MORTRAN)

CONDUCTIVE
DTPMAX
FLUXGL
FLUXGR
FLUXGT
FX,FY,FZ
GL ,GR
NODES
SLFWBK
STATST
SUBROUTINES
TIMEN
*VARIABLES*1
*VARIABLES*2

1 INTRODUCTION

The introductory chapter illuminates and describes the drivers of a thermal control system (TCS), specifically for space applications. The need for even better performance of instruments is constantly increasing. The more stringent requirements usually reach the limits of technical feasibility. Derived from the general problems and the intrinsic demand for permanent performance improvement of space systems, the motivation of the Infused Thermal Solutions (ITS) research, which is coupled with this doctoral thesis, is formulated.

1.1 Problem Statement and Motivation

Satellites in Earth orbits with its subsystems and payloads are exposed to large unsteady heat fluxes and strongly fluctuating external heat flows over the entire mission duration, which in turn result in extreme and periodic temperature fluctuations. Moreover, satellites operate in different operational modes during the mission time, which also leads to fluctuating internal heat flows. The consequences are the degradation of the thermal performance on subsystem and component level, carried on with thermo-elastic deformations, which degrade especially the instrument performance.

The permanent demand of higher instrument accuracy in satellite payloads is a significant driver for the instrument stability requirements and thus the instrument design. That’s why it is inevitable to encounter and restrain temperature instabilities in order to meet even more strict stability requirements.

Therefore, the instrument can be thermally or mechanically decoupled from the external environment or the internal heat loads to fulfil the stability requirements.

Another option is to use structures which are thermally stable due to embedded thermal features (e.g. meta structures) or advanced active thermal control, like smart structures.

Using standard mechanisms to diminish the heat loads like radiator with louvers, sunshades, looped heat pipes, multi-layer insulation (MLI), etc.

Indeed, a thermal design can also accept a certain level of temperature instabilities due to technical reasons (limited in state of the art) or physical limitations.

Nevertheless, with even stricter instrument stability requirements, the classical tools of thermal control beginning to approach their current limits. To address this issue, the ITS concept is intended to provide relief in order to diminish temperature fluctuations by reducing heat peak loads and to narrow the range of temperature variations.

In thermal control there is in most applications a time discrepancy between energy surplus to be dissipated and energy demand to be supplied for thermal control tasks. Up to now most satellite thermal control concepts relate on the classic cold bias concept. Excess thermal energy is dissipated into space via radiators and is then no longer available for thermal control, while heating elements prevent supercooling of the component by maintaining the operational minimum temperature.

As a logical consequence from this context, the ITS technology can provide remedy to some extent for this problem by using the embedded latent heat storage mass as an energy hub. The stored energy, in form of latent heat, can temporarily bridge and shift the time gap between energy surplus and energy demand needed by the TCS. This measure can increase the system efficiency by reducing the energy demand or system expenditure of the TCS.

The mitigation of heat peak loads during heating phases (hot case) as well as the reduction of required energy during cold phases (cold case) can also lower the interface and power requirements of the TCS and therefore the system mass.

The ITS technology provides a fully integrated passive thermal control concept, in order to reduce temperature instabilities of satellite components. This shall lead to an improved general thermal stability behaviour (improved thermal bias) of the component. However, if the passive ITS technology alone is not sufficient to provide the required stabilisation to achieve the requirements, an active TCS can be used additionally.

1.2 Research Scope and Question

This doctoral thesis is related on the ITS research project. The research question of this doctoral thesis is concerned with the analysation of the feasibility, predictability, scalability and the quantification of the passive temperature stabilisation performance, which is provided by the ITS technology.

The material used for additive manufacturing must be thermally characterised. Thermal characterisation is supported by specimen series, which are made by additive manufacturing to determine the thermal material properties of the sintered additive manufacturing material.

The thermo-physical modelling of the ITS technology is supported by thermal analyses and tests for correlations. The proof of the feasibility and thermal predictably of the ITS technology is to be provided by strategically defined small scale specimens. Based on the findings and results gained from the specimen series a large-scale hardware demonstrator is fabricated and used for the final ITS technology validation. The demonstrator is selected based on use case trades, which indicate the highest potential for thermal performance improvements.

Another part of the scope is the implementation and validation of a thermo-physical numerical modelling method of the ITS technology. This numerical PCM subroutine shall be a fully comprehensive generic thermal modelling method and needs to be embedded in the thermal modelling suite ESATAN, to simulate the thermo-physical phase change behaviour of a two-phase latent heat storage.

The analysis results with the applied PCM subroutine shall be validated and correlated on small scaled thermal specimens and finally on the large-scale ITS demonstrator. The achievable thermal stabilisation shall be quantified by suitable metrics, also with regard to the mass efficiency of the PCM used in the thermal design.

In parallel to the research scope mentioned so far, it is necessary to develop pre- and post-processing software tools, which can be used generically and thermal model independent.

2 STATE OF THE ART AND TECHNOLOGY

This chapter summarises the current state of the art in thermal modelling and analysis, thermal testing and validation of additively manufactured structures and components in conjunction with embedded latent heat storage (PCM). The following scheme shows the general review structure.

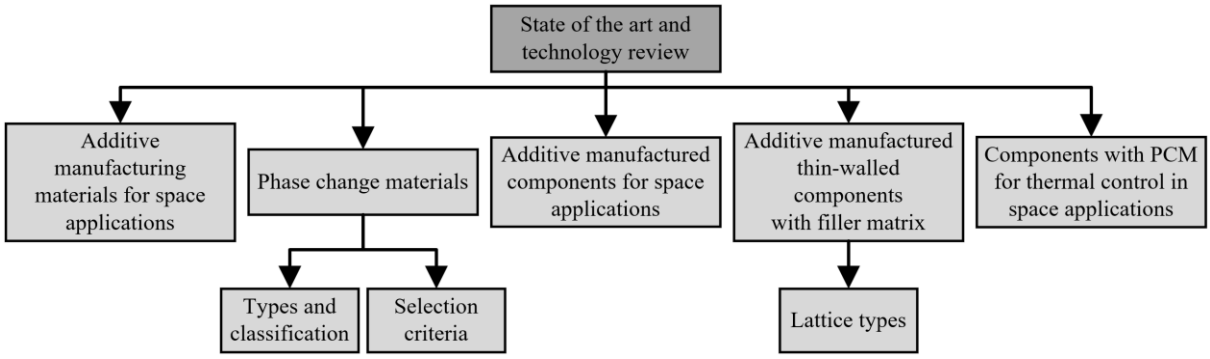

Figure 2.1: Overview of the state of the potential state of the art and technology breakdown to be reviewed

2.1 Review on Materials with Potential for Space Applications

To date the most widespread materials for additive manufacturing are clearly light metal alloys like aluminium due to its low cost, light weight, high strength to weight ratio and good thermal conductivity. Beneath aluminium there exist in aerospace applications also alloys like stainless steel, titanium, nickel- and iron-based super alloys, cobalt and copper alloys. [BLA-21]

Blakey-Milner et al. [BLA-21] concluded that specially for space applications there is a need of light metal alloys with an enhanced strength to weight ratio, the need for chemical stability, good corrosion resistance and high-temperature stability. Those potentially interesting alloys for space applications are listed in the following Table 2.1.

Table 2.1: Overview of the commercially available additive manufacturable metal alloys for space flight applications [BLA-21]

Material group	Alloys	Applications and properties
Ni-based	Inconel 625, Inconel 718	Disks, blades, high-pressure turbines, cryogenic applications
Fe-based	NASA HR-1	Propulsion system, fuel injection, good durability, good mechanical properties at high temperatures
Cu-based	GRCop-42, GRCop-84, C18150, C18200	Combustion chambers for liquid rocket engines (high strength and thermal conductivity required)
Al-based	AlSi10Mg, 2024, 4047, 6061, 7050	Enhanced strength to weight ratio, high thermal conductivity, but also high CTE
Ti-based	Ti6Al4V, γ-TiAl, Ti-6-2-4-2	High specific strength, good corrosion resistance, high-temperature and good cryogenic stability, low CTE

2.2 Phase Change Material Classification

Phase change materials (PCMs) are typically subject to a solid-liquid phase transformation. During the phase change the PCM absorbs or releases energy in form of latent heat. The temperature of the PCM remains nearly constant.

Outside the phase change temperature window, PCM behaves thermally according to the terminology of sensible heat. A compact overview of the PCM classifications, based on [ELI-18], is visualised in Figure 2.2.

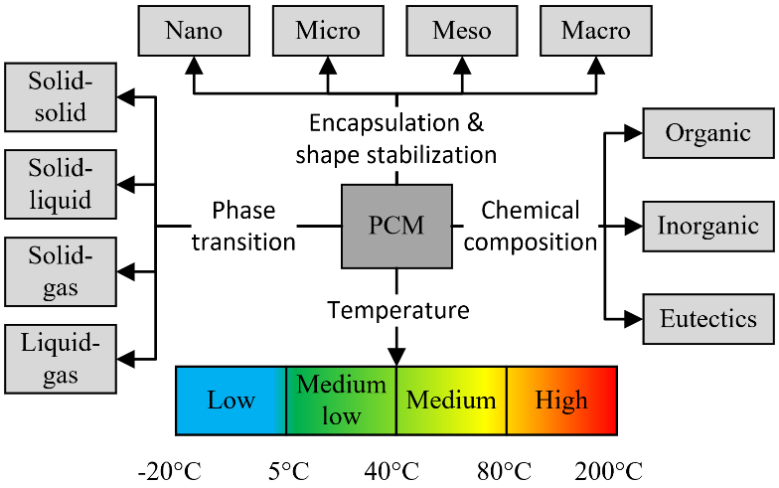

Figure 2.2: Compact overview of the PCM classifications, based on [ELI-19]

Liquid-liquid PCM store only very small amounts of energy and are thus not efficient in their effect. Such PCMs are not considered further in this work. Furthermore, the use of phase change materials in encapsulated structures with solid-gas or liquid-gas phase transitions are extremely challenging due to large volume changes and the associated pressure differences in the system. This has a major impact on the requirements, which are placed on the design and safety of such thermal control devices. In addition in space applications, there is a possible increase in design complexity due to the need for passivation when the system must be finally decommissioned. [LEI-09]

2.2.1 Criteria relevant for Selection

As [MEH-08], [LEI-09] and [HAL-71] et al. reviewed from a thermal point of view, the most important criterion for the selection of a suitable PCM are the specific latent heat of fusion, the density, reversibility of the phase change, moderate volume change and chemical cycle stability. The characteristic phase change temperature is critical to define the thermal stabilisation window.

Based on the reviews of Humphries et al. [HUM-77] and Gilmore et al. [GIL-02] it is clarified that solid-liquid PCMs can exchange a high amount of mass specific energy, combined with moderate volume changes. That's why the focus in the analytical and experimental environment within this work lays on solid-liquid PCMs. Within the ITS research project paraffin (organic PCM) is used within the medium-low temperature range.

The collective term paraffin is applied for chemical hydrocarbon compounds. Paraffins belong to the group of saturated hydrocarbons. Its chemical formulation can generally be expressed by C_nH_{2n+2}. As the number of carbon atoms (n) increases, so does the melting temperature, allowing flexible designs with different working temperature ranges for passive thermal control.

The relevant thermo-physical data of the PCMs are listed in a short summary in Table 10.1. Note that a complete listing of the PCM data can be found in the data base script of the FORTRAN-based PCM subroutine. The specific heat capacity and density data are referred to 20°C.

2.3 Review on Additive Manufactured Components for Space Applications

Van Gerner et al. [VAN-19] developed the TOPMOST two-phase mechanically pumped fluid loop cooling system to cool high-power electronic components in aerospace applications. This system consists mostly of aluminium components, which are made by additive manufacturing. The most interesting part is the high-pressure gas supply tank with a wall thickness around 1.0 mm, designed for a pressure of 17 bar. This technology demonstration reveals the general technical feasibility to manufacture thin-walled structures with large extend (walls) using the Concept Laser X-Line plant, which is also used for all ITS parts.

2.4 Review on Additive Manufactured Components with Embedded PCM

In 1971 Hale et al. [HAL-71] had already tested that if the temperature of a component rises unacceptably despite embedded PCM, high conductive filler matrix must be integrated. The reason is the low thermal conductivity of non-metallic PCM, which inhibits the heat transfer into the PCM mass. That statement proves true so far for most designs with large PCM volumes, even for ITS components, which use a highly conductive aluminium lattice as filler structure.

Leimkuehler et al. [LEI-10] and Yamada et al. [YAM-14] investigated an easy-to-implement concept to counteract the volume change of PCM due to temperature changes. Possible microgravity applications have not been considered. The PCM was treated incompressible. To handle the volume expansion a relative volume fraction of about 20% of the heat exchanger's volume was filled with air. At least 45 freeze/thaw cycles were carried out in different heat exchanger orientations to identify the possible influence of gravity. It was found that the position of the air cushions relative to the phase front are crucial and not controllable for designs, which are subject the varying accelerations. All specimens showed multiple damages mostly around the outer edges and the centre of the part. Those damage was presumably caused by the localised blocking of solidified PCM, as solidification occurs from the coldest to the warmest regions of the components. That's why the approach of actively embedded air volumes to encounter PCM volume changes is not considered further in this work.

Hatakenaka et al. [HAT-17] successfully demonstrated in 2017 the feasibility of a light-weight, thin-walled classical PCM capacitor, which is depicted in Figure 2.3, in collaboration with the Japan Aerospace Exploration Agency (JAXA). The heat storage unit is a PCM container, which is additively manufactured by the aluminium alloy AlSi10Mg. The exterior skin has a thickness of approx. 0.5 mm. A filler matrix in the form of fins is integrated inside the PCM container to improve the effective heat conduction and the structural stability. The paraffin octadecane ($C_{18}H_{34}$) was used as latent heat storage material (PCM), which demonstrated a very good cycle stability. Derived from these results, an internal filler structure and organic PCMs (paraffin) should also be considered for the ITS technology. The ITS research project also uses the aluminium alloy AlSi10Mg, which is already be proven by Hatakenaka.

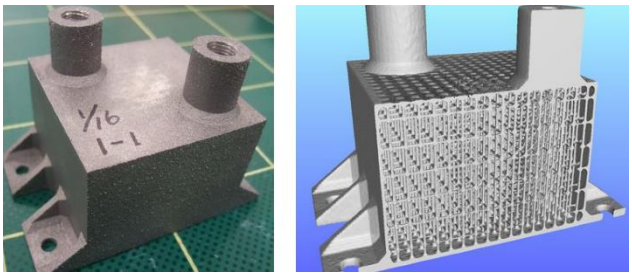

Figure 2.3: Thin-walled test specimen made by additive manufacturing with integrated fins [HAT-17]

Figure 2.4: PCM panel with an additive manufactured aluminium casing and integrated heat transfer structure for the thermal stability control of a CubeSat [ISA-17]

Isaacs et al. [ISA-17] manufactured and tested an aluminium casing with embedded PCM for 1U CubeSats, which is shown in Figure 2.4. The panel is made by additive manufacturing with an integrated aluminium structure to increase the component stiffness and the effective conductance. The remaining voids are filled with PCM. Thermal models were compared with TVC measurement data. The results indicated that the use of PCM in a structure with an already low capacitance achieves potential temperature stabilisation.

Choi et al. reviewed in [CHO-15], [CHO-17], [CHO-18] and [CHO-19] the accommodation of multiple PCM panels filled with paraffins to the IceCube 3U-CubeSat. The PCM panels are primarily attached to the CubeSat instrument and the command and data handling system (C&DH). The CubeSat was launched from the International Space Station (ISS), which means that there is a large variation in the beta angle. In addition, the optical instrument in the CubeSat only switches on during solar phases to capture images in the visible range. The panels enabled a passive thermal stability of approx. +1°C at 20°C by using ca. 30 gr PCM.

Quinn et al. conducted in [QUI-15] and [QUI-18] an ISS flight experiment, where a highly thermally isolated PCM TES heat sink was operated in an ISS double EXPRESS rack for several month in 2016 and thus was proven in the microgravity environment. The TES system was subject to multiple freeze and thaw cycles. The findings pointed out that the thermal performance of the heat sink is not dependent on gravity. This approach is also relevant for the ITS research in order to simulate PCM behaviour without considering gravity.

Dudon et al. [DUD-19] demonstrated in 2019 with Thales Alenia Space the thermal performance improvement of a classical PCM capacitor and the feasibility to predict the PCM behaviour numerically. The PCM module is coupled to high dissipative units and absorbs cyclic heat loads. One specimen is made by additive manufacturing and contains an integrated lattice filler matrix. Whereas the second specimen is made by conventional machining with welded aluminium fins, to enhance the thermal conductance. The performance improvement of the additively manufactured specimen with integrated lattice exceeded that of the conventionally manufactured variant due to better heat distribution within the PCM mass, which can be attributed to the monolithic structure and the resulting increased thermal conductance.

Zhang et al. [ZHA-19] also developed a phase change temperature controller unit in form of an additively manufactured box with integrated lattice in a classic container design. In the characterisation and prediction of the thermal behaviour of the breadboard boxes, only the conductive heat transfer mode was assumed. The boxes are filled with paraffin. The predictions were correlated with measurement data and indicate a good agreement. The outlines are that the distribution of porosity and the wall thickness of the container indicate the major influence on the phase change process of the numerical model, but not convective heat transfer. This will be further investigated by thermal analyses in this thesis.

Righetti et al. have been working in [RIG-19], [RIG-20] and [RIG-21] on combining PCM with the additive manufacturing of light metal structures with an integrated filler matrix on breadboard level. In 2020 Hu et al. [HUU-20] have also applied additive manufacturing in order to facilitate a porous aluminium structure with cubic cells for the enhancement of the heat transfer through PCM mass. The melt front propagation had been recorded by optical cameras and compared against the analytical predictions. The experimental results indicate that the heat transfer rate can be increased by 38% by a general use of a high conductive (aluminium) filler.

Hatakenaka et al. [HAT-21] has been validating the heat transfer characteristics of a spacer-type PCM device with integrated vertically aligned fins, which is completely made by additive manufacturing. The heat storage device is sandwiched between the spacecraft structure and a heat source. The prototype was sealed by a welding process. TVC cycles revealed that the chemical long-term stability of the PCM is given, which in turn confirms the results of the ITS measurements. Another point of interest of the ITS research is to identify a reliable sealing method.

Guo et al. [GUO-21] facilitated and tested in 2021 flat plate TES prototypes made by additive manufacturing (AlSi10Mg) and filled with the paraffin tetradecane. The plate is intended to be used for space applications. The aim is to investigate the transient PCM melting process by TVC cycling. The measurement data are compared with the simulation results. The lattice cell side length is 10 mm, whereas the plate has a wall thickness of 0.5 mm. The evaluated thermal storage process during phase change was underlying different tests with different initial temperatures and heating gradients. The simulations had been conducted with ANSYS Fluent by applying the enthalpy method. The influence of natural convection was not considered. The results showed a good agreement (± 3K) with the measurement data.

Piacquadio et al. [PIA-22] from the RWTH Aachen published in 2022 also research results of combining additive manufactured containers with different lattice structures and embedded PCM. They investigated different types of lattice cell geometries on its heat transfer rate through the PCM mass. The results to date show that a general BCC lattice strut matrix is one of the most effective filler structures and thus confirms the previous results of the ITS research, in which a BCC2 lattice is used.

2.5 Review on Components with PCM for Thermal Control in Space

This chapter shall give a compact overview about the already flight proven technologies and components, which contain PCM for thermal control or to fulfil dedicated thermal tasks.

Humphries et al. [HUM-77] and Hale et al. [HAL-71] summarised that passive phase change devices (without moving parts) for thermal control had already been used at this time on several missions for specific tasks. For the terminology it has to be noted that already in 1977, a conventional passive phase change capacitor was consisting of an external metallic housing with integrated PCM. Optionally, a thermal filler material was integrated into the PCM housing, in various configurations. As Hale et al. [HAL-71] mentioned, in literature a PCM capacitor is also known by different names such as fusible mass device, thermal flywheel, heat of fusion device or latent heat device.

Passive PCM solutions for thermal control in space systems are already known. Hale et al. [HAL-71], Creel et al. [CRE-01], Gilmore et al. [GIL-02], Gottero et al. [GOT-14] and Perotto et al. [PER-11] reported that the first applications of PCM (heat sink) for passive thermal control can already be traced

back to the Apollo missions with the Apollo Lunar Rover Vehicle (LRV), the MESSENGER probe for a Mercury exploration mission and also to ExoMars. [ALA-10]

Choi et al. validated in [CHO-12], [CHO-14] and [CHO-16] PCM panels, which are used for the NASA Vegetation Canopy Lidar project, reported by R. Knowles in 1993. The panels were proposed to be used in the scan telescope cavities of an imager, which is operated in a GEO satellite. In the cyclic loading process of the panels, it was possible to prove that no degradation could be detected after 5000 thermal vacuum cycles. The TRL at this time was 7. The paraffin panel had a ratio of 2:1 of PCM mass to the total mass of the panel.

Choi et al. [CHO-12], [CHO-13] and Hawkins et al. [HAW-01] reviewed the Mercury Dual Imaging System (MDI) TCS, which is a subsystem of the MESSENGER probe, launched in 2004. Therein two PCM wax packs with 240 g each were filled with dodecane ($C_{12}H_{26}$). The wax packs are attached to the camera detectors (CCDs) via thermal straps and had a melting temperature of -10°C. The data indicated a good cycle stability and regeneration rate of the PCM, which is critical for cyclic use.

According to Quinn et al. [QUI-12], Hatakenaka et al. [HAT-17] and Stephan et al. [STE-02] and [STE-10] reviewed TCSs' for the Orion capsule and the lunar surface systems (e.g. Lunar Electric Rover). The rover contained a PCM heat exchanger for radiator advancement, which therefore stores the excess heat and is conductively attached to a radiator. The Orion capsule has also been equipped with PCM heat exchangers. Lillibridge et al. [LIL-17] and [LIL-09] further summarised that the heat exchangers are coupled to the active TCS via a pumped fluid loop for support. Choi et al. [CHO-16] added that multiple paraffin panels are also used for the Orion crew module, in order to stabilise payload components that operate cyclical. The PCM in the panels is octadecane ($C_{18}H_{38}$). The thickness of the paraffin panels is approx. 1 cm.

Choi et al. [CHO-12] and [CHO-13] presented in 2012 a concept in which paraffin wax is housed in ten separated panels (in sum 4.78 kg PCM) at different locations at the Neutron Star Interior Composition Explorer (NICER) experiment payload. The panels were attached in the unpressurised trunk of the SpaceX Dragon vehicle. The PCM panels use a common thermal sharing plate that is linked to electronic units and to all side plates.

Geismyar et al. [GEI-20] investigated the thermal stabilisation effect of PCM, which surrounds the direct camera housing without thermal filler. The camera will be used in a 3U CubeSat to detect wildfire and other high temperature events. Thermal stabilisation within the temperature requirements could be achieved for 75% of an entire year's cycle through the use of PCM.

Schulz et al. [SCH-22] at Airbus Defence and Space in Friedrichshafen (Germany) have tested additive manufactured PCM heat capacitor prototypes for potential space applications, like for radar satellites or rover missions. The classical PCM heat capacitors are filled with octadecane. Additionally, heat spreaders are integrated to enhance the effective thermal conductance. The validation process is similar to that of ITS components, but they do not develop integral structures. The thermal models are validated by thermal cycling tests. Mechanical tests and a CT scan had been performed as well. It seems that the team has also applied a similar PCM filling procedure, as previously used for filling ITS components. The thermo-physical PCM behaviour is modelled with ESATAN. The calculations to create the energy balance of the thermal PCM nodes seems to be done with the identical approach as the ITS subroutine. However, the ITS subroutine was already presented at ICES in 2020.

2.6 Review on Additive Manufactured Filler Matrix

There exist several heat transfer enhancement techniques to increase the effective thermal conductance in the PCM mass such as metallic lattice, metallic fins, metallic foam (open and closed cells), rigid filler structures like ribs, vanes or bars, high conductive honeycomb structures, nano particles (additives), nano impregnated additives (graphite, graphene, etc.), coatings, metallic wool or metallic gleans.

The main focus in the review of possible filler matrix shapes and types for the ITS technology, is on light-metallic materials such as aluminium. This is because the lattice matrix has to be made of the same material as the rest of the component, which are made by additive manufacturing.

Tao et al. [TAO-16] provides a good overview of heat transfer techniques in order to enhance the effective thermal conductance of pure PCM in a capsuled housing. All concepts combine that the PCM is embedded in a porous metallic matrix structure, which consists of a high conductive material. Solid filler matrix by additive manufacturing can be based on stochastic structures (foam) or non-stochastic lattice structures.

2.6.1 Cellular Open Cell Foams

A promising technique to increase the effective thermal conductivity is the application of cellular metal foams with an open cell architecture, in order to provide a high porosity. Compared to conventional lattice structures, cellular metal foams have a better surface area to volume ratio and good stiffness/strength properties. [SWE-19]

However, they cannot currently be integrated into ITS components via additive manufacturing due to process limitations. In the literature there exist several applications with metal foams, made of various metals e.g. graphite, aluminium, copper, nickel, etc. [CHE-14], [ZHA-15]

2.6.2 Metallic Lattice Structures

According to Gen3D et al. [GEN-21], which reviewed the manufacturable types of lattice structures for additive manufacturing, it can be distinguished between three common groups of lattice structures, which are the a) surface lattice, b) strut or truss based lattice and c) planar based lattice.

A lattice structure is a monolithic architected array of spatial periodic unit cells consisting of faces and/or edges. Strut based or truss-based lattice consists of series of periodic rod-like forms, which are linked in different orientations to other struts in order to form a periodic lattice unit cell. These different unit cell forms are classified in the literature due to their appearance or the location of the joints of the individual cell struts. For the implementation of the ITS technology through additive manufacturing, a body-centre cell (BCC2) strut lattice type is used. [GEN-21], [TAO-16]

3 ITS TECHNOLOGY VALIDATION STRATEGY

In an initial feasibility study in 2019, first thermal analyses of the thermo-physical behaviour of embedded PCM were carried out as part of student work at the FH Aachen. Therein a first simple version of a subroutine was applied to simulate PCM behaviour. This simple version is used as starting point for further subroutine developments in this thesis. The results of the preliminary work are reported in the documents of Gräbener et al. in [JOS-01] and [BER-19] as well as Reiswich et al. [REI-19].

For the development of an analysation and validation strategy, the international space systems engineering standards of the European Cooperation for Space Standardisation (ECSS) was applied in a strongly tailored manner. The aim is to define the general framework conditions and limit values for TVC testing.

3.1 Technological Gap Identification

The introduction of the ITS technology is going to fill an elementary gap in the need for a fully integrated passive TCS, which is able to minimize the time shift between the surplus and the demand of energy in a thermal design to stabilize temperatures. The following scientific and technological approaches address the proposed ITS technology gap, based on the already formulated research question.

1. The ITS integral design infuses the passive thermal storage capability directly into the component by a double wall technique. This makes classic PCM capacitors obsolete and replace them with the new disruptive ITS technology.
2. If the passive thermal control measure is sufficient alone, the ITS technology can participate as major and only TCS without any active TCS.
3. The ITS concept provides versatility to integrate passive thermal control capability directly into the main structure with geometries of any complexity, enabled by additive manufacturing.
4. The passive storage of thermal energy can counteract or even completely bridge the aforementioned physical and technical need for intermediate storage of waste heat between the event of the surplus and the subsequent demand for thermal energy.
5. Identification of a scaling concept, to scale the ITS technology due to the additive manufacturing process and through the possibility of selecting different PCMs for an ideal system response.
6. Additive manufactured parts have a monolithic layout, which enables to minimize thermal contact resistance and further the number of interfaces that in turn lower the system and component complexity.
7. Mass neutral designs shall be reached by thin-walled manufacturing of components.
8. The so far very widespread problem of weak thermal conductivity in PCM storage compartments is completely bypassed by the use of interior lattice, which is anyway necessary for structural integrity and stiffness within the ITS double-wall design.

The key characteristic of the ITS technology is the integral design method. This method is able to join on the one hand components with simple and plane geometries and on the other side also complexly shaped structures. The added value addressed by ITS is, that the PCM mass is directly embedded and sealed as macro-encapsulation into the functional component structure, which is thermally controlled.

3.2 ITS Integral Design Baseline

As already described in [WIL-21] the Infused Thermal Solutions (ITS) technology introduces a monolithic integral design method with fully integrated passive thermal control capability in order to stabilize temperatures, without the need of active heating and cooling systems. Passive in this context means that the ITS TCS has no moving parts and do not need any external supply to be operated.

Figure 3.1: The specimen sectional view illustrates the monolithic double wall ITS integral design, where lattice matrix is integrated and PCM is embedded in the void as macro-encapsulation (left: without PCM, right: PCM infused) [WIL-21]

The ITS concept is a heat storage technology, which makes use of the benefits of the thermo-physical properties of phase change material (PCM) combined with the performance and versatility of the cutting-edge additive manufacturing technology in sintering metallic powder in a Laser Power Bed Fusion (LPBF) process. The fusion of these key technologies enables the synergetic ITS integral method and addresses a unique technological gap to date. For passive temperature stabilisation, the effect of the almost constant temperature during the phase change of the PCM is exploited. During the process heat is stored by the PCM mass as latent heat. With this TCS approach the required heater power (for heating) and radiator size (when cooling) in space can be reduced, in a cold-bias spacecraft design.

Figure 3.2: ITS demonstrator exhibit variant without completed additive print job, to visualize the ITS double wall design with integrated lattice structure [FHA-21]

The ITS design method is based on a double wall design and introduces a novel integral structure with embedded passive thermal control. An additional heat transfer structure is integrated intermediate the double wall design, which is depicted in Figure 3.1.

This intermediate structure is a metallic lattice structure. The enclosing double wall design capsules and seals the PCM as macro-encapsulation, to achieve a vacuum-tight mechanical encapsulation for the proposed use in space, seen in Figure 3.2.

The key characteristic compared to previous technologies is, that the PCM is directly embedded in the additive manufactured integral structure, which is at the same time the primary component structure. Furthermore, the ITS integral method enables to join even complexly shaped free-form surfaces and geometries to one monolithic component, combined with the capability of directly embedded passive thermal control. The monolithic integral design does significantly minimize the number of interfaces and therefore the complexity, which in turn can sharply improve the reliability of the component.

The double wall structure is manufactured in the same process with the intermediate contiguous lattice matrix from one cast, which provides the necessary structural stiffness and significantly enhances the thermal conductance of the monolithic built component. This reduces the drawback of the low thermal conductivity of organic PCM, like paraffin. After manufacturing and post-processing steps, the PCM is infused as filling compound in the voids of the integral structure, based on filling procedures.

The additive manufacturing of all specimens, breadboards and the final demonstrator within the framework of the ITS project had been carried out at the FH Aachen University's internal centre of excellence for additive manufacturing, called GoetheLab.

3.3 Technology Analysation and Validation Concept

The analysation and validation of the ITS technology basically takes place along two branches, at the breadboard level and demonstrator level. The breadboard development campaigns initially involve the empirical and experimental determination of robust machine parameter sets. Once reliable machine parameters and the optimal process-related boundary conditions of the manufacturing plant were obtained, design feasibility studies can be carried out in the following steps.

The test specimens are used to characterise the thermal material properties of the aluminium alloy. These material properties are mandatory to ensure that the thermal and structural models used for simulations and predictions continue to be approximately accurate and reliable.

A simulation method was also developed, analysed and validated within the ESATAN simulation environment to map the thermo-physical PCM behaviour and to be able to predict it in thermal models. The general concept of the analysis and validation methodology can be seen in the following Figure 3.3. However, the focus of this thesis is on the thermal analysation and validation of the ITS technology.

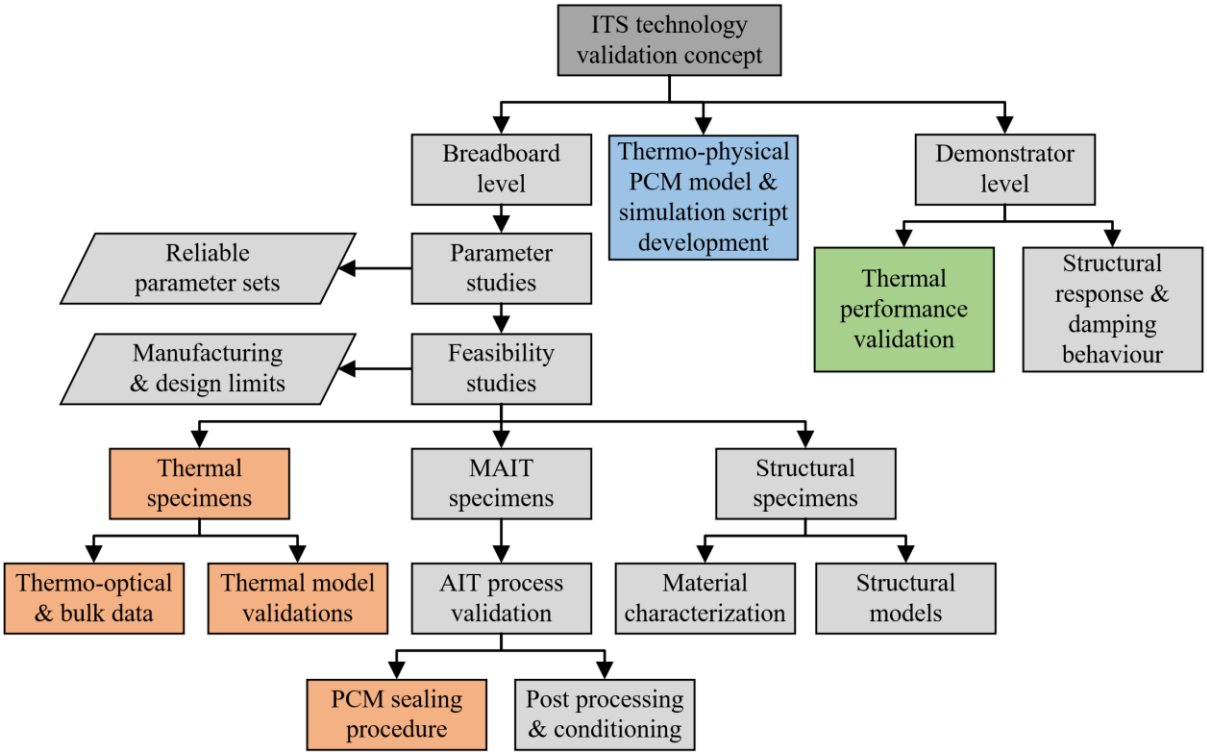

Figure 3.3: ITS technology analysation and validation concept, with a focus on thermal validation

4 ITS THERMAL MODELLING CONCEPT AND DESIGN LAYOUT

This chapter is essential for the understanding of the process of thermal energy storage, which takes place in a thermal mass. Furthermore, this chapter presents a review and concise description of the concepts and mathematical formulations how to model thermo-physical PCM behaviour.

4.1 Thermal Energy Storage with Phase Change Material

Mehling et al. [MEH-08], Sweidan et al. [SWE-19] and Verevkin et al. [VER-18] describe that thermal energy storage (TES) is physically known by the three concepts of (a) mechanical energy, (b) electrical energy and (c) thermal energy. Thermal energy can be accounted by the presence of sensible heat, latent heat, thermo-chemical heat or by a combination of these forms.

It is important to distinguish that sensible heat $q_{sensible}$ defined by equation (1) is stored only by the cause of the change in temperature, depending on the specific heat capacity c_p of the material. In contrast and based on equation (2), latent heat q_{latent} is only stored when the PCM is subject to phase change, depending on the material's mass specific latent heat of fusion L_{PCM}, when considering a solid-liquid phase change. Whereas the effective absorbed enthalpy *H* is defined by equation (3). f_{PCM} is the PCM liquid fraction and m_{PCM} the PCM mass. The index *i* is the initial, *m* the melting and *f* the final temperature. ΔT yields the temperature difference, Δt a specific time span, $\dot{m}_{PCM}$ the PCM mass flow rate (if liquified) and *Q* the incoming heat flow.

$$q_{sensible} = \int_{T_i}^{T_m} c_{p\,solid} \cdot dT + \int_{T_m}^{T_f} c_{p\,liquid} \cdot dT \qquad q_{latent} = f_{PCM} \cdot L_{PCM} \qquad (1) \text{ and } (2)$$

$$H = L_{PCM} \cdot m_{PCM} = m_{PCM} \cdot c_p \cdot \Delta T = \dot{m}_{PCM} \cdot c_p \cdot \Delta T \cdot \Delta t = \int_{t_1}^{t_2} Q \cdot dt \qquad (3)$$

Cabeza et al. [CAB-15] and Barz et al. [BAR-14] clarified that any system, which is subject to TES is able to store energy. TES affects that the gap between energy consumption and energy emission can be reduced to some extent. Every complete TES cycle takes place by applying three principal processes, which are (1) charge, (2) storage, and (3) discharge.

Cabeza et al. [CAB-15] mentioned that a distinction must be made between active and passive concepts. The heat transfer in active storage systems is dominated by forced convection of heat into the storage materials. An active storage system can be direct or indirect configured. In a direct system, the heat transfer fluid is also the storage medium. An indirect system is a dual-medium storage system, where the heat transfer fluid does not store the energy, but an additional second medium.

Furthermore, Pointner et al. [POI-13] classified a latent heat storage system more precisely and expands the categorisation between a stationary system and a transient (moving) system. The breakdown of the classifications is shown in Figure 4.1. In a stationary system the PCM remains more or less at its local position, meanwhile in a transient system pure PCM is generally in move or does not stay at one place.

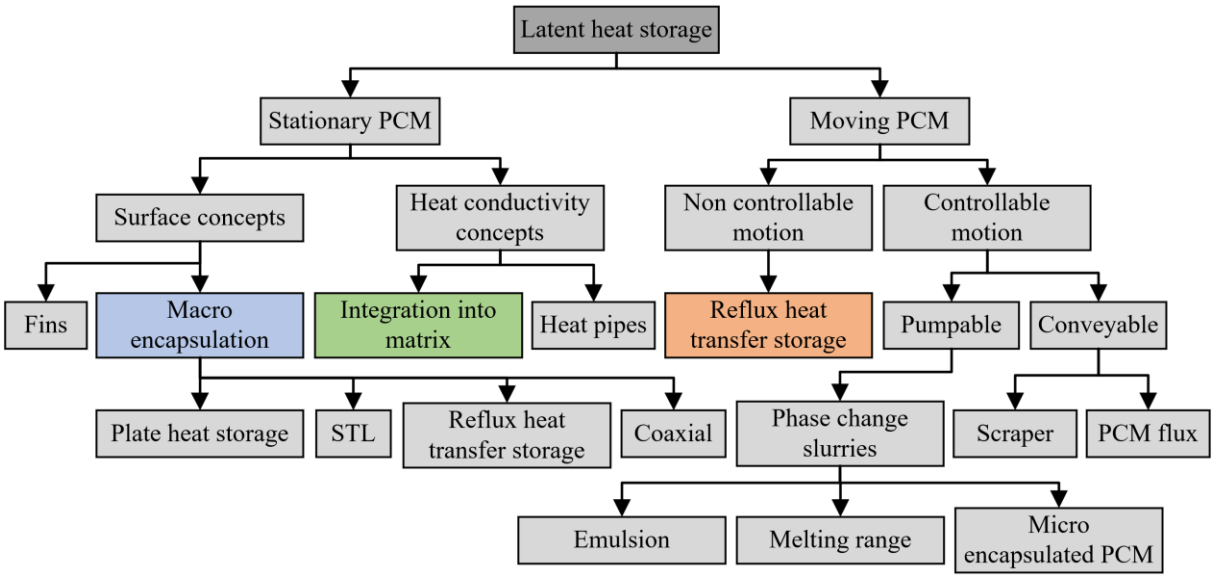

Figure 4.1: Further categorisation of latent heat storage systems, based on Pointner et al. [POI-13]

4.1.1 Storage with Stationary PCM

According to Pointner et al. [POI-13] the stationary PCM storage concept is the origin of surface concepts and heat conductivity concepts.

Surface concepts are known to maximise the surface area, e.g. through fins to increase the external inflow able area when the surface is exposed to convection, or internal to enlarge the area for the heat flow into the PCM mass. For a space related concept, increased radiant power can be achieved by increasing the surface area, as long as there exists no radiative shielding. [POI-13]

Another option is the general macro encapsulation of a PCM void, which is applicable to classical PCM capacitors and to the newly introduced ITS technology. In reflux heat transfer storage systems is the heat transfer fluid not in direct contact with the PCM, but an additional working medium, which takes over the heat transport between the PCM and the fluid to be tempered. The stockage latent (STL) concept uses multiple small capsuled PCM spheres within a heat transfer fluid, which is not further relevant for this work. The coaxial method uses PCM for the encapsulation of pipes, in which a heat transfer fluid is conveyed, which is also not further relevant for this work. [POI-13]

Another potential method which is applicable for stationary PCM storage is the penetration of the PCM volume with a high conductive heat transfer structure or matrix to enable larger PCM layer thicknesses and generally large PCM voids with a good heat transfer characteristic. [POI-13]

4.1.2 Storage with Moving PCM

PCM concepts with a non-controllable motion of the PCM within the encapsulation, can be subject to gravity and convective effects, which is yielded by a reflux heat transfer storage. This behaviour is also investigated in the context of this work, whether convective heat transfer exists and further can dominate the strongly coupled conductive heat transfer mode, enabled by the intermediate aluminium lattice. PCMs with any controllable motions are not further considered in this work. [POI-13]

4.1.3 ITS Technology Storage Definition

In this context and to recap the classifications of latent heat storage systems, the ITS technology combines the synergy of three categories of a latent heat storage, which are summarised hereafter, with the visualisations referred to Figure 4.1.

a) On the one hand, the effect of increased surface area is exploited by the macro encapsulation of the PCM voids within the ITS design (blue: macro encapsulation).
b) In addition, a heat transfer structure in the form of a highly thermally conductive aluminium lattice is embedded intermediate the PCM void (green: integration into matrix).
c) The influence of gravity and convection on the melting behaviour of PCM storage systems is further classified as non-controllable for the ITS technology, and its effects and impacts shall be investigated within this work (red: reflux heat transfer storage).

4.2 Review on Numerical Modelling of PCM Behaviour

According to Barz et al. [BAR-18] the major problem in the multi-phase modelling of the thermo-physical PCM behaviour is the numerical representation of the

a) time-varying melting front,
b) the cyclically cumulative absorbed and emitted energy by the PCM and
c) the influence and magnitude of conductive and possibly also convective heat transfer.

In literature, different methodical approaches are known to model PCM behaviour. First is the concept of stochastic modelling of the nucleation processes to mimic PCM behaviour. However, in a numerical model the implementation is limited by the identification of probabilities, depending on the observed heating and cooling rates of the PCM. This concept will not be pursued further in this work.

Secondly there exists the concept of phenomenological modelling. Thereby the model is based on a deterministic approach, in which PCM behaviour is imitated, based on measured data and empirical results. This classical approach is also used in this work for modelling ITS technology. [BAR-18]

4.2.1 Modelling Framework

In relation on Faden et al. [FAD-18] the numerical simulation of the time-varying melt front and the phase change region of a solid-liquid phase change problem, is also called the Stefan condition. The zone of the phase transition region, which contains solid and liquid PCM constitutes is regarded as a blurred two-phase melt front, which is also called mushy zone.

Mallya et al. [MAL-21] encounters that a transient heat transfer problem in the PCM is described by a non-linear Stefan problem, due to the non-linear behaviour and propagation of the melt fronts.

4.2.1.1 Stefan Problem

According to König-Haagen et al. [KOE-17], Idelsohn et al. [IDE-94] and Fleischer et al. [FLE-15] solid-liquid phase change problems, where the heat transfer is conductively (and convectively) driven, are generally known in the literature as Stefan problem. From the mathematical point of view the Stefan problem treats the phase change process as a moving boundary problem, where the movement of the interface (which is the phase front) is non-linear.

Dutil et al. provided in [DUT-11] and [DUT-14] a comprehensive review related on formulations for the mathematical modelling of phase change problems for different geometries. Basically, the Stefan model is the fundamental mathematical description of the phase change phenomenon and is named after Jožef Stefan, a Slovene physicist who introduced the general class of such problems in 1889. The solid and liquid phases are separated by an infinitesimal thin layer.

Sweidan et al. [SWE-19] summarised further that the thermo-physical properties of both phases can vary. The bulk properties appear to an indifferent, steep change along the phase change interface. Tracking of the moving interface between the solid and liquid phase is only analytically possible for 1D or 2D problems with a specific melting temperature (ideal PCM behaviour). But this so-called sharp model is limited for complicated shapes with a variable phase transition temperature or even more when using phase transition hystereses to describe the PCM behaviour within the phase transition zone (real PCM behaviour).

4.2.1.2 Grid Scheme

It is further summarised by Idelsohn et al. [IDE-94], Faden et al. [FAD-19] and König-Haagen et al. [KOE-17] that the numerical methods for modelling the moving boundary problem, which considers and applies the Stefan problem, can be classified into

a) deforming grid schemes and
b) fixed grid schemes.

In the method of deforming grid schemes, the position of the mushy zone is achieved by rearranging the mesh. This means that the solid-liquid phase boundary is explicitly determined and can be sharply identified. [FAD-18]

When using fixed grid schemes, the change of the phase front is therefore not explicitly tracked. Instead, the mushy zone is determined by an additionally introduced parameter that indicates the local specific PCM liquid fraction at the fixed grid thermal node, which is also known in literature as the enthalpy-porosity factor. Within the fixed grid scheme the local position and global extent of the PCM mushy zone is determined as a function of temperature or enthalpy. [FAD-18]

Faden et al. [FAD-19] and König-Haagen et al. [KOE-17] stated that the fixed grid scheme can be embedded more flexibly and easily in numerical environments and subroutines, which use a finite element method (FEM) or finite difference method (FDM). This is why the fixed grid scheme is the most widely used method for solving phase change problems. Another reason for applying the fixed grid scheme is, that the ESATAN environment can only handle the FDM with lumped parameters.

4.2.2 Numerical Modelling Approaches

Sweidan et al. [SWE-19] and Faden et al. [FAD-18] claimed, the energy equation has a non-linear behaviour applying the fixed grid method over the entire phase change process. This is because the

a) thermo-physical properties of the solid and liquid PCM constituents vary.
b) Secondly the absorbed latent heat during the phase change process with the associated propagating melt front is very dynamic and therefore no longer linear, as it is the case with sensible heat, where the specific heat is solely linearly dependent on temperature.

Faden et al. [FAD-18] reviewed that for most applications with industrial grade (technical-grade) PCMs a non-isothermal phase change behaviour is given. The non-isothermal behaviour is mainly due to the impurities of technical grade PCM. Even when using initially high-purity PCM a non-isothermal behaviour is stated. Although contact with other materials or the ambient air often leads to unwanted contamination, these impurities do not mean that the PCM is permeated with other substances. The purity from production of > 99.9% is no longer achieved but is usually in the range of > 99%.

König-Haagen et al. [KOE-17] reviewed the most common macroscopic formulations for solid-liquid phase change models in the literature, which are depicted in Figure 4.2. The reviewed modelling approaches also consider partially conductive and convective heat transfer modes.

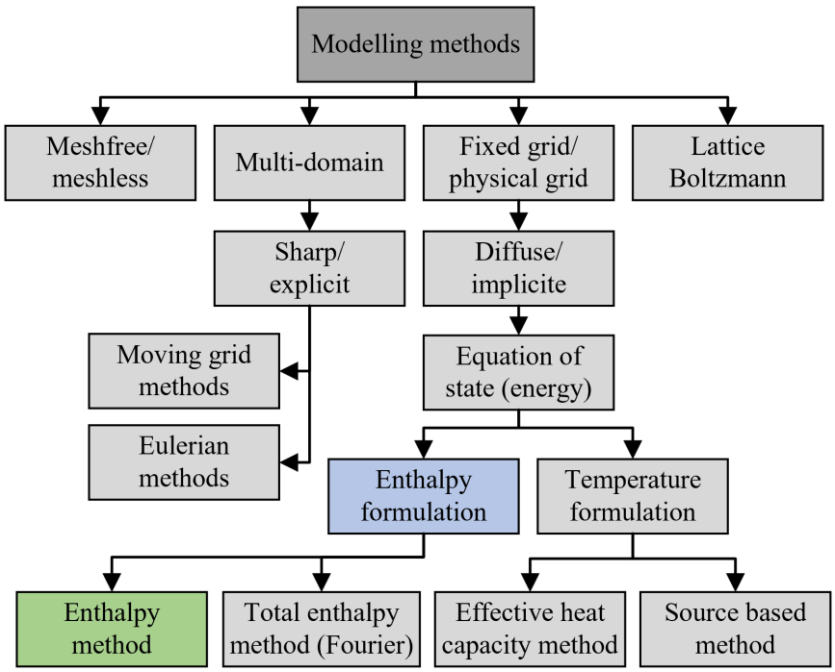

Figure 4.2: Scheme of a comprehensive review of PCM modelling methods in order to describe the thermo-physical PCM behaviour by numerical models, based on König-Haagen et al. [KOE-17]

In general, there exist four concepts for numerical PCM modelling. These are the meshfree, multi-domain, fixed grid and lattice Boltzmann approaches. The meshfree concept is not further discussed. The Boltzmann method is described in chapter 4.2.2.4. Multi-domain models are sharp and explicit formulated numerical models based on a moving grid or an Eulerian method, which are also not considered further. [KOE-17]

Mathematical formulations of a phase change problem can relate on the explicit or implicit domain. The most interesting and potential approach is the fixed grid concept. This concept is based on implicit mathematical formulations and the phase front is therefore diffusively tracked. Due to the diffusive interface the thermo-physical parameters are smeared for discretisation at the diverse grid points (thermal nodes), within the macroscopic model. [KOE-17]

However, the equation of state (energy formulation) can basically be defined by two different thermo-physical approaches, which are based on temperature or enthalpy formulations. The enthalpy balance can further be calculated by the most common enthalpy method or total enthalpy method. The temperature based formulations are further related on the source based method or the apparent (effective) heat capacity method and are for these reasons not applied in this work. [KOE-17]

4.2.2.1 Enthalpy Method

The enthalpy method is the most common method applied to date and is formulated in the implicit domain with diffusive interfaces. Thereby the phase change regime is described by a mushy zone, where the PCM can coexist in both phases, which is named a diffusive interface. The energy balance of the entire PCM mass (solid and liquid phase fractions) is overall defined by one energy equation for both phases. The enthalpy method is the simpler concept, which can handle complex geometries as well as phase transition hystereses. The only unknown (dependent) parameter of this concept is the current temperature of the local PCM node. This simplified but precise method can be solved by FEM or FDM calculations. [SWE-19]

In the total enthalpy method, the Fourier's law is defined as a function of enthalpy and integrated over a certain temperature range. Within this dedicated temperature window the net enthalpy balance absorbed in the PCM mass will be derived. [KOE-17]

Pernsteiner et al. [PER-21] clarified that heat transfer by conduction in more than one dimension is only possible by applying the enthalpy method. With an additional heat transfer mode (convection) within the PCM void, the effective heat capacity method in combination with FEM shows a good agreement in solving the two-dimensional Navier-Stokes equations. The Navier-Stokes equations are partial differential equations, which describe the motion of incompressible fluid flows within the liquid phase, due to the influence of natural convection.

Voller et al. [VOL-90] claimed that the enthalpy method does not require any explicit conditions with regard to the PCM phase change boundary. Furthermore, this method allows to treat the numerical modelling of the two-phase solid-liquid phase change problem on the basis of a fixed grid scheme. The enthalpy formulation is based on a conduction-controlled phase change problem.

The advantage of the enthalpy method is that the heat flow integral can be directly integrated over a time interval from step-wise data, using the trapezoidal method. This procedure yields also the only way to determine the absolute enthalpy of a virtual PCM thermal node in ESATAN. Furthermore, this method works independently of temperature changes (rates) and variations in temperature gradients. For these reasons, the enthalpy method is applied as modelling standard for the PCM subroutine in this thesis, in order to predict the PCM behaviour within the ITS research.

4.2.2.2 Effective Heat Capacity Method

The apparent heat capacity method is also known as equivalent or effective heat capacity method. Zheng et al. [ZHE-19] reviewed that the apparent heat capacity method applies a two-phase mass and heat transfer model. Thereby the solid to liquid phase change process is thermo-physically modelled by an enthalpy-porosity formulation. The mushy zone is assumed to be the porous region, where the porosity describes the fraction of solid and liquid PCM, which is the same circumstances as for the enthalpy method.

For mathematical formulations in FDM schemes the heat capacitance of a material is initially fixed. A dynamic manipulation of the effective heat capacitance is going to lead to a violation of the conservation of mass and thus to a physically incorrect change of the total capacitance of the entire thermal model. Hence, this method is not applicable in the ESATAN environment, which is mandatory for the PCM subroutine. [KOE-17]

4.2.2.3 Source Based Method

The source based method separates the total energy being absorbed into sensible heat and latent heat. The source-based method is usually used in the global calculation of thermo-physical states, where this concept also provides a potentially good accuracy in the models and the nodal enthalpy balance. However, this method can only be used if the calculation method supports one overall energy formulation, which is not applicable in ESATAN. [KOE-17]

4.2.2.4 Lattice Boltzmann Method

Xinyi et al. [LI-19] reviewed that the enthalpy-based lattice Boltzmann method belongs to the implicit methods and was firstly introduced by Jiaung et al. in order to simulate phase change processes with heat conduction. Building on this model, Li et al. introduced a pore-scale lattice Boltzmann kinetic model to simulate the melting behaviour of PCM with embedded metal foam in 2D space based on quasi-particles.

Jianqing et al. [CHE-14] reviewed that Gao et al. and Zahn et al. simulated the PCM melting process with integrated metal foams using a lattice Boltzmann model. They assumed a thermal non-equilibrium between the PCM and the heat transfer structure. The velocity field of the liquid PCM phase was described by a density distribution function. The phase change problem was numerically considered by using an enthalpy model, as described above. The location of the melting front in the numerical model is dependent on time and temperature, which are dictated by the lattice Boltzmann model.

Due to the fact that the ESATAN thermal solver interprets thermal data as lumped parameters in the FDM scheme, it is not possible to apply this variant. The reasons are that the spatial information about the positions and locations of the thermal nodes can neither be known nor processed. Furthermore, the velocity fields can neither be determined in 2D nor 3D in the ESATAN environment.

4.3 Review on PCM Hysteresis Models

To anticipate the further course of action, it will become clear in chapter 4.4 that hysteresis models are applied, in order to model the thermo-physical enthalpy-temperature behaviour of the PCM.

4.3.1 Static Hysteresis Model

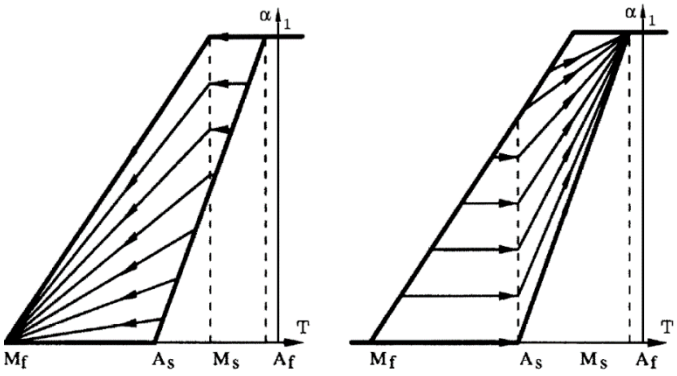

Figure 4.3: α-trajectory model, which describes the intermediate rescaling path algorithm, related on the PCM liquid phase fraction of the last continuous value along the hysteresis [IVS-94]

Ivshin et al. [IVS-94] already presented in 1994 a static hysteresis model, which is based on rate independent enthalpy or temperature induced hystereses.

Ivshin introduced the approach of a combined linear dual unfolding hysteresis for phase change processes, which is still relevant today. These hystereses are depicted in Figure 4.3, where the y-axis yields the phase fraction α. The outer curves represent completed or continuous phase changes. For interrupted phase change cycles, the intermediate directional hystereses are dynamically defined by an internal rescaling path algorithm. The intermediate internal path family, which is called the α-trajectories, are dependent on the current state of charge of the PCM cell (PCM liquid phase fraction).

4.3.2 Diagonal Model

Zoltán et al. [ZOL-19] introduced in 2019 a novel PCM modelling concept with hystereses, which is called the diagonal model. This model also covers the phenomenon of interrupted phase change cycles. The findings in the study are based on differential scanning calorimetry (DSC) measurement data with paraffin wax. The evaluation of the measurement results for complete and interrupted phase changes yielded a good approximation for interrupted cycles. Those cycles are modelled by two intermediate lines with the respective corner point on the diagonal connecting line, visualised in Figure 4.4. The diagonal line of the model is always spanned between the characteristic values of the initial point T_s^m (start of melting) on the melting hysteresis and the initial point T_l^s (start of solidification) on the solidification hysteresis at which PCM begins to solidify.

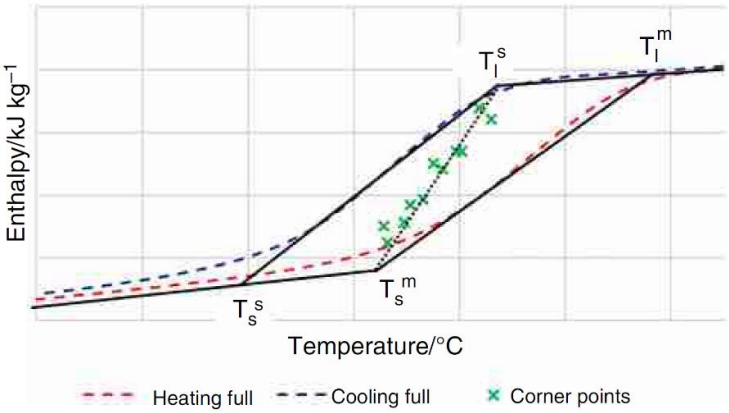

Figure 4.4: Novel diagonal model for thermo-physical modelling of an industrial-grade PCM, which is subject to complete and also interrupted phase change cycles, based on Zoltán et al. [ZOL-19]

The great advantages of this hysteresis model are that it can be applied to any two-phase solid-liquid PCM problem, as long as the characteristic corner points of the hysteresis are known. In addition, the simple interpolation of the intermediate points of the line fitting algorithm for an incomplete phase change process require only little computing power, during which the model shows a good accuracy. That's why this model approach is applied for the thermo-physical modelling of PCM, which is embedded in the ITS technology.

4.3.3 Curve Scale Model

Barz et al. in [BAR-18] and [BAR-19], Cabeza et al. [CAB-15] and Li et al. [LI-18] have focused in several publications on the definition of phenomenological macroscopic modelling approaches of technical-grade PCMs by using hystereses models. The same independent work has been also performed by Klimes et al. [KLI-20]. The data to generate hystereses are derived from DSC measurements of complete phase transition cycles. However, the researchers have investigated complete and incomplete phase transition cycles, which take place over the temperature range where both phases (solid and liquid) coexist. Rate-dependent static hysteresis models and rate-independent models with dynamic hystereses have been investigated. The PCM liquid fraction is used to derive the current state of the local phase change progress. The dynamic hysteresis parameters are indirectly derived from correlations of micro-kinetic models related on experimental data. The experiments include multiple successive melting and solidification cycles with incomplete phase transitions and direction changes. Based on the findings they introduced modified enthalpy-temperature models, which are depicted in Figure 4.5.

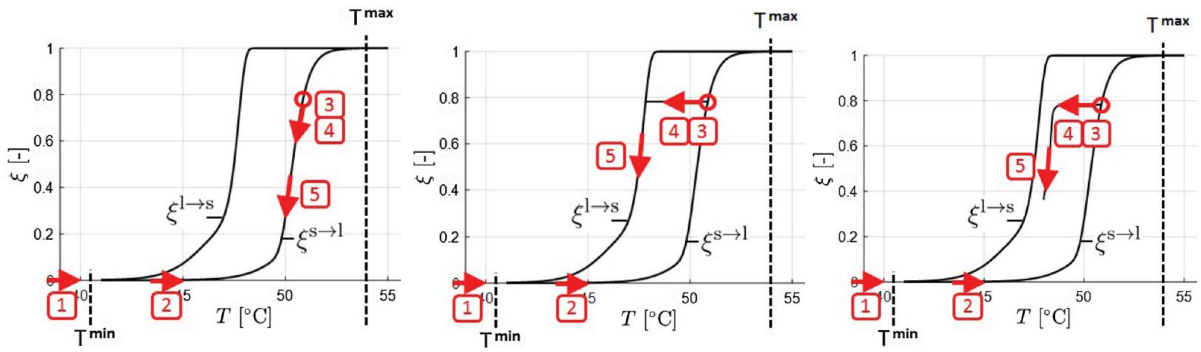

Figure 4.5: Phase transitions with the curve track model (left), the curve switch model (middle) and the curve scale model (right) in order to simulate a realistic PCM behaviour in presence of incomplete phase change cycles along the melting and the solidification hysteresis [BAR-19]

The curve track model (left), curve switch model (middle) and curve scale model (right). The classical curve track model (Figure 4.5, left) is not different from standard numerical models that define a hysteresis region without interceptions. The curve track model reproduces the temperature behaviour of continuous phase changes. In the case of incomplete phase change processes, the temperature behaviour is fed back to the currently active hysteresis.

The curve switch model (Figure 4.5, middle) changes the hysteresis in the case of an incomplete phase change and returns the temperature to the corresponding opposite hysteresis.

The third and novel curve scale model (Figure 4.5, right) had been based on a variant by Delcroix et al. and was further optimised by Barz et al. The slope of the intermediate transition line is always parallel to the slope of the respective major hysteresis. However, the relative position of the intermediate hysteresis depends on the PCM liquid fraction and thus on the progress of the previously interrupted phase change progress. Quantitative analyses through cross validations have shown that in principle the dynamic model of the curve scale model can follow and address the real PCM behaviour with good accuracy, also in the case of incomplete phase changes. That's why this type of model is guided as baseline, as those of Zoltán et al., to develop and advance the PCM subroutine within the ITS research.

4.4 Applied Thermo-Physical PCM Model

The correct performance of a numerical model to simulate a thermal energy storage system, based on latent heat with a two phase solid-liquid envelope, mainly depends on the thermo-physical PCM properties and the data-based non-ideal phase transition behaviour. [BAR-19]

The baseline for the ITS PCM model is given by the LHS method in a fixed grid scheme to simulate the thermo-physical behaviour of PCM. According to Barz et al. [BAR-21] most technical-grade PCMs are subject to impurities. From this follows that the phase transition temperature ranges are expanded to some extent, which in turn addresses a non-isothermal PCM behaviour.

Within this expanded zone the PCM coexists in the solid and liquid state, also called mushy regime. In contrast to ideal PCM, technical-grade PCM has neither fixed nor a sharp transition temperature. Furthermore, the temperature plateaus do not remain constant during phase transition. This phenomenon is known as a non-isothermal phase transition behaviour. However, in an idealised model with ideal PCM a discontinuity will exist, where the PCM is immediately in phase transition with constant temperature and an extremely steep enthalpy gradient. This would be physically not correct and can lead to numerical problems. [WIL-21]

Since the framework conditions are given by the fact that thermal simulations and predictions of the PCM behaviour must be embedded in ESATAN, the definitions of the thermal models by using the FDM and lumped parameters are also mandatory. It shall be noted that the ITS PCM modelling concept does not consider the effects of natural convection so far. However, the possible influences of convection on specimens are analysed and tested within the framework of thermal analyses and TVC tests. The results are listed in chapter 6.6.

Dudon et al. [DUD-19] also used ESATAN to simulate the thermo-physical PCM behaviour within their thermal models. Therefore, they may have developed a subroutine which is able to simulate the PCM behaviour.

According to a review of Fleischer et al. [FLE-15], in literature most concepts approximate PCM behaviour by using a rate-independent enthalpy-temperature formulation, where the current state of temperature dictates the liquid phase fraction f_{PCM} (enthalpy porosity). This means that these concepts are temperature driven. In contrast to that, the numerical PCM model of the ITS technology is enthalpy driven for the approximation of the thermo-physical PCM behaviour.

The amount of heat (enthalpy) h_{eff} absorbed or released is determined by the integral of the heat flow q_{net} tracked over time between two specific thermal nodes (i, j), which is formulated in the equation (4). Where h_{max} is the maximal enthalpy absorbable and h_{old} represents the already absorbed enthalpy from previous calculation steps.

$$f_{PCM} = \frac{h_{eff}}{h_{max}} = \frac{h_{old} + \int_{t1}^{t2} q_{net} \cdot dt}{h_{max}} \tag{4}$$

According to Paul et al. [PAU-01] and related on the ESATAN user manuals [ESA-22] the total energy balance E_i represented in the lumped parameter formulation in the FDM scheme is given by the equation (5). The indices *i* and *j* define the link between two thermal nodes. Where C_i is the nodal capacitance, T_i the nodal temperature and σ the Stefan-Boltzmann constant. The linear conductor *GL* and radiative conductor *GR* are considered in interaction with remaining heat flows, such as solar irradiation *QS* and internal heat loads Q_i to affect the temperature change of the system. Thereby the conservation of mass and energy is given.

$$E_i = C_i \cdot \frac{dT_i}{dt} = \sum_j GL(j,i) \cdot \left(T_j - T_i\right) + \sigma \cdot \sum_j GR(j,i) \cdot \left(T_j^4 - T_i^4\right) + Q_i \tag{5}$$

That's why the feedback parameter enthalpy porosity, which controls the heat storage process and quantifies the dynamically stored local enthalpy amount in the ITS PCM subroutine, addresses the equivalent net heat flow. The effective enthalpy is calculated from the net heat flow by step wise trapezoidal integration as linear superposition.

The non-isothermal phase transition behaviour is numerically implemented by hystereses in order to consider the different PCM state parameters, which is also partly introduced by Barz et al. [BAR-18]. This means that the PCM behaviour is approximated by a two phase hystereses model with a distinct solid and liquid phase with a non-isothermal behaviour, which is discussed hereafter.

4.4.1 Enthalpy-Temperature Hysteresis Model

Hysteresis models are applied to decouple the melting and solidification process, in order to enable an acceptable approximation to an industrial-grade or non-isothermal PCM behaviour. To roll into a more realistic model concept for modelling ITS, the temperature within the transition zone is dependent on the latent heat absorbed. Within this regime the solid and liquid PCM fractions do coexist. For the ITS numerical model enthalpy-temperature profiles are applied to address the hysteresis for solid-liquid (melting) and liquid-solid (solidification) phase transitions. [WIL-21]

The enthalpy-temperature profiles are generally related on heat capacity data, which in turn are derived from DSC measurements. For most tests and measurements in this work, the paraffin hexadecane ($C_{16}H_{34}$) with a purity > 99% is used. The calorimetric data for the corner points of the hystereses relate on data from the work of Vélez et al. [VEL-15], which are depicted in Figure 4.6. The hysteresis data are not drawn to scale and vary for different PCMs. The hysteresis curves between the corner points along the melting and solidification profiles are linearised. [WIL-21]

The temperatures T_l^c and T_s^c span then solidification hysteresis, whereas T_s^m and T_l^m define the melting hysteresis. The diagonal model is based on the enthalpy points h_s^m and h_l^c with the related temperature points T_s^m and T_l^c. Where *m* addresses the liquefying and *c* the solidifying phase state. If one donates *l* as the liquidus limit and *s* as the solidus limit, is *x* the state of stored enthalpy at the current phase state. $T_{s,x}^c$, $T_{d,x}^c$ and T_x^c as well as $T_{s,x}^m$, $T_{d,x}^m$ and T_x^m define the interrupted cycles. [WIL-21]

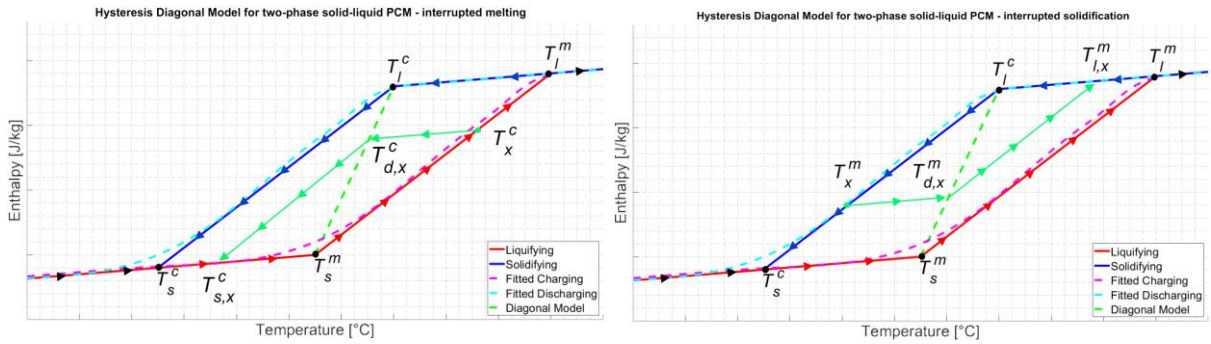

Figure 4.6: Thermo-physical modelling of an industrial-grade, non-isothermal PCM behaviour with decoupled melting (red) and solidification (blue) hysteresis for uninterrupted phase transitions. The intermediate green profiles indicate incomplete phase transitions for a melting (left) and for a solidification problem (right), by applying the diagonal model of Zoltán et al. [WIL-21]

4.4.2 Subcooling Effects

Another point for using hystereses is to consider the effect of subcooling for phase change problems, especially at organic PCM, which further contributes to a non-isothermal behaviour. [WIL-21]

According to Barz et al. [BAR-18], Cabeza et al. [CAB-15] and Mehling et al. [MEH-08] subcooling (or supercooling) means that the liquid PCM fraction only starts to solidify at lower temperatures, than the theoretical temperature. This phenomenon is problematic and significantly decreases the latent heat storage efficiency. The probability of subcooling can be greatly reduced by technical measures. Subcooling occurs primarily during solidification of liquid PCM. Due to the crystallisation kinetics and the initial solidification around a nucleus, a solid phase is formed. Accordingly, the stored latent heat of the liquid to be solidified is actually released into the environment. However, organic paraffins in particular have a weak thermal conductivity. Another deteriorating effect is the thermal resistance over a phase boundary (melt front) between solid and liquid. These effects can lead to that the heat may could not be dissipated back into the system and results then to the phenomenon of supercooling.

According to Uzan et al. [UZA-17] and Barz et al. [BAR-21] subcooling can also result from slow heat release during solidification. The reasons could be a slow diffusion process, a slow formation of the crystal lattice at crystalline (microscopic) scale or different chain length in the PCM mixtures of various PCM types or compounds. However, since no mixing of different PCM types, compounds or additives are desired within the ITS research, these effects are not taken into account for the numerical simulation of the PCM behaviour.

Indeed, the ITS aluminium lattice is a high conductive heat transfer structure. The local effect of subcooling can be largely eliminated as Cabeza et al. suggested. This is because the increased effective thermal conductance leads to a slightly inert isothermal behaviour. This means that the thermocline (isolating) behaviour of pure PCM is minimised due to the lattice structure, which is continuously and coherently embedded in ITS parts. This lattice evenly pervades the PCM mass, in order to enable a permanent heat transfer bypass. The approach of negligible subcooling effects is validated by various TVC measurements within the ITS research, where no distinct subcooling behaviour can be identified.

Chen et al. [CHE-14] was also able to determine this system behaviour in his work with similar specimens.

4.4.3 Complete Phase Change

A complete (non-interrupted) melting or solidification cycle takes place along the individual hysteresis and is mathematical described by equation (6). Therein the current nodal PCM liquid fraction f_{PCM} along the melting hysteresis (red profile) or the solidification hysteresis (blue profile) are defined for non-interrupted transition cycles, related on the work of Zoltán et al. [ZOL-19]. The reference points are the points in Figure 4.6, which span the red and blue profiles. [WIL-21]

$$f_{PCM} = \begin{cases} 0 & h_x < h_s \\ \dfrac{h_x^m - h_s^m}{h_l^m - h_s^m} = \dfrac{T_x^m - T_s^m}{T_l^m - T_s^m} & h_s \le h_x \le h_l \;\; and \;\; \Delta h > 0 \\ \dfrac{h_x^c - h_s^c}{h_l^c - h_s^c} = \dfrac{T_x^c - T_s^c}{T_l^c - T_s^c} & h_s \le h_x \le h_l \;\; and \;\; \Delta h < 0 \\ 1 & h_x > h_l \end{cases} \tag{6}$$

4.4.4 Interrupted Phase Change

In addition to completed cycles, incomplete cycles can also occur. The PCM nodes of a model can be subject to an incomplete phase change process. This behaviour comes into play when the phase fraction of a single PCM node or even of multiple PCM nodes are neither completely solid nor liquid. If the phase state toggles between the solidifying or melting hysteresis, which is triggered by a varying heat flow, the model must handle the enthalpy-temperature crossover between both hystereses. To consider the interrupted enthalpy charging and discharging process, a dynamic intermediate enthalpy-temperature profile must be embedded. [WIL-21]

Many concepts are reviewed from literature. The numeric representation of an interrupted phase change process in the PCM subroutine is adopted from the diagonal model, which has been introduced by Zoltán et al. [ZOL-19]. The diagonal model is based on an extension and combination of the "Transition scenario" suggested by Bony and Citherlet et al., together with the "Stay scenario" model described by Chandrasekharan et al. The mathematical definition is given by equation (7), which defines the temperature-enthalpy relations of an incomplete phase change. [WIL-21]

This algorithm can be applied to solve a two-phase problem with a distinct hysteresis regime. The algorithm also enables die implementation of multiple PCM types within one model and further formulates the conditions and states, based on Zoltán et al. diagonal model during an incomplete cycle. [WIL-21]

$$f_{PCM} = \begin{cases} 0 & h_x < h_s \\ \dfrac{T_x^m - T_s^m}{T_l^m - T_s^m} = \dfrac{T_{d,x}^c - T_s^m}{T_l^c - T_s^m} = \dfrac{T_s^m - T_{s,x}^c}{T_s^m - T_s^c} & h_s \le h_x \le h_l \;\; and \; interr. \; melting \\ \dfrac{T_x^c - T_s^c}{T_l^c - T_s^c} = \dfrac{T_{d,x}^m - T_s^m}{T_l^c - T_s^m} = \dfrac{T_l^m - T_{l,x}^m}{T_l^m - T_l^c} & h_s \le h_x \le h_l \;\; and \; interr. \; solidifi. \\ 1 & h_x > h_l \end{cases} \tag{7}$$

This resulting diagonal model is defined by a diagonal connection line (see Figure 4.6, dashed green line), which is always aligned between the characteristic hysteresis temperatures T_s^m and T_l^c. Through an integrated software switch, the selection of the hysteresis profile is situational given to enable intermediate curve fitting. This switch is generally triggered by the enthalpy difference (delta), which is in turn calculated by the current enthalpy subtracted by the enthalpy of the previous step. [WIL-21]

4.5 ITS Design Heat Transfer Model

Hale et al. [HAL-71], Gilmore et al. [GIL-02] and Collette et al. in [COL-11], [COL-12] and [COL-13] formulated years ago preliminary steps and considerations on the general design and layout of a classic PCM capacitor. It was assumed that low conductive PCMs (e.g. paraffins) would be used to implement the design, because of their low specific weight to latent heat ratio. To minimise the drawback of low thermal conductivity in the pure PCM mass, the use of filler material was also recommended by them, which is in line with the findings of the ITS research.

For all additively manufactured test specimens and demonstrators within the ITS research a strut-based lattice is used to consolidate thermal predictability and quasi three-dimensional modelling.

4.5.1 Heat Transfer Structure

The in-plane (IP) and out-of-plane (OP) linear conductors (in ESATAN: GL) are essential for the numerical PCM behaviour. The heat transfer model with the related phase change problem is mainly driven by heat conduction via the aluminium lattice. A single conductor (GL) is defined between two specific adjacent thermal nodes. In this way various in-plane and out-of-plane GLs are defined in an interdependent quasi-three-dimensional domain, which can be seen as a quasi-three-dimensional conductive network. The schematic of the conductive network is visualised in Figure 4.7. [WIL-21]

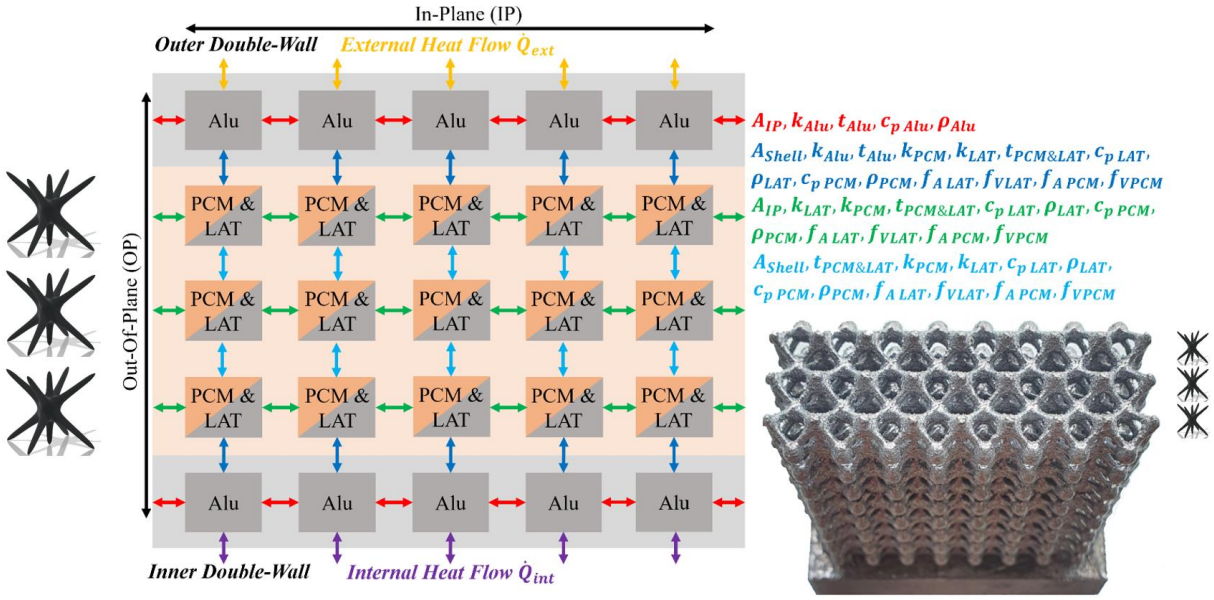

Figure 4.7: Thermal linear conductor scheme of the ITS heat transfer model, representing a principle ITS PCM infused double walled integral structure. The quasi three-dimensional conductive network is composed of partial multiple one-dimensional conductive heat transfer links, to rebuild a numerical heat transfer model. [WIL-21]

The total number of in-plane PCM nodes in a PCM layer is identical to the number of the direct parallel proximity thermal nodes (non-PCM nodes, Alu), which represent the solid ITS aluminium double wall. To simplify the modelling concept, the three out-of-plane PCM&LAT (LAT: lattice) element rows are numerically combined into one row and thus into one effective intermediate PCM layer, which is then exactly the number of in-plane PCM nodes. Finally the outer aluminium thermal nodes (Alu), which are interfacing the interior PCM&LAT nodes represent the ITS double wall design with the intermediate PCM layer. [WIL-21]

The effective capacitance of the infused PCM/LAT volume is defined by numerically smeared bulk properties in dependence on the PCM/LAT volume fractions. The thermal model is formulated in the fixed grid scheme by lumped parameters representation, applying FDM. The effective volume of the PCM and LAT fractions are determined by the product of effective PCM/LAT areas times the virtual thickness of the respective PCM&LAT layer. [WIL-21]

Belcher et al. [BEL-19] claimed for modelling the effective thermal conductivity k_{eff} through a lattice structure, that the individual lattice cells need to be simplified. This is done by parsing them into nodes with corresponding linear conductors. But Belcher's approach seems to be too fine for a FDM scheme. Each unit lattice cell contains multiple nodes to represent all the filigree conductive links of all strut-beams to all surrounding unit cell element beams. However, this approach is further pursued on a modified and simplified macroscopic level for the modelling of the ITS technology. [WIL-21]

The linear conductors are considered constant and therefore not temperature dependent, in both solid and liquid state, for the fractions PCM and LAT respectively. As mentioned, a significant drawback of paraffin based PCMs is its low thermal conductivity k_{PCM}. The mono-directional heat flow between two distinct PCM&LAT nodes is related on the linear conductor values, which in turn relate on the effective PCM ($k_{PCM} \cdot f_{A\,PCM}$) and LAT ($k_{LAT} \cdot f_{A\,LAT}$) thermal conductivity. The sum of both results in the effective lumped thermal conductivity k_{eff}. Where $f_{A\,PCM}$ yields the PCM areal fraction and the LAT areal fraction $f_{A\,LAT}$ is donated as $f_{A\,LAT} = 1 - f_{A\,PCM}$. Due to the three orders higher thermal conductivity of the additive manufactured aluminium LAT compared to the PCM, the heat flow is mainly passed through the lattice aluminium bulk material. [WIL-21]

$$k_{eff} = k_{PCM} \cdot f_{A\,PCM} + k_{Alu} \cdot (1 - f_{A\,PCM}) \tag{8}$$

For consistent modelling and looking forward using many different PCMs in one ITS thermal model with various thermal conductivities, the PCM conductor fractions are still considered in the numerical model. The equation (9) defines the thermal conductor values for a parallel link, whereas equation (10) defines a thermal conductor in a serial link. These equations (9) and (10) provide insight into calculating an in-plane and out-of-plane linear conductor as well as how to interface the thermal conductor *GL* between the LAT and PCM bulk properties (node 1 and node 2) with the structural double wall of the component. [WIL-21]

$$GL_{parallel} = \sum_{i=1}^{n} GL_i \qquad GL_{serial} = \frac{1}{\frac{1}{GL_1} + \frac{1}{GL_2}} = \frac{GL_1 \cdot GL_2}{GL_1 + GL_2} \qquad \text{(9) and (10)}$$

By an appropriate interconnection and consideration of the LAT and PCM bulk properties it is possible to define a generic and fully parametric term for an end-to-end in-plane as well as out-of-plane GL. By using the area-specific and volume-specific normalisation factors (fractions), the corresponding bulk material properties can be considered in an equivalent manner. The PCM and LAT (Alu) infused nodes are considered as virtual nodes in ESATAN. The PCM-LAT volume fractions ($f_{V\,PCM}$ and $f_{V\,LAT}$) and the area fractions ($f_{A\,PCM}$ and $f_{A\,LAT}$) primarily dictate the properties and parameters for each PCM node. $f_{L\,PCM}$ and $f_{L\,LAT}$ donate the PCM-LAT length fractions. Further the properties layer thickness t_{eff} of the PCM&LAT layer, the effective area A_{node} for heat flow depending on the effective area fractions, the density ρ and specific heat capacity c_p. The effective capacitance C_{eff} depends on the derived PCM-LAT volume fractions and are automatically calculated by the subroutine. [WIL-21]

$$C_{eff} = t_{eff} \cdot A_{node} \cdot \left((1 - f_{V\,PCM}) \cdot \rho_{Alu} \cdot c_{p\,Alu} + f_{V\,PCM} \cdot \rho_{PCM} \cdot c_{p\,PCM}\right) \tag{11}$$

The following equation (12) defines a generic and fully parameterised in-plane thermal conductor, whereas equation (13) represents a generic out-of-plane linear conductor. Therein l_1 and l_2 are the distances between the FDM note centre and the node edge of the thermal node. A_{Shell} is the shell area and A_{Edge} is the joining surface of the fused thermal conductive link. The thicknesses t_1 (inner wall) and t_2 (outer wall) are the structural double wall thicknesses.

$$GL_{IN-PLANE} = \frac{1}{\left(\frac{1}{\left(\frac{k_{PCM} \cdot f_{A\,PCM}}{f_{L\,PCM}} + \frac{k_{LAT} \cdot f_{A\,LAT}}{f_{L\,LAT}}\right)}\right) \cdot \left(\frac{l_1 + l_2}{A_{Edge}}\right)} \tag{12}$$

$$GL_{OUT-OF-PLANE} = \frac{1}{\left(\frac{1}{\frac{k_{LAT} \cdot A_{Shell}}{0.5 \cdot t_{1/2}}} + \frac{1}{\left(\frac{k_{PCM} \cdot f_{A\,PCM}}{f_{L\,PCM}} + \frac{k_{LAT} \cdot f_{A\,LAT}}{f_{L\,LAT}}\right) \cdot \frac{A_{Shell}}{0.5 \cdot t_{eff}}}\right)} \tag{13}$$

4.5.2 Lattice Cell Architecture

There exists a huge number of metallic lattice types and variants in literature. The decision was to use strut-based lattice structure as intermediate filler matrix for the interior of the ITS components.

Strut-based lattice structures have a good surface area to volume ratio (increased heat transfer area), provide a high effective stiffness of the entire part due to periodic and continuous alignment, enable simple PCM filling even in contiguous large-volume voids due to its open cell type, provide continuous support effects of the entire ITS component during additive manufacturing and further enables large-scale and complexly shaped parts with overhangs. Furthermore, the continuously and coherently permeation of the PCM mass minimizes the influence of the thermal non-equilibrium subcooling effect.

An exemplary contiguous ITS lattice structure has already been shown in Figure 4.7. This coherent lattice architecture consists of multiple identically structured lattice cells linked together. The definition of such a single lattice cell is described hereafter.

For the modelling and the associated thermo-physical generic definition of the PCM-LAT cell architecture of an ITS component, normalised and fully parameterised mathematical models are necessary. Baseline of the ITS design for the LAT geometry of a single lattice cell is the strut based Body-Centered Cubic (BCC2) periodic and tessellated lattice cell, which is depicted in Figure 4.8. The lattice cell topology is for parametrisation uniquely defined by three parameters, which are

a) the side length of the cubical unit cell, (red arrow lines)
b) the effective strut diameter, which is averaged the same for all struts of a unit cell (blue arrows)
c) and the approximated diameter of the central joining point of all struts as a correlation factor (green circle).

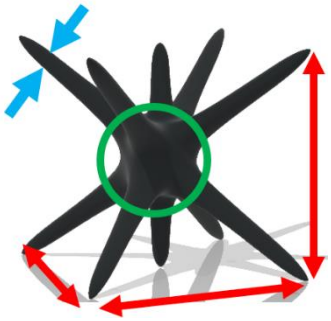

Figure 4.8: Strut based (BCC2) ITS lattice cell topology [WIL-21]

All three parameters have been determined by measurements with different lattice configurations of the BCC2 lattice topology within the ITS research.

Based on these three parametric values, it is necessary to introduce additional normalisation factors in the next step. These factors should generically guarantee the exact smearing of the bulk properties for FDM modelling in the lumped parameter notation.

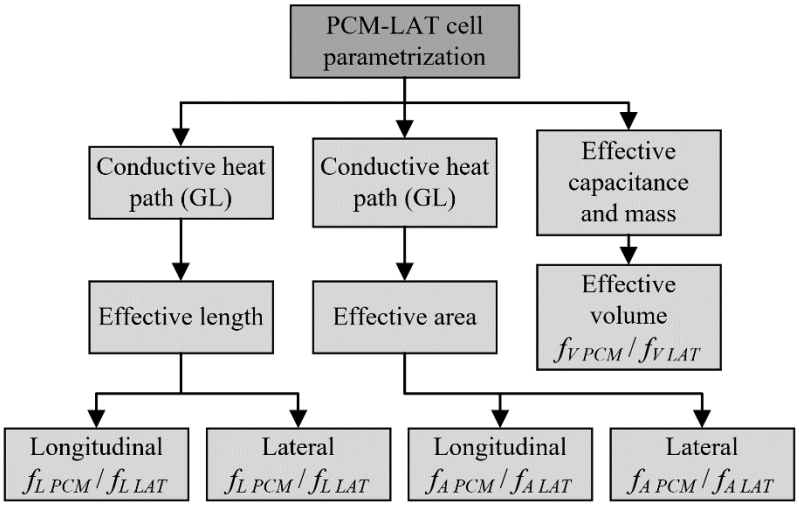

Figure 4.9: Dimensionless factors for the parametrisation of the strut based (BCC2) lattice cell topology, in order to provide generic and cell dimension independent designs

The normalisation factors summarised in Figure 4.9 and described in Table 4.1 are necessary because the BCC2 cell element has on the one side an anisotropic topology.

This is because typically for the BCC2 configuration, the cell element has in vertical direction additional strut elements. This direction is called longitudinal, while the other two main directions do not contain additional struts and are called lateral, also shown in Figure 4.8.

Table 4.1: Overview of the dimensionless factors for the parametrisation performance determination of the strut based (BCC2) lattice cell topology layout

Description	Parameter
Effective lattice cell porosity / volume (V) fractions [m³/m³]	$f_{V\,PCM}$ and $f_{V\,LAT}$
Effective area (A) ratios [m²/m²]	$f_{A\,PCM}$ and $f_{A\,LAT}$
Effective heat path length (L) ratios [m/m]	$f_{L\,PCM}$ and $f_{L\,LAT}$

This type of lattice enables an increased stiffness, buckling stability and support effect to be provided in the layer build-up process during additive manufacturing. Through an appropriately choice of the orientation and alignment of the contiguous lattice topology, reliable production of thin-walled and complex geometries with overhangs and abstract shapes are enabled. [WIL-21]

Considering the thermally optimal support, the BCC2 lattice topology allows spatially uniform enhanced heat transfer rates within the ITS component. The formations of local melt fronts due to poor thermal conductivity of organic PCMs are suppressed. [WIL-21]

4.5.3 Lattice Topology Layout Sensitivity

Based on the BCC2 lattice cell topology the influence of the thermal conductance of the aluminium lattice is compared with the achievable effective PCM volume fraction. The mathematical formulation of the PCM-LAT nodes in ESATAN and the corresponding linear conductors are generated automatically by developed software tool, depending on generic parameters.

The study deals with the sensitivity of the dependent parameters, which are listed in Table 4.2 and generically define the PCM-LAT architecture of ITS components. Figure 4.10 visualizes the characterisation of the lattice topology in order to build a numerical model, which considers the contiguous lattice cell elements (green) and the rigid walls (red).

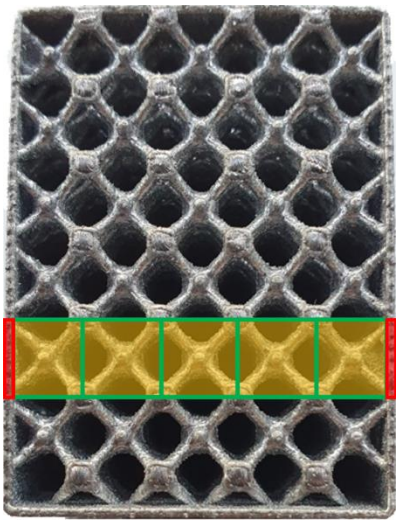

Figure 4.10: Sectional cut of an ITS part to visualize the subdivision of the lattice topology, which shall be represented by a numerical model

As already remarked, the aluminium alloy AlSi10Mg is used for manufacturing of all ITS components. The thermal conductivity of this alloy is more than 1000 times higher, compared to organic PCM, like paraffin. The thermal conductivity variation of low- and medium temperature paraffins with a melting temperature between -30°C and +100°C is neglected.

Table 4.2: Thermal performance dependent parameters to determine the thermal performance of the PCM-LAT lattice cell architecture

Description	Parameter
Effective PCM volume fraction [m³/m³]	$f_{V\,PCM}$
Effective lattice area ratio [m²/m²]	$f_{A\,LAT}$
PCM mass [kg]	m_{PCM}
PCM layer thickness [m]	t_{PCM}
Strut diameter [m]	d_{Strut}
Lattice cell side length [m]	l_{Cell}
Skin-to-skin thermal conductance GL (OOP: out-of-plane) [W/K]	GL_{OOP}
Thermal conductance GL (IP: in-plane) [W/K]	GL_{IP}

Based on the generic mathematical definition of the ITS PCM-LAT architecture, the performances of the parameter variations are evaluated. The main driver for the sensitivity studies of the lattice cell topology layout is the specification of a certain mass of PCM for a design, which is the starting point of each iteration. The amount of PCM mass increases linearly step by step. The entire iteration process of the sensitivity studies is visualised in Figure 4.11.

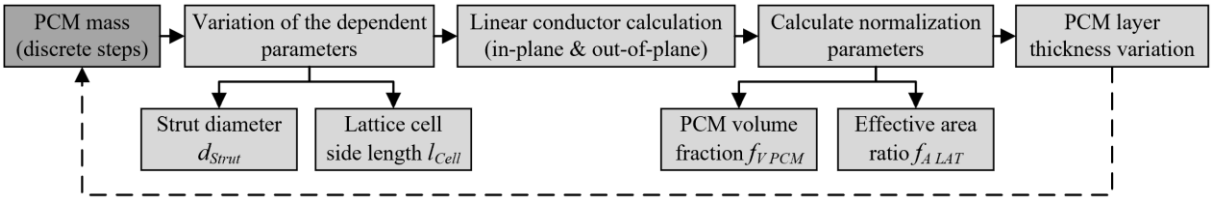

Figure 4.11: PCM layer sensitivity study iteration procedure to derive the optimal lattice cell topology layout and to give design recommendations

Consequently, the presumed PCM mass is increased in linear discrete steps, up to the maximal initially defined PCM mass. Based on the varying requirements of the total available PCM mass in the design, a variation of the dependent parameters takes place within the individual discrete mass steps, in order to calculate the sensitivity spectrum and further to evaluate an optimal lattice architecture layout for various PCM layer thicknesses. The sensitivity study is performed by a lattice architecture analysis tool, which has the purpose to give general design recommendations or limits in dependence on the PCM mass and lattice configurations used. The dependent parameters are listed in Table 4.3.

For the sensitivity studies, the correlated thermal model flat plate from the Figure 6.17 in chapter 6.8 was used. The specimen has a square mesh consisting of first-order CQUAD4 elements.

Table 4.3: PCM-LAT architecture sensitivity and dependent parameters

Sensitivity	Dependent parameters and variation
Strut diameter d_{Strut}	0.5 to 4.0 mm
Lattice cell cubical side length l_{Cell}	3.0 to 20.0 mm
Lattice BCC2 cell topology orientation	const. longitudinal
PCM type	Hexadecane ($C_{16}H_{34}$)
Layer thickness t_{PCM}	3.0 to 30.0 mm
Skin thickness t_{Skin} (each double wall)	const. 0.5 mm
Specimen reference area (mesh fineness)	100.0 mm², side length of 10.0 mm

The lattice topology sensitivity study does not consider three-dimensional heat transfer effects. Regardless of this the study shall predefine a general ITS design guideline related on the complement ITS research findings to date and model correlations based on test data. The design guideline rates the most efficient lattice topology in dependence on (a) the out-of-plane thermal conductance between the outer wall towards the PCM layer centre compared with (b) the highest achievable PCM volume fraction $f_{V\,PCM}$.

The resulting ITS lattice design guideline is depicted in Figure 4.12. Therein the out-of-plane thermal conductor is defined by the lattice cell topology, which in turn is mainly dictated by the two parameters (a) unit cell size l_{Cell} and (b) the strut diameter d_{Strut}. The PCM layer thickness t_{PCM} is dictated by the $f_{V\ PCM}$ and the discrete PCM mass steps.

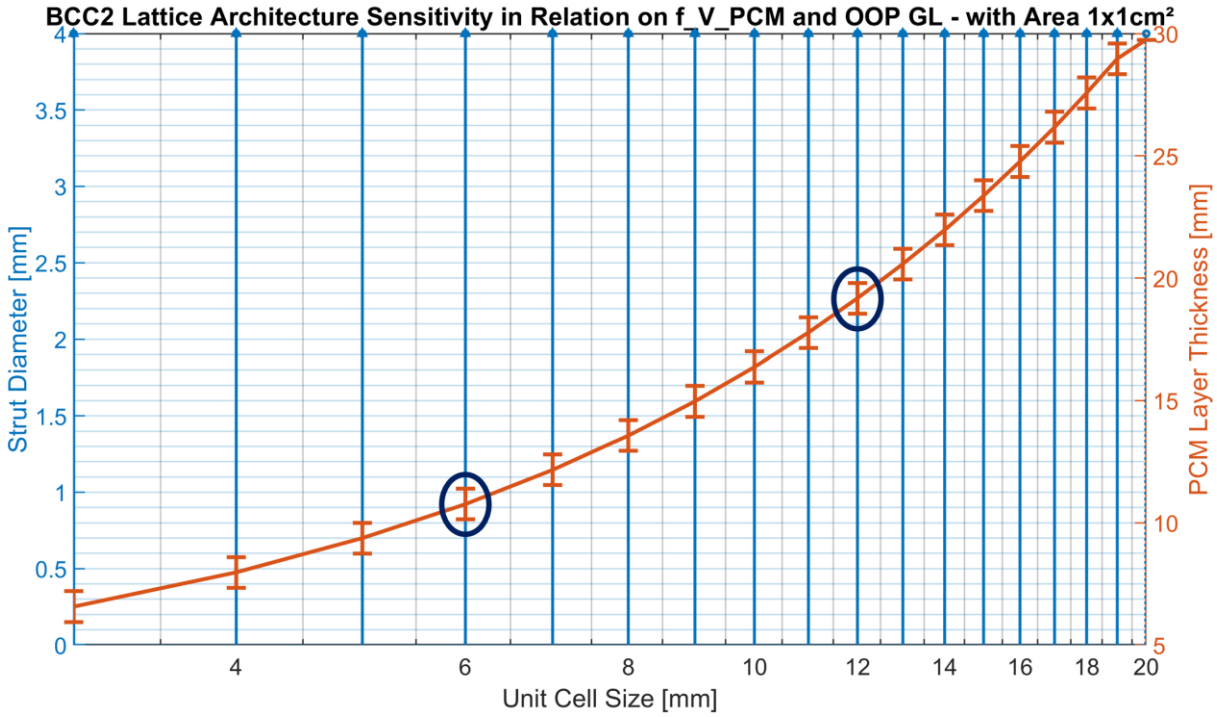

Figure 4.12: Results of the lattice topology sensitivity analyses in dependence on the lattice architecture, which is defined by the cell cubical side length (unit cell size) and the strut diameter

The results of the guideline are to be interpreted as follows. The first step is the requirement of the needed PCM mass for passive thermal control. On this basis, an average PCM layer thickness is first determined, which is to be embedded in the walls or the geometry of the component. The PCM layer thickness is plotted on the right-hand Y-axis in Figure 4.12. The optimum configuration of the unit cell size (X-axis) and strut diameter (left Y-axis) can be then estimated in the diagram by pointing horizontally from the set PCM layer thickness to the left.

The value range for the millimetre-steps of the unit cell size (X-axis) has been restricted by corresponding error bars to enable practicable designs. It can also be seen that a theoretical lattice topology design with lattice cells smaller than 4 mm (X-axis) is currently not technically feasible, as the minimum achievable thickness through the additive manufacturing process is currently around 0.5 mm.

The analyses with the currently used BCC2 lattice have also shown that from a lattice cell size (X-axis) of approx. 12 mm, it is possible to halve the single lattice element side length (unit cell size) in order to obtain two half-size contiguous elements, each with a cell side length of 6 mm. This should allow additional design flexibility.

The sensitivity study is also used as the basis for determining the lattice cell topology of the ITS demonstrator. The ITS demonstrator lattice setup is summarized in Table 10.11 and Table 10.12.

4.6 ITS PCM Model Algorithm Implementation

This section yields the implementation of the numerical algorithm in the ESATAN simulation environment, related on findings and set boundary conditions.

4.6.1 PCM Subroutine Limitations

The limitations of the PCM subroutine, already outlined in the 2021' ICES paper [WIL-21] are summarised and updated with findings from Pernsteiner et al. in [PER-20], [PER-21] as follows.

1. The PCM subroutine can handle a general two-phase solid-liquid phase change problem.
2. Multi-step phase transitions, which normally contribute to an expanded temperature transition zone, do not take place. [BAR-21]
3. The PCM voids are generally treated as macro-encapsulation.
4. The numerical latent heat storage implementation is related on the enthalpy-temperature formulation, in a fixed FDM grid scheme.
5. The enthalpy-temperature relation is formulated by a two-phase rate-independent static hysteresis model with two decoupled hystereses for melting and solidification, in order to consider non-ideal PCM behaviour.
6. Heat transfer via the PCM and the interior heat transfer structure (lattice) is dominated in-plane and out-of-plane by conduction. Hence convective heat transfer is not considered.
7. The motion of solid PCM patterns within the liquid phase is inhibited by the heat transfer structure. The velocity of the motion of the solid PCM fraction is regarded as zero.
8. There exists no shrinking of PCM within the solidifying phase.
9. There are neither air inclusions nor air voids within the solidified PCM mass.
10. The PCM mass is considered isotropic and homogeneous with a non-isothermal phase transition behaviour as well as nodal smeared bulk properties and capacitance.
11. The zone in which phase change occurs is called the mushy zone. Hence in this zone both the solid and liquid phase fractions are coexistent.
12. The change of phases between the solid and liquid states are treated as reversible.
13. Material properties are treated constant within each phase but can vary for solid and liquid phase conditions.
14. The PCM is treated incompressible. This means that pressure induced volume changes during phase transitions and beyond are neglected.
15. Any viscous dissipations within the liquid PCM phase are neglected.
16. Surface effects (surface tension) are neglected. Furthermore, no dendrite growth takes place.
17. Wall boundary layer effects are neglected.

The PCM subroutine applies an enthalpy-temperature formulation to calculate the latent heat of fusion of each PCM node. The enthalpy data are given by the trapezoidal integration of the step wise conductive heat flow. The PCM subroutine must be executed in the *$VARIABLES2* section within the ESATAN TMM main deck. It is important that the PCM nodes activity is set to *CONDUCTIVE* for both sides, to prevent that ESATAN interpret the nodes area doubled. [WIL-21]

4.6.2 PCM Subroutine Function and Features

The ITS PCM subroutine is not a standard ESATAN routine. The PCM subroutine was initiated at the FH Aachen in a first issue in 2017 by Czupalla et al. [CZU-17]. Therein the basic idea was to gather the heat flow between two distinct thermal nodes and track the values of stored enthalpy between two time steps using ESATAN. The subroutine was completely hard coded for one specific thermal model and only able to handle a static number of nodes with static properties. The enthalpy-temperature behaviour was modelled as classic slope without transition zone. The initial subroutine was not able to handle varies PCM nodes with different paraffin PCM types within the same model. [WIL-21]

Ongoing the subroutine *$SUBROUTINES* has been further developed from the first version within this thesis into an advanced and validated parametric and generic script, which has plug-and-play functionality to fit modularly into any ESATAN based thermal model. The entire PCM subroutine is encapsulated in functions. The formulations for the definition of the thermo-physical PCM behaviour is based on the enthalpy method, in which enthalpy-temperature profiles decouple the melting process and the solidification process by hystereses. [WIL-21]

The virtual PCM *$NODES* are treated within a fixed grid scheme, to solve a generic solid-liquid phase change problem, which means that the phase boundary (phase front) is not explicitly and sharply tracked. The location and expansion of the PCM melt front, where the solid and liquid phase do coexist, is treated by the PCM liquid fraction $f_{V\,PCM}$. [WIL-21]

It is also necessary to define the PCM *$NODES* fully parametrised with the following properties:

1. Node number (index of the absolute PCM node number) with diffusive (*D*) node entity,
2. node label (contains the information which PCM is allocated to the node),
3. initial node temperature,
4. effective capacitance (contains lattice (LAT) and PCM fractions),
5. nodal area and
6. the applicable PCM $f_{V\,PCM}$ and lattice $f_{V\,LAT}$ volume fractions, defined via *FX* and *FY* of the individual *$NODES* definition. [WIL-21]

In general, the subroutine provides a step wise computation of the enthalpy-temperature formulation and updates the properties and parameters of all PCM nodes. The subroutine is fully encapsulated in functions and uses a specially generated PCM database to retrieve the material properties. The parameters of all PCM nodes, which are the node thickness t_{eff}, the effective PCM node thickness t_{PCM}, the assigned PCM node mass m_{PCM}, the total amount of latent heat H_{tot} storable in the PCM node related on the node's heat flow Q_{PCM}, the current node temperature T_{PCM}, the current thermal node state (diffusive or boundary), the current node phase state and other data are dumped into a meta data file and standard ESATAN thermal model data (TMD) binary file. The TMD file is readout and post-processed by a MATLAB tool. [WIL-21]

The subroutine identifies and processes different types of PCMs within one thermal model, which enables to have different PCM types in one thermal model. The PCM nodes do not have to be defined contiguously but can also be distributed throughout the thermal model. Because the subroutine identifies PCM nodes in dependence on the node label and assigns then the correct thermal properties. [WIL-21]

The PCM enthalpy balance is primarily calculated with the knowledge of the node temperature *T*, the PCM node state and based on the total linear heat flow Q_{PCM}. The equations of state of the enthalpy-temperature relation *h* are formulated by the equations (14) and (15).

$$\begin{cases} T < T_{solid} \\ T_{solid} \leq T \leq T_{liquid} \\ T > T_{liquid} \end{cases} \quad with \quad \begin{cases} h = 0 \\ 0 \leq h \leq h_{tot} \\ h = h_{tot} \end{cases} \tag{14}$$

The calculation of the mass specific effective heat (latent heat and sensible heat) absorbed by the PCM is shown hereafter for the three states. Whereby the sensible heat is already considered by an averaged specific heat capacity $c_{p\,mean}$ in the ESATAN *NODES* capacitance definitions. The enthalpy values *h* related on the latent heat, are permanently tracked and manipulated by the PCM subroutine. Where *T* donates the temperature and h_{tot} the maximal enthalpy absorbable by the thermal node.

$$q = \begin{cases} c_{p\,mean} \cdot T \\ c_{p\,mean} \cdot T_{solid} + f_{V\,PCM} \cdot h_{tot} \\ c_{p\,mean} \cdot T_{solid} + h_{tot} + c_{p\,mean} \cdot (T - T_{liquid}) \end{cases} \quad with \quad \begin{cases} T < T_{solid} \\ T_{solid} \leq T \leq T_{liquid} \\ T > T_{liquid} \end{cases} \tag{15}$$

The heat transfer within the ITS parts is considered conductive. The corresponding linear heat flow is derived by the *FLUXGL* function for each PCM node, with respect to the remaining nodes in the model. [WIL-21]

4.7 Environmental Effects

Environmental effects and phenomenon, which are present in the laboratory environment but not in space and conversely, can misinterpret the predictability and performance of the ITS technology and its numerical models. These influences need to be examined more closely.

4.7.1 Gravity Effects

Quinn et al. [QUI-18] have focused on the demonstration of a PCM TES system on the ISS. The results from the experiments, which led several months in microgravity on-board the ISS, revealed that a non-negligible amount of dissolved air was present in the paraffin, which affected the pressure response of the system. A remedy could be the degassing of the paraffin mass, which will be used and embedded in systems for space applications. It is assumed that the air molecules have dissolved out through constant circulation in the closed loop system under the influence of microgravity.

4.7.2 Close Contact Melting and Settling

The phenomenon of close contact melting can manipulate the analyses and correlated understanding of the effective heat transfer within ITS components. It describes the process of melting of a PCM pattern under the influence of a gravitational field due to the density difference. Since solid PCM (especially paraffin) has a higher density than liquefied PCM, it sinks down inside the encapsulation. This means that the distance between the not yet melted PCM and the heat source remains almost small, which can decrease the required melt time of the PCM, which in turn leads to a deviations compared to the thermal predictions, where no solid PCM motion is considered. [FAD-18]

However, in macro encapsulated ITS structures the solid PCM constitutes are treated that they cannot float in the direction of the weight force, since the movement is inhibited by the embedded coherent lattice.

From the findings of the experiments carried out in the chapter 6.7, it can be concluded that the effect of close contact melting could not be observed for the ITS technology.

4.7.3 Energetic Radiation

The influence of energetic effects of the space environment outside the Earth's atmosphere on the thermo-physical material properties can only be investigated and tested to a limited extent within the framework of the ITS research.

In general, in all TVC tests high vacuum of $< 10^{-5}$ mbar was achieved. However, according to the availability of the test facilities neither low-temperature tests of < -20°C nor radiation effects tests were possible to analyse the chemical stability of the used PCM.

The influence of ionised particles or energetic radiation in the electromagnetic field in the Earth radiation belts may can affect the chemical stability of the PCM. Furthermore, the high energetic radiation exposure from outer space or high energetic emissive objects can lead to chemical decomposition and increased impurities on organic molecules like organic paraffin.

Another point is that impermissible heating of the PCM mass due to high energetic radiation exposure or permanent sun intrusion on the ITS part, can lead to overheat and to further decompose the PCM with the consequence of a high gas-formation potential in encapsulated voids.

5 MANUFACTURING OF ITS INTEGRAL STRUCTURES

This chapter is partly based on already published findings in paper and reports from the ITS research, generated by Wild et al. in [WIL-21] and [WIL-23] and is shortly summarised for the line of argument. My colleague Mr. Schrezenmeier was mainly in charge of the additive manufacturing discipline in the ITS project. The additive manufacturing, as a disruptive technology, is a central aspect for the successful implementation of the ITS technology.

In particular, the fabrication of double walled ITS parts with integrated coherent lattice are not feasible without additive manufacturing, in order to fully exploit the strengths of ITS technology. According to Gebhardt et al. in [GEB-16] and [GEB-17] the essence of additive manufacturing is to apply an automated and computer-controlled layer construction process with LPBF. The boundary conditions and findings for a reliable additive manufacturing process of ITS parts are briefly summarised in this chapter. [WIL-23]

5.1 Additive Manufacturing Process and Method

As a selective laser melting (SLM) process is the LPBF technology process the most applied state of the art process, which is also applied for the manufacturing of the ITS parts. According to Brandl et al. [BRA-12] current manufacturing methods can achieve a relative density around 99.5% for components fabricated from the aluminium alloy AlSi10Mg using LPBF. The following Table 5.1 lists the relevant information about the infrastructure used for the fabrication of all ITS parts, breadboards, specimen and demonstrators. [WIL-23]

Table 5.1: Infrastructure and material used for the LPBF additive manufacturing process of the ITS parts at FH Aachen [CON-02], [WIL-23]

Specification	Parameter and data
Machine supplier	General Electric (GE) Xline
Type	GE Concept Laser X-Line 2000R
Manufacturing material	AlSi10Mg(b)
Manufacturer designation	CL 32AL aluminium alloy
Material standard	According to DIN EN 1706
State of raw material (alloy)	Powder form
Grain fraction	45 - 75 µm

The standard material for all ITS components is the aluminium alloy AlSi10Mg. The raw material of the aluminium alloy is available in powder form. According to the material supplier, the grain diameter of the aluminium alloy powder is in the range of 45-72 µm. The alloy is corrosion-resistant, has a high specific strength and high thermal conductivity. [WIL-23]

Normally, the averaged density of the manufactured alloy is determined on solid material with thick walls. ITS components usually have very thin walls with a relatively large surface. Due to the process, the standard hatch vector parameter sets cannot be used for the fabrication of thin walls. As the name implies, the hatch cycles are responsible for generating the main solid substance (hatch contour) of the component, while the fill cycles are only used for filling fine cavities or edges and thus for generating the finer fill contour. The fill contour parameters are strongly adapted hatch contour parameters. Therefore, the relative density could not be determined on thin-walled components until the end of the ITS project. The findings of the ITS research showed that the manufacturing of thin-walled structures with hatch parameters up to a minimum wall thickness of approx. 1.0 mm is possible. Below 1.0 mm, the fill parameters had to be used. [WIL-23]

According to the company Concept Laser [CON-02] and [WIL-23], critical during and after the manufacturing process is the constant temperature tracking of the aluminium alloy. With optimal temperature tracking, the resulting residual stresses can be kept low. Nevertheless, the powder manufacturer recommends a separate downstream heat treatment, which is the stress relief annealing process, to increase the thermal conductivity and reducing residual stresses.

5.2 Critical and Process Relevant Parameters

Part of the ITS manufacturing design studies are wide-ranging parameter studies to determine robust manufacturing parameter sets for the reliable fabrication of thin-walled ITS components with integrated lattice, made by the alloy AlSi10Mg. The validation of all test specimens, partially with systematically varying manufacturing parameters is related on visual inspections, empirical values based on measurements and pressure tests. The gas (vacuum) tightness was tested with a relative pressure of ca. 5.0 bar. The Figure 5.1 depicts the critical parameters to be validated. These critical manufacturing parameters are defined as follows. [WIL-23]

1. Laser power P_L,
2. beam diameter d_S,
3. layer thickness D_S,
4. track spacing Δy_S and
5. scan speed v_S.

Another topic to be validated is the typical value of maximal overhang angle, which is also mentioned in the work of Kabir et al. [KAB-21]. In this study, the limit value for repeatedly reliable production was 45° of overhang angle. This geometrical limit is also being confirmed by the breadboard series conducted within the ITS research. [WIL-23]

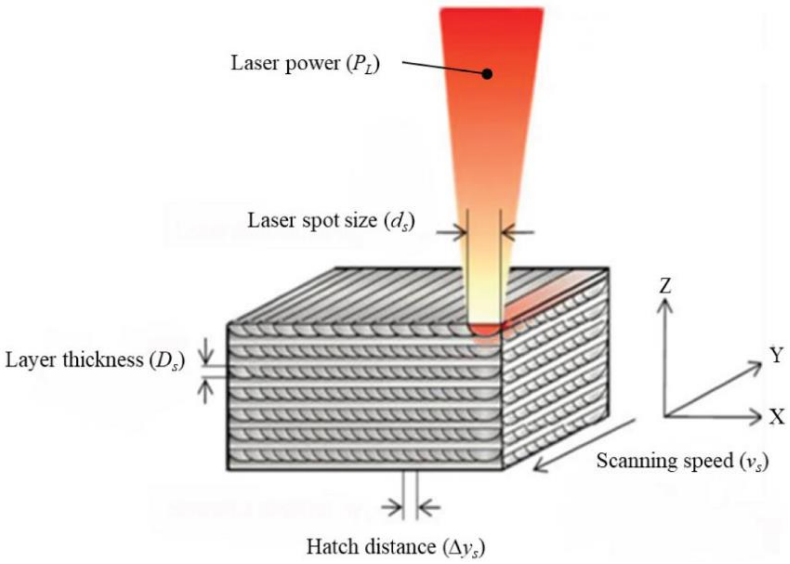

Figure 5.1: Schematic overview of the LPBF additive manufacturing process critical parameters [KOS-21]

5.3 ITS Component Manufacturing Parameter Set

The optimum amount of energy per powder volume (energy power density) unit is dictated by the material. However, due to process related and application related influences the energy power density is not universally transferable. The most critical reasons are that the ITS parameter sets have to handle hatch contours, finer component contours lattice structures and support structures. [WIL-23]

That's why a suitable parameter window must be found as a compromise to enable an optimal manufacturing. This parameter window was determined by preliminary parameter studies, based on hatch parameters. The results of the parameter studies are summarised in Table 5.2, which provide an optimal coverage of all known ITS use cases and geometries. [WIL-23]

Table 5.2: Parameter set for optimal coverage of all ITS use cases and geometry variations for additive manufacturing with the highest possible relative density [WIL-23]

Parameter	Value
Laser power P_L	420 W
Layer thickness D_S	50 µm
Beam diameter (laser focus) d_S	200 µm
Scan speed v_S	700 mm/s
Track spacing Δy_S	120 µm

5.4 PCM Filling Procedure

Watter et al. [WAT-15], Isaac et al. [ISA-17] and Quinn et al. [QUI-18] recommended to degas the paraffin before sealing any PCM void. That means that the PCM shall harden under vacuum after filling to dissolve bound air molecules.

Bentilla et al. [BEN-66] and Hale et al. [HAL-71] already mentioned in 1966/1971 the system critical aspect of reliable and permanent PCM void sealing of rigid PCM containers, in order to withstand temperature induced volume changes. Countermeasures can be (a) to integrate expansion reservoirs, (b) embedded compressible air volumes or (c) to evacuate the remaining free void, which is not occupied by PCM.

The ITS PCM filling and sealing process takes place at standard atmosphere pressure level. Thereby two main effects must be considered for sealing the PCM voids. One is the sealing of the PCM voids of the ITS component against the prevailing exterior vacuum after venting during launch or further in space. Secondly and the major driver for reliable sealing is the expected volume expansion of paraffin when it is heated, which inevitably increases the pressure difference in the system under isochoric conditions. For these reasons it is necessary to develop a reliable PCM filling and sealing strategy for ITS integral structures, which is validated by tests and ensure component survival.

Due to the known and accepted process-related fluctuations associated with additive manufacturing of light metal alloys the theoretical fillable PCM volume usually deviates slightly from the actual values. This is because the available PCM volume can be smaller or larger due to non-removable powder residues or geometrically slightly different manufactured structures. Therefore, the exact amount of PCM for a complete filling has to be determined by actively filling and weighing of the mass differences.

To minimize air inclusions due to filling or overhanging void sections, the ITS component shall be tilted at different angles about all three axes, in order to distinguish existing air bubbles. This process shall be repeated several times during the entire filling process.

For all filling procedures, the PCM void openings (filling inlets) should always stay at the hydrostatically highest point, similar to metal casting, to ensure that the entire void volume is used and air can escape. Ultimately a commercially available syringe has proven to be the most practical and effective tool. There are two potential filling procedures identified, which are described hereafter.

5.4.1 Cold Filling

The first procedure (cold filling, then cooling and then cold sealing) of cold filling and sealing is as follows. It starts with the complete filling of the void, followed by the removal of the excess PCM required to compensate the intended volume expansion. In the last step the PCM is cooled down and the part is being sealed. The entire procedure is detailed below.

1. Heating the PCM up until the PCM mass in completely liquid around room temperature. The ITS component shall have a temperature of +5°C above the PCM melting temperature.
2. Determine the mass of the empty ITS component (without PCM).
3. Fill in the PCM until the entire void is fully filled and determine then the mass increase of the ITS component, which is donated m_{T1}.
4. Determine the PCM mass to be removed by considering the expected volume expansion from current filling temperature state (T1) to maximal operational temperature including a margin of +5°C (T2). Therefore, the following equation (16) shall be used to derive the PCM mass to be removed ($\Delta m_{T1 \rightarrow T2}$), where ρ is the temperature dependent PCM density.

$$\Delta m_{T1 \rightarrow T2} = m_{T1} \cdot \left[\left(\frac{\rho_{T2}}{\rho_{T1}} \right) - 1 \right] \tag{16}$$

5. Remove the excess PCM mass from the void and let the mass cool down until the entire PCM mass is completely solidified.
6. Seal the PCM void with the contracted and completely solidified PCM. In this way there exists beneath the PCM volume an enclosed air volume like an air cushion in the macro encapsulation, against which the PCM can expand and compensate the volume change, since air is quite good compressible.

5.4.2 Hot Filling

The second procedure relates completely on hot filling and hot sealing, where the ITS component is being permanently heated up to the maximal operational condition also including +5°C margin. The liquid PCM, which is hold at approx. room temperature is filled in the voids in parallel. If the ITS component to be filled contains multiple encapsulated PCM voids, repeat this procedure for each void.

1. Heating the PCM up until the PCM mass in completely liquid.
2. Determine the mass of the empty ITS component (without PCM).
3. Start heating up the ITS component to the expected maximal operational temperature profile including the margin.
4. Fill in the PCM until the entire voids are fully filled.
5. Wait until the ITS component temperature reach the maximal temperature state again and remove permanently the excess PCM, which will exist at the filling inlets due to the temperature increase induced volume expansion.
6. If then the maximal temperature state of the ITS component is reached, balanced and all PCM voids are filled with the specific PCM, measure the mass increase of the ITS component to determine the net PCM mass added to the system.
7. Seal all PCM voids in the maximal temperature state.

Both variants of the PCM filling and sealing procedure had been successfully tested, as part of a delta qualification, several times for diverse specimen and breadboard setups. When filling the ITS demonstrator, both variants were also applied and validated on its feasibility.

Compared to the hot filling method, the cold filling method is less complex and “hazardous”, since the hot filling method maybe requires filling at very high temperatures, depending on the operational temperature profile. On the other hand, the hot filling method includes virtually no air inclusions in the macro encapsulation. If the ITS component is then completely cooled down in the hot filling method, there is a relative vacuum in the PCM voids from the outset, which means an additionally increased margin of the system against failure. Therefore, the hot filling and sealing method was set as the standard for all ITS components and the final demonstrator to be tested.

5.5 PCM Chamber Sealing Concept

Dudon et al. [DUD-19] tested two different approaches for sealing classical PCM containers, which are depicted in Figure 5.2. Right hand, an expansion sealing plug has been used, in which a ball is pressed into a sleeve to create a seal. Left hand, the end piece of the filling nozzle is sealed by crimping and subsequent soldering. Latter is already established at Thales and is used for sealing heat pipes.

Figure 5.2: Sealing concepts in order to capsule a PCM void, where the container is made from aluminium. The two sealing variants consist of a pressed queusots with a welded nozzle exit (left) and a ball plug inlet (right) which provides a form-fit seal [DUD-19]

The sealing strategies of PCM voids are discussed in this section. According to Höhlein et al. [HOE-18] the sealing method is primarily dependent on the capsule material. It is also essential that the filling and sealing process, combined with corrosion protection, shall be compatible with each other. Another major impact on the choice of the ideal sealing method is the selected PCM. If e.g. welding is applied, the temperatures of the sealing process shall not exceed the critical temperature where the PCM could theoretically decompose, ignite or is subject to (accelerated) corrosion. The following Figure 5.3 summarises the review of available sealing techniques, created by Höhlein et al.

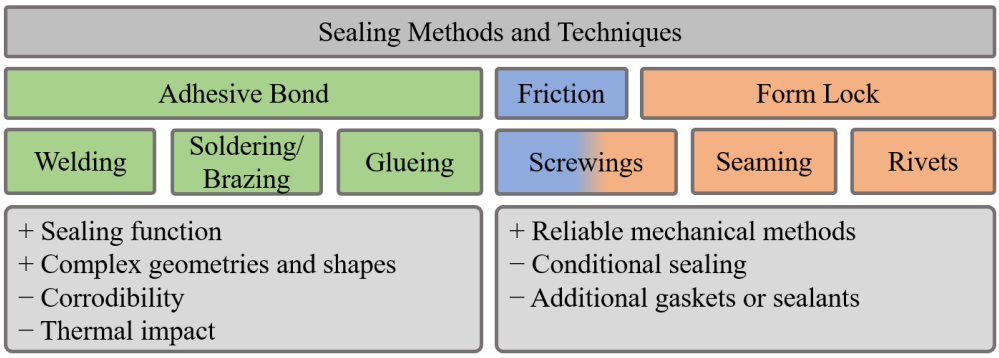

Figure 5.3: General PCM sealing methods and techniques, based on a summary of Höhlein et al. [HOE-18]

The following requirements had been applied to define a reliable vacuum-tight sealing concept.

a) Vacuum-tight single or multiple PCM voids to avoid any leakage.
b) Non-permanent sealing, which can be non-destructively and residue-freely removed in order to empty and refill the PCM voids with different PCM types in multiple tests.
c) The sealing concept shall enable multiple and decoupled multiple-chamber-sealing, to increase the system reliability.

Within ITS research, various sealing methods were investigated. Welding or brazing of the additive manufacturing material AlSi10Mg was technically not possible with the equipment at the FH Aachen. Furthermore, a sealing method shall be found, which is not permanent and can therefore be removed again without leaving any residue. This is because the various breadboards and the demonstrator are tested in different configurations, orientations and with different PCMs during various test campaigns. At the same time, the sealing method has also to enable a vacuum-tight testing via structural-mechanical as well as thermal tests. The Figure 5.4 below depicts the applied non-permanent sealing concept for all ITS components.

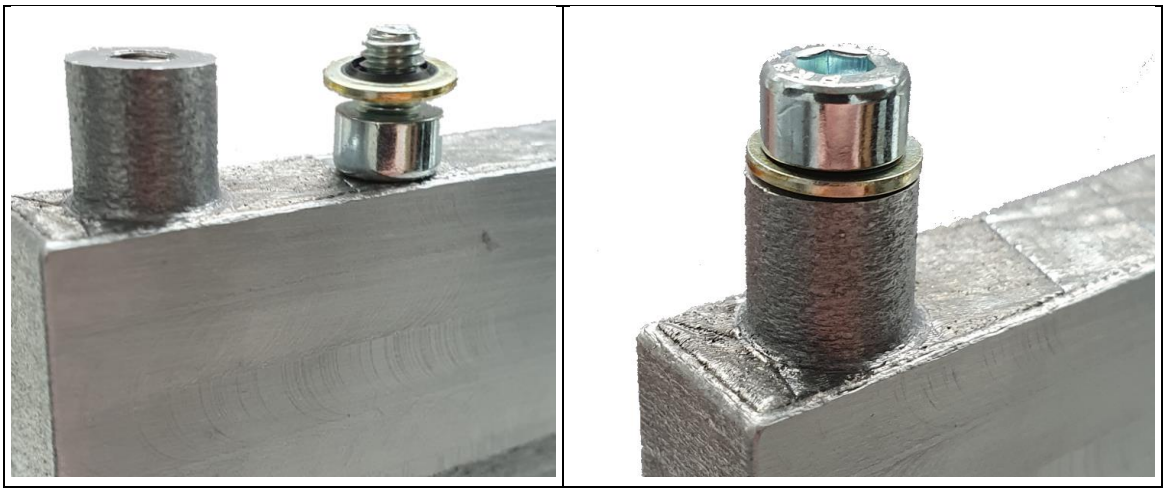

Figure 5.4: Non-permanent self-centering bonded seal with vulcanised rubber sealing lip, which are used for all ITS components to seal the PCM voids

The company Hennlich [HEN-20] supplies the necessary sealing elements, which consist of a metal outer ring with a vulcanised rubber sealing lip. The sealant is suitable for static sealing of flanged joints, screwed connections and screw-in nozzles. Self-centering screw seals are required, since an external centering of the bonded seal is usually not possible for ITS components. The centering is achieved by a thin diaphragm, whose inner diameter corresponds to the core diameter of the thread. In addition to a simple and reliable assembly/disassembly of the non-permanent gasket, the design of the bonded seal prevents gasket failure caused by over-compression or seal settling, which can generally occur with static sealings. The following Table 5.3 summaries the technical details of the sealing technology.

Table 5.3: Technical data of the ITS sealing technology, based on a self-centering bonded seal [HEN-20]

Parameter	Technical data and features
Type	Self-centering bonded seal
Material sealing	NBR (Nitril-Butadien-Rubber) / vulcanised rubber sealing lip
Outer ring	Yellow chromated outer ring / made of mild steel
Dimension [mm]	5.6 x 10.0 x 1.0
Temperature range	-30°C to +100°C
Maximal pressure	ca. 400 bar (without groove or countersink)
Contact pads	Maximal roughness values: Ra ≤ 3 µm (R_{max} ≤ 15 µm)

6 THERMAL CHARACTERISATION AND VALIDATION OF ITS

Topic in this chapter is the thermal validation of the ITS thermal models in the ESATAN environment, which are related on the PCM subroutine to simulate the thermo-physical PCM behaviour. Another focus lies on the thermal characterisation of the used materials in terms of the bulk and thermo-optical properties.

6.1 Temperature Sensors and Equipment

The temperature sensors used for the TVC tests are thermocouples. In order to determine the common zero drift and the relative deviation of all thermocouples to each other, initial calibration measurements are carried out using an ice point block calibrator. The thermocouples are connected to a Keithley DAQ6510 using two-wire technology via a suitable measuring card. The following Table 6.1 lists the specific measurement hardware.

Table 6.1: Overview of the measurement equipment used for the ITS TVC tests

Calibration measurement	Device
Ice point reference	KAYE instruments, K140 ice point reference
Temperature sensors	PTFE insulated thermocouples type-T, art.-nr.: 158-907
Data acquisition system for temperature measurements	Keithley DAQ6510 (40 channels, each 2-pole) with 2x20 Keithley 7710, 2x20 channel thermocouples

As generally known and listed in [DON-16] to minimize heat losses due to conduction through the wires of the thermocouples, it is recommended to use thermocouples (a) with a small wire diameter, (b) wire types with a low thermal conductivity and (c) a two-wire technique (differential thermocouples).

For this reasons, Cu-CuNi thermocouples with a wire cross-section of 0.032 mm² are used. The thermocouple reference measurements are proceeded at the ice point temperature of water. The results indicate a maximal error of 0.21K, which is assessed to be acceptable.

6.2 Characterisation of Bulk Material Properties

For a fundamental material characterisation of the light metal alloy AlSi10Mg, which is used for additive manufacturing the thermal conductivity and the thermo-optical properties need to be determined.

The underlying results of the measurements and the corresponding material property findings are already reported in the final ITS research report [WIL-23]. Since the supplier of the aluminium powder raw material recommends a stress relief heat treatment for the microstructure optimisation (recovery), the measurement results are carried out on both at non-treated and heat-treated test specimens.

6.2.1 Thermal Conductivity

The results of experimental tests conducted at the Fraunhofer Institute for Lasertechnology at Aachen [BRA-12] clarify, that additively manufactured parts made of the material AlSi10Mg, which are subject to a subsequent stress release heat treatment process, exhibit a significant increase in fatigue resistance and static tensile strength, have an effective density of > 99% and an measured porosity of < 300 µm. It was also declared that the achievable fatigue resistance depends only slightly on the building direction, but strongly on the platform temperature. This critical parameter is already discussed in chapter 5.1.

As already mentioned and according to the manufacturer's data sheet [CON-01] of the additive material AlSi10Mg, which is used for the fabrication of the ITS parts a subsequent stress relief heat treatment is recommended.

Due to the limited experience and availability of validated thermo-optical and bulk properties of the additive manufacturing material used in conjunction with the production system, characterisation measurements had to be carried out. This measure is also essential to increase the confidence of thermal predictions, which relate on these bulk data. In order to characterise both the additively manufactured material without and with post-heat treatment, specific test specimen series were manufactured for both variants and their bulk material properties were characterised. The test specimens used are depicted in Figure 6.1, with the relevant data in Table 6.2. [WIL-20]

All measurements are conducted inside the TVC at high vacuum of < 10^{-5} mbar during all tests. The test equipment consists of silicone surface heater and type-T thermocouple sensors. The heaters are farthermost attached from the heat sink (cold plate) to measure convincing temperature gradients along the specimen’s thermocouple assembly line. [WIL-20]

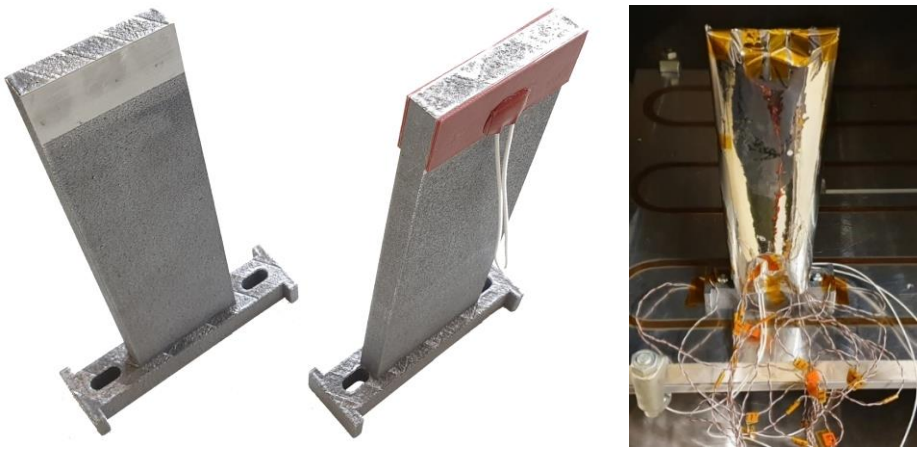

Figure 6.1: Specimens for the characterisation measurements, to determine the thermal conductivity of the additively manufactured material. The specimens are solid bars with accommodated surface heaters. [WIL-20]

Table 6.2: Thermal specimens, which were subject to thermal conductivity measurements [WIL-20]

Parameter PCM specimen	Characteristic values
Dimensions (WxHxL)	100 x 160 x 30 mm
Mass of single plate sample	47 mm bar: ca. 258 g / 60 mm bar: ca. 313 g

According to Tritt et al. [TRI-04] heat losses can occur during the measurement process due to (a) thermal conductivity of the thermocouple leads, (b) high contact resistance between heater and specimen and (c) radiative heat losses. The radiative heat losses are treated as low, since a total of 30 layers of MLI achieve an adequately good radiative decoupling from the TVC environment. The total losses are assessed to be about 6.5%, which is derived from thermal model correlations. [WIL-20]

The test procedure to characterise the thermal conductivity is based on the steady-state method with an absolute technique. This method is commonly applicable for measurements of rectangular and cylindrical specimens. [WIL-20]

Based on the Fourier's law the resulting thermal conductivity k_{eff} is calculated by equation (18). Q_{cond} represents the net power input into the specimen via the heater patches, L is the distance between the reference thermocouples, A is the constant kept cross sectional area along the bar of the specimen where the temperature gradient ΔT evolves. [WIL-20]

$$k_{eff} = \frac{Q_{cond} \cdot L}{A \cdot \Delta T} = \frac{Q_{cond} \cdot L}{A \cdot (T_1 - T_2)} \tag{18}$$

The calculated results of the characterisation measurements are listed in Table 6.3. The test cycles were repeated with increasing heater power values.

Table 6.3: Results of the thermal conductivity measurements of the depicted specimen series, where one series is kept originally and another series is undergone a heat treatment [WIL-20]

Heater power Q_{cond} [W]	**Thermal conductivity [W/mK]**	
	w/o heat treatment	**with heat treatment**
5.80	144.02	165.71
9.30	147.25	163.94
12.80	146.35	165.07
14.60	153.38	163.82
17.50	150.75	165.44
	Mean: 148.35	**Mean: 164.80**

The experimental derived values of thermal conductivity can be consolidated with thermal predictions, as the correlation with the calculated data show a good overall agreement with TVC measurements of diverse specimens and the ITS demonstrator. On average, an increase in thermal conductivity of 10.8% was achieved through post-treatment. It is also evident that the heat treatment reduces the scatter of the thermal conductivity values, which is due to the optimisation of the microstructure. [WIL-20]

Moreover the results above show a good compliance with the experimental data of Hatakenaka et al. [HAT-17], where the same aluminium alloy had been characterised.

6.3 Characterisation of Thermo-Optical Material Properties

With regard to the thermal characterisation of the aluminium alloy AlSi10Mg, measurements were also carried out to determine the thermo-optical properties of the aluminium alloy, which are the absorptivity α and the emissivity ε. According to current knowledge, no material properties of the additively manufactured material AlSi10Mg in connection with the X-Line 2000R production system can be found in the literature, which made a basic characterisation necessary. [WIL-23]

The thermo-optical properties typically vary between machined (milled) surfaces and porous surfaces (as fabricated). Therefore, the aim is to determine the optical properties of the surfaces in all configurations. The specimens used for testing are rectangular plates with a side length of 80 mm. These flat plates are depicted in Figure 6.2. The test plan provides for the flat plates the configurations of different orientations of the layer structure planes (0°, 45° and 90° to horizon), with and without machined surfaces, and with and without post-heat treatment. All specimens were cleaned with isopropanol. The measurements were performed by the OHB System AG in Munich. [WIL-23]

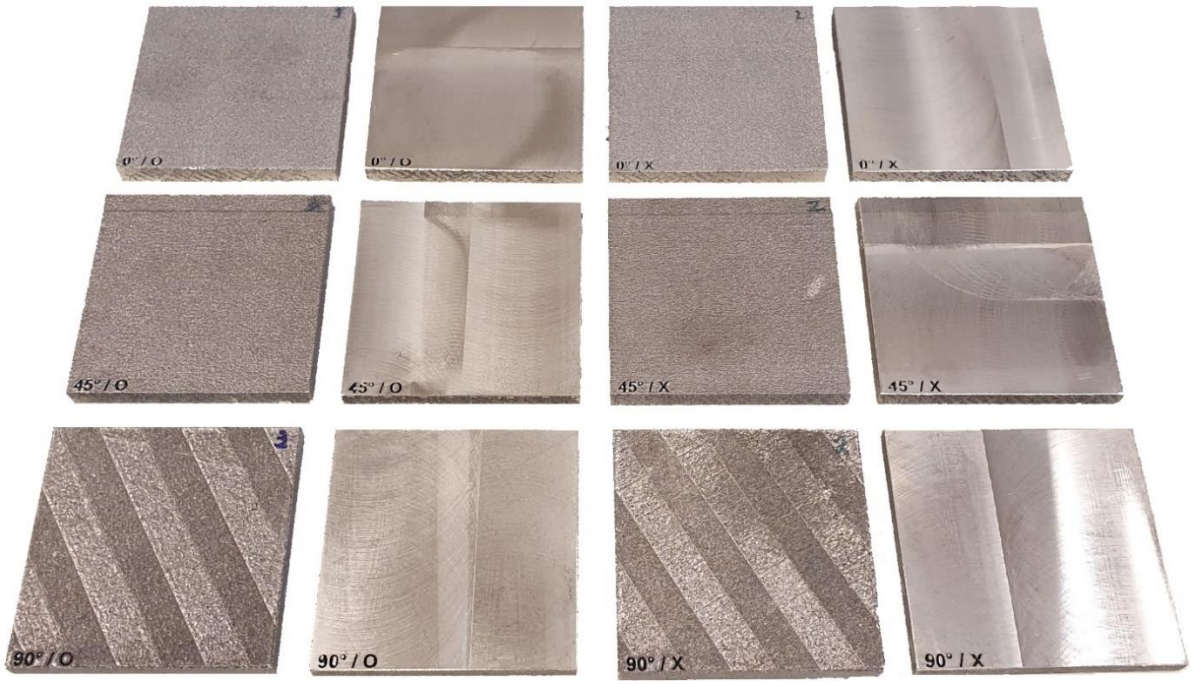

Figure 6.2: Test plate samples in order to derive the thermo-optical surface properties of the additively manufactured aluminium alloy, being both machined and originally porous, with various relative orientation of the construction layers (0°, 45° and 90°) as well as with and without heat treatment [WIL-20]

The measurement results of the thermo-optical properties are listed in Table 10.2 in the appendix. These measured values form the basis for the definition of the thermo-optical properties in the thermal models. For the emissivity spectrum the hemispherical emissivity ε_H data are used. [WIL-23]

6.4 Conductive Lattice Heat Transfer Model Validation

Before validating the heat transfer model in interaction with the TES capability of embedded PCM mass, it is primarily mandatory to validate the conductive heat transfer model of the net lattice geometry. For this aim, additional lattice geometry specimens without wall structures were additively manufactured, so that only the intermediate lattice structure is existent. One type of this specimen is shown in Figure 6.3.

The deviations (scattering) of the CAD model compared to the fabricated specimens have been determined in the range of ± 10% of the nominal diameter of the lattice struts, by CT scans. The same amount of scattering can also be found for the demonstrator.

For the lattice thermal tests in the TVC, the specimens were covered in MLI. The thermocouples were attached along the lattice structure struts at evenly spaced intervals, all around via carbon adhesive tabs.

The results of the measurement series are depicted in Figure 6.4 and confirm the generic heat transfer model designed for the ITS components, with a maximum deviation of ca. 1.2K, which is acceptable.

Figure 6.3: ITS thermal lattice specimen without structural double walls to validate the conductive heat

Table 6.4: ITS thermal lattice specimen specifications

Parameter PCM specimen	Characteristic values
Dimension (WxHxD)	50 x 155 x 30 mm
Mass	234.5 g w/o PCM
Strut diameter	0.75 mm
Lattice cell size	6x6x6 mm cubical cell side length

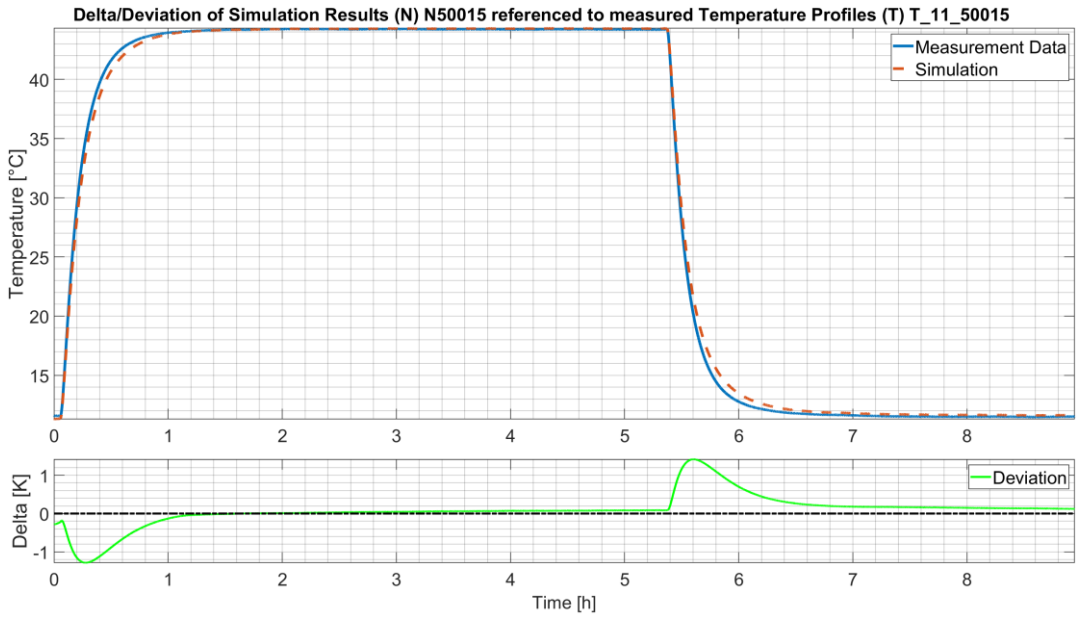

Figure 6.4: ITS lattice specimen TVC tests results, with the correlated predictions related on the measurements

6.5 PCM and Lattice Model Validation

For the discretisation of the thermal model geometry 2D first-order elements of the type CTRIA3 and CQUAD4 are used, which have zero extent. The thermo-optical and bulk properties of each element are defined related on FDM, which is the mandatory model environment in ESATAN. The elements represent thermal nodes in the ESATAN FDM environment and are coupled to the global thermal network, in dependence on their heat transfer coupling. [WIL-21]

For the validation of the ITS conductive heat transfer model with PCM and the simulation of the numerical PCM behaviour, test specimens have been manufactured and tested in series. Figure 6.5 and Figure 6.6 depict a representative specimen series with the related model discretisation applied for predictions, tests and model correlations. The Table 6.5 lists the relevant specimen parameters. The surface heater positions are highlighted by red faces. They heat the model during cycling and are attached to the specimens by adhesive. The temperatures of the specimen surfaces are measured by type T thermocouples. [WIL-21]

Table 6.5: ITS specimen specifications [WIL-20]

Parameter PCM specimen	Characteristic values
Dimensions (WxHxL)	100 x 60 x 30 mm
Mass	75.5 g w/o PCM
Wall thickness	0.5 mm
Strut diameter	Integrated lattice / 0.75 mm strut diameter
Lattice cell size	6x6x6 mm cubical cell side length

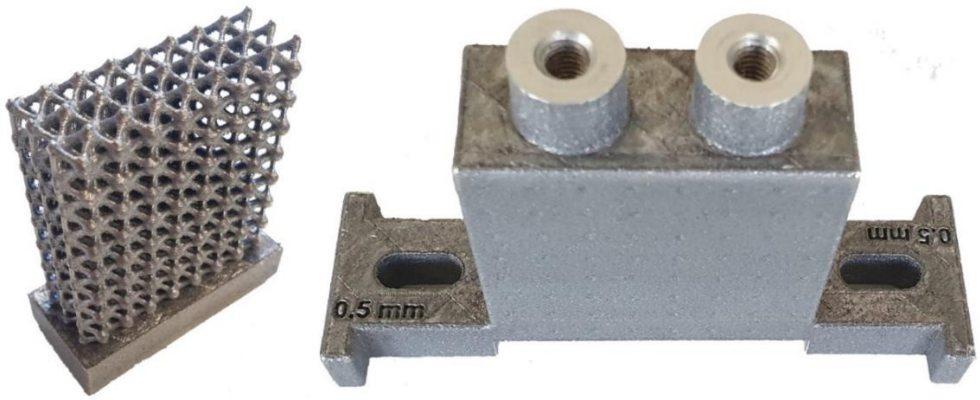

Figure 6.5: ITS specimen without structural double walls (left) to show the intermediate heat transfer structure, which is a lattice matrix and a specimen (right) with manufactured double walls with a thickness of ca. 0.5 mm and even intermediate lattice. On top sealable inlets enable the filling of the void with PCM [WIL-20]

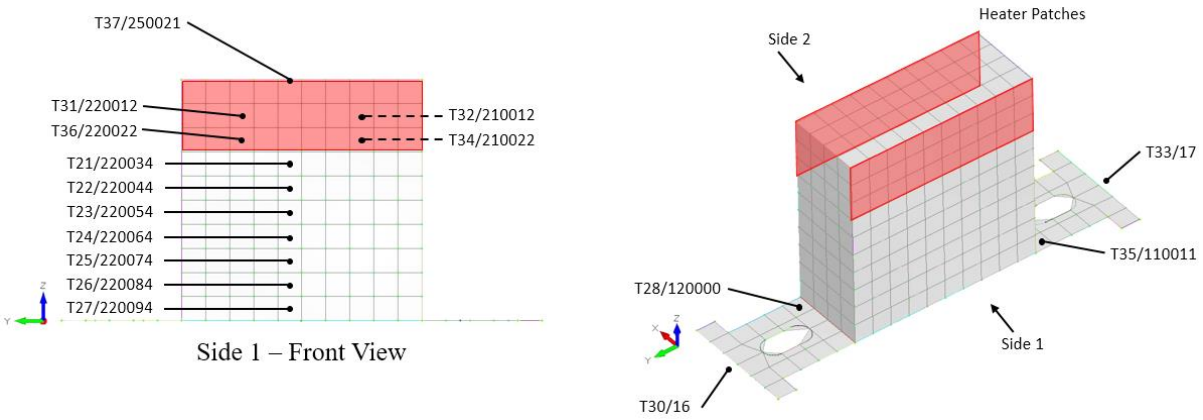

Figure 6.6: Discretisation of a thermal ITS specimen to convert the geometrical information into a FDM model, where the shell discretisation is provided by 2D first-order CTRIA3 and CQUAD4 elements [WIL-21]

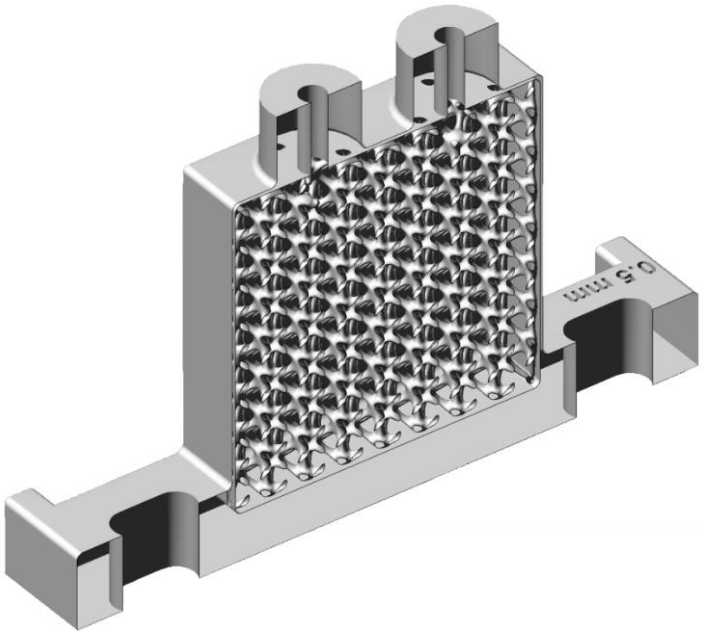

Figure 6.7: Sectional view of the thermal specimen, which was used for the validation of the PCM and lattice model [WIL-21]

The Figure 6.7 depicts the ITS specimen in a sectional view. This specimen has wall thickness of ca. 0.5 mm and an integrated lattice matrix. On top, two filling inlets with screw fittings enable the PCM filling and subsequent sealing of the macro encapsulation in the laboratory. This is the typical ITS design. [WIL-21]

The PCM nodes are embedded as virtual nodes. The implementation of virtual PCM nodes is exclusively based on ESATAN lumped parameter formulations. A PCM node, as virtual thermal node, combines and thus smears the proportional PCM and lattice bulk properties. [WIL-21]

The thermal (conductive) coupling of the virtual PCM nodes with the remaining regular (structural) thermal nodes of the thermal model takes place via linear conductors between 2 specific nodes. The global thermal network is then generated from the interdependent links of all specifically defined thermal conductors (GL). [WIL-21]

6.5.1 Experimental Setup

Figure 6.8: Experimental test setup accommodated on the cold plate inside the thermal vacuum chamber for cycling tests [WIL-21]

The test setup of the thermal specimen in order to validate the PCM and lattice model is shown in Figure 6.8. The specimen is conductively anchored to the cold plate by screws to provide a strong coupling to the heat sink. The cold plate temperature is controlled by a circulating pumped silicone oil system. During the entire test interval the vacuum in the TVC was permanently < 10^{-5} mbar. [WIL-21]

Surface mounted silicon heaters provide the required heat input. The heaters are attached to the specimen's surface by heat conductive silicone adhesive, at the farthest point away from the cold plate. The sensors (type-T thermocouples) are mounted via high conductive carbon adhesive tabs to the surface. The following Table 6.6 contains the relevant specimen data and parameters. [WIL-21]

Table 6.6: Parameters of the representative ITS PCM specimen, which was subject to thermal vacuum tests with the embedded paraffin hexadecane [WIL-21]

Parameter PCM specimen	Characteristic values
Dimensions	50 x 50 x 20 mm
Wall thickness	ca. 0.5 mm
Dry mass (screws, seals and embedded lattice matrix)	75.5 g
PCM	Hexadecane ($C_{16}H_{34}$)
PCM mass	28.8 g
Volume PCM void space (entire macro-encapsulation)	49 x 49 x 19 mm
Total mass (screws, seals, embedded lattice matrix and PCM)	111 g
Lattice volume fraction	ca. 15.5%
Lattice cell size	6x6x6 mm
Strut diameter	0.75 mm

6.5.2 Thermal Model and PCM Subroutine Sensitivity Analyses

The sensitivity analyses are performed with the identical thermal setup from the chapter before. The first step of the analyses is to investigate the sensitivity and thus the thermal behaviour of the specimen in the direct temperature range of phase change of hexadecane, which is around 18°C.

The comparison and correlation of the predictions with the measurement data in Figure 6.9 indicate, that the transition region around the characteristic melting temperature of hexadecane show a similar behaviour. After the switch on of the heater power the temperature of the empty model (without PCM) quickly rises, as the effective capacitance is considerably lower than the specimen with PCM. [WIL-21]

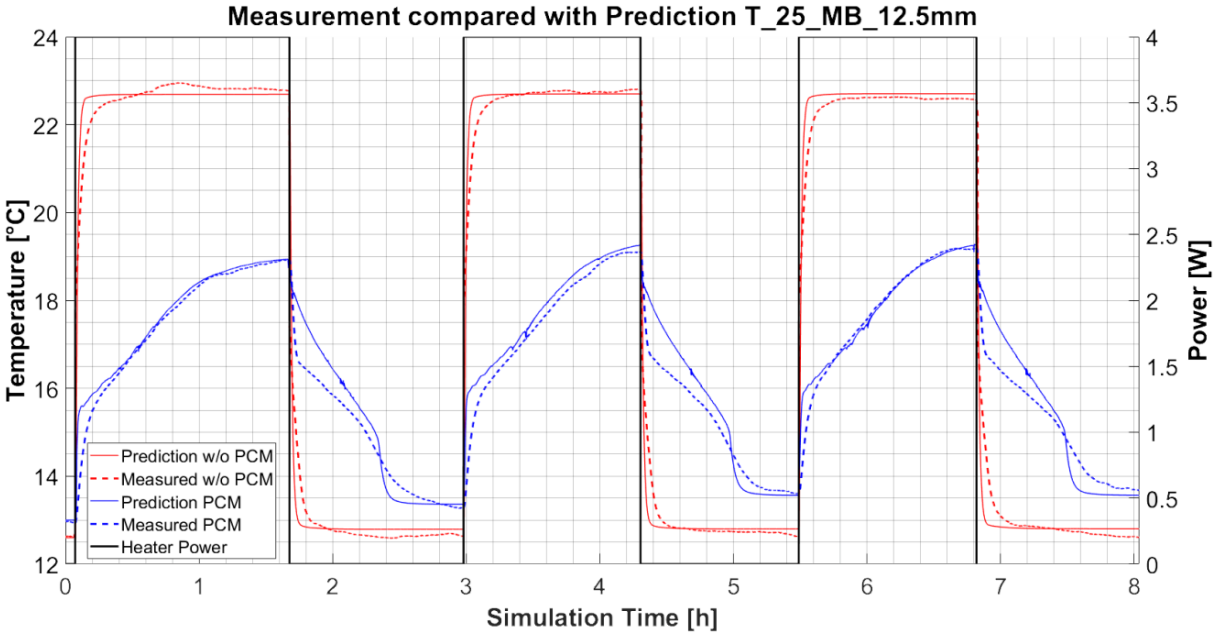

Figure 6.9: Predictions compared with measurement results of a ITS PCM thermal specimen without PCM (red profiles) and infused with the PCM hexadecane (blue profiles) [WIL-21]

Table 6.7 lists the applied heater power together with the maximum temperature differences of the predictions compared to the measurements during the charging (heating) and discharging (cooling) state. For the predictions and the test results it is relevant, that the PCM is fully solid at beginning. [WIL-21]

Table 6.7: Overview of the experimental test setup and the thermal test settings of the thermal specimen, compared with the resulting deviations between prediction and test [WIL-21]

Specimen type	Power [W]	Min. T [°C]	Max. T [°C]	Max. ΔT [K]
Without PCM (red curves)	4	12.5	23.1	0.9
With PCM (blue curves)	4	13.2	19.2	charge: 0.7 / disc.: 1.2

The thermal cycles as a whole show a high agreement with the data from the measurements and provide a good stability even for low heater power in combination with a small peak-peak temperature band close around the characteristic PCM melting temperature.

The experimental data indicate that the predictions are reproducible with a maximal deviation of ca. 0.7K for the charging and ca. 1.2K for the discharging cycles. [WIL-21]

Nevertheless, at the beginning of the cooling (recharge) cycles the temperature curve propagates faster than predicted. On the one side the thermal anchoring of the specimen to the cold plate was under-predicted. This was cross validated with additional TVC tests, where the anomaly of the deviating cooling curve was then no longer observed. [WIL-21]

6.5.3 Thermal Model and PCM Subroutine Step Size Sensitivity

Another sensitive parameter is the time step width of the transient solver in ESATAN. Most thermal models are sensitive to the step size, as this parameter has a significant influence on the stability of the thermal model. The transient solver can set the step size dynamically, by considering primarily the temperature relaxation criterion, the maximum number of allowed iterations in one step, the maximum step size or the maximum allowed temperature gradient between two steps. [WIL-21]

The PCM subroutine is triggered to manipulate the thermal model when the relevant node temperature is within the PCM hysteresis zone. If the temperature increase between two successive simulation steps is too large, the hysteresis is completely bypassed numerically, which results in a malfunction of the subroutine. For this reason the criterion for the maximal allowable change in temperature between two solver steps (*DTPMAX*) turned out to be the main driver, where the ITS model is most sensitive, visible as jitter effect in Figure 6.10. [WIL-21]

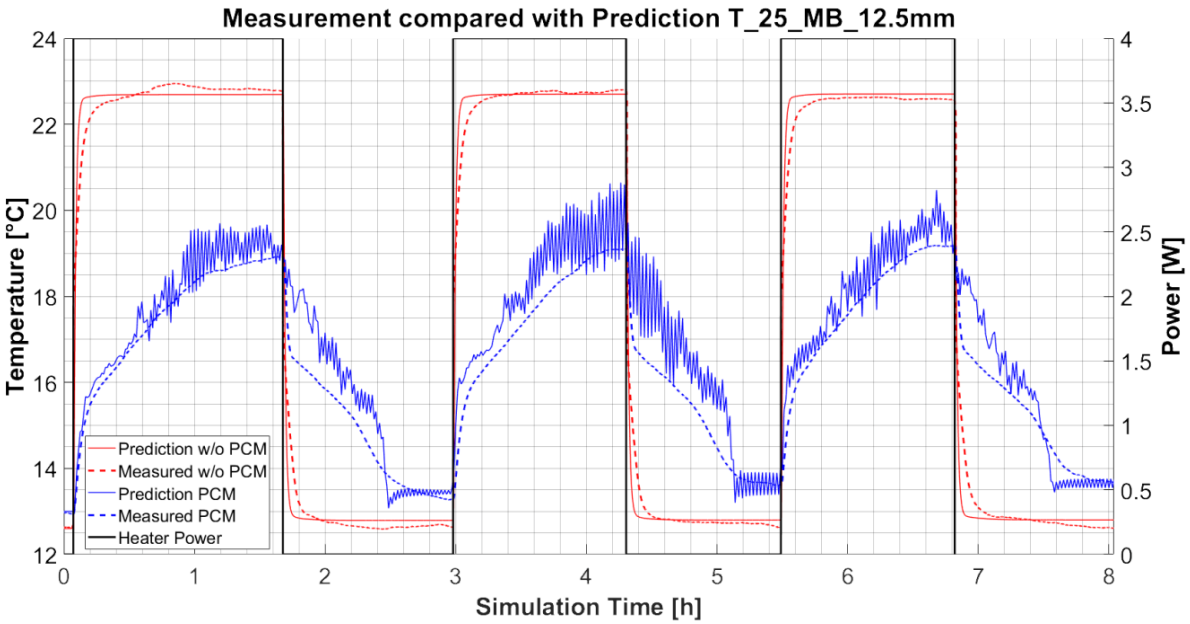

Figure 6.10: Sensitivity study of the time step lengths setup to identify sensitive parameters and settings of PCM subroutine. The DTPMAX criterion for the maximal allowable change in temperature between two solver steps shall be set to lower values, than the temperature width of the PCM hystereses [WIL-21]

That's why the *DTPMAX* criterion shall be set to values lower than the temperature span width of the PCM hysteresis. This will ensure that the PCM subroutine is reliably triggered to manipulate the local PCM nodes, which can be successfully observed in Figure 6.9. An overview of the PCM subroutine function and features are defined in chapter 4.6.2. [WIL-21]

6.6 Characterisation of the Influence of Convection on the Phase Change Process

The influence of convective heat transfer on the heat transfer model is reflected in this section. In the current state of development of the PCM subroutine convection effects are not considered. Nevertheless, the presence of convection can be detrimental to the expected thermal behaviour of the ITS component if there is significant heat transport due to convection within the liquid phase.

The validation of the influence of convection for ITS components took place in the laboratory environment. Cabeza et al. [CAB-15], Sánchez et al. [SAN-20], Tumilowicz et al. [TUM-14], Faden et al. [FAD-19] and many other authors mention that natural convection can take place on the one side as fluid flow due to density changes (buoyancy) with associated volume changes in presence of gravity in the liquid phase. An additional option can be solid body movements (solid PCM patterns) due to density differences between the solid and liquid phase. Contrary to that, in a microgravity environment the Marangoni effect (or thermo-capillary effect) becomes relevant.

Derived from the summary of Pernsteiner et al. [PER-21] the influence and magnitude of natural convection and the associated convective transport of energy in a PCM void is dependent on (a) the filler matrix and those geometrical parameters which permeates the PCM mass, (b) the orientation, size and shape of the PCM void, (c) the type of PCM encapsulation used and (d) the value of viscosity of the PCM in its liquid phase, which is clearly temperature dependent.

Duan et al. [DUA-01] investigated the solidification and melting process inside a rectangular enclosure filled with hexadecane paraffin. He found out that natural convection is existent but rather weak within the entire liquid phase. Natural convection can have some influence in the vicinity of the phase front, which is however still comparable small when considering only the conductive heat transfer.

Humphries et al. [HUM-77] pointed out from a similar point of view that convective motion in enclosed or respectively encapsulated voids shall be considered if the liquid PCM phase is subject to effects of not negligible magnitude. These effects could be (a) hydrodynamic instabilities due to buoyancy forces, (b) variations of the surface tension and surface forces or (c) motion of the liquid PCM phase due to density changes during the transition process and beyond.

Kasper et al. [KAS-20] discussed the implementation of the convection governing equations (Navier-Stokes equation) into a FDM modelling frame. Roesler et al. [ROE-14] had also been working on the discretisation and numerical implementation of the convection formalism in the environment of an FDM model. This is not further considered in this work.

Baehr et al. [BAE-06] mentioned that for the determination of the convective heat transfer coefficient it is essential that the temperature field is known. For the determination of the temperature field, it is in turn necessary to know the velocity field of the liquid phase. However, due to the limitations of the geometry independent lumped parameter representation of ESATAN thermal nodes in the FDM scheme, it is not feasible to simulate convection behaviour and corresponding 3D or even 2D velocity fields. The arrangement of the thermal nodes and the respective neighbouring nodes must be clearly assignable with coordinates and extent, which is not possible in the ESATAN environment.

As already defined the ITS heat transfer model relates on the fixed grid. In a classical PCM capacitor without any filler structure, the solid PCM patterns remain unfixed and can float due to the density difference. The ITS technology solves this problem elegantly, as continuous lattice (heat transfer structure) is embedded in the additive manufactured integral structure, which inhibits the movement of solid PCM constitutes.

6.6.1 Assessment of Convective Influence at Different Inclination Angles

Ernot et al. [ERN-19] investigated the heat transfer modes via natural convection and conduction in a triangular enclosure, which had been filled with a porous medium. The enclosure contained a metallic lattice of BCC type. The findings are that the dominant heat transfer mechanism is the conductive transfer of energy, especially if a highly conductive heat transfer structure is integrated.

The work of Guo et al. [GUO-18] concentrated on the influence of the inclination angle of PCM filled components with integrated copper foam as thermal heat transfer enhancer. In dependence on the inclination angle of the specimen, the thermal performance and melting front propagation are derived. It was found that the melting rate and the melt front of the PCM mass changes with different inclinations. Nevertheless, it is concluded that inclination changes of containers with a uniformly integrated heat transfer structure, like lattice, have only a little and thus negligible influence on the melting behaviour.

In order to assess the influence of convection effects at different inclinations on the heat transfer behaviour, it is necessary to test ITS components at different inclination angles in the TVC. One of the convection test specimens, which is a large-scale flat plate is depicted in the following Figure 6.11, with the thermal test setup at different inclination angles. The heat input into the specimen is provided by surface heaters, which are attached on the underside of the specimen. Detailed data of the specimen used for inclination dependent measurements are listed in the appendix in Table 10.3.

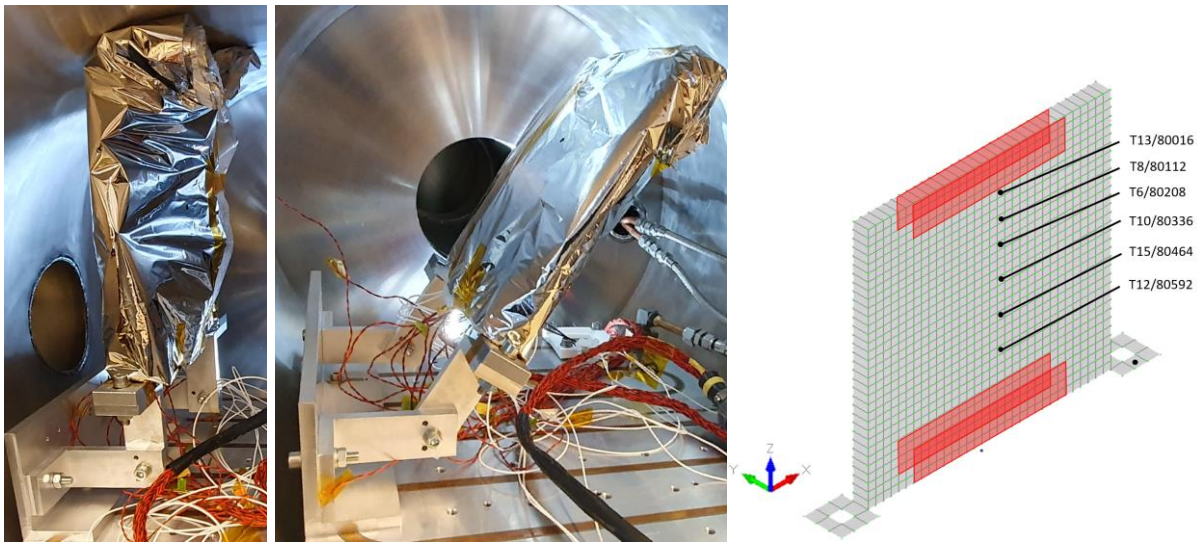

Figure 6.11: Various test setups of one of the ITS flat plate specimen at different inclination angles (left: 0°, middle: 30°) for validation of possible convective heat transfer effects within the liquid PCM phase, together with the thermal model discretisation scheme (right) and the surface heater positions (red shells)

Before the specimens can be filled with PCM and tested, it was necessary to perform reference tests on the unfilled specimens using the same setup and settings of the TVC at different heater power values, in order to correlate the model with the net conductive behaviour. Another reference measurements were performed with PCM only in vertical orientation. The correlations of the empty model (without PCM) provided for various inclinations and heater power values an acceptable model accuracy with a maximum temperature deviation of 0.6K, with a timely averaged deviation of 0.4K.

In the next step, the convection specimen (filled with PCM) was subjected to TVC test cycles. By successively variation of the inclination of the specimen, exactly the same heater profiles were run. The constant cold plate settings and cooling capacity are monitored by appropriate temperature sensors distributed across the cold plate. The heaters are operated with a constant power of 20 W in each test cycle. The results of the various inclination dependent TVC cycles are depicted in Figure 6.9.

The temperature profiles in Figure 6.12 show that there is a maximum temperature deviation of 0.5K between the various curves with a corresponding change in inclination. It can also be concluded from the measurement results that no valuable effects on the overall thermal behaviour of the PCM-filled specimen can be seen in direct comparison with varying inclinations. Even if slightly large convective heat transfer exists, this has no measurable and clearly verifiable thermal effects on the overall model.

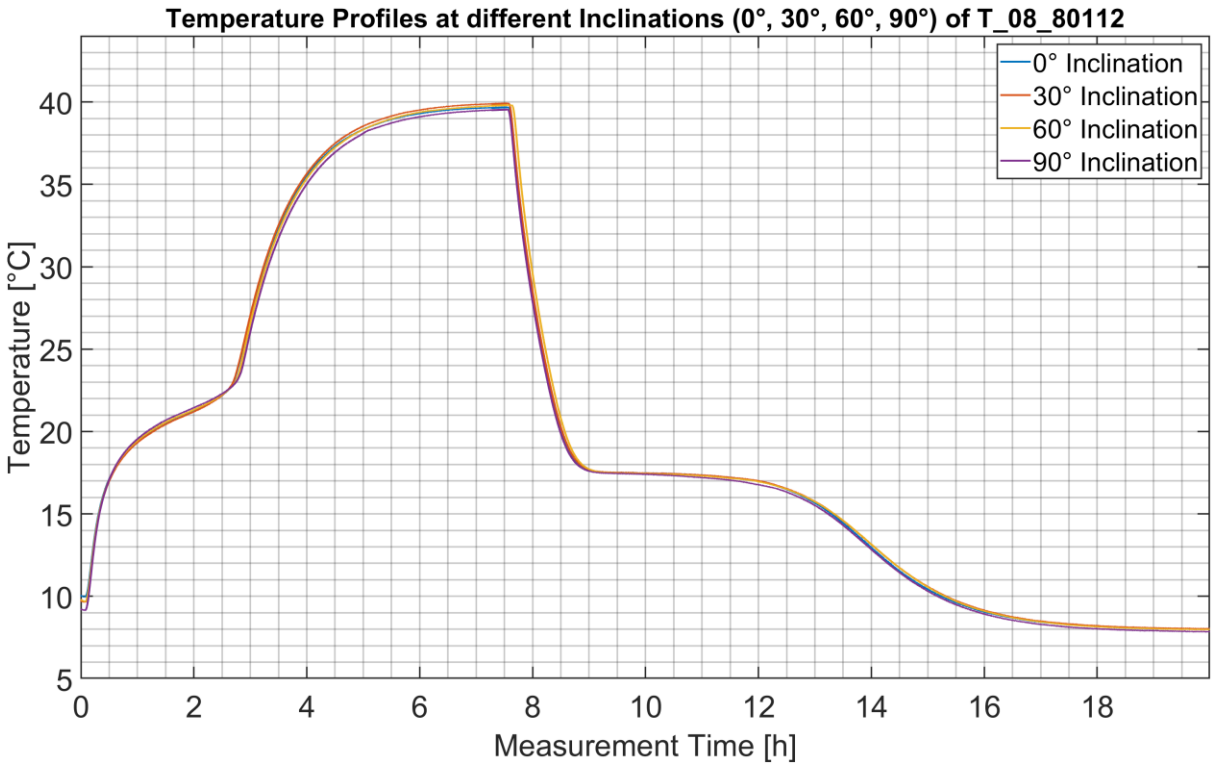

Figure 6.12: Inclination dependent measurements of the PCM filled convection specimen with a heater power of 20 W, in order to identify possible convective effects inside the large-scale flat plate

6.6.2 Equivalent Heat Transfer Sensitivity Study

As mentioned, ITS thermal models cannot predict convection in the current state of development. For the validation of the inclination dependent magnitude of convection on the performance of ITS components, convective equivalent sensitivity studies have been carried out.

As already mentioned, one of the requirements for the software development of the ITS thermal models and the PCM subroutine in the ESATAN environment is that the entire ITS software shall be in a fully parameterised framework. It is further assumed that hypothetic convection flows exist mainly within the PCM void along the in-plane directions. Based on the parametric thermal design variability, sensitivity studies could be carried out. The dependent parameters are listed below in Table 6.8.

For an initial assessment, thermal nodes in the following ITS models are assumed to be convectively active if the averaged PCM liquid fraction of the thermal node pairs involved has reached a minimum liquid fraction of 50%.

The convection specimen is taken as the reference model, with an orientation of 0° which is the vertical orientation of the plate, as seen in Figure 6.11 on the left side. In this state when operating the lower heaters, the greatest influence of convection will be generally expected.

Table 6.8: List of the dependent parameters and its range or variation, applied in the convection sensitivity study

Dependent parameters	Value / range
In-plane linear conductor (GL) equivalents	1.0 ... 0.1 ... 2.0
Nodal rate of total absorbable enthalpy for convection onset	$f_{V\,PCM} \geq 0.5$

The approach is to superimpose a hypothetical increasing convective heat transfer effect on top the existing in-plane conductive network. This is done by multiplying the existing linear conductor (GL) values between in-plane nodes. The specific GL value is manipulated when the thermal node pair of the corresponding conductive link have reached in the mean at least 50% of its enthalpy capacity.

The results of the analyses can be seen in Figure 6.13. The net thermal conductive model from Figure 6.13 is additionally depicted as reference curve (black solid curve). Table 6.9 lists the sensitivity results in dependence on the step wise increase of the linear conductor equivalent.

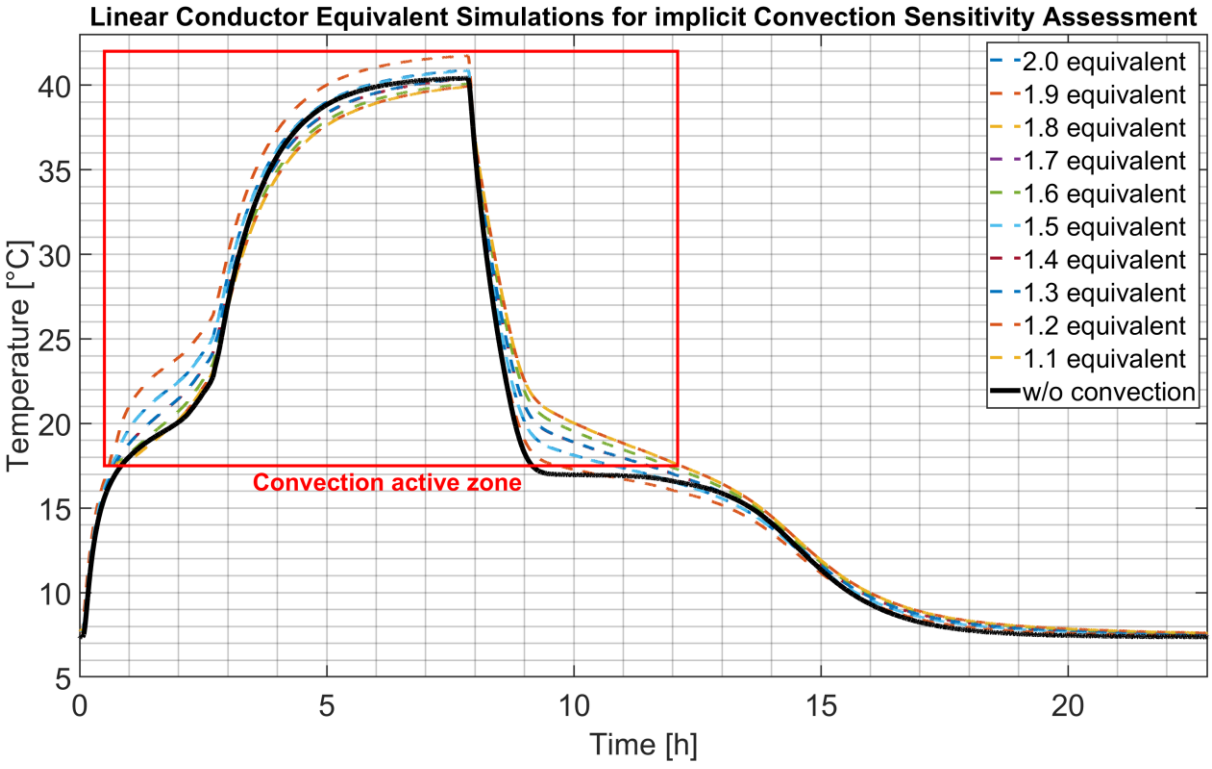

Figure 6.13: Results of the convection sensitivity study for step wise increasing linear conductor (GL) equivalents, to simulate the increasing influence of convective heat transfer rates. It can be seen that with an increasing convective influence the model is more and more under-predicted and inaccurate

Table 6.9: Influence of the increase of the linear conductor equivalents, in order to simulate a rising convective heat transfer mode to derive a possible onset of convective dominance. The deviations are calculated as amounts from data within the convection active zone only

Linear conductor equivalent	Mean Deviation [K]	Maximal Deviation [K]
1.1	1.5	2.5
1.2	1.6	2.9
1.3	1.6	3.4
1.4	1.8	4.1
1.5	2.0	4.8
1.6	2.2	5.3
1.7	2.3	5.9
1.8	2.5	6.5
1.9	2.7	6.9
2.0	3.1	7.4

With the stepwise increase of the effective conductor values from factor 1.0 to 2.0 in order to simulate a rising convection influence, it can be seen that the thermal models tend to underpredict. A maximum temperature of 42°C is reached in the simulations, with a total temperature variation of 34.4K (peak-peak). The model becomes more and more inaccurate and reaches a maximum deviation of about 7K, at twice the value of the original conductor value. It is also striking that the largest deviations and the widest spread of the temperature profiles occur during the melting interval. The deviations of the only conductive driven model (Figure 6.13, black graph) are within an acceptable range of approx. 2.5K, compared to the measurement data in Figure 6.12.With an increase of the thermal conductor equivalents due to an imitated increasing convection heat transfer behaviour the model accuracy steadily decreases, primarily in the area of the melting phase.

It is clear that this approach cannot replace the prediction of convection behaviour, as possible in CFD models or other suitable models. The aim is to determine in an initial assessment the temperature deviations due to the increasing influence of a convective in-plane heat transfer within the ESATAN environment. Nevertheless, the topic of convection should be investigated in more depth in follow-up work.

6.6.3 Buoyancy driven Convection Assessment by Dimensionless Parameters

In the previous section 6.6.2, the influence of convection on ITS PCM (hexadecane) parts was considered by means of similarity analyses of an equivalent thermal conductance approach in ESATAN, related on the net conductive heat transfer model. In this section, the determination and quantification of convection behaviour is considered using relevant dimensionless parameters.

Based on results available in literature, Chen et al. [CHE-14] summarised that the natural convection in the liquid PCM phase, with PCM-saturated metallic foam as heat transfer structure, are mostly suppressed by the heat transfer structure itself. The reasons are the high viscosity of the liquid PCM, the low thermal expansion ratio within the liquid state and a high effective flow resistance of the PCM due to the increased frictional effects by the heat transfer structure.

Therefore, with the focus on the viscous behaviour of PCM it will be followed to obtain a further assessment of the behaviour of convection by considering similarity parameters, which take viscosity dependencies into account. Humphries et al. [HUM-77], Faden et al in [FAD-20] and [FAD-21], Roesler et al. [ROE-14], Baehr et al. [BAE-06], Mallya et al. [MAL-21], Fleischer et al. [FLE-15] and Vogel et al. [VOG-19] provide a good overview and description of dimensionless numbers to evaluate the influence of convection in a PCM model. Mallya et al. [MAL-21] as well as Azad et al. in part I [AZA-20] and part II [AZA-21] also reviewed the validation of numerical analyses with experimental data, to identify the magnitude of the onset of natural convection in melting PCM in dependence on the inclination angle of the PCM layer, inside a rectangular enclosure.

6.6.4 Assessment of Convection in a Vertical Plate

Described especially by Humphries et al. [HUM-77] and Fleischer et al. [FLE-15] the Rayleigh number is an important indicator to interpret whether the heat flow is conduction, conduction-convection or only convection dominant. The critical Rayleigh number indicates the onset and the further increasing dominance of convective heat transfer. Convection is onset at the critical Rayleigh number, when a temperature difference (gradient) causes the buoyancy forces to exceed the viscous forces. Viscous forces prevail in the PCM voids of ITS components wherever PCM is in direct contact with aluminium and within the PCM mass. These contact zones are the boundary layer at the void chamber walls, the zone between PCM and the metal lattice and along the solid-liquid phase front.

According to Faden et al. [FAD-19] and König-Haagen et al. [KOE-17] it is generally assumed in literature that for idealised analyses, the convective flow in the liquid PCM fraction is laminar and an incompressible Newtonian fluid. The velocity in the solid phase is zero and the density change is dependent on temperature. Any further laminar and turbulent PCM behaviour is not considered.

Based on the critical Rayleigh number for the onset of convection the setup of the ITS convection specimen from Figure 6.11 was analysed. It is further assumed that the highest potential for convection is existent in the vertical orientation of the flat plate, with active heaters on the underside of the specimen. To not violate the ratios $l/H \gg 1$ and the $W/H \gg 1$ the length l to be analysed is limited to 5 mm (with height *H*), which is also the unit cell size of the lattice inside the specimen and identical to the model discretisation. The PCM layer thickness or width W is approx. 10 mm.

The temperature dependent Rayleigh number Ra is calculated related on equation (19), to analyse in a first instance the influence and onset of convection. The results are listed in Table 6.10. Where g is the acceleration of gravity, β is the thermal expansion coefficient (liquid state), ν is the kinematic viscosity, α is the thermal diffusivity and l is the characteristic length.

$$Ra = \frac{g \cdot \beta \cdot \left|T_{wall} - T_{melt\ point}\right| \cdot l^3}{\nu \cdot \alpha} = \frac{9.81 \frac{m}{s^2} \cdot \beta(T_{PCM}) \cdot \left|T_{PCM} - T_{melt\ PCM}\right| \cdot l^3}{\nu(T_{PCM}) \cdot \alpha(T_{PCM})} \qquad (19)$$

It must be noted that a homogeneous PCM layer without lattice and thus friction effects between the lattice and PCM is assumed. $|T_{PCM} - T_{melt\ PCM}|$ is the temperature difference between the boundary temperature T_{PCM} (wall or phase front) and the melting temperature $T_{melt\ PCM}$ of the PCM at 18.2°C (see Table 10.1).

Table 6.10: Thermal coefficients and the resulting Rayleigh number of hexadecane in order to derive the onset and influence of convective heat transfer

Temperature T_{PCM} [°C]	**Thermal expansion coefficient β [1/K]**	**Kinematic viscosity ν [m²/s]**	**Thermal diffusivity α [m²/s]**	**Rayleigh number [-]**
20	$11.12 \cdot 10^{-4}$	$4.46 \cdot 10^{-6}$	$0.78 \cdot 10^{-7}$	7055
30	$11.25 \cdot 10^{-4}$	$3.59 \cdot 10^{-6}$	$0.77 \cdot 10^{-7}$	58888
40	$11.37 \cdot 10^{-4}$	$2.93 \cdot 10^{-6}$	$0.76 \cdot 10^{-7}$	136,494
50	$11.5 \cdot 10^{-4}$	$2.43 \cdot 10^{-6}$	$0.74 \cdot 10^{-7}$	249,382
60	$11.62 \cdot 10^{-4}$	$2.06 \cdot 10^{-6}$	$0.73 \cdot 10^{-7}$	396,069
70	$11.75 \cdot 10^{-4}$	$1.74 \cdot 10^{-6}$	$0.65 \cdot 10^{-7}$	659,909
80	$11.88 \cdot 10^{-4}$	$1.62 \cdot 10^{-6}$	$0.61 \cdot 10^{-7}$	910,043
90	$12.0 \cdot 10^{-4}$	$1.42 \cdot 10^{-6}$	$0.52 \cdot 10^{-7}$	1,430,846
100	$12.13 \cdot 10^{-4}$	$1.21 \cdot 10^{-6}$	$0.41 \cdot 10^{-7}$	2,452,584
References	[KLO-22]	[DDB-23]	[VEL-15]	

Vogel et al. [VOG-19] reviewed and applied the work of Batchelor et al. [BAT-54] in his doctoral thesis in order to derive the influence of natural convection on the melting behaviour of PCM, which is embedded in an vertical plate. The critical Rayleigh numbers are summarised in Table 6.11 below at which convection will begin to be the dominant heat transfer mode.

Table 6.11: Limit values determined from experiments and analyses in order to indicate an increased convective influence on the overall heat transfer in a vertical plate, based on Vogel et al. [VOG-19]

Parameter	**Limit values**	**Heat transfer behaviour (vertical plate)**
Ra_{CR}	$\geq 500 \cdot A^4$	Convection begins to be the dominant heat transfer mode
Ra_T	$\geq 10^{10}$	Onset of turbulence flow

With the underlying geometric data of the convection specimen with a height *H* of approx. 150 mm and a PCM layer thickness *W* of approx. 10 mm, the following critical Rayleigh number results for a dominant convection behaviour, considering that the entire height of the PCM mass is liquified.

$$Ra_{CR} = 500 \cdot \left(\frac{H}{W}\right)^4 = 500 \cdot \left(\frac{0.15}{0.01}\right)^4 = 25{,}312{,}500 \tag{20}$$

If one compare the results of Table 6.10 with the critical Rayleigh number from equation (20) it can be concluded, that in theory no convection dominant heat flow have exist within the tested ITS specimens, depicted in Figure 6.12.

The analytical approach to stimulate a steadily increasing convective influence relative and parallel to the conductive heat transfer mode is summarised in Figure 6.13. The results of these analyses indicate that in the presence of an increasing magnitude of the convective heat transfer mode, intensifying deviations occur in the predictions of the thermal models.

These deviations can be clearly attributed to the influence of convection since the strongest deviations occur in the zones around the melting and solidification temperature of the PCM.

However, the theoretical approach by applying the Rayleigh number and the vertical flat plate clearly shows that convection effects are theoretically present related on the calculations listed in Table 6.10.

It can be further implicitly concluded from the summarised results of the calculations that possible convection effects may have existed in the experiments. However, the dominance of convection effects could not be proven by measurements. As Chen et al. [CHE-14] has already argued the absence of effective detectable convective heat transfer could be explained by the viscosity of the PCM and associated friction effects between the PCM and the lattice structure.

6.6.5 Marangoni Convection Assessment

To complete the consideration and estimation of the influence of convective heat transfer modes in ITS components, the Marangoni convection shall be also discussed.

Humphries et al. [HUM-77] reviewed the influence of surface tension driven convection in a microgravity environment, which is known as the Marangoni flow. The phenomenon occurs with temperature variations across a liquid interface. The temperature variations cause a change or variation in the shear forces along the interface layer. This behaviour can be explained with an example. In the case of a locally occurring hot spot, the fluid moves away from the hot spot to the colder zone due to the changed surface tension, which onsets a thermo-capillary flow.

Humphries et al. [HUM-77] further reviewed that in a microgravity environment the Rayleigh number has a very small value, which indicates that natural convection in space has negligible or no buoyancy induced effects. Already during NASA's Apollo 14 mission, experiments were conducted to find out whether PCM (paraffin) is subject to classical buoyancy-driven forces in microgravity. This could not be confirmed. In contrast, the presence of significant high surface tension driven convection could be clearly verified.

Humphries et al. [HUM-77] further concluded from the review of several studies, which had been investigating the magnitude of influence of natural convection and the Marangoni flow in a 1-g field, that the flow of natural convection in liquid thicknesses thinner than 10 mm triggered by buoyancy is mostly dominant compared to a Marangoni flow in the same gravity field. The trend is different for layer thicknesses of less than 10 mm. It has been shown that below this limit and with further decreasing fluid layer thickness, the influence of the Marangoni effect increases for fluids at moderate temperatures. These small fluid layer thicknesses and moderate temperature up to 90°C could be also present for ITS designs. The magnitude of the Marangoni flow is defined by the Marangoni number Ma. From experimental data it is known that the critical Marangoni number Ma_{CR} between a rigid and free surface is approximated to be 80, where thermo-capillary driven flows could theoretically onset.

Due to the existing differential equations and the initial as well as boundary conditions, the Marangoni equation can neither be determined in ESATAN nor analytically. A solution can only be achieved through corresponding knowledge of the gradient fields of the interfacial tensions and the surface tensions within a CFD mass transport model, which is not in focus in this work. Nevertheless, the topic of convection (buoyancy and Marangoni) should be investigated in more depth in follow-up work, accompanied by experimental tests in the microgravity environment.

6.7 Optical and Infrared Validation of PCM Melt Front Dynamics

The ITS design is based on a double wall layout with interior lattice structure. The PCM embedded in the chamber is therefore not visible from the outside. To correlate the macroscopic melting behaviour, the melting front and the phase regions against predictions by visible and infrared (IR) systems, it is necessary to use specimens with transparent walls.

For this reason, single-sided open large-scale specimens were manufactured. The open side was covered with a macrolon pane and sealed by a round cord sealing. All faces, expect the macrolon side, are covered with multiple layers of MLI. The specimen is depicted in Figure 6.14. All experiments were conducted in the laboratory, mounted on a TVC cold plate.

Figure 6.14: ITS specimen open wall window without any MLI cover, in order to verify the macroscopic PCM melting behaviour and the melting fronts by optical (visible and IR) recordings of a large-scale flat plate with integrated lattice

The specimen is filled with hexadecane PCM, which has a melting temperature of around 18°C. On the top of the specimen there are two nozzles, which are used as filling nozzles. The Table 10.5 in the appendix summarises the technical data of the open wall window specimen.

The results of a representative measurement series are depicted in Figure 6.15. Figure 6.16 contains the thermal model predictions, which were correlated with the IR data. Solid PCM, especially paraffin, has a milky white colour. Molten or liquid PCM is almost as transparent as water. The kapton surface heaters are located on the back side of the specimen at the top and bottom. In the example shown, power was applied only to the upper centre heater panels.

A visible effect resulting from the optical experiments is that the highly conductive aluminium alloy weakens hot spots due to its high thermal conductance of the aluminium wall and lattice structure, by dispersing the local heat load well appropriate to the surrounding zones. This can be seen from the fact that on the one side the propagating melt front becomes more and more homogeneous and straight. On the other side, the local temperature spots of the kapton heaters are hardly recognisable.

Time	Optical	Infrared
50 s solid		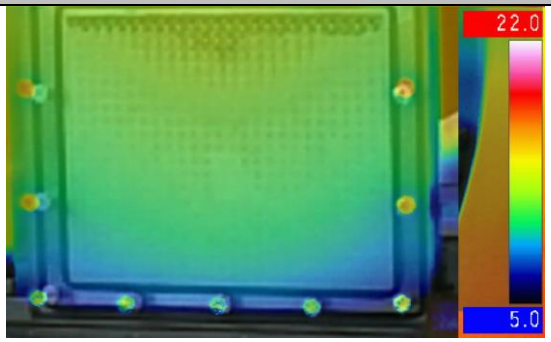
250 s		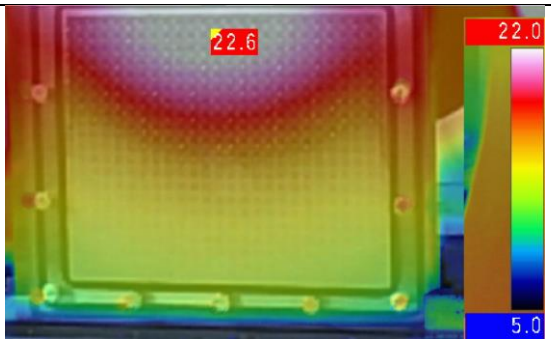
500 s		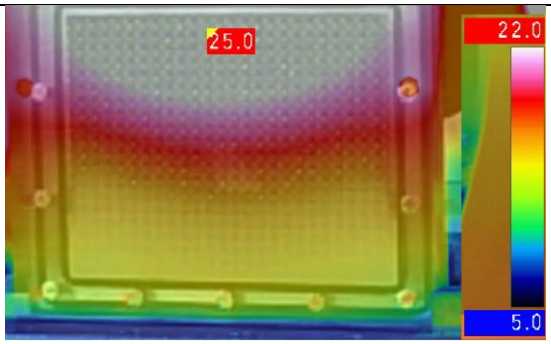
750 s		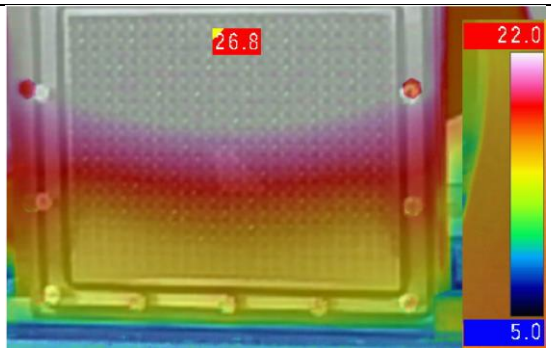
1000 s liquid		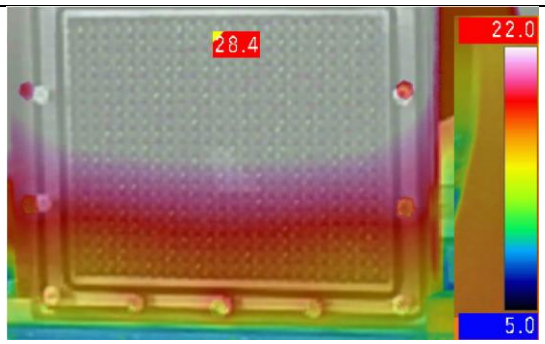

Figure 6.15: PCM melt front propagation made visible by parallel optical (left) and infrared recordings (right) in order to verify the melt front dynamics and the conductive heat transfer via the aluminium lattice

6.7.1 Thermal Model Correlation with IR Heat Map Data

Time	Thermal prediction (5°C to 22°C scale)	Infrared
50 s solid	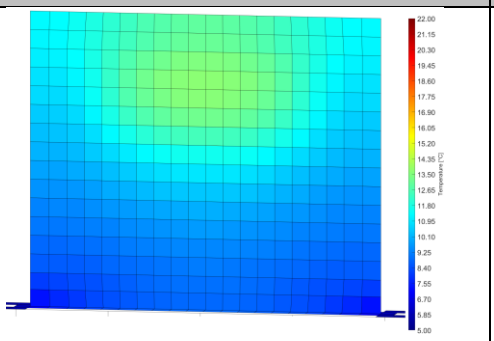	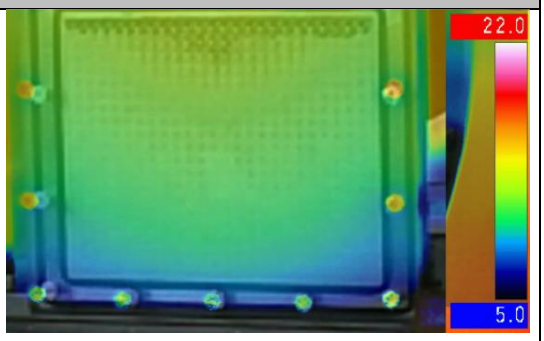
250 s	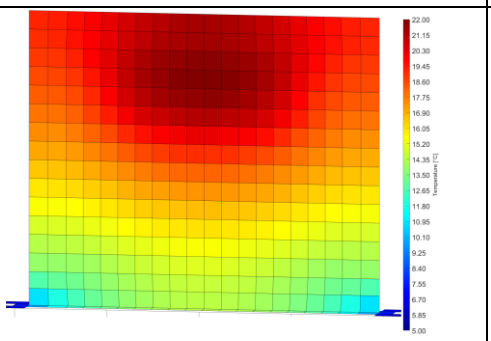	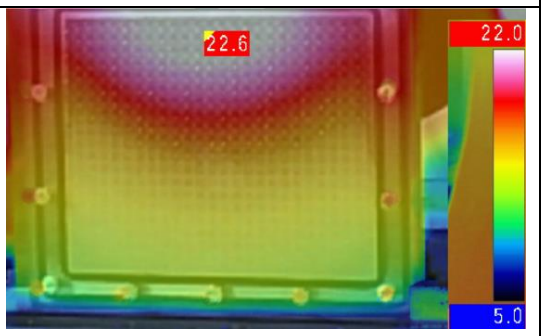
500 s	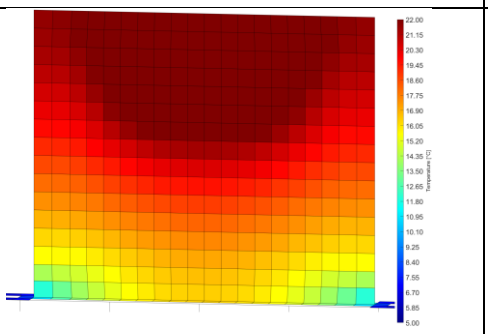	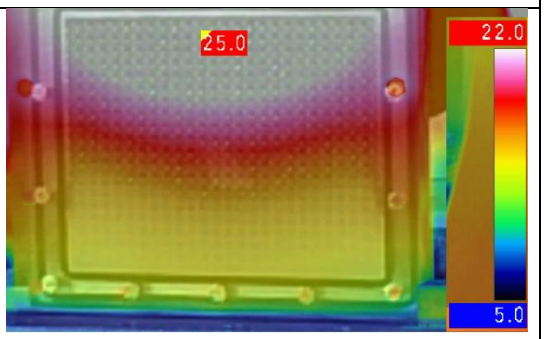
750 s	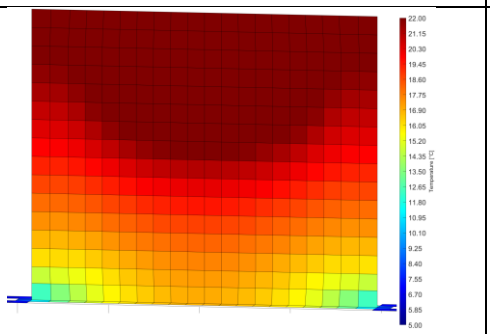	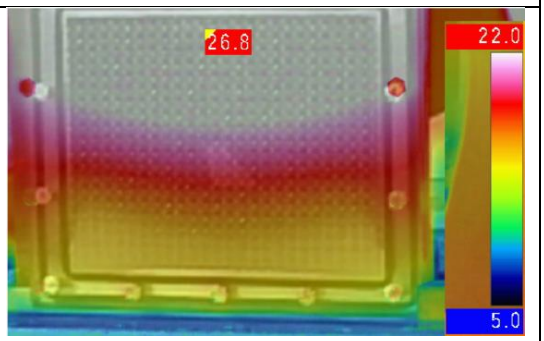
1000 s liquid	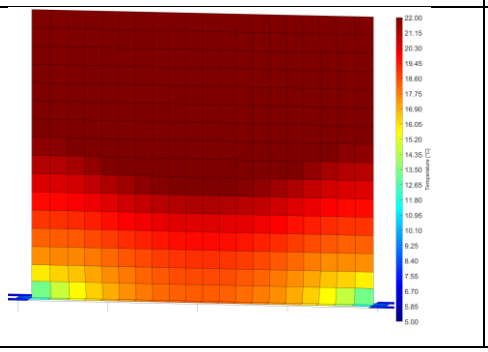	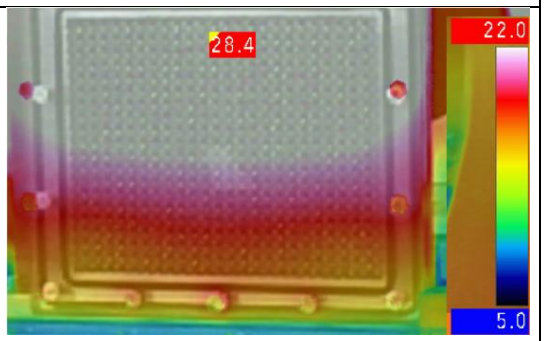

Figure 6.16: PCM melt front propagation between the thermal prediction (left) and infrared recordings (right) in order to correlate the melt front dynamics and the conductive heat transfer via the aluminium lattice

After the correlation of the thermal predictions with the IR heat map data, a mean deviation between the predictions and the test results of 1.4K can be determined, which is deemed to be acceptable. In conclusion, the aim was primarily to predict the formation and propagation of the PCM melt front and to correlate it with measured data, which had been achieved with acceptable accuracy.

It should be noted that the measurements with the specimen in the TVC on the cold plate took place under atmospheric conditions. The reason is that neither the IR camera nor the optical sensor are vacuum-capable. This means that the measurements are additionally affected by natural convection, which are locally present in the opened TVC.

The additional thermal coupling due to convection has not been taken into account in the predictions. It is therefore assumed that the cooling power provided by the cold plate at -5°C is completely dominant compared to the convective cooling. This is because the entire window specimen, except for the front macrolon side, has been completely encased in multiple layers of MLI. This shall reduce the effect of possible convective cooling to a minimum. Furthermore, the cold plate temperature was permanently measured and used for thermal model correlations.

6.8 Model Cycle Stability with Interrupted Phase Changes

Within the scope of the sensitivity studies, several thermal cycle runs are carried out with different specimens in the TVC. One of these specimens is the flat plate specimen, which is shown in the Figure 6.17.

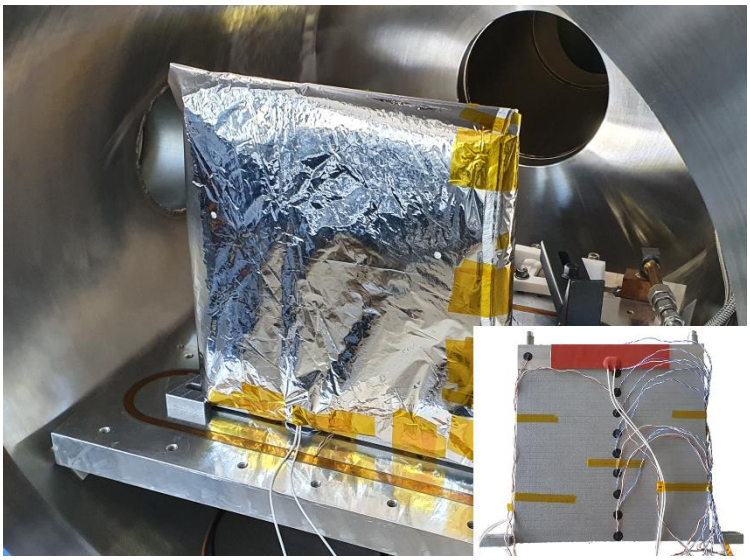

Figure 6.17: ITS thermal large-scale flat plate specimen, which is used for validation measurements of the thermal stability and as basis for thermal sensitivity studies

The aim of these measurement campaigns are to thermally cycle diverse specimens, like the flat plate specimen, in order to validate the cycle stability of the PCM with completed and interrupted phase changes.

The phase change is passed through completely, so that possible model instabilities or cyclic stabilities, if present can be detected. The technical data and the thermal test setup of the flat plate specimen are listed in the Table 10.4 in the appendix. As can be seen from the Figure 6.17, the specimen is completely covered by MLI. The thermocouples are attached vertically by high conductive carbon tabs. This time the surface heaters are attached to the bottom of the test specimen to enable maximal temperature gradients between the heat source (heater) and the heat sink (cold plate).

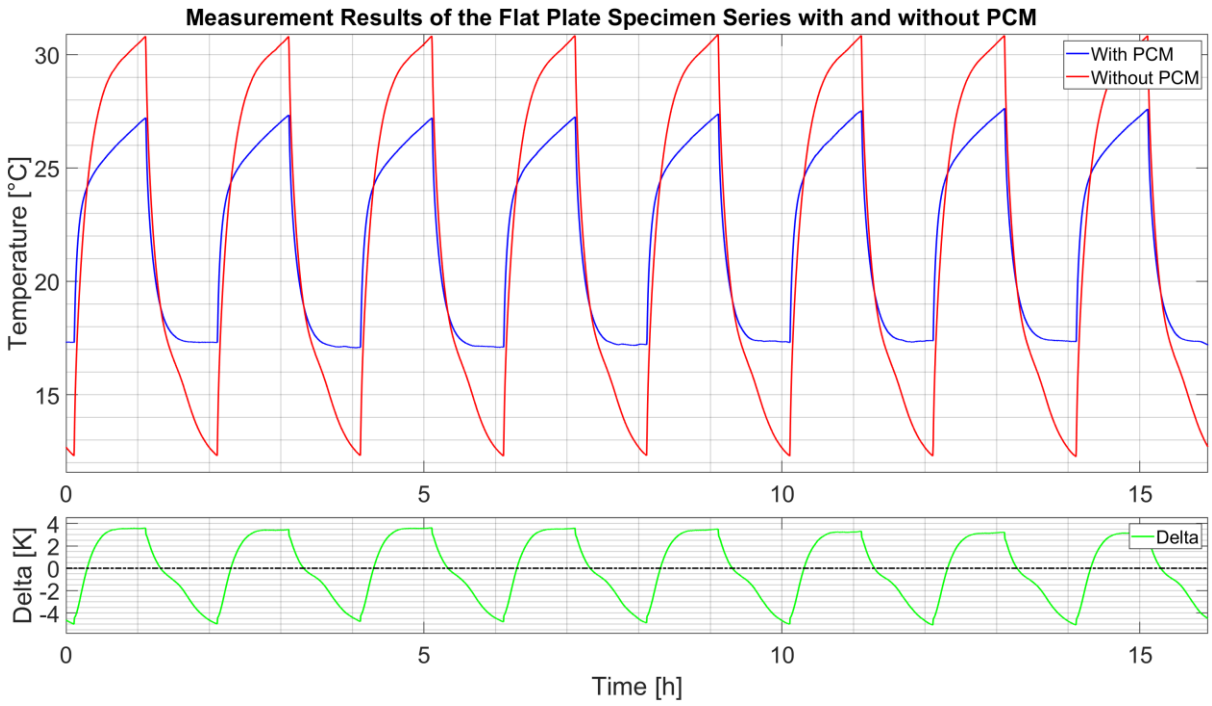

Figure 6.18: ITS PCM flat plate specimen measurement results of the TVC cyclic stability test sequences

The thermal performance results of the empty (without PCM) and the PCM filled specimens are summarised in Table 10.6 also in the appendix. The heating and cooling intervals are constant and repeated with 60 minutes each.

It is shown that an acceptable cycle stability of approx. ± 0.3K is achieved. The temperature span is being reduced by -45.6%. However, it is clear that eight continuous and consecutive cycles, according to ECSS, are not sufficient for the validation of the long-term stability of ITS the technology. Within the framework of the ITS research, it was not possible to carry out long-term cycle demonstrations in the TVC due to the reduced testing time, as a large number of specimens had to be tested in the TVC for the progress of the ITS research project.

6.9 Thermal Mesh Convergence Analyses

For the further thermal validation of the ITS parts, sensitivity studies are carried out related on the flat plate specimen. The aim is to estimate the mesh convergence as well as the maximum mesh size for a sufficiently accurate prediction in dependence on the PCM mass to be embedded. Therefore, the complete range of all thermal models are proven to its minimal and maximal mesh sizes.

All ITS specimen thermal models have mesh sizes of CQUAD4 shells between 3 and 22 mm. For the sensitivity study, the thermal setup is identical to that in Table 10.6. The results of the mesh convergence analyses are summarised in the Figure 6.19 visualising temperature heat maps, which are all colour-scaled between 5 to 30°C. The aspect ratio of the CQUAD4 shell elements is constant one.

Mesh	Time: 750 s / step: 16	Time: 2300 s / step: 47	Time: 3850 s / step: 78
24 mm 8x8 CQAUD4	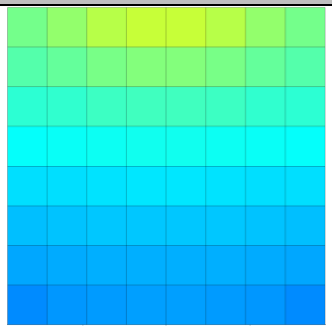	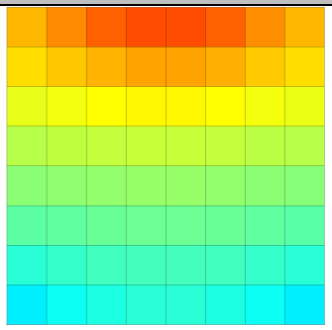	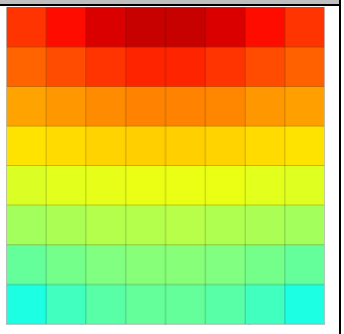
12 mm 16x16 CQAUD4	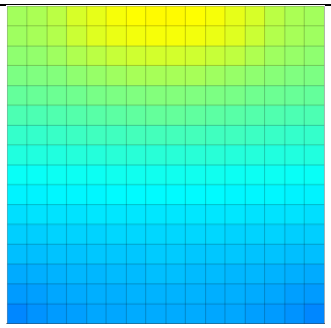	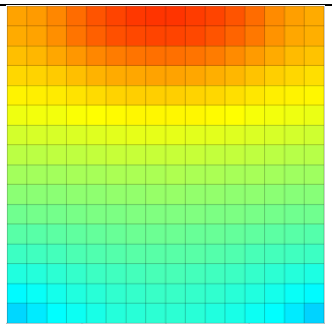	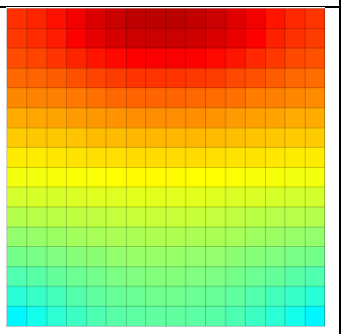
6 mm 32x32 CQAUD4	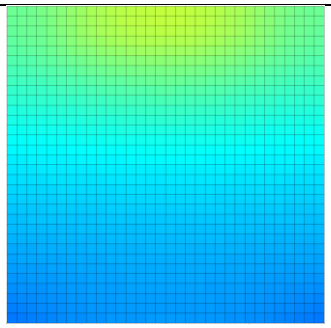	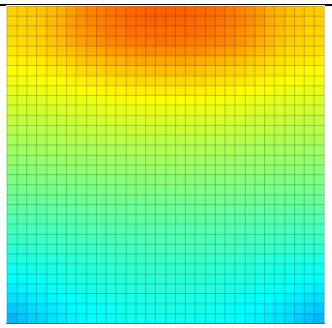	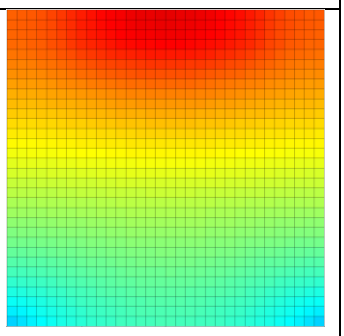
3 mm 64x64 CQAUD4	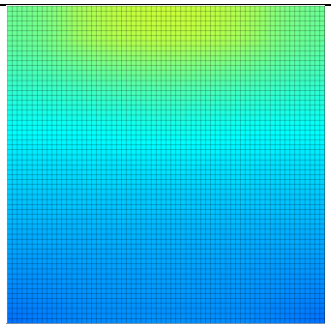	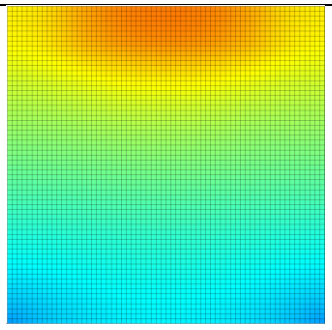	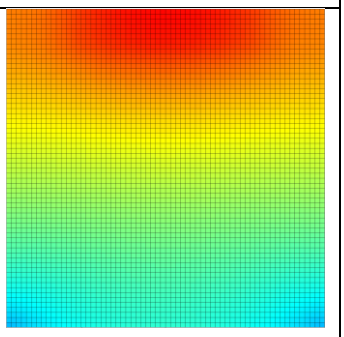

Figure 6.19: Results of the mesh size sensitivity study in dependence on the thermal setup and the PCM, in order to estimate the applicable mesh size as well as the minimum mesh size for a sufficiently accurate prediction

The Table 10.7 located in the appendix, summarises the prediction results of the evaluated heat map mesh convergence analyses related on the average and maximal temperature deviations of the models. The average and maximum temperature deviations indicate in Figure 6.19 that the applied mesh sizes up to a mesh size of 12x12 mm are sufficient accurate with proper convergence. Above this, the deviation increases slightly, but is still within the limits, which are formulated in the ECSS standard for temperature deviations. The PCM layer thickness of the test specimen is 10 mm. As a result, for all further predictions and models the benchmark of the mesh size divided by the PCM thickness shall not exceed a factor of 0.12 mm/mm.

6.10 Thermal Model Validation with Multiple PCM Types

In more advanced applications, it may be possible that not only one specific PCM but multiple PCMs are used section by section, in order to overcome different heat loads or requirements to passive thermal control of a component. That's why another aspect is the validation of the ITS thermal models with different embedded PCM types in one model. The representative specimen is shown with the thermal setup in Figure 6.20.

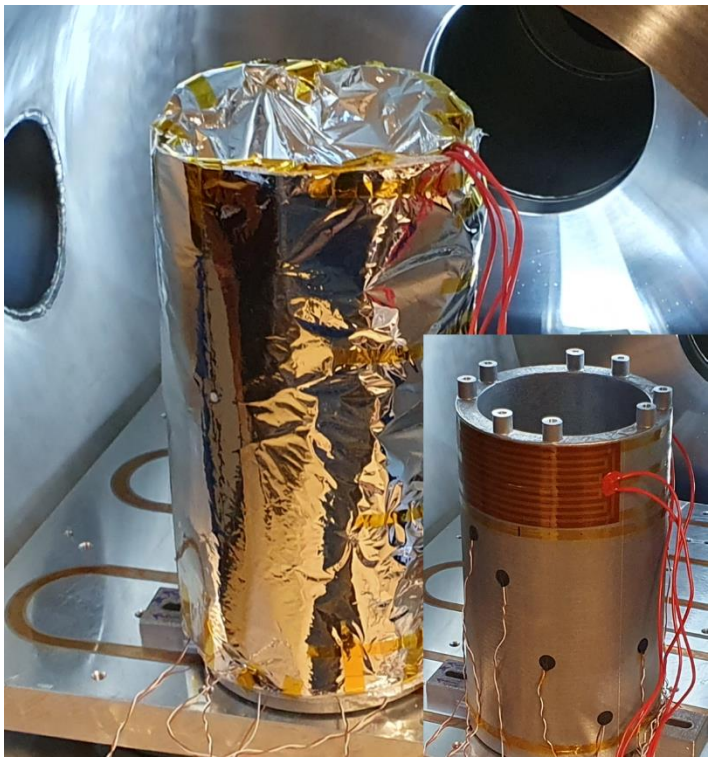

Figure 6.20: ITS thermal large-scale cylinder specimen, which is used for validation measurements of the thermal stability and as basis for thermal sensitivity studies

Furthermore, the ITS qualification strategy also involves the validation of the predictability of round or complexly shaped geometries (cylinder, cone, etc.). For technical reasons, this type of geometry is also very often used for optical satellite payloads (telescopes, etc.). This is also the case with the final ITS demonstrator.

Another use case to be covered by this cyclic test campaigns of the cylinder specimen are high temperature gradients caused by high heat flows, induced by thermal shocks. The kapton surface heaters are therefore powered with more than 100 W. It is intended to simulate the influence of extremely fast or strong thermal fluctuations, such as those that occur when a satellite payload enters or leaves the shadow phase.

Combining these further aspects, the validation takes place on a cylinder whose thermal setup is shown in Figure 6.20. The cylinder specimen contains four PCM compartments, which are equal in size, encapsulated from each other and occupy 90° of the cylinder circumference respectively. The specimen test setup data are listed in Table 10.8 in the appendix. Each of the four chambers is filled with a different PCM. The added value of this dissertation is mainly demonstrated on the basis of this test specimen.

The results indicate that the ITS thermal model concept delivers reliable results even in the case of extreme temperature jumps triggered by high heat flows. The comparison of the measurement results with the results from the thermal model predictions can be seen in Figure 6.21.

The following Table 6.12 summarises the thermal test setup data and the results of the performance evaluation. After reaching nominal cycle state, the average deviation between the prediction and the measurement data is 1.4K, which is acceptable. The overall course of the temperature curves also shows good confidence with the measurements and therefore confirm that the current ITS thermal model concept can reliably predict the above-mentioned new combined design aspects.

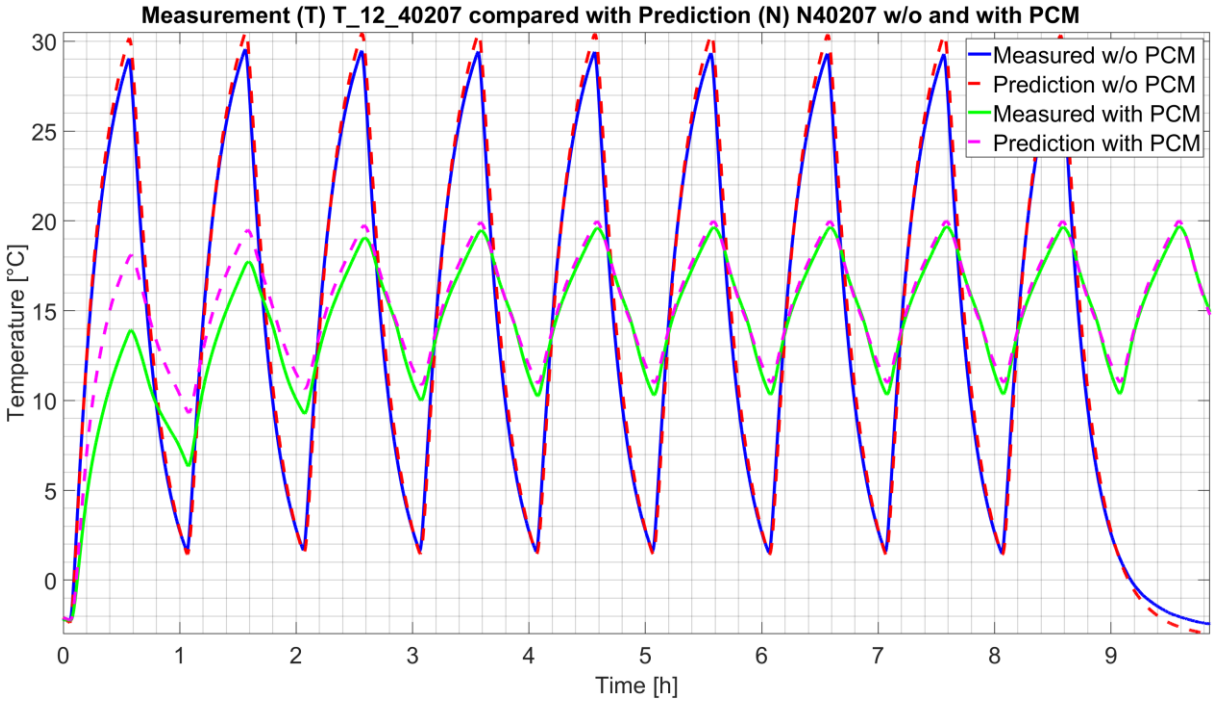

Figure 6.21: ITS PCM specimen cylinder measurement and thermal model prediction results of the cyclic stability test sequences without and with PCM, with higher power input to simulate thermal shocks

Table 6.12: Cyclical stability thermal test setup and test results of the large-scale specimen cylinder, which is subject to thermal shocks and contains 4 different PCM types in individual sealed chambers

Cyclical stability tests	Values
Heater power	const. 2x60 W
Heating time / cooling time	30 min / 30 min
Cycle period	60 min
Minimal temperature w/o PCM	1.6°C
Maximal temperature w/o PCM	29.7°C
Minimal temperature with PCM	10.3°C
Maximal temperature with PCM	19.7°C
Temperature span reduction due to PCM (peak-peak)	-66.5% / -18.7K
Cycle stability (maximal deviation)	± 1.4K

6.11 Temperature Dependent Material Properties

The analysation of the temperature dependent material properties is another important factor that needs to be evaluated for a complete thermal validation of the ITS technology. Therefore, model variations of the bulk material properties have been carried out with the already sufficiently correlated large-scale thermal models. The Table 10.9, which is listed in the appendix, gives a summary of the influences taken into account.

The results of past thermal model correlations indicate that the variation of the thermal conductivity of the PCM has no significant influence on the thermal model behaviour. Li et al. [LI-21] also analysed the influence of temperature dependent thermo-physical properties of liquid paraffins in combination with porous metallic structures. As expected, is the effective thermal conductivity of liquid PCM and its temperature dependent variation less sensitive for the common heat transfer mode, since the net thermal conductivity of liquid paraffin is factor 100 smaller than aluminium. The variation of the conductivity of the aluminium alloy is also not relevant for the temperature range used for the ITS validation.

The different values for the latent heat of fusion related on the solid and liquid state of the PCM are neglected, which means that both solid-liquid and liquid-solid hysteresis profiles are identical in the specific amount of latent heat, in all thermal models.

The temperature dependence of the specific heat capacity and the density variations are also not represented in the ITS model method. Due to the framework of mandatory lumped parameter definitions in the FDM scheme in ESATAN, a variation of the specific heat capacity or the density would lead to a violation of the mass conservation within the simulations.

Finally, the variation of the density is not relevant since no convective influences are simulated anyway. However, the initial values for specific heat capacity and density are used to define the overall thermal node capacitance at the very beginning of the prediction.

7 THERMAL DEMONSTRATION OF THE ITS TECHNOLOGY

This chapter introduces the large-scale demonstrator of the final ITS research, which had been used for use case based thermal validation of the ITS technology. Besides a short description of the manufacturing and AIT process, the thermal models and the test setup are presented. The TVC results are compared with predictions, the thermal performance enhancement is evaluated and the PCM storage degree of utilisation of the passive thermal control design is assessed. Furthermore, the ITS technology scaling concept, which is introduced in this thesis, is analysed for its representativeness in relation on the original MTG reference model.

7.1 ITS Demonstrator Hardware Assessment

A use case study had been carried out to determine the principal demonstrator model. An overview of the use cases considered and specifications rated are summarised in a comprehensive trade-off matrix in the appendix in Table 10.10. As a result, the highest potential for thermal stabilisation is attributed to an optical baffle system.

That's why the MTG weather satellite and therein especially the Entrance Baffling Assembly (EBA) emerged as candidate for an ITS demonstrator platform. Figure 7.1 below depicts these models whereby on the left side the MTG satellite as a whole, in the middle the EBA submodel and on the right side the inner baffle assembly are shown. However, the inner baffle assembly structure on the right side yields the ITS demonstrator design baseline.

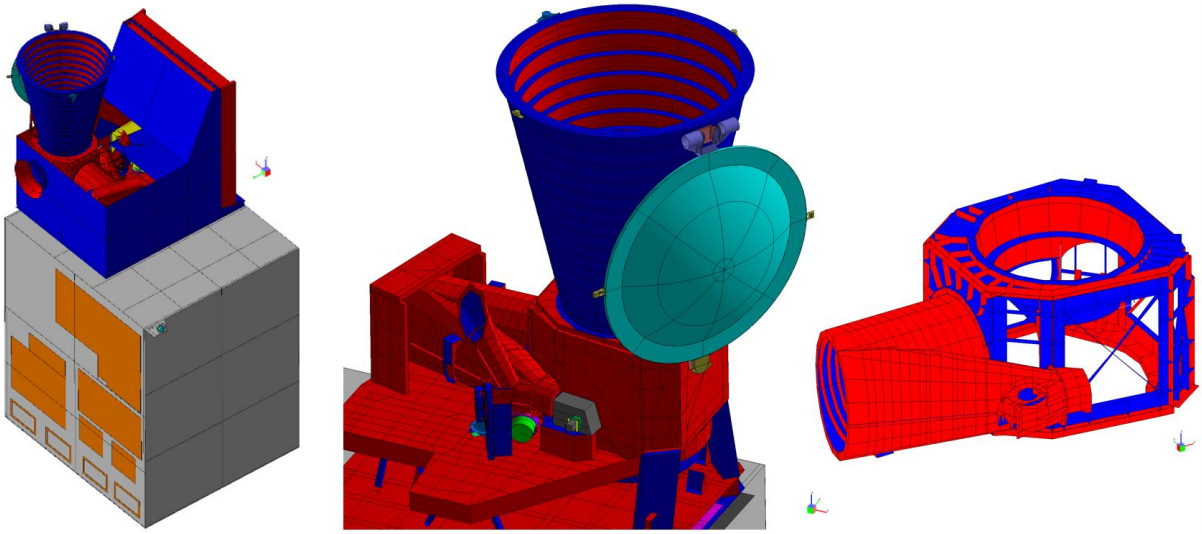

Figure 7.1: Thermal model of the MTG satellite (Rev1666) (left) provided by OHB, with a more detailed view on the EBA submodel (middle) and the inner baffle assembly (right) are depicted [OHB-19]; [WIL-23]

The MTG thermal model was provided by OHB System from Munich. According to the report of OHB by Triebig et al. [TRI-15], the MTG satellite is intended to be placed in the GEO. The instrument is permanently pointed in nadir (+Zs) direction. Especially at specific days of the year in orbit it cannot be avoided that the sun intrusion directly enters the baffle system, especially the inner baffle assembly shown in Figure 7.1 on the right side.

During these events the sun radiates on the structure's skin, on the baffle vanes and on the aperture (interface of the solar baffle assembly) and the structure cyclical heats up at certain points to +110°C. As consequence of that, infrared heating occurs from the heated inner baffle assembly structure towards the optical bench. This leads in turn to temperature instabilities of the optical bench, where the mirrors are attached and thus also degrades the optical performance. Structures of optical instruments such as baffle structures and the corresponding optical bench where the mirrors are attached at, have high demands on the thermal and further on the thermo-elastic stability. The optical performance is clearly temperature sensitive and thermo-elastic deformations are caused due to temperature instabilities, which are aimed to be diminished by the ITS technology.

The considered MTG orbit cases of extreme temperatures and instabilities are treated as hot cases and are summarised in the Table 7.1 below. These hot cases are known firstly as Equinox (EQ), which is on equinox day at 0° inclination. At that time the sun vector points direct in the field of view of the instrument during the entrance and exit of the Earth shadow. The second most critical hot case is the 56th day in orbit in 2016 (D56) at ca. +9°/-9° inclination. These cases provide a high potential to validate the temperature stabilisation of the ITS technology by analyses and supported by tests. [WIL-23]

Table 7.1: Definition of the MTG thermal model orbit hot cases D56 and EQ [OHB-19]

MTG IRS thermal model potential hot cases	Solar inclination	Hot case name
Highest peak temperatures	ca.10°	D56
Largest temperature gradients, most unstable case	ca. 0°	EQ

Furthermore, the inner baffle assembly (Figure 7.1, right) as part of the EBA, to date is manufactured and assembled by classic methods. The structure at the whole has complex surfaces and geometries with high integration effort. Therefore, the potential of the reduction of interfaces and its connecting elements (screws, rivets, etc.) due to the monolithic additively manufacturing method are treated high.

The MTG temperature curves of the inner baffle assembly thermal shells are shown for the case D56 in the following Figure 7.2 to better illustrate the core problem of the occurring temperature instabilities. The MTG temperature profiles of case EQ are depicted in Figure 10.13 in the appendix.

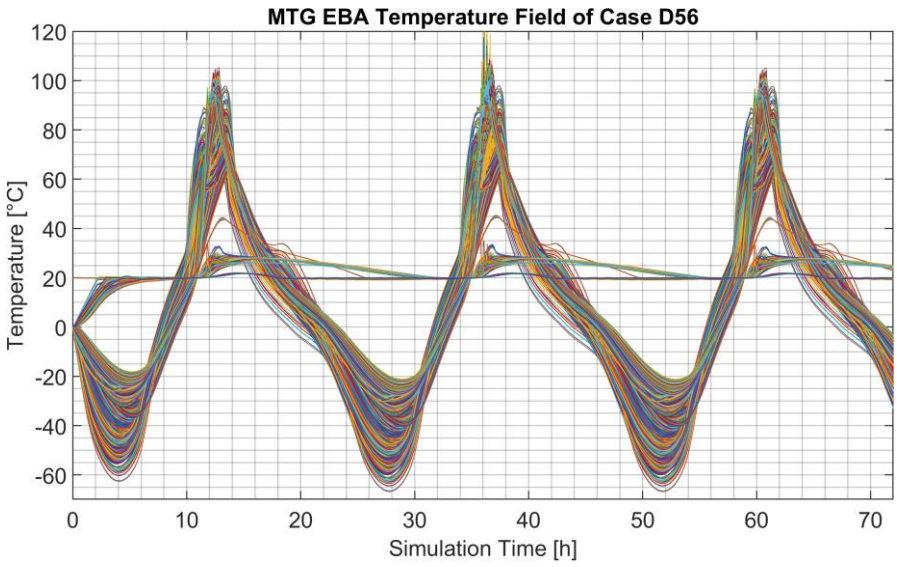

Figure 7.2: Temperature curves of the MTG thermal model orbit hot case D56 [OHB-19]

7.2 Demonstrator Redesign for Thermal Model Preparation

For the additive manufacturability the submodels prism and inner baffle have been fundamentally simplified and redesigned. A comparison of the original MTG design and the ITS demonstrator redesign CAD model can be found in chapter 10.11 in the appendix.

The thermal model redesign retained the characteristic shapes and proportions related on the original model, which is shown in Figure 7.1 on the right side. The method for the necessary structural reduction and scaling of the demonstrator structure, due to the limited dimensions of the available additive manufacturing plant and TVC facility, are explained in the appendix in chapter 10.12.

As already mentioned, the ITS design baseline is generally transposed by a double wall design technique with intervening and encapsulated PCM voids. This CAD integral design with the characteristic double walls in combination with an integrated lattice structure are made visible by sectional views in the Figure 7.3 for the submodels prism (left) and inner baffle (right). In principle, the ITS CAD models are assembled using Boolean operations.

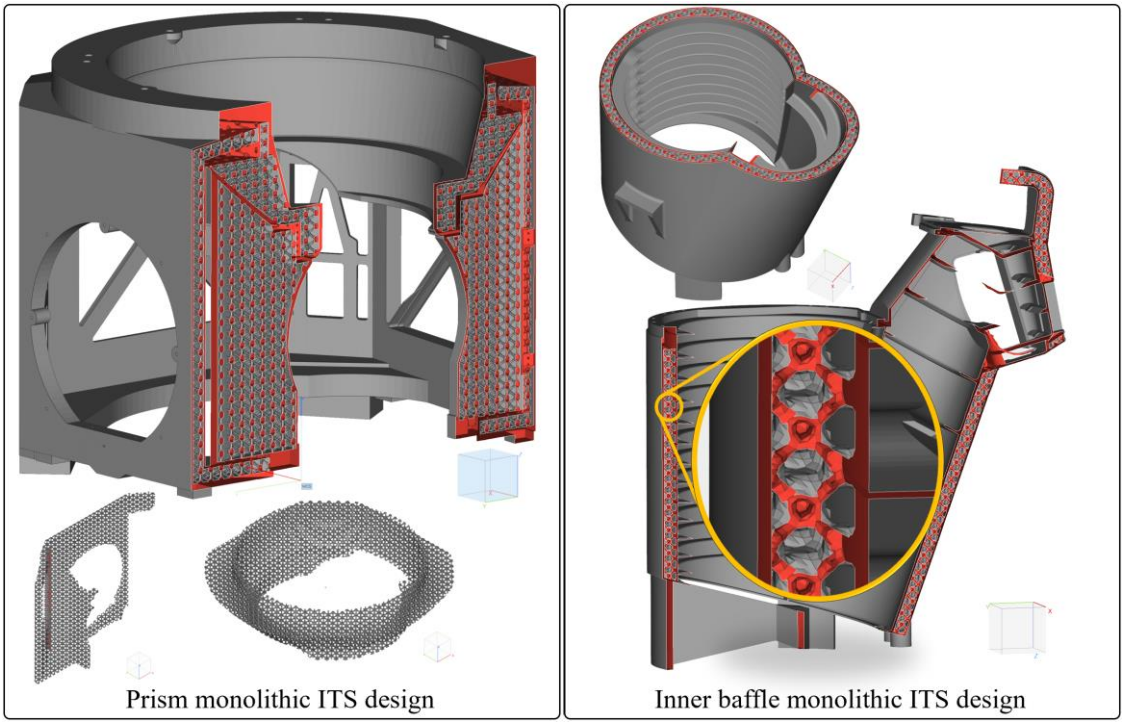

Figure 7.3: ITS demonstrator monolithic CAD integral design with integrated lattice made visible, sectional views of the part prism with sun shield (left) and the inner baffle (right) ITS double wall design

A coherent lattice matrix is integrated into the voids of the double wall design to primarily stiffen the lightweight structure and secondarily to enhance the effective in-plane and out-of-plane thermal conductance of the component. The mentioned PCM for passive thermal control is embedded in the remaining space within the voids and has therefore direct contact with the cohesive lattice and the walls.

Due to the ITS integral design technique diverse and separated components can be structurally combined into one monolithic component, which in turn minimizes the number of thermal interfaces significantly. With these benefits of the monolithic integral method, no separate or additional parts are necessary. The multi-chamber technique also allows different PCMs to be embedded within the same component in separated chambers. This increases the variability of the ITS thermal design.

7.3 ITS Demonstrator Thermal Model

A detailed overview of the ITS demonstrator thermal submodels are available in the appendix in chapter 10.17, together with a comprehensive listing of the bulk data, thermo-optical data and general thermal model data. Detailed information on the thermal interfaces of the submodels inner baffle and prism can be found in the appendix in chapter 10.10.

Since the thermal modelling suite ESATAN had been used for thermal modelling and predictions, the thermal model was created according to the FDM scheme with lumped parameter formulations. The TVC was created as an environmental enclosure based on ESATAN primitives through previous work and is used for the thermal simulations in this work. The thermal model assembly with the TVC enclosure is shown in Figure 7.4, where the front side of the TVC is kept transparent for visualisation.

The demonstrator assembly is thermally coupled to the cold plate (Figure 7.4, blue plate) by three screwed on GSE adapters, two on the prism and one on the inner baffle side. The adapters are made of aluminium AW-6082. The cold plate provides the heat sink. No thermal filler is used.

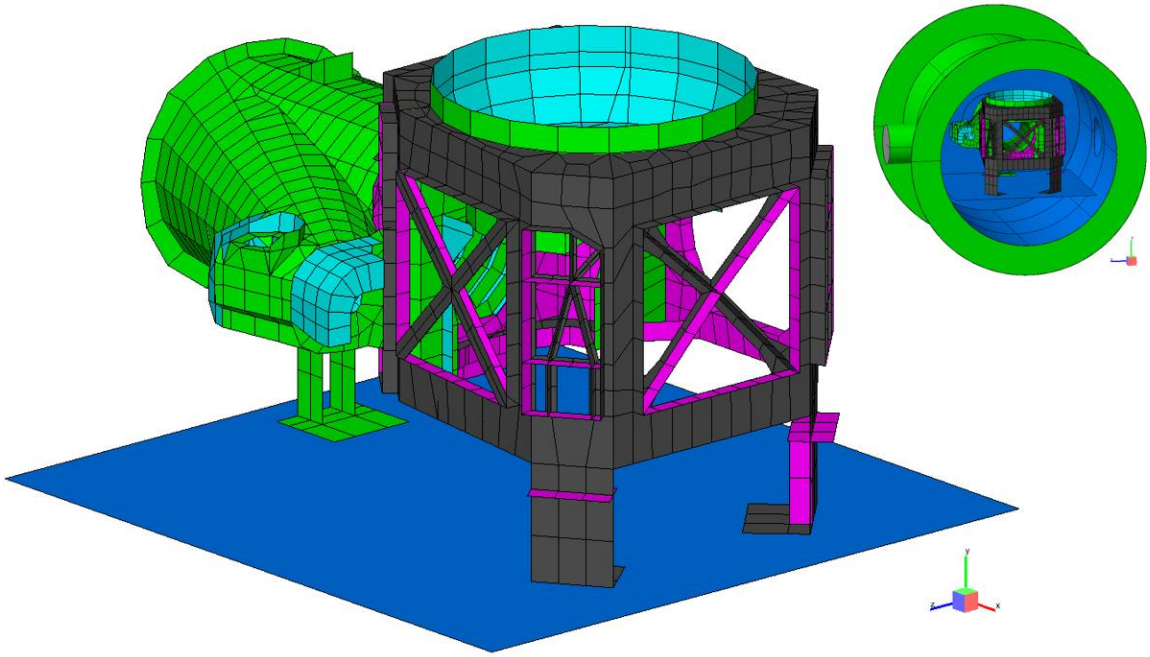

Figure 7.4: Detailed thermal model of the ITS demonstrator without MLI cover, with accommodated GSE adapter and coupled to the TVC cold plate (left) with the integrated demonstrator in the TVC (right) [WIL-23]

7.4 ITS Technology Scaling

Another core of this thesis is the assessment of a generic approach to the scalability of the ITS technology if geometry scaling cannot be avoided. Since the geometry of the ITS demonstrator had been scaled to 1:3 an equivalent heating profile must be defined, with which the scaled and modified ITS demonstrator is equivalently heated, also related on the available cooling power of the cold plate. This means that the corresponding heat loads of the original MTG inner baffle assembly cannot be directly applied to the ITS demonstrator due to differing power densities as the shell areas, masses and the related capacitances are strongly different due to model scaling and modifications.

As mentioned, the scaling takes place between the original MTG model towards the ITS redesign in the unfilled state (without PCM). The geometry scaling method is depicted in Figure 10.5 in the appendix. The scalability of the ITS technology is dependent on three main aspects, which are (a) the total thermal model capacitance, (b) the equivalent power heating profiles and (c) the PCM mass to be determined, related on the capacitance ratio.

The model scaling approach relates on experimental data, in order to assess the equivalent heating profiles by using PI controlled heaters, with temperature pilot sensors as reference points. The heater PI control is required to follow the original MTG orbit temperature profiles, in order to determine the required equivalent heating curves to simulate the same temperature behaviour on the ITS demonstrator in the unfilled state.

7.4.1 Capacitance Scaling

In a first step the capacitance ratio between the ITS redesign compared to the reduced but not yet scaled MTG thermal model was determined, related on geometry (.erg) data. This ratio is mandatory to finally derive the necessary PCM mass for equivalent passive thermal control of the demonstrator. The ITS demonstrator geometry, used in ESATAN, is based on a surface model with shells of infinitesimal thickness. The thicknesses of the shells are kept constant, since the necessity lies in the planar scaling, whereas the thickness information are stored numerically anyway. The results of the model scaling are summarised in Table 7.2.

Table 7.2: Scaling of the total thermal model capacitance with the original MTG data (left, blue) compared with the reduced and scaled ITS redesign (middle, green) and the resulting capacitance scaling factor

Parameter	Reduced MTG model	Reduced, scaled and ITS modified redesign	Ratio
Total area	2.775485 m²	0.329629 m²	-88.12% / factor 0.118764
Total mass	10.529 kg	2.647 kg	-74.87% / factor 0.241347
Total capacitance	10058.14 J/K	2373.91 J/K	-76.4% / factor 0.236019

The evaluation of the .erg (geometry) data has thus indicated that the total capacitance must be finally scaled with the relevant factor listed in the Table 7.2, which is $f_{C\ scale} = 0.236019$. As mentioned, the scaling factor is relevant to derive the equivalent PCM mass.

7.4.2 PCM Mass Scaling

Optical baffle and telescope structures for space applications should be kept stable in the temperature range in which they typically have been assembled. Normally in such baffle designs for space applications the assembly and integration process is proposed to take place at clean room conditions around room temperature. That is why the PCM hexadecane with a melting temperature around room temperature (ca. 18°C) is used for the ITS demonstrator thermal analyses and TVC validation tests.

The development goal and major requirement to the PCM storage is to absorb the heat energy by the PCM mass, which passes the EBA structure due to solar irradiation (QS) and other heat flows in the

orbit cases EQ and D56. Indeed, the PCM can only realise its useful effect of stabilising temperatures if the geometry sections of the demonstrator with embedded PCM reach the melting temperature, which enables then to store additional energy in form of latent heat. Before that point, the PCM is only treated as additional sensible mass with a certain sensible heat accounted by the ESATAN solver.

The demonstrator consists of several dedicated and encapsulated PCM sections (chambers), which are visualised in Figure 10.10 and Figure 10.11 in the appendix.

For the determination of the PCM mass it is necessary to consider that the PCM mass feature can only be actively used for passive thermal control, when the temperature of the section reaches or exceeds the characteristic melting temperature, where PCM is proposed to be embedded. The resulting mean temperature profile of each section (node group) then defines the interval limits of interest, related on the original MTG model. The cumulative intervals for the cases D56 and EQ are depicted in the appendix in chapter 10.19. Within these interval limits, the cumulative net heat flows are integrated over time to derive the nominal amount of energy to be stored by the PCM mass. The minimum amount of PCM can then be calculated from this energy requirement.

The resulting intervals are further listed in the Table 7.3 together with the calculated PCM storage capacity. It can be seen that slightly different PCM masses are resulting for the orbit cases D56 and EQ. However, since the MTG satellite inevitably passes through both cases, the higher PCM mass linked to the D56 orbit case is used from here on. A complete overview of the PCMs' used and its material properties is given in Table 10.1 in the appendix.

Table 7.3: Theoretical PCM active interval times and the resulting thermal energy, which shall be stored by the PCM as latent heat, related on the MTG orbit cases D56 and EQ and for the redesigned ITS demonstrator

MTG case	Interval [s]	Required capacity [kJ]	MTG PCM mass [g]	ITS PCM mass [g]
D56	30,700	656.845	2,770.3	approx. 654
EQ	23,220	640.287	2,700.5	approx. 637

For the final scaling of the PCM mass the total capacitance ratio, which was already determined in Table 7.2 and is $f_{C\ scale} = 0.236019$, is taken into account. The so calculated PCM mass, which relates on the ITS demonstrator capacitance is approx. 654 grams. The following Table 7.4 summarises the distribution of the entire PCM mass to each section of the entire ITS demonstrator geometry.

Table 7.4: Overview of the entire PCM mass embedded in the ITS demonstrator, with the corresponding mass division into the encapsulated PCM sections of the submodels inner baffle (blue) and prism (green)

ITS demonstrator section	Embedded PCM mass [g]
Inner baffle (complete)	181.5
Prism – Front	55.5
Prism – Sun shield	202.5
Prism – Right	90.5
Prism – Back	67.0
Prism – Left	70.5
Complete demonstrator	667.5

Once the minimum required PCM mass is identified, the demonstrator redesign can be started. Requirements especially for the PCM void design of the ITS demonstrator are that the PCM mass shall be distributed in approximately equal thicknesses throughout all demonstrator sections.

7.4.3 Heater Setup Assessment

The dynamic temperature maps of the MTG inner baffle assembly during the EQ and D56 orbits have to be imitated in the TVC tests on the ITS demonstrator skin.

The thermal test setup of the ITS demonstrator is revealed in Figure 7.5 and consists of adhesive kapton heaters to supply the thermal energy to the structure.

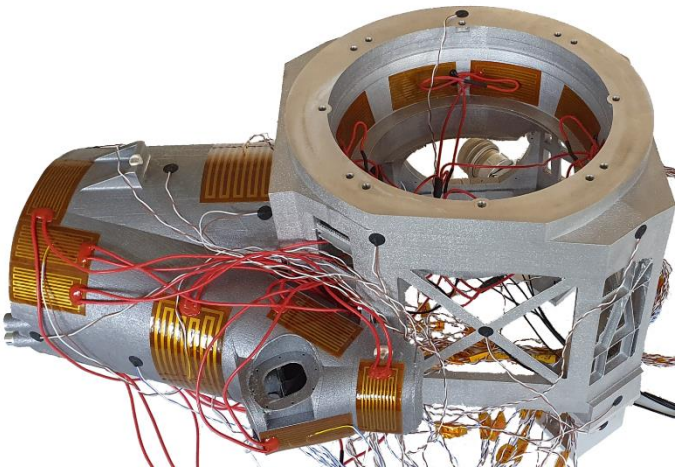

Figure 7.5: ITS demonstrator kapton heater setup preview

As Gräbener et al. [JOS-01] in a preliminary study already claimed to begin with, it is necessary to identify the local hot spots of the inner baffle assembly structure, which arise from temperature mapping of the hot cases EQ and D56. The positions of these hot spots yield the neuralgic points of the basic heater positions, on which the further heater layout process is based. It is further necessary to identify the accessible exterior surfaces around the hot spots on the skin of the inner baffle geometry, which enable proper heater attachment. The identified areas are then recombined into local heater sections, which can be used for attachment of adhesive kapton heaters.

In the next step, MATLAB post-processing scripts are used to determine the cumulative net heat flows, which affect the individual heater sections and the corresponding thermal nodes of the geometry. In parallel the amount of energy of the individual heater sections is calculated.

For further considerations the cumulative total power profile from all sections is determined. Arising from this, the required peak power of the overall heater control is derived to ca. 160 W. Ongoing the curves of the individual power profiles of the heater sections are compared for their profile similarity.

This has made it possible to migrate and recombine the power profiles of the individual heater sections to three globally controllable power channels, in order to mimic the overall temperature behaviour of the geometry. The heater setup definition, the recombined heater channels and the accommodation concept of the demonstrator can be found in the appendix in chapter 10.20. Also part of the documentation is a heater pre-test, in order to verify the proper adhesive attachment of the kapton heater elements to the demonstrator's aluminium skin. In order to compensate for efficiency losses, the total power requirement had been conservatively increased by 20%, which means that the heater network as a whole has to enable 192 W peak power.

7.4.4 Temperature Sensor Setup and Accommodation

The temperature sensor setup and thermocouple accommodation plan of the demonstrator can be found in the appendix in chapter 10.21.

7.4.5 Experimental Heater Power Profiles Determination

A state-of-the-art approach for determining an unknown heater power profile to heat a component according to a specified temperature curve, is the experimental method of operating PI controlled heater. The PI controller enables to follow a specified temperature profile to reproduce the power curve to be defined. In the experimental setup the PI controller controls the three individual ITS heater power channels with the respective heater circuits. The PI controller uses the identical control values for all three channels. Thereby the controller minimises the control deviation (feedback) between the actual temperature and the set temperature. The actual temperatures are measured individually by corresponding pilot sensors for each of the three channels. The time dependent set temperature is preset by the extracted MTG orbit temperatures, which can be reviewed in chapter 10.15 in the appendix.

The pilot sensors attached on the demonstrator's aluminium skin, the referenced heaters and additional sensors directly attached on specific heaters to prevent overheating are defined in Table 10.19 also in the appendix. A comprehensive overview of the ITS demonstrator heater and sensor setup can be found in the appendix in chapter 10.20.

The PI controller is based on the continuous time principle, since the MTG temperature data are available as set points in continuous time format from the TMD data. The evaluation of the actual and target temperature curves has shown that a PI controller is completely sufficient to follow the target temperature curves with adequate derivations within ± 1.6K.

The control values are for the proportional gain $P = 5.0$ and for the incremental gain $I = 1.0$. The PI controller is only triggered for regulation every 10 seconds. This is because test experiences have shown a varying latency of the end-to-end signal processing chain, between the measuring and power supply units. Another reason is the thermal inertia of the ITS demonstrator in combination with the strong thermal coupling to the cold plate via the aluminium adapters.

The Figure 10.32 and Figure 10.33 in the appendix depict the derived heater power curves of the three PI controlled channels, for the cases D56 and EQ. The original MTG heat flow profiles, shown in Figure 10.22 for case D56 and in Figure 10.23 for case EQ, indicate a high degree of agreement. The maximum deviation is given with 1.3 W and the global mean deviation in comparing the shape progression of the profiles is given by 0.65% related on the peak power if the magnitude of the profiles are scaled accordingly.

7.5 Experimental Test Environment

All thermal tests are carried out at FH Aachen in the SpaceLab at the department of aerospace engineering, by the TVC test facility HVK100.

To minimise the radiative coupling of the ITS demonstrator with the environment of the TVC the entire structure, except the GSE adapter, is covered with 2 total layers of MLI. The MLI used is of type COOLCAT 2 NW (article no.: PL100047) from the company RUAG. The MLI consists of a 12-µm-foil, which in turn is double-sided aluminised, perforated and interleaved with 10 layers of non-woven polyester foil as spacer material. The MLI layers are ultrasonic spot-welded. [RUA-17]

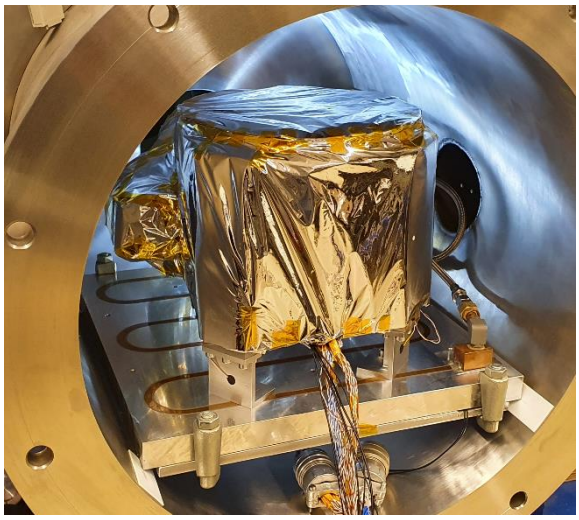

Figure 7.6: ITS demonstrator thermal test setup with accommodated kapton heaters, integrated thermocouples, wrapped in MLI and mounted on the TVC's cold plate for cooling purposes [WIL-23]

During all TVC tests the maximum pressure in the TVC was always less than 10^{-5} mbar (high vacuum). For the thermal predictions and tests the ITS demonstrator is simulated and tested in the enclosure, which yields the TVC chamber with integrated cold plate. For a recap of the demonstrator thermal model, please refer among others to Figure 7.4.

Figure 7.6 above depicts the installed demonstrator in the opened TVC and Figure 7.7 below shows the demonstrator from the side. In the TVC environment the integrated cold plate replaces the base plate used in the MTG thermal model, to provide conductive cooling. The cooling of the ITS demonstrator only takes place via conductive coupling through the GSE adapter to the cold plate.

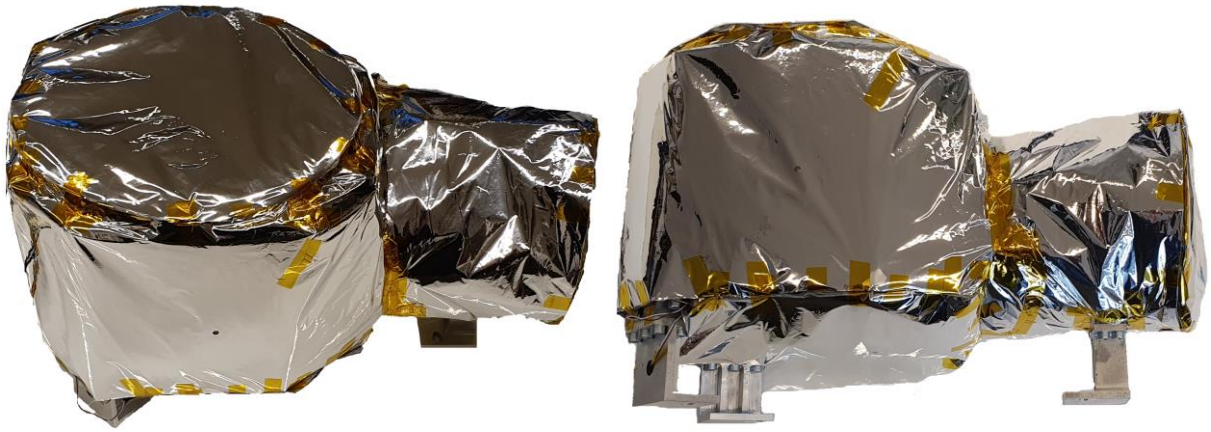

Figure 7.7: ITS demonstrator thermal test setup with accommodated kapton surface heaters, thermocouples and wrapped in MLI. The additive manufactured demonstrator is mounted on aluminium GSE adapter [WIL-23]

The measurement technology used to measure and store the temperatures is provided by the Keithley DAQ6510 data acquisition system in conjunction with type T thermocouples. An overview and detailed listing of the measurement equipment used for all thermal TVC tests is already provided in Table 6.1.

The power supply units for the heater circuits with integrated power control for three independent channels, is realised by USB remote controllable Manson SSP-8160 full-voltage-regulators. Three heater lines with individual heater circuits are operated in parallel by three independent controlled Manson power units, to supply the time varying heater power profiles. One central MATLAB programme records and stores the measured temperatures. The power units used to operate the heater circuits are also controlled by the same programme and return the actual voltage and power values. A summary of the test conditions and the relevant test parameters, applicable for all demonstrator TVC tests can be found in the appendix in Table 10.20.

7.6 Conductive Interface Validation Tests

The validation of the conductive interfaces is carried out by various TVC steady-state tests. Thereby the aim is the correlation of the intermediate conductive interfaces of the demonstrator assembly between the inner baffle and prism flange as well as the conductive interfaces of the GSE adapters, which accommodate the ITS demonstrator with the cold plate. The steady-state TVC tests are performed with the unfilled demonstrator (without PCM).

The correlation of the predictions with measurement data are shown in Figure 10.34 together with the summarised TVC measurement parameters in Table 10.21 in the appendix. According to ECSS-E-ST-10-03C [ECS-22], the steady-state stability criterion is fulfilled and therefore the TVC test successful if a maximum temperature variation of 1.0K is not exceeded within 2 hours (max. 0.5K/h). The convergences are verified for all temperature sensors within all convergence corridors. The maximum deviation is derived to 0.5K, which is treated as acceptable. For a complete overview of the overall attached and used temperature sensors, please refer to chapter 10.21.

7.7 Cycling Tests and Correlation of the Demonstrator

Another task is to test and validate the equivalent EQ and D56 power profiles by cyclic TVC tests, which are determined in chapter 7.4. Consequently, the demonstrator is first subjected to cyclic tests in the unfilled state (without PCM). The predictions are then correlated with the measurement results. Subsequently, this procedure is repeated with the filled demonstrator (with embedded PCM) in the TVC. The predictions of the thermal models with PCM are then also correlated with the corresponding measurement results. The results are visualised in the figures on the following pages.

Based on the PCM subroutine for simulating the thermo-physical PCM behaviour, which has been further developed to the current version as part of this doctoral thesis, thermal predictions are carried out with the thermal modelling suite ESATAN of release 2022. The PCM subroutine is used as a fully packed function for all thermal predictions, where PCM is applied for passive thermal control. The PCM subroutine is already fundamentally validated using small-volume specimen test series, beginning in chapter 6.4. [WIL-23]

To recap the impact of the ITS technology, the primary effect is to reduce the maximum temperature of a component. The secondary effect is, that the ITS technology can delay cold phases longer, as the PCM necessarily releases thermal energy back into the system during the cooling and solidification process. All measured temperature curves of the demonstrator are recorded in total by 32 thermocouples at 32 significant measuring points once per second and stored by the DAQ system. [WIL-23]

7.7.1 Demonstrator Correlation Results of the EQ Orbit Case

In the Figure 10.35 in the appendix the TVC measurement sequence and thermal prediction of the unfilled demonstrator (without PCM) are compared for the hot case EQ. The Figure 10.36 in the appendix depicts the thermal correlation of the predictions of the filled demonstrator (with embedded PCM) compared to the corresponding TVC measurement results. For the hot case EQ, an accuracy with a maximum deviation of the prediction from the measurement result in the unfilled state (without PCM) of 2.8K can be achieved. The average deviation is 1.7K. Both results are acceptable correlations. For the hot case EQ in the filled state (with PCM), even a maximum temperature deviation of 1.5K is not exceeded. The average deviation for the demonstrator with embedded PCM is 0.6K.

7.7.2 Demonstrator Correlation Results of the D56 Orbit Case

Figure 10.37 and Figure 10.38 in the appendix show the results of the TVC measurement sequences compared with the thermal predictions, related on unfilled demonstrator (without PCM) and the filled demonstrator (with embedded PCM) for the hot case D56.

The comparison of the correlation results between the measurement results and the predictions for the hot case D56 show the same tendency. In the unfilled state, a maximum deviation of 2.8K was achieved. The demonstrator models with embedded PCM are within a maximum deviation of 1.7K.

7.8 Assessment of the Demonstrator Temperature Stabilisation Attributed to PCM

The ITS demonstrator was subject to thermal cycling tests in the unfilled state (without PCM) and in the filled state (with embedded PCM), placed in the TVC at FH Aachen in order to assess the transient performance and the resulting temperature stabilisation attributed to the PCM mass. In tailored reference to ECSS-E-ST-10-03C for thermal cycling and thermal design validation, it is mandatory to validate the component surveillance due to thermal cycling by replicating the operational temperature range with completed and settled cycles. [ECS-22]

While case EQ was selected due to the strongest temperature gradients, case D56 has lower temperature gradients, but higher maximum temperatures. The MTG inner baffle assembly structure is subject to temperature variations in the cases D56 and EQ between -50°C to +110°C, visualised in chapter 10.15. The cold plate in the TVC is cooled by circulation-pumped silicone oil and is set to a temperature of +5°C for all demonstrator TVC tests, to simulate the operational behaviour of the base plate related on MTG model data. Lower temperatures could not be achieved because no cryogenic cooling was available for the TVC setup during the research project. However, it is considered more important to reproduce the temperature curves above 5°C with the peak temperatures, described in chapter 10.11 and 10.12. All mean temperature curves in chapter 7.8 are derived from the cumulative averaged temperature curves of all structural inner baffle and prism shells. [WIL-23]

Another factor is the cooling capacity available for cooling the inner baffle structure. The MTG baffle structure can draw on an average cooling capacity (chapter 10.19) in case D56 of ca. -28.1 W and in case EQ of ca. -29.6 W. The correlated ITS demonstrator thermal model in the TVC environment has a lower cooling capacity of ca. -16.5 W in case D56 and in case EQ of ca. -17.2 W. Due to scaling and redesign from the MTG model towards the ITS demonstrator, resulting in less capacitance and therefore thermal mass to be cooled, the cooling capacity provided by the TVC cold plate is relatively higher.

7.8.1 Demonstrator Temperature Stabilisation Results of Case EQ

The following Figure 7.8 depicts the TVC test results of the EQ hot case of the ITS demonstrator in the unfilled state (without PCM, red graph) compared to the filled state (with embedded PCM, blue graph) over one GEO TVC cycle. The magenta coloured area represents the achieved temperature stabilisation. The cyan coloured areas identify the potential reduction of subcooling phases.

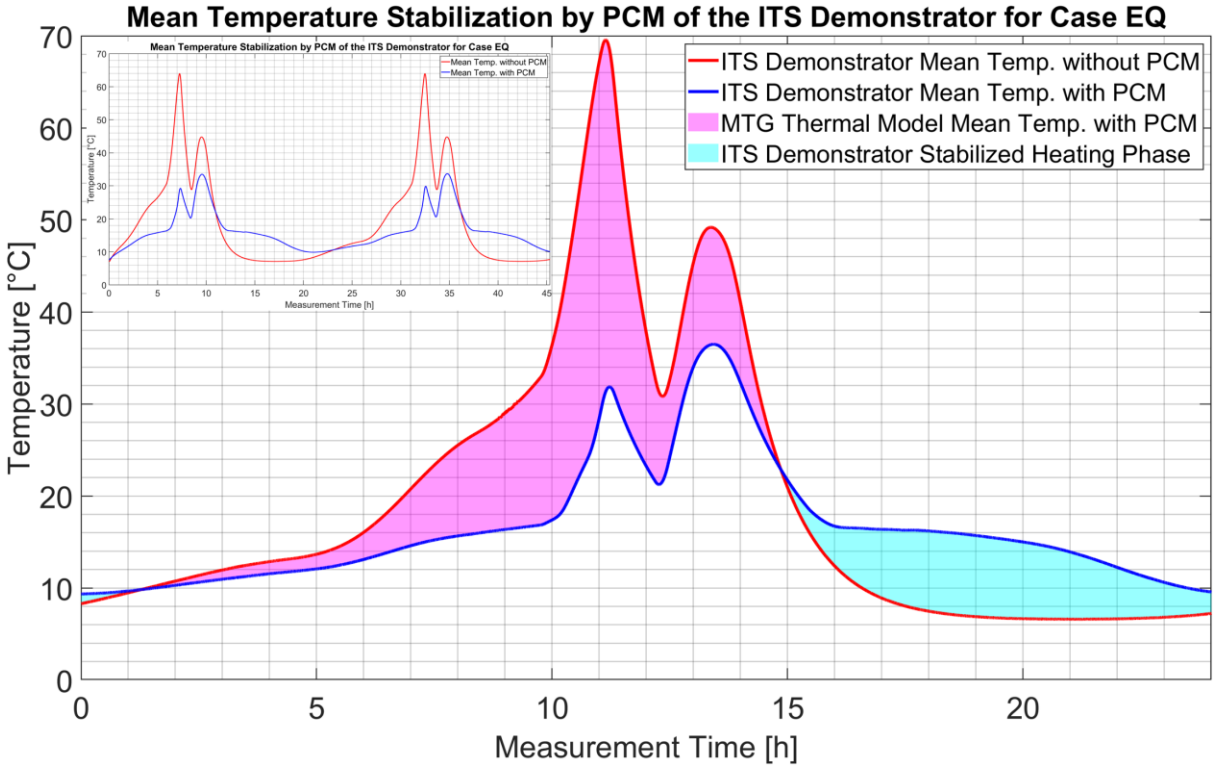

Figure 7.8: Test results from representative EQ thermal cycling tests of the ITS demonstrator without PCM (red curve) compared to with embedded PCM (blue curve). The coloured magenta area indicates the achieved temperature stabilisation, while the cyan areas mark the reduced subcooling of the component [WIL-23]

Especially for the case EQ with the strongest expected temperature gradients and thus instabilities, the demonstrator model with embedded PCM shows an opposite behaviour compared to the setup without PCM when looking at the temperature maxima at hour 13.5. By the way the same tendential temperature behaviour is also visible in the MTG orbit predictions in Figure 7.12 for case EQ. The Table 7.5 below quantifies the maximal temperature stabilisation achieved for the case EQ.

Table 7.5: Overview of the achieved thermal stabilisation of the ITS demonstrator, related on the derived EQ measurement results [WIL-23]

Demonstrator – case EQ	Without PCM [°C]	With PCM [°C]	Difference [K]
Mean temperature	19.4	16.5	-2.9
Minimum temperature	6.6	9.3	+2.7
Maximum temperature	69.6	36.5	-33.1

The Table 7.6 below quantifies the achieved thermal stabilisation and reduced cooling phases, averaged respectively over the entire interval of the heating phases and the cooling phases respectively.

Table 7.6: Overview of the achieved temperature stabilisation (magenta) as primary effect, together with the potentially decreased subcooling phases (cyan) as secondary effect of the demonstrator in case EQ [WIL-23]

Demonstrator stabilisation performance – case EQ	Values
Mean temperature stabilisation heating phase (magenta)	-9.3K
Mean temperature stabilisation cooling phase (cyan)	+6.2K

7.8.2 Demonstrator Thermal Model PCM Storage Efficiency of Case EQ

To evaluate the degree of utilisation of the ITS demonstrator PCM design, the charge und discharge rates of the PCM storage are determined. The efficiency or degree of utilisation of the PCM design with its related PCM storage capacity is evaluated on the one hand by determining the cyclic maximal cumulative storage capacity used. On the other hand, the PCM storage should be fully recharged through the regeneration phases (cooling phases) to benefit from reduced cooling phases.

The results are based on correlated demonstrator thermal model data. The cumulative heat flow curves of all PCM nodes are depicted in the appendix in Figure 10.40 for the case EQ. The heat flow of the PCM nodes is analysed within fully consecutive GEO orbits. The integral is calculated to determine the amount of energy absorbed as latent heat or dispensed back into the system by the PCM mass.

In the following Figure 7.9 the temperature fields are mapped at the time of highest (peak) temperatures, considering the hot case EQ at approx. hour eleven (Figure 7.8) in the second orbit interval. The temperature mapping range of the ITS demonstrator geometry starts at 0°C as a minimum value (blue) up to a maximum temperature of 90°C (red). The right-hand side temperature field shows the stabilisation effect of the ITS technology, whereby the filled demonstrator (with embedded PCM) has a significantly lower and more homogenised temperature field.

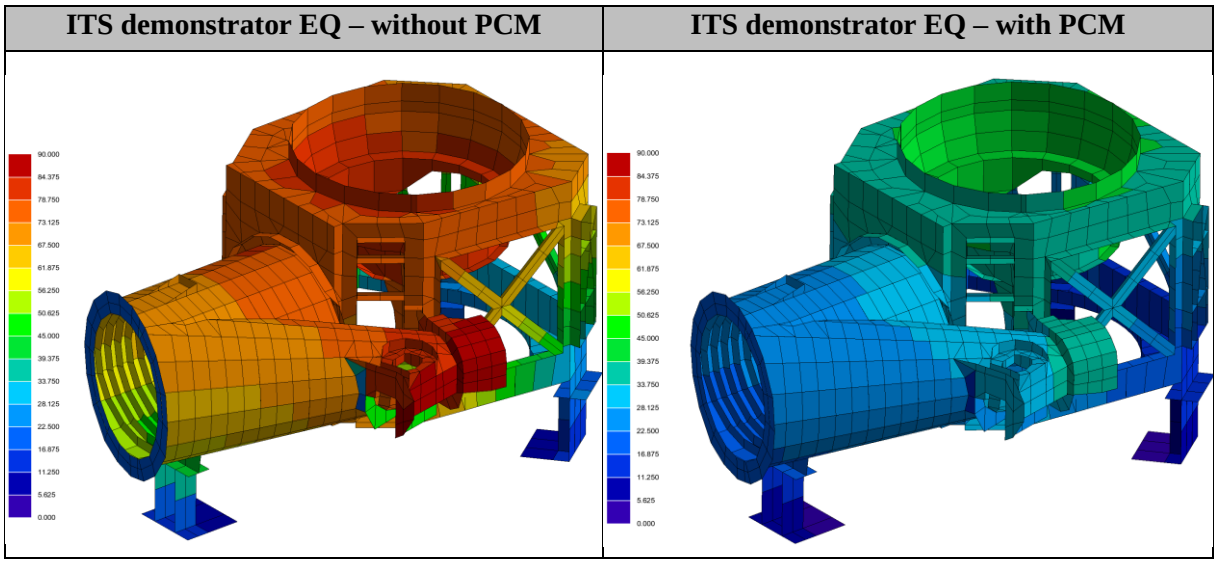

Figure 7.9: Comparison of the mapped temperature fields of the ITS demonstrator at the time of the maximum expected peak temperatures for the EQ case without PCM (left) and with embedded PCM (right). The temperature mapping range starts at 0°C (blue) and is limited by a maximal temperature of 90°C (red)

As mentioned, a total of approx. 668 g of hexadecane PCM is embedded in the ITS demonstrator structures. An overview of the demonstrator PCM mass distribution is listed in Table 7.4. According to Table 10.1 hexadecane is considered in this thesis with a constant and specific latent heat of fusion of 237.1 kJ/kg. This results in a total latent heat capacity available of approx. 158.264 kJ.

The following Table 7.7 contains the complete listing of the evaluated degree of utilisation of the latent heat storage of the demonstrator for case EQ.

Table 7.7: Calculated amounts of energy, which are absorbed and dispensed by the PCM mass during the heating (charge) and the cooling (recharge) cycles of the hot case EQ, compared with the overall efficiency (storage ratio) and the delta PCM mass, related on the total storage capacity available

ITS demonstrator – case EQ	Storage capacity	Storage ratio	Delta PCM
First charge cycle	139.713 kJ	88.2%	78.8 g
First discharge cycle	-55.241 kJ	53.4%	-
Second charge cycle	+73.458 kJ	99.8%	1.3 g
Second discharge cycle	-157.930 kJ	0.0%	-

After the completion of the first charge cycle the PCM storage is utilised to approx. 88% around hour eleven in Figure 7.8, which means that the PCM storage capacity is not fully utilised at this state as expected. The regeneration phase (first discharge cycle) until the second temperature rise around hour twelve, empties the latent heat storage to ca. 53% in combination with only moderate temperature changes, compared to the configuration without PCM. This behaviour proofs the claimed secondary effect of the ITS technology, to damp cooling phases and minimize temperature gradients.

During the second heating phase (second charge cycle) the PCM storage is then fully utilised and the PCM mass behaves further just as sensible mass. This makes a further rise in temperature beyond the first local maxima plausible.

The fact that 100% storage capacity utilisation is not reached numerically after a completed charging cycle, is due to the interpretation of the PCM subroutine. If specific thermal nodes are very strongly conductively coupled and are close to interfaces near colder spots like a cold plate with a dominant and constantly colder capacitance, it is possible that these few nodes cannot be fully utilised for their maximum latent heat capacity. The reason is that the strong coupling results in periodic charging and discharging of the nodes. In the demonstrator thermal model with a total of 1103 PCM nodes, only six PCM nodes show this anomaly. These nodes are all located in the vicinity of the adapter interfaces. Furthermore, it has been shown that for larger nodes with increasing PCM mass this effect becomes weaker or is no longer detectable at all and thus behaves nominally.

In fact, it could presumably also be the case that similar effects occur at the interface nodes in the existing demonstrator hardware but are not measurable. It could be claimed that the majority of the heat flow is always channelled through the interface area towards the cold plate in the TVC setup.

However, according to multiple analyses, this behaviour only occurs when there is a constantly cooler spot in the immediate vicinity of the nodes. On the one hand, this is a numerical anomaly that has not yet been resolved in this thesis. On the other hand, all configurations of all thermal models show that this behaviour has no distorting influence on the overall performance of the PCM mass and the corresponding thermal model.

7.8.3 Demonstrator Temperature Stabilisation Results of Case D56

The Figure 7.10 below shows the TVC test results of the D56 hot case of the ITS demonstrator in the unfilled state (without PCM, red graph) compared to the filled state (with embedded PCM, blue graph). Analog to the case EQ before, the magenta coloured area yields the achieved temperature stabilisation. The reduction of the demonstrator subcooling phases are depicted by the cyan coloured areas.

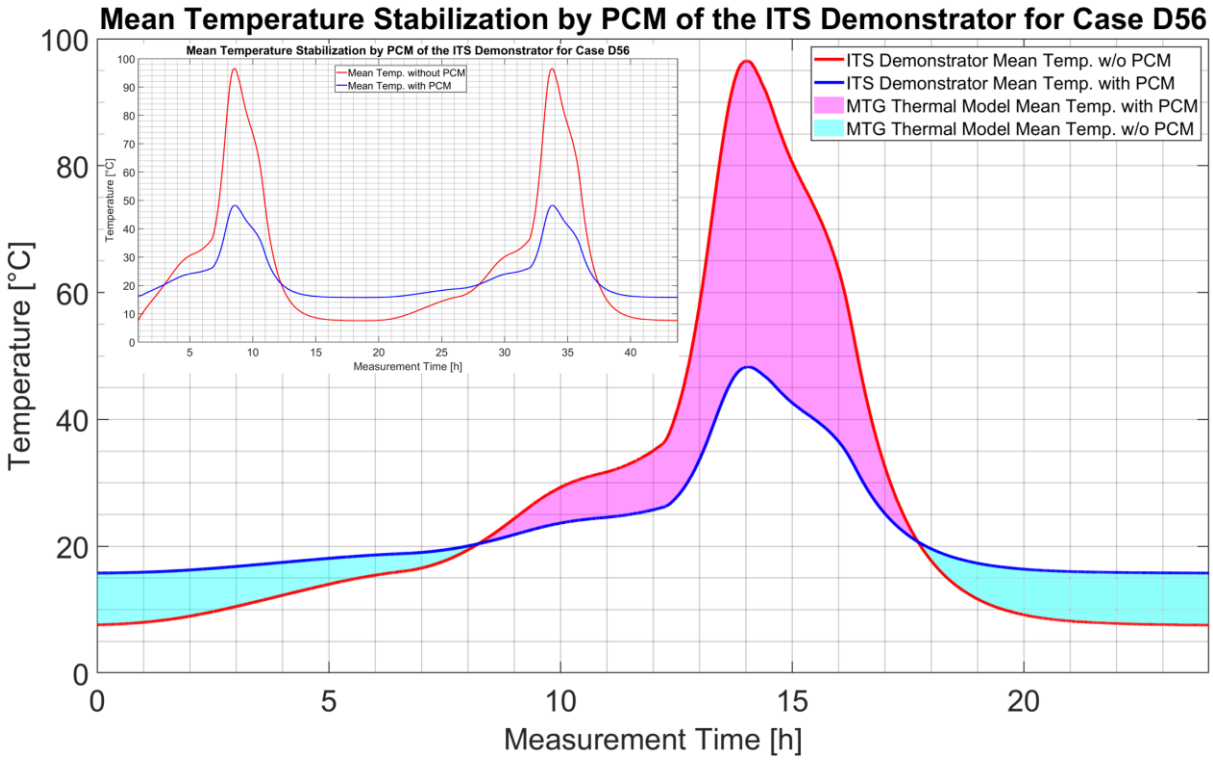

Figure 7.10: Test results from representative D56 thermal cycling tests of the ITS demonstrator without PCM (red curve) compared to with embedded PCM (blue curve). The coloured magenta area indicates the achieved temperature stabilisation, while the cyan areas mark the reduced subcooling of the component [WIL-23]

The following Table 7.8 indicates the maximum temperature stabilisation achieved in the case D56. The highest temperatures are expected with the D56 hot case. Accordingly, the ITS technology should reduce these maximum temperatures as much as possible with the PCM mass available for passive thermal control. As a result, the PCM design enables a reduction of the maximum temperature of approx. -51% compared to the configuration without PCM, which is enormous.

Table 7.8: Overview of the achieved thermal stabilisation of the ITS demonstrator, related on the derived equivalent D56 heater power profiles [WIL-23]

Demonstrator – case D56	Without PCM [°C]	With PCM [°C]	Difference [K]
Mean temperature	30.3	22.9	-7.4
Minimum temperature	7.6	15.8	+8.2
Maximum temperature	96.6	48.3	-48.3

Ongoing, the following Table 7.9 lists the achieved temperature stabilisation of the heating phase and the reduction of the subcooling phases of the case D56. The values are averaged over the entire interval of the heating phase and the cooling phases respectively, to make them also comparable to the results from case EQ.

Table 7.9: Overview of the achieved temperature stabilisation (magenta) as primary effect, together with the potentially decreased subcooling phases (cyan) as secondary effect of the ITS technology, in case D56 [WIL-23]

Demonstrator stabilisation performance – case EQ	Values
Mean temperature stabilisation heating phase (magenta)	-17.7K
Mean temperature stabilisation cooling phase (cyan)	+9.1K

7.8.4 Demonstrator Thermal Model PCM Storage Efficiency of Case D56

Analog to the EQ case, the Figure 7.11 depicts the corresponding temperature fields of the correlated ITS demonstrator thermal model results, which are mapped at the time of maximum (peak) temperatures at approx. hour fourteen for the D56 case. The temperature mapping range starts at 0°C at a minimum value (blue) up to a maximum temperature of 110°C (red).

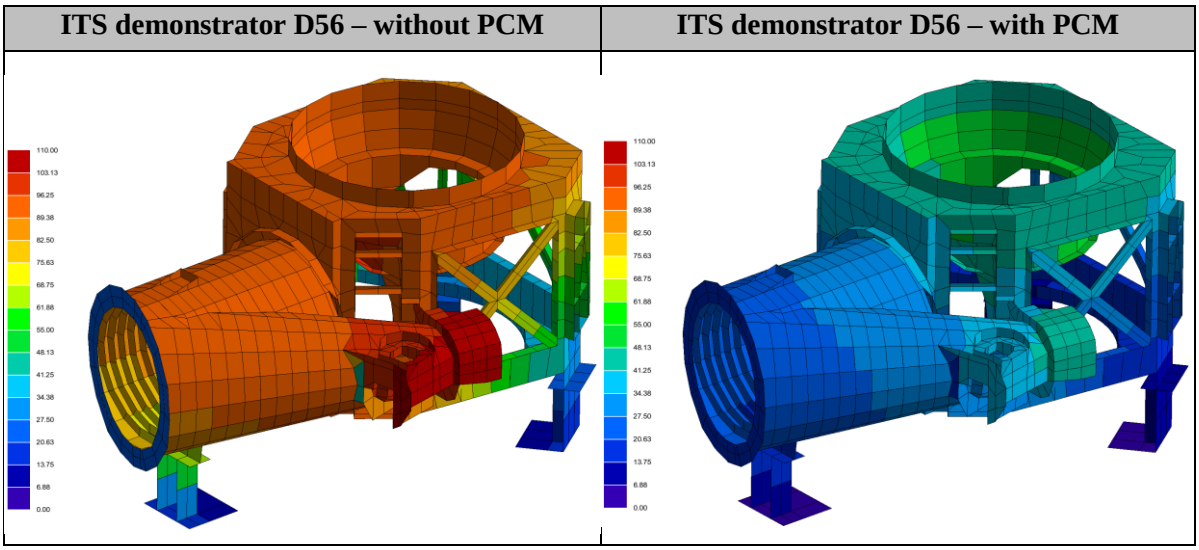

Figure 7.11: Comparison of the mapped temperature fields of the ITS demonstrator at the time of the maximum expected peak temperatures for the D56 case without PCM (left) and with embedded PCM (right). The temperature mapping range starts at 0°C (blue) and is limited by a maximal temperature of 110°C (red)

The enthalpy data in Table 7.10 indicate that the entire PCM storage is utilised for passive thermal control, as the cumulative PCM capacity of ca. 99.9% is used for passive thermal control. Indeed, all PCM nodes virtually release its stored latent heat back into the system in any case when the component is cooled down, so that the entire PCM mass can be discharged from latent heat. Hence with a progressive and periodically recurring temperature profile as D56 is, the full temperature stabilisation potential addressed to lower maximum (peak) temperatures can be achieved. The cumulative heat flow curves of all PCM nodes are depicted in the appendix in the Figure 10.39 for case D56.

Table 7.10: Calculated amounts of energy, which are absorbed and dispensed by the PCM mass during the heating (charge) and the cooling (recharge) cycles of the hot case D56, compared with the overall efficiency (storage ratio) and the delta PCM mass, related on the total storage capacity available

ITS Demonstrator – case D56	Storage capacity	Storage ratio	Delta PCM
Charge cycle	158.057 kJ	99.9%	1.1 g
Discharge cycle	-158.057 kJ	0.0%	-

7.9 Assessment of the MTG Model Temperature Stabilisation Attributed to PCM

Finally, the results of the demonstrator tests and models from chapter 7.8 are compared with the MTG thermal model in order to draw final conclusions about the reliability and success of the ITS scaling approach. In the original MTG thermal model a total of approx. 2770 g of hexadecane PCM is embedded, which is also listed in Table 7.3. As shown in Table 10.1 the hexadecane used in the research project is considered with a latent heat of fusion of ca. 237.1 kJ/kg. Hence the PCM mass embedded in the MTG model results in a total latent heat capacity available of approx. 656.767 kJ.

7.9.1 MTG Thermal Model Predictions of the EQ Orbit Case

The following Figure 7.12 depicts the results of the MTG thermal model predictions of case EQ in the unfilled state (without PCM, red graph) compared to the filled state (with embedded PCM, blue graph). Hence the magenta coloured area also yields the achieved temperature stabilisation. The reduction of the MTG thermal model subcooling phases are depicted by the cyan coloured areas.

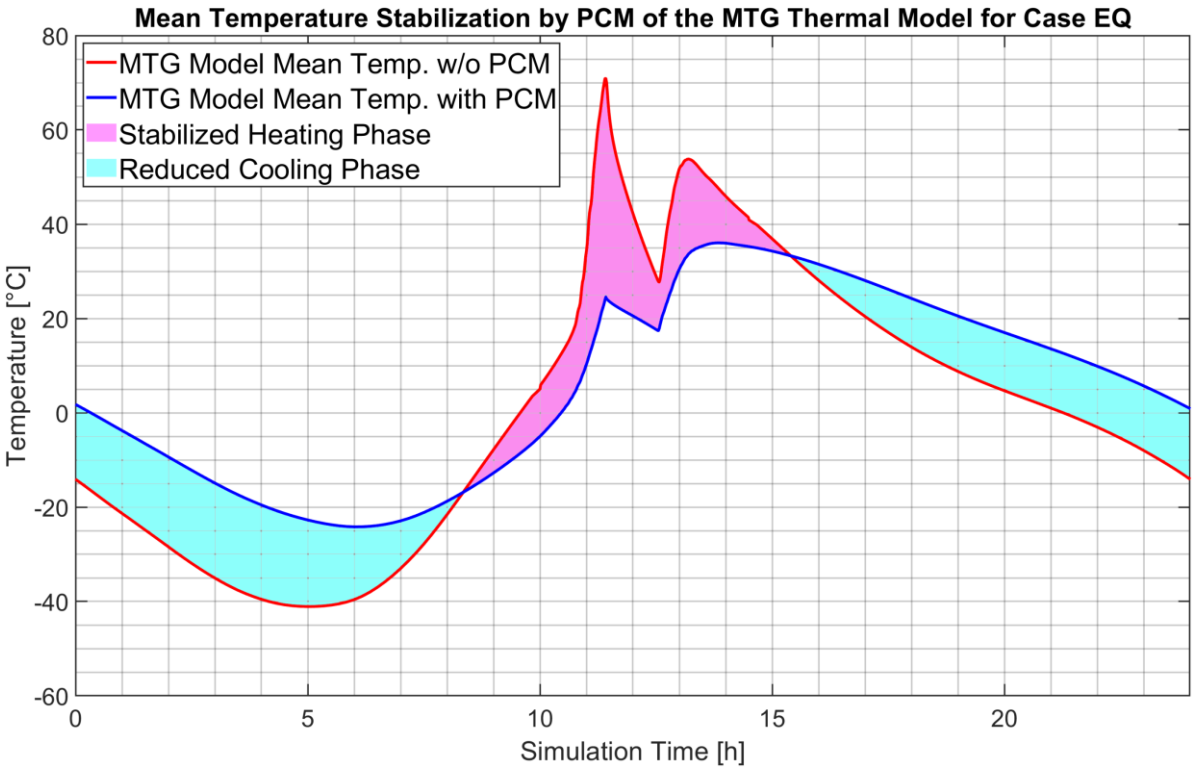

Figure 7.12: MTG thermal model EQ predictions without PCM (red curve) compared to with embedded PCM (blue curve). The coloured magenta area indicates the achieved temperature stabilisation, while the cyan areas mark the reduced subcooling of the component

In comparison with the ITS demonstrator, it is clear that ITS technology can be used not only in the primary effective range but also in the secondary effective range to damp subcooling phases.

Table 7.11: Overview of the achieved thermal stabilisation of the MTG thermal model predictions in case EQ

MTG thermal model EQ	Without PCM [°C]	With PCM [°C]	Difference [K]
Mean temperature	14.9	11.5	-3.4
Minimum temperature	-41.1	-24.9	+16.2
Maximum temperature	71.9	39.8	-32.1

Comparing the results of the demonstrator TVC tests (Table 7.5 and Table 7.6) and the correlated PCM subroutine predictions to the original MTG thermal model (Table 7.11 and Table 7.12) for case EQ, the maximum temperatures (magenta) without and especially with embedded PCM can be measured and predicted with good accuracy. In application of the introduced ITS scaling concept in this thesis it can be concluded that reliable predictions about the achievable temperature stabilisation performance of the ITS technology can be proceeded.

Table 7.12: Overview of the achieved temperature stabilisation (magenta) as primary effect, together with the potentially decreased subcooling phases (cyan) as secondary effect of the MTG thermal model in case EQ

MTG stabilisation performance – case EQ	Values
Mean temperature stabilisation heating phase (magenta)	-15.1K
Mean temperature stabilisation cooling phase (cyan)	+16.4K

Nevertheless, the reduction in low temperatures (cyan) during cooling phases in Table 7.12, to benefit from the secondary ITS effect, cannot be verified by TVC tests in this work for the reasons already explained. This should be validated in future follow-up work. However, the MTG model predictions have also shown a significant improvement by raising the lower temperature band.

7.9.2 MTG Thermal Model PCM Storage Efficiency of Case EQ

The evaluation of the stored latent heat, compared to the demonstrator in Table 7.7, shows that the utilisation after the first charge cycle behaves similar to approx. 88%. During the first discharge cycle approx. 3% more latent heat can be returned to the system in the MTG model, as for the demonstrator.

Table 7.13: Calculated amounts of energy, which are absorbed and dispensed by the PCM mass during the heating (charge) and the cooling (recharge) cycles of the hot case EQ, compared with the overall efficiency (storage ratio) and the delta PCM mass, related on the total storage capacity available

MTG orbit model – case EQ	Storage capacity	Storage ratio	Delta PCM
First charge cycle	572.044 kJ	87.1%	357.3 g
First discharge cycle	-241.691 kJ	50.3%	-
Second charge cycle	+326.414 kJ	100%	0 g
Second discharge cycle	-656.767 kJ	0.0%	-

7.9.3 MTG Thermal Model Predictions of the D56 Orbit Case

The Figure 7.13 shows the results of the MTG thermal model predictions of case D56 in the unfilled state (without PCM, red graph) compared to the filled state (with embedded PCM, blue graph). The magenta coloured area also yields the achieved temperature stabilisation. The reduction of the MTG thermal model subcooling phases are depicted by the cyan coloured areas.

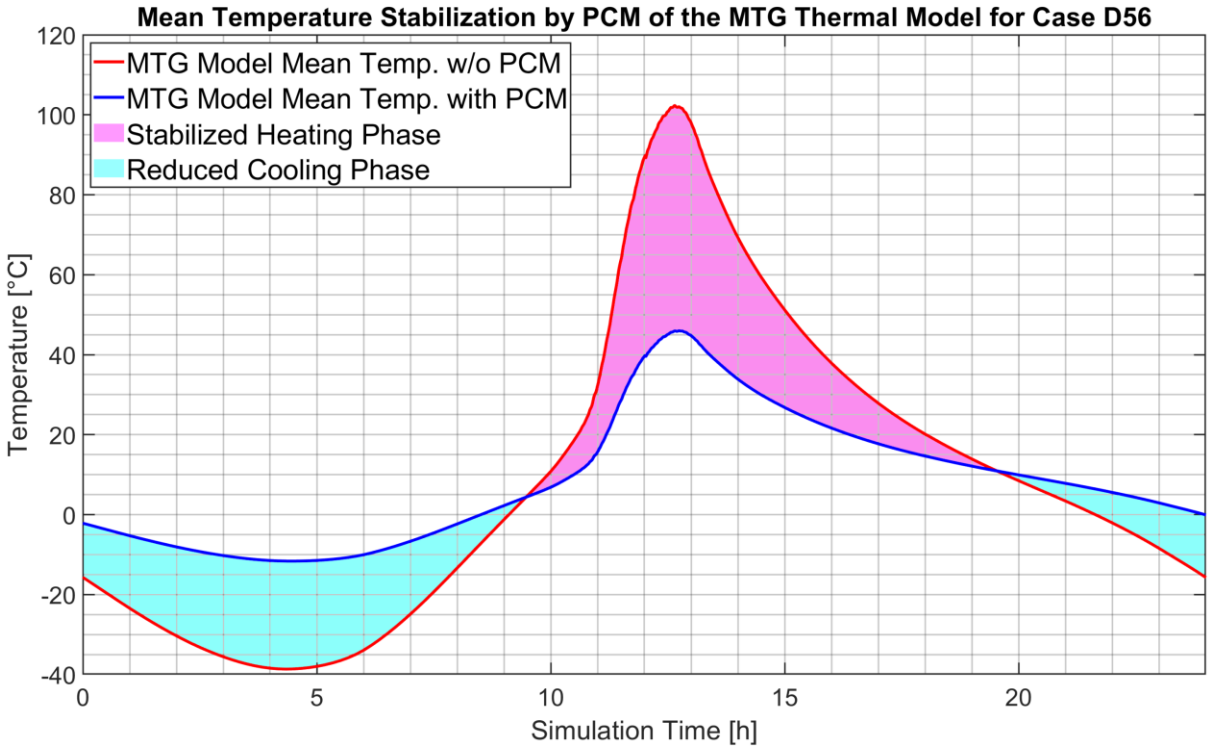

Figure 7.13: MTG thermal model D56 predictions without PCM (red curve) compared to with embedded PCM (blue curve). The coloured magenta area indicates the achieved temperature stabilisation, while the cyan areas mark the reduced subcooling of the component

If one compares the results from the demonstrator tests in Table 7.8 and Table 7.9 with the MTG predictions in Table 7.14 and Table 7.15, the maximum temperatures can also be predicted with sufficient accuracy. Similar to the MTG case EQ, also the case D56 shows an attenuated cooling behaviour of the structure by the PCM. The already known reason is that the MTG model simulates the low temperature environment ins space, which can be seen in Figure 10.12 in the appendix for case D56.

Table 7.14: Overview of the achieved thermal stabilisation of the MTG thermal model predictions in case D56

MTG thermal model D56	Without PCM [°C]	With PCM [°C]	Difference [K]
Mean temperature	29.2	15.7	-13.5
Minimum temperature	-38.7	-15.2	+23.5
Maximum temperature	102.3	46.0	-56.3

Table 7.15: Overview of the achieved temperature stabilisation (magenta) as primary effect, together with the potentially decreased subcooling phases (cyan) as secondary effect of the MTG thermal model in case D56

MTG stabilisation performance – case D56	Values
Mean temperature stabilisation heating phase (magenta)	-11.2K
Mean temperature stabilisation cooling phase (cyan)	+13.4K

7.9.4 MTG Thermal Model PCM Storage Efficiency of Case D56

Related on Figure 7.13 the degree of utilisation of the total PCM storage summarised in Table 7.16 is maximal. Compared to the ITS demonstrator model, the maximum latent heat capacity can be applied numerically to all nodes. Once the discharge process was completed, no more latent heat was virtually considered. It can therefore be concluded that the PCM subroutine is working correctly in its basic function.

Table 7.16: Calculated amounts of energy, which are absorbed and dispensed by the PCM mass during the heating (charge) and the cooling (recharge) cycles of the hot case D56, compared with the overall efficiency (storage ratio) and the delta PCM mass, related on the total storage capacity available

MTG orbit model – case D56	Storage capacity	Storage ratio	Delta PCM
Charge cycle	+656.767 kJ	100%	0 g
Discharge cycle	-656.767 kJ	0.0%	-

7.10 ITS Demonstrator Temperature Stability related on Thermal Predictions

In the MTG thermal design the EBA structure is primarily intended to shield the optical beam path and absorb incident radiation. It also serves as the structural mounting platform for the solar baffle (see Figure 10.5). There are neither mirror brackets nor other optical parts directly attached to the EBA structure. For the determination of the temperature stabilities neuralgic nodes of the ITS demonstrator thermal model, which consists of the prism and inner baffle submodels are taken into account and are listed in Table 7.17.

The neuralgic nodes correspond to those nodes with the highest instabilities related on the unfilled ITS demonstrator (without PCM). According to the MTG thermal analysis report [TRI-15] the stability intervals of 600, 900 and 3600 seconds are relevant to consider. These values can be attributed to the required optical stability during an observation cycle in orbit, in order to gather and record images via the optical sensors.

The assessment of the temperature stability is based on a state-of-the-art sliding window. The width of the sliding window corresponds constantly to the stability requirement to be evaluated. The sliding window dynamically propagates along the entire simulation time and is determined by the absolute difference between the maximal and minimal occurring temperature within the dynamic window. The temperature profiles from chapter 7.8 form the basis for analysing the temperature stabilities.

7.10.1 Temperature Stability EQ Orbit Case

The Table 7.17 below and Figure 10.41 located in the appendix, contain the temperature instabilities of the demonstrator thermal nodes of the case EQ without embedded PCM as reference.

Table 7.17: Summary of the temperature stability calculations of the most instable thermal nodes of the unfilled ITS demonstrator (without PCM) for the case EQ

Temperature stability without PCM – case EQ [mK]	600 s	900 s	3600 s
Prism shield (N22229)	7.1	63.6	29.1
Inner baffle M0-M1 (N51609)	10.7	63.7	34.0

Derived from this the Table 7.18 below and Figure 10.42 located in the appendix, show the improved temperature instabilities of the ITS demonstrator thermal model with embedded PCM of the case EQ. The relative improvement of the temperature stability behaviour, compared to the demonstrator model without PCM is summarised in Table 7.21 for the case EQ.

Table 7.18: Summary of the temperature stability calculations of the most instable thermal nodes of the unfilled ITS demonstrator (with PCM) for the case EQ

Temperature stability with PCM – case EQ [mK]	600 s	900 s	3600 s
Prism shield (N22229)	2.8	34.7	11.5
Inner baffle M0-M1 (N51609)	5.5	36.4	13.3

7.10.2 Temperature Stability D56 Orbit Case

Ongoing, the Table 7.19 below and Figure 10.43 located on the appendix, yield the temperature instabilities of the demonstrator thermal nodes without embedded PCM for the case D56.

Table 7.19: Summary of the temperature stability calculations of the most instable thermal nodes of the unfilled ITS demonstrator (without PCM) for the case D56

Temperature stability without PCM – case D56 [mK]	**600 s**	**900 s**	**3600 s**
Prism shield (N22229)	7.9	93.0	39.3
Inner baffle M0-M1 (N51609)	8.3	97.8	43.1

Table 7.20 below and Figure 10.44 located in the appendix, show the improved temperature instabilities of the demonstrator thermal model with embedded PCM of the case D56. Also, the relative improvement of the stability behaviour of the temperature field, compared to the demonstrator model without PCM for the case D56 is summarised in Table 7.21.

Table 7.20: Summary of the temperature stability calculations of the most instable thermal nodes of the unfilled ITS demonstrator (with PCM) for the case D56

Temperature stability with PCM – case D56 [mK]	**600 s**	**900 s**	**3600 s**
Prism shield (N22229)	4.0	60.5	22.8
Inner baffle M0-M1 (N51609)	6.5	60.1	29.7

7.10.3 Temperature Stability Improvement

The relative improvement of the temperature stability is determined in relation on the ITS demonstrator without embedded PCM. The results are listed in Table 7.21 for the cases EQ and D56.

In conclusion, it can be stated that for the case EQ an averaged improvement of the temperature stability behaviour of approx. 53.2%, over the different intervals considered is achieved. Whereas for the case D56 an averaged improvement of the temperature stabilities of approx. 36.3% is achieved, also attributed to the embedded PCM mass.

Table 7.21: Evaluation of the temperature stability improvements, considering only the values of highest temperature instability of each node at the respective intervals, for the case EQ and D56

Temperature stability improvement – case EQ [%]	**600 s**	**900 s**	**3600 s**
Prism shield (N22229)	-60.6	-45.4	-60.5
Inner baffle M0-M1 (N51609)	-48.6	-42.9	-60.9
Temperature stability improvement – case D56 [%]	**600 s**	**900 s**	**3600 s**
Prism shield (N22229)	-49.4	-35.0	-42.0
Inner baffle M0-M1 (N51609)	-21.7	-38.5	-31.1

8 CONCLUSIONS

The primary research task accompanied with the research question of this doctoral thesis is defined as to thermally validate the scalability of the ITS technology and further to quantify the passive temperature stabilisation effects of a large-scale use case based ITS demonstrator.

8.1 Added Value

The first instance of innovation developed in this doctoral thesis is the novel combination of the enthalpy-porosity method modelled in ESATAN, together with embedded hysteresis models to mimic technical-grade PCM behaviour. Thereby the hysteresis models decouple the melting and solidification process rate independent. The thermal predictions provide well correlated results for both moderate heat flows and thermal shocks.

There is also the complementary multi-chamber concept, which allows to increase on the one hand the reliability of passive thermal control and reduces the probability of failure in the event of damage of the component. On the other hand due to the multi-chamber concept it is possible to embed different PCMs within the same model, which further favours the flexibility and variability of the passive thermal control design of ITS structures. However, this multi-chamber technique is only made possible by additive manufacturing of the components.

The introduced ITS conductive heat transfer model considers simultaneous and independent modelling of metallic lattice and different PCM types with individual thermo-physical properties in the same thermal model. This heat transfer model can generically scale geometrically complex components under the only influence of conductive heat transfer, which also reduces computing time.

For the modelling of ITS technology, it was also necessary to define a generic lattice cell architecture in order to represent a coherent lattice architecture, which consists of multiple identically structured lattice cells linked together.

Additionally, it was necessary to develop and validate a reliable filling and sealing method for embedding the PCM in the ITS integral structures. The filling process is delta qualified applying the cold and hot filling methods in combination with a non-permanent sealing method for laboratory use.

Due to developed automated ITS model design and layout tools it is possible to perform thermal model sensitivity analyses to derive the optimal ITS design in terms of PCM type, lattice dimensions and PCM layer thickness.

The dissertation did not focus on software development. The software scripts developed have been used to handle and automate the mass of data-processing, e.g. to generate the thermal models for the predictions and to evaluate the results.

8.2 Discussions

The numerical modelling of the PCM behaviour in ESATAN is implemented by applying the enthalpy-porosity method in combination with distinct solid-liquid hysteresis models, which is described in chapter 4.4. The background is that this method can implicitly represent the heat balance equation of the solidified and liquefied PCM fractions absolute by one equation. Moreover, this method can be applied regardless of the complexity of the geometry and the PCM hystereses used.

As mentioned in chapter 4.4, hysteresis models are used to define the enthalpy-temperature relation of PCMs in this work. Most available PCMs are treated as technical-grade one with a certain impurity. Such technical-grade PCMs, especially paraffins, do not have a sharp and ideal isothermal transition temperature, but hystereses along which phase change take place.

After reviewing relevant hysteresis models in chapter 4.3, the diagonal hysteresis model according to Zoltán et al. [ZOL-19] for a two-phase problem is being applied. In these reviews measurements have shown that with repeated phase changes between incomplete melting and solidification states of the PCM mass, the thermal models with an ideal PCM behaviour show an increasing cumulative inaccuracy compared to the measured results. Whereas the hysteresis models can predict the temperature profile sufficiently reliably, as described in chapter 6.8. In addition, the hysteresis model can be applied fully parametrised. This enables to consider the thermal behaviour of different PCM types, which are capsuled from each other and coexist in the same thermal model. Thus, the different PCMs used, can undergo independent of each other phase changes related on its individual characteristic melting temperatures. The multi-PCM behaviour could be successfully predicted on the test specimen and correlated with measurement results in chapter 6.10.

Another critical topic for the thermal validation of the ITS technology is the possible influences of convection in the liquid PCM phase. The alleged convection effects are considered analytically in chapter 6.6. By applying equivalent multiples of the thermal conductance values (GL) within the liquid phase, possible heat transfer enhancements due to a hypothetically increasing influence of convection are analytically estimated. The method for determining the relative influence of convection is based on implicit assumptions. The results of the analyses indicate that, based on the Rayleigh number as similarity parameter, convection can exist within the double walls. But implicitly derived from the measurements made and the analyses, convective heat transfer is not dominant.

The prediction of the phase front dynamics had been conducted in chapter 6.7 in dependence on the mesh size of the specimen, but with constant thickness. The expansion and propagation of the phase front is on the one side predicted by sensitivity analyses. On the other side, the temperature fields had been recorded by IR measurements in addition to the use of thermocouples. The test specimen is a rectangular flat plate of constant thickness measured in an upright configuration, also to make possible convective influences maximum visible. The evaluation of the predictions with the recorded IR data shown that the phase front can be predicted with sufficient accuracy. It should be noted that only the conductive heat transfer model was used for the predictions. Thus, convective heat transfer was not taken into account, which further confirms the hypothesis that convection in the liquid PCM phase in ITS parts is not relevant for the temperature range studied and measurements made.

Non-destructive as well as destructive tests are carried out on specific test specimen series for further analysation of the ITS technology beyond thermal. The scatter of the wall thickness determined on the ITS demonstrator, is in the range of -9% to +12% for target wall thicknesses around 1.0 mm. The existing scatter is due to the fact that contour runs (refer to chapter 5.1) with the derived manufacturing parameter set in such a large construction space and small wall thicknesses are only moderately controllable with the current state of the art technology. Nevertheless, the deviations are acceptable. The thermal models can nevertheless be correlated with sufficient accuracy in their total mass and capacity, when considering the ECSS standard. Detailed results of the CT scans, conducted on specimens and on the demonstrator are not reported in this work, but available in the success-control-report [WIL-23].

The final validation of the ITS technology is proceeded based on a large-volume and scaled hardware demonstrator, which is described in chapter 7. The introduced scaling concept in this thesis at first is based on the capacitance ratio of the demonstrator models, which are scaled and modified in chapter 10.12. The ratio is used to derive the effective PCM mass needed for passive thermal control. Secondly, the equivalent heating concept is realised by surface heaters, whose power profiles have been determined experimentally in chapter 7.4.5. The determination of the heater attachment positions based on the occurring hot spots has proven to be valid for both hot cases EQ and D56. The definitions of the hot cases EQ and D56 are given in chapter 7.3.

Furthermore, the experimental determination of the equivalent heating profiles of the demonstrator to reproduce and thus mimic the MTG reference temperature profiles are performed with a PI controller. The obtained heater power profiles are experimentally validated via TVC cyclic tests of the ITS demonstrator with embedded PCM. The measurement results are compared with the MTG thermal model predictions with active PCM subroutine and embedded PCM.

The results of the ITS demonstrator correlations in chapter 7.8 clarify that the ITS scaling concept, applied to calculate the effective PCM mass and to experimentally determine the heater power profiles, comply with acceptable accuracy related on the MTG predictions. The translation and comparison of the measurement results of the scaled ITS demonstrator to the MTG thermal model predictions show that the ITS scaling concept is representative. The temperature curves of the original MTG orbit model show a sufficiently accurate agreement with the TVC measurement results of the scaled demonstrator in the unfilled state (without PCM). The heating phase with its maximum peak temperatures can be predicted within the limits, according to ECSS. Indeed, the cooling concepts between the ITS demonstrator in the TVC and the MTG thermal model in the space environment still differ. The primary aim of the scaling is to achieve scaling in the temperature effective range of the PCM used. Significant temperature stabilisation is being achieved both in the maximum temperature range and in the subcooling phases. This also effectively reduced the temperature band (peak-peak). As described in chapter 7.10, the temperature stability of component d was significantly improved throughout.

The aluminium alloy AlSi10Mg of which all ITS components are fabricated, already has a high thermal conductivity. The ITS thermal model baseline, which relates only on conductive heat transfer has correlated well between predictions and experimental data of all specimens so far. The thermal models can be correlated with acceptable accuracy, without taking convective heat transfer into account.

The evaluation of the degree of utilisation of the PCM storage tends to show that the scaling method presented in this work can be an initial solid approach for determining a PCM design related to scaled and modified components in a first estimate.

8.3 Future Work and Outlook

During the ITS research, a large number of tests campaigns and validation procedures are successfully completed. The research goals set are at least achieved. Nevertheless, at the end of the ITS basic research phase verification campaigns are still pending, which will be discussed in the following.

A major issue that has arisen during the research work is a possible structural-mechanical stabilisation behaviour of embedded PCM. Through various vibration tests on the shaker, it has become evident that the PCM, which is encapsulated in chambers can contribute to structural damping. Test scenarios are carried out with liquid and solidified PCM mass, which are not dealt within this work.

It is also unclear to what extent a shaken PCM mass behaved and continues to provide the expected thermal stabilisation performance, or whether there is any difference at all. This needs to be investigated in future research as well.

As part of the ITS research, the steady-state and cycling test are carried out on numbers of specimens and the demonstrator orientated on the ECSS. However, within the framework of the currently completed ITS research no long-term TVC cycling tests with approx. many 100 cycles could be carried out to qualify the cycling stability and chemical stability of the PCM mass as well as the PCM chamber sealing concept. This should be a key focus in ITS follow-on research, as the ITS design must be designed for the entire lifetime of a satellite.

It is also not clear how a long-term stay of an ITS component in space behaves under microgravity and harsh radiation. This should also be further validated through a technology demonstration in space, also to increase the TRL.

The most critical risk of ITS designs is located in the qualification of a reliable space suitable PCM chamber sealing method. Such a sealing method must prevent leakage and outgassing of PCM into the vacuum. The laboratory method used so far with elastomer seals is not permissible for space applications, as elastomers typically outgas and become brittle in space. It is mandatory to develop and qualify a sealing method that withstands the harsh environment in space. Possible sealing methods may involve welding, soldering, material squeeze processes or a combination of these. [WIL-23]

Another question is the influence of convection on the heat transfer behaviour within ITS components. Through similarity analyses and equivalent considerations related on the thermal conductance values, a first analytical estimate is made to which extent the change in the heat transfer rate relative to the existing conductive coupling allows convective behaviour to be dominant. So far, the convective influences are treated as negligible. However, the phenomenon of convection in liquefied PCM should be investigated in the future work using CFD analysis models or similar.

As Leimkuehler et al. [LEI-09] mentioned, the requirements which shall be placed on the design and safety of a PCM passive thermal control structure shall be discussed. The ECSS standard related on ECSS-E-ST-32-02 in [ECS-07] classifies the ITS hardware as Metallic Pressurised Structure (MPS). In this context, the topic passivation of ITS component should be discussed. Passivation measures can certainly lead to an increase in system complexity when decommissioning is required.

In the ITS demonstrator TVC measurements and thermal model predictions in chapter 7.8, the secondary effect of the ITS technology could not be fully mapped. In contrast to that, the results of the MTG thermal models in chapter 7.9 indicate a significant effect of stabilising lower temperatures. This behaviour should be investigated further in future work.

9 REFERENCES

[ALA-10] Alary, C.; Lapensée, S.: Thermal Design of the ExoMars Rover Module: AIAA-2010-6188. European Space Agency, ESTEC, Netherlands International Conference on Environmental Systems. American Institute of Aeronautics and Astronautics, Inc., 2010

[AZA-20] Azad, M.; Groulx, D., et al.: Natural convection onset during melting of phase change materials: Part I – Effects of the geometry, Stefan number, and degree of subcooling Department of Mechanical Engineering, Dalhousie University; Department of Process Engineering and Applied Science. Dalhousie University. International Journal of Thermal Sciences 170 (2021) 107180, 2021-07-21

[AZA-21] Azad, M.; Groulx, D., et al.: Natural convection onset during melting of phase change materials: Part II – Effects of Fourier, Grashof, and Rayleigh numbers Department of Mechanical Engineering, Dalhousie University; Department of Process Engineering and Applied Science. Dalhousie University. International Journal of Thermal Sciences 170 (2021) 107062, 2021-06-21

[BAE-06] Baehr, H. D.; Stephan, K.: Heat and Mass Transfer. ISBN-10 3-540-29526-7, Second, revised Edition Thermodynamics, University of Hannover, Germany; Institute of Thermodynamics and Thermal Process Engineering, University of Stuttgart. Berlin, New York, March 2006

[BAR-14] Barreneche, C.; Navarro, H., et al.: New Database on Phase Change Materials for Thermal Energy Storage in Buildings to Help PCM Selection. Energy Procedia 57 (2014) 2408-2415, 2013 ISES Solar World Congress Department of Materials Science & Metallurgical Engineering, Universitat de Barcelona; GREA Innovació Concurrent, Universitat de Lleida, Edifici CREA, Pere de Cabrera. 2014-01-01

[BAR-18] Barz, T.; Sommer, A.: Modeling hysteresis in the phase transition of industrial-grade solid/liquid PCM for thermal energy storages. Int. J. Heat Mass Transfer, 127, 701-713, Journal of Heat Mass Transfer AIT Austrian Institute of Technology GmbH, Giefingasse 2, 1210 Vienna; Interdisciplinary Center for Scientific Computing (IWR), Heidelberg University. 2018-12-01

[BAR-19] Barz, T.; Emhofer, J., et al.: Phenomenological modelling of phase transitions with hysteresis in solid/liquid PCM. 2019, VOL. 12, NO. 6, 770–788, Journal of Building Performance Simulation AIT Austrian Institute of Technology GmbH, Giefingasse 2, 1210 Vienna, Austria; GREiA Research Group, INSPIRES Research Centre, University of Lleida, Pere de Cabrera s/n, 25001 Lleida, Spain. 2019-11-02

[BAR-21] Barz, T.: Paraffins as phase change material in a compact plate-fin heat exchanger - Part II: Validation of the “curve scale” hysteresis model for incomplete phase transitions. Journal of Energy Storage 34 (2021) 102164, Journal of Energy Storage AIT Austrian Institute of Technology GmbH, Giefingasse 2, 1210 Vienna, Austria. 2020-11-27

[BAT-54] Batchelor, G. K.: Heat transfer by free convection across a closed cavity between vertical boundaries at different temperatures. Quarterly of Applied Mathematics, Vol. 12, No. 3 (October, 1954), pp. 209-233, Quarterly of Applied Mathematics Brown University is collaborating with JSTOR to digitize, preserve and extend access to Quarterly of Applied Mathematics. 2016-03-06

[BEL-19] Belcher, T.; Schunk, G.: Thermal Characterization of 3D Printed Lattice Structures. Travis Belcher, NASA MSFC Thermal & Fluids Analysis Workshop (TFAWS) 2019; NASA Langley Research Center. 2019-08-26

[BEN-66] BENTILLA, E. W.; Sterrett, K. F., et al.: Research and Development Study on Thermal Control by Use of Fusible Materials: NAS 8-11163; NSL 65-16-1. Northrop Space Laboratories George C. Marshall Space Flight Center International Aeronautics and Space Administration Huntsville, Alabama; Northrop Space Laboratories 3401 West Broadway, Hawthrone, California 90250. April 1966

[BER-19] Bergmann, K.; Gräbener, J. B. M., et al.: Study on thermal stabilization of a GEO-stationary telescope baffling system by integral application of phase change material: ICES-2019-72, 49th International Conference on Environmental Systems 7-11 July 2019, Boston, Massachusetts FH-Aachen University of Applied Sciences, 52064 Aachen, Germany; OHB System AG, 82234 Weßling, Germany. 2019-07-07

[BLA-21] Blakey-Milner, B.; Gradl, P., et al.: Metal additive manufacturing in aerospace: A review. Materials & Design 209 (2021) 110008, Materials & Design Research Group 3D Innovation, Stellenbosch University, Stellenbosch 7602, South Africa; Component Technology Branch, NASA Marshall Space Flight Center, United States; Aerospace Systems Research Group (ASReG), Discipline of Mechanical Engineering, University of KwaZulu-Natal (UKZN), Durban, South Africa. 2021-11-01

[BRA-12] Brandl, E.; Heckenberger, U., et al.: Additive manufactured AlSi10Mg samples using Selective Laser Melting (SLM): Microstructure, high cycle fatigue, and fracture behavior EADS Innovation Works, Metallic Technologies & Surface Engineering, D-81663 Munich; Fraunhofer Institute for Lasertechnology (ILT), Steinbachstr. 15, D-52074 Aachen, Germany. 2012-02-01

[CAB-15] Cabeza, L. F.: Advances in thermal energy storage systems: Methods and applications. ISBN 978-1-78242-096-5, Elsevier Woodhead publishing series in energy. Amsterdam, 2015

[CHE-14] Chen, J.; Yang, D., et al.: Research Progress of Phase Change Materials (PCMs) Embedded with Metal Foam (a Review). Procedia Materials Science 4 (2014) 389 – 394, 8th International Conference on Porous Metals and Metallic Foams, Metfoam College of Mechanics and Materials, Hohai University, Nanjing 210098 China; Department of Materials Science and Engineering, University of Delaware, Newark, DE 19716-3106, USA. 2014

[CHO-12] Choi, M. K.: Using Pre-melted Phase Change Material to Keep Payload Warm without Power for Hours in Space: AIAA 2012-3894. Heat Transfer, AIAA Associate Fellow, American Institute of Aeronautics and Astronautics NASA Goddard Space Flight Center, Greenbelt, MD 20771. 2012-07-11

[CHO-13] Choi, M. K.: Using Paraffin with -10°C to 10°C Melting Point for Payload Thermal Energy Storage in SpaceX Dragon Trunk: AIAA-2013-4099. American Institute for Aeronautics and Astronautics, International Energy Conversion Engineering Conference (IECEC) GSFC-500-13-D-0191 NASA Goddard Space Flight Center, Greenbelt, MD 20771. 2013

[CHO-14] Choi, M. K.: Phase Change Material for Temperature Control of Imager or Sounder on GOES Type Satellites in GEO: ICES-2015-311. International Conference on Environmental Systems, 45th International Conference on Environmental Systems Planetary Protection Engineer, Spacecraft Mechanical Engineering Section, Jet Propulsion Laboratory/California Institute of Technology (M/S 125-224) 4800 Oak Grove Drive, Pasadena CA91109. 2015-07-12

[CHO-15] Choi, M. K.: Paraffin Phase Change Material for Maintaining Temperature Stability of IceCube Type of CubeSats in LEO: AIAA 2015-3984, American Institute of Aeronautics and Astronautics NASA Goddard Space Flight Center, Greenbelt, MD 20771. 2015

[CHO-16] Choi, M. K.: Using Paraffin PCM to Make Optical Communication Type of Payloads Thermally Self-Sufficient for Operation in Orion Crew Module: AIAA-2016-4601. American Institute for Aeronautics and Astronautics, AIAA Propulsion and Energy GSFC-E-DAA-TN32171 NASA Goddard Space Flight Center, Greenbelt, MD 20771. 2016

[CHO-17] Choi, M. K.: Using Paraffin PCM, Cryogel and TEC to Maintain Comet Surface Sample Cold from Earth Approach through Retrieval: AIAA 2017-4784, American Institute for Aeronautics and Astronautics NASA Goddard Space Flight Center, Greenbelt, MD 20771. 2017

[CHO-18] Choi, M. K.: Thermal Assessment of Paraffin Phase Change Material Mini-Packs on IceCube 3U CubeSat in Flight: AIAA 2018-4490, American Institute of Aeronautics and Astronautics NASA Goddard Space Flight Center, Greenbelt, MD 20771. 2018

[CHO-19] Choi, M. K.: Using Paraffin PCM for Thermal Management of BOLAS Planetary CubeSats with Ion Thrusters: AIAA 2019-4300, American Institute for Aeronautics and Astronautics NASA Goddard Space Flight Center, Greenbelt, MD 20771. 2019

[COL-11] Collette J.P; Rochus P., et al.: Phase Change Material Device for Spacecraft Thermal Control: IAC-11.C2.8.1, International Astronautical Congress Rochus Pierre, University of Liège, Belgium; Peyrou-Lauga Romain, ESA-ESTEC, The Netherlands; Pin Olivier, ESA-ESTEC, The Netherlands. 2011

[COL-12] Collette J.P; Rochus P., et al.: Prototyping of a Phase Change Material Heat Storage Device: IAC-12,C2,8,5,x14815, International Astronautical Congress Rochus Pierre, University of Liège, Belgium; Peyrou-Lauga Romain, ESA-ESTEC, The Netherlands; Pin Olivier, ESA-ESTEC, The Netherlands. 2012

[COL-13] Collette J.P; Rochus P., et al.: Advanced Thermal Control of Launcher Equipment Bay using Phase Change Material: IAC-13, C2,8,7x18233, International Astronautical Congress Rochus Pierre, University of Liège, Belgium; Peyrou-Lauga Romain, ESA-ESTEC, The Netherlands; Pin Olivier, ESA-ESTEC, The Netherlands. 2013

[CON-01] Concept Laser: CL 30AL / CL 31AL Aluminium alloys: CL 31AL according to DIN EN 1706 AlSi10Mg(b). CL 30AL and CL 31AL can be used for production of lightweight components in the field of automotive and aerospace industries., Datasheet. 2024-01-07

[CON-02] Concept Laser: CL 32AL AlSi10Mg(b) alloy: According to DIN EN 1706. CL 30AL, CL 31AL and CL32 AL can be used for production of lightweight components in the field of automotive and aerospace industries, Datasheet. 2024-01-07

[CRE-01] Creel, R. A.: Apollo Rover Lessons Learned Apollo Rover Lessons Learned. presentation, Applying Experiences On The Apollo Lunar Rover Project To Rovers For Future Space Exploration Capture of Apollo Lunar Module Reliability Lessons Learned: Program/Engineering Management. July 2007

[CZU-17] Czupalla, M.: Phase Change Material Subroutine for Thermal Simulations FH Aachen - University of Applied Sciences. 2017-01-01

[DDB-23] DDBST GmbH: Kinematic Viscosity of Hexadecane Dortmund Data Bank. 2024-01-07

[DON-16] Zhao, D.; Qian, X., et al.: Measurement Techniques for Thermal Conductivity and Interfacial Thermal Conductance of Bulk and Thin Film Materials, Journal of Electronic Packaging, Transactions of the ASME Vol. 138 / 040802-1. December 2016

[DUA-01] Duan, Q.; Tan, F. L., et al.: A numerical study of solidification of n-hexadecane based on the enthalpy formulation, Journal of Materials Processing Technology 120 (2002) 249–258 School of Mechanical and Production Engineering, Nanyang Technological University, 50 Nanyang Avenue, Singapore 639798, Singapore. 2001-06-14

[DUD-19] Dudon, J.-P.; Raynaud, M., et al.: Optimized Phase Change Material Module for Thermal Regulation of Cycled Dissipative Units: ICES-2019-178, 49th International Conference on Environmental Systems Thales Alenia Space, 5 allée des Gabians, BP99, 06150 Cannes la Bocca Cedex, France; INFLUTHERM SAS, Parc Lyon Sud, 61 rue Mathieu Dussurgey, 69190 St Fons, France. 2019-07-07

[DUT-11] Dutil, Y.; Rousse, D. R., et al.: A review on phase-change materials: Mathematical modeling and simulations, Chaire de Recherche Industrielle T3E, Ecole de technologie supe´rieure, Universite´ du Que´bec, 801 Boul. Mgr, Bourget Le´vis, QC G6V 9V6, Canada;Laboratoire MMP, Ecole Supe´rieure des Sciences et Techniques de Tunis, 5 Avenue Taha Hussein, BP 56, Baˆb Manara, Tunis, Tunisia Renewable and Sustainable Energy Reviews 15 (2011) 112–130. 2011-01-01

[DUT-14] Dutil, Y.; Rousse, D. R., et al.: Mathematical Modeling of Phase Change Materials: An Updated Review, Chaire de Recherche Industrielle T3E, École de technologie supérieure Université du Québec (yvan.dutil@estml.ca, daniel.rousse@estml.ca). 2014-11-03

[ECS-07] European Cooperation for Space Standardization: ECSS-E-ST-32-02C Rev. 1: Structural design and verification of pressurized hardware, ECSS Secretariat Secretariat ESA-ESTEC Requirements & Standards Division Noordwijk, The Netherlands European Cooperation for Space Standardization. 2008-11-15

[ECS-22] European Cooperation for Space Standardization: ECSS-E-ST-10-03C Rev.1: Testing, ECSS Secretariat Secretariat ESA-ESTEC Requirements & Standards Division Noordwijk, The Netherlands European Cooperation for Space Standardization. 2022-05-31

[ELG-16] Elguea, M.; Gálvez, G.: Mechanical Architecture of the MTG Intstruments Supporting Structure (FCI-TA & IRS): A56153EM, ECSSMET-2016 Toulouse, France AirbusDS, Avda. de Aragon 404, 28022, Madrid. 2016-09-27

[ELI-18] Elias, C. N.; Stathopoulos, V. N.: A comprehensive review of recent advances in materials aspects of phase change materials in thermal energy storage, 2nd International Conference on Sustainable Energy and Resource Use in Food Chains Laboratory of Chemistry and Materials Technology, Department of Electrical Engineering, School of Technological Applications, Technological. 2018-03-01

[ERN-19] Ernot, J.; Verdin, P. G., et al.: Analytical and numerical predictions of the thermal performance of multi-layered lattice structures, International Journal of Heat and Mass Transfer 145 (2019) 118752 Centre for Thermal Energy Systems and Materials, Cranfield University, Bedfordshire MK43 0AL, UK; SAFRAN Electrical & Power UK LTD, Pitstone, Buckinghamshire LU7 9GT, UK. 2019-02-10

[ESA-22] ITP Engines UK Ltd.: ESATAN-TMS: ESATAN Manual Complete 2022. Modelling Suite User Manual ITP Engines UK Ltd. Whetstone, Leicester, UK. December 2021

[FAD-18] Faden, M.; König-Haagen, A., et al.: An implicit algorithm for melting and settling of phase change material inside macrocapsules, International Journal of Heat and Mass Transfer 117 (2018) 757–767 Chair of Thermodynamics and Transport Processes (LTTT), Centre of Energy Technology (ZET), University of Bayreuth, Universitätsstraße 30, 95440 Bayreuth, Germany. 2017-10-09

[FAD-19] Faden, M.; König-Haagen, A., et al.: An Optimum Enthalpy Approach for Melting and Solidification with Volume Change, Energies Chair of Thermodynamics and Transport Processes (LTTT), Centre of Energy Technology (ZET) University of Bayreuth, Universitätsstraße 30, 95440 Bayreuth, Germany. 2019-03-05

[FAD-20] Faden, M.; Linhardt, C., et al.: Velocity field and phase boundary measurements during melting of n-octadecane in a cubical test cell, International Journal of Heat and Mass Transfer 135 (2019) 104–114 Chair of Thermodynamics and Transport Processes (LTTT), Centre of Energy Technology (ZET), University of Bayreuth, Universitätsstraße 30, 95440 Bayreuth, Germany. 2019-01-12

[FAD-21] Faden, M.; König-Haagen, A., et al.: Influence of density change during melting inside a cavity: Theoretical scaling laws and numerical analysis, International Journal of Heat and Mass Transfer 173 (2021) 121260 Chair of Thermodynamics and Transport Processes (LTTT), Centre of Energy Technology (ZET), University of Bayreuth, Universitätsstraße 30, Bayreuth a Chair of Thermodynamics and Transport Processes (LTTT), Centre of Energy Technology (ZET), University of Bayreuth, Universitätsstraße 30, Bayreuth, 95440 Germany. 2021-03-21

[FLE-15] Fleischer, A. S.: Thermal Energy Storage Using Phase Change Materials: Fundamentals and Applications. ISBN 978-3-319-20921-0, Springer Briefs in Applied Sciences and Technology, Thermal Engineering and Applied Science Department of Mechanical Engineering Villanova University. Minneapolis, MN, USA, 2015

[GEB-16] Gebhardt, A.: Additive Fertigungsverfahren: Additive Manufacturing und 3D-Drucken für Prototyping - Tooling - Produktion. ISBN: 978-3-446-44401-0, Hanser Fachbuch, 5., neu bearbeitete und erweiterte Auflage Professor an der Fachhochschule Aachen, Lehrgebiet: Hochleistungsverfahren der Fertigungstechnik und Additive Manufacturing. München, 2016

[GEB-17] Gebhardt, A.; Hötter, J.-S.: Additive Manufacturing: 3D Printing for Prototyping and Manufacturing. ISBN: 978-1-56990-582-1, Hanser Fachbuch Professor an der Fachhochschule Aachen, Lehrgebiet: Hochleistungsverfahren der Fertigungstechnik und Additive Manufacturing. 2017

[GEI-20] Geismayr, L.; Schummer, F., et al.: Thermo-Mechanical Design and Analysis of a Multispectral Imaging Payload using Phase Change Material: IAC-20,C2,5,13,x59152. International Astronautical Congress, 71st International Astronautical Congress (IAC) – The CyberSpace Edition Chair of Astronautics, Technical University of Munich (TUM), Bolzmannstr. 15, 85748 Garching, Germany; Orbital Oracle Technologies GmbH, Agnes-Pockels-Bogen 1, 80992 Munich, Germany. 2020-10-12

[GEN-21] Gen 3D: Types of lattices for additive manufacturing: ALTR Innovation Centre. 2021-05-21

[GIL-02] Gilmore, G. D.: Spacecraft Thermal Control Handbook - Volume 1 Fundamental Technologies: Second Edition. American Institute of Aeronautics and Astronautics, 2. edition The Aerospace Press • El Segundo, California; American Institute of Aeronautics and Astronautics, Inc. • Reston, Virginia. El Segundo, Calif., 2002

[GOT-14] Gottero, M.; Perotto, V., et al.: Phase-change thermal capacitors for ExoMars 2016 mission: ICES-2014-147, 44th International Conference on Environmental Systems Thales Alenia Space Italia, Torino, Italy; ERG Materials and Aerospace Corp., Oakland (CA), USA. Tucson, Arizona, 2014-07-13

[GUO-18] Guo, Z.; Bai, Q., et al.: Experimental investigation on the melting behavior of phase change materials in open-cell metal foams in an inclined rectangular enclosure, Energy Procedia 152 (2018) 215–220 Institute of the Building Environment & Sustainability Technology, School of Human Settlements and Civil Engineering. 2018-06-05

[GUO-21] Guo, Y.; Huning, Y., et al.: Thermal performance of a 3D printed lattice-structure heat sink packaging phase change material, Chinese Journal of Aeronautics, (2021), 34(5): 373–385 Chinese Society of Aeronautics and Astronautics & Beihang University; Laboratory of Fundamental Science on Ergonomics and Environmental Control, School of Aeronautic Science and Engineering, Beihang University, Beijing 100083, China. 2020-08-15

[HAL-71] Hale, D. V.; Hoover, M. J., et al.: Phase Change Materials Handbook: NASA CR-51363, NASA contractor report Lockheed Missiles and Space Company, Huntsville Research and Engineering Center, 4800 Bradford Drive, Huntsville-Alabama. September 1971

[HAT-17] Hatakenaka, R.; Kinjo, T., et al.: Heat-transfer Characteristics of a Light-weight, Fin-integrated PCM Unit Manufactured by Additive Manufacturing: ICES-2017-346, 47th International Conference on Environmental Systems Japan Aerospace Exploration Agency, Tsukuba, Ibaraki, 305-8505, Japan; University of Tsukuba, Tsukuba, Ibaraki, 305-8571, Japan. 2017-07-16

[HAT-21] Hatakenaka, R.; Saitoh, M., et al.: Heat-transfer Characteristics of a Spacer-type, Fin-integrated PCM Device by Additive Manufacturing: ICES-2021-247, 50th International Conference on Environmental Systems Japan Aerospace Exploration Agency, Tsukuba, Ibaraki, 305-8505, Japan; Orbital Engineering Inc., Yokohama, Kanagawa, 221-0822, Japan. 2021-07-12

[HAW-01] Hawkins, S. E.; Murchiea, S. L., et al.: In-Flight Performance of MESSENGER's Mercury Dual Imaging System: 2012-7441 The Johns Hopkins University Applied Physics Laboratory, 11100 Johns Hopkins Road, Laurel d Physics Laboratory, 11100 Johns Hopkins Road, Laurel, MD 20723, USA. 2012

[HEN-20] Hennlich: Self-centering bonded seal: Schraubendichtungen Standard-Bauform U, https://www.hennlich.at/produkte/dichtungstechnik-statische-dichtungen-11/schraubendichtungen-bonded-seals.html. 2024-01-07

[HOE-18] Höhlein, S.; König-Haagen, A., et al.: Macro-Encapsulation of Inorganic Phase-Change Materials (PCM) in Metal Capsules, Materials Chair of Engineering Thermodynamics and Transport Processes (LTTT), Center of Energy Technology (ZET) University of Bayreuth, Universitätsstraße 30, 95440 Bayreuth, Germany. 2018-09-17

[HUM-77] Humphries, W. R.; Griggs, E. I.: A design handbook for phase change thermal control and energy storage devices: NASA Technical Paper NASA-TP-1074, NASA Marshall Space Flight Center Huntsville, AL, United States Scientific and Technical Information Office. 1977-01-11

[HUU-20] Xusheng, H.; Xiaolu, G.: Experimental and numerical investigation on thermal performance enhancement of phase change material embedding porous metal structure with cubic cell, Applied Thermal Engineering 175 (2020) 115337 Charles Delaunay Institute, LASMIS, University of Technology of Troyes, 12 Rue Marie Curie, 10004 Troyes, France. 2020-04-16

[IDE-94] Idelsohn, S. R.; Storti, M. A., et al.: Numerical methods in phase-change problems: Archives of Computational Methods in Engineering State of the art reviews, Archives of Computational Methods in Engineering Vol. 1, 49–74, (1994) Grupo de Tecnologıa Mec´anica del INTEC Gueemes 3450, 3000 Santa Fe, Argentina. May 1994

[ISA-17] Isaacs, S.; Arias, D., et al.: Development of a Lightweight and Low-Cost 3D-Printed Aluminum PCM Panel for Thermal Management of CubeSat Applications: ICES-2017-108, 47th International Conference on Environmental Systems Roccor, LLC, Longmont, CO, 80503. Charleston, South Carolina, 2017-07-16

[IVS-94] Ivshin, Y.; Pence, T. J.: A constitutive model for hysteretic phase transition behavior: Int. 1. Elsevier Scicncc Ltd, Johnson Controls inc., Milwaukee, WI 53201-0591, U.S.A.;Department of Materials Science & Mechanics, Michigan State University Johnson Controls inc., Milwaukee, WI 53201-0591, U.S.A.; Department of Materials Science & Mechanics, Michigan State University East Lansing, MI 48824-1226, U.S.A. 1994

[JOS-01] Gräbener, J. B. M.: Temperature Stabilization of a Geostationary Satellite Baffle – Thermal Test Planning and Prediction: Bachelor Thesis FH Aachen - University of Applied Sciences. 2017-08-21

[KAB-21] Kabir, M.; Gemeda, T., et al.: Design and Development of a PCM-Based Two-Phase Heat Exchanger Manufactured Additively for Spacecraft Thermal Management Systems, International Journal of Heat and Mass Transfer 180 (2021) 121782 Center for Advanced Manufacturing in Space Technology & Applied Research (CAM-STAR), University of the District of Columbia, Washington D.C., USA. 2021-07-26

[KAS-20] Kasper, Lukas: Modeling of the Phase Change Material of a Hybrid Storage using the Finite Element Method, TU Wien Academic Press 2020 Institut für Energietechnik und Thermodynamik; Institute for Energy Systems and Thermodynamics (IET) of the Faculty of Mechanical and. Vienna, 2020

[KLI-20] Klimeš, L.; Charvát, P., et al.: Computer modelling and experimental investigation of phase change hysteresis of PCMs: The state-of-the-art review, Applied Energy 263 (2020) 114572 Sustainable Process Integration Laboratory (SPIL), Brno University of Technology, Brno, Czech Republic; Energy Institute, Brno University of Technology, Brno, Czech Republic. 2020-01-26

[KLO-22] Klochko, L.; Noel, J., et al.: Thermophysical properties of n-hexadecane: Combined Molecular Dynamics and experimental investigations Universit´e de Lorraine, CNRS, LEMTA, 54000 Nancy, France. 2022-07-15

[KOE-17] König-Haagen, A.; Franquet, E., et al.: A comprehensive benchmark of fixed-grid methods for the modeling of melting, International Journal of Thermal Sciences 118 (2017) 69e103 University of Bayreuth, Centre of Energy Technology (ZET), Bayreuth, Germany; Univ. Pau & Pays Adour, Laboratoire de thermique, energetique et procedes e IPRA, EA 1932, 64000 Pau, France. 2017-04-05

[LEI-09] Leimkuehler, T. O.; Powers, A., et al.: Demonstration of Super Cooled Ice as a Phase Change Material Heat Sink for Portable Life Support Systems: 2009-01-2405, NASA Johnson Space Cente Paragon Space Development Corporation, NASA Johnson Space Center. 2009

[LEI-10] Leimkuehler, T.; Stephan, R., et al.: Development, Testing, and Failure Mechanisms of a Replicative Ice Phase Change Material Heat Exchanger: AIAA-2010-6138, American Institute of Aeronautics and Astronautics Paragon Space Development Corporation, Houston, Texas, 77058; NASA-Johnson Space Center, Houston, Texas, 77058. 2010

[LI-18] Li, P.-W.; Chan, C. L.: Thermal Energy Storage Analyses and Designs. ISBN: 978-0-12-805344-7, Academic Press is an imprint of Elsevier Department of Aerospace and Mechanical Engineering The University of Arizona (USA). 125 London Wall, London EC2Y 5AS, United Kingdom, 2017

[LI-19] Li, X.; Zhu, Z., et al.: Effect of supergravity on heat transfer characteristics of PCM with the pore-scale lattice Boltzmann method, 10th International Conference on Applied Energy (ICAE2018), pp gy (China) Institute of Applied Electronics, China Academy of Engineering Physics, Mianyang, Sichuan, 621900, P.R. China. Hong Kong, 2018-08-22

[LI-21] Li, Z.; Gariboldi, E.: Review on the temperature-dependent thermophysical properties of liquid paraffins and composite phase change materials with metallic porous structures, Materials Today Energy 20 (2021) 100642 Politecnico di Milano, Department of Mechanical Engineering, Via La Masa 1, Milan, 20156, Italy. Elsevier Ltd., 2021-01-09

[LIL-09] Lillibridge, S.; Stephan, R.: Phase Change Material Heat Exchanger Life Test: 2009-01-2589, NASA Lyndon B. Johnson Space Center SAE International. 2009

[LIL-17] Lillibridge, S.; Stephan, R.: Heat-transfer Characteristics of a Light-weight, Fin integrated PCM Unit manufactured by Additive Manufacturing: ICES-2017-346, 47th International Conference on Environmental Systems Japan Aerospace Exploration Agency, Tsukuba, Ibaraki, 305-8505, Japan; University of Tsukuba, Tsukuba, Ibaraki, 305-8571, Japan. 2017-07-16

[MAL-21] Mallya, N.; Haussener, S.: Buoyancy-driven melting and solidification heat transfer analysis in encapsulated phase change materials, International Journal of Heat and Mass Transfer 164 (2021) 120525 Laboratory of Renewable Energy Science and Engineering, Institute of Mechanical Engineering, École Polytechnique Fédérale de Lausanne, Switzerland. 2020-10-20

[MEH-08] Mehling, H.; Cabeza, L. F.: Heat and cold storage with PCM: An up to date introduction into basics and applications. ISBN: 978-3-540-68557-9, Springer-Verlag Berlin Heidelberg Heat and mass transfer Institut für Verfahrenstechnik Universität Hannover. Berlin, 2008

[OHB-19] OHB: Thermal Model (Rev1666) of the MTG satellite: ESATAN thermal model data and CAD model data. Provided by OHB, IRS Analyses Report MTG-KT-IR-RP-0013 / Issue 04. 2015-12-22

[PAU-01] Pauken, M. T.; Emis, N.: Thermal Energy Storage Devices Jet Propulsion Laboratory TFAWS 2006. 2006-08-08

[PCM-01] PCM: n-Tetradecane data sheet: 629-59-4, Material Safety Data Sheet SDS/MSDS cdhfinechemical.com. 2024-01-07

[PCM-02] PCM: n-Hexadecane data sheet: 544-76-3. abcr Chemie, Material Safety Data Sheet SDS/MSDS. 2024-01-07

[PCM-03] PCM: n-Octadecane data sheet: 593-45-3. Sigma-Aldrich, Material Safety Data Sheet SDS/MSDS. 2024-01-07

[PCM-04] PCM: n-Eicosane data sheet: 112-95-8. ThermoFisher Scientific, Material Safety Data Sheet SDS/MSDS. 2024-01-07

[PER-11] Perotto, V.; Gottero, M., et al.: Design and Test of ExoMars Thermal Breadboard: AIAA-2011-5118, 41st International Conference on Environmental Systems (ICES) Home Thales Alenia Space Italia, Torino, Italy. 2011-07-17

[PER-20] Pernsteiner, D.; Schirrer, A., et al.: State estimation concept for a nonlinear melting/solidification problem of a latent heat thermal energy storage, Computers and Chemical Engineering 153 (2021) 1074 4 4 TU Wien, Institute of Mechanics and Mechatronics, Getreidemarkt 9/BA, Vienna 1060, Austria; TU Wien, Institute for Energy Systems and Thermodynamics, Getreidemarkt 9/BA, Vienna 1060, Austria. 2021-07-07

[PER-21] Pernsteiner, D.; Schirrer, A., et al.: Data-based model reduction for phase change problems with convective heat transfer, Applied Thermal Engineering 184 (2021) 116228 TU Wien, Institute of Mechanics and Mechatronics, Getreidemarkt 9/BA, 1060 Vienna, Austria; TU Wien, Institute for Energy Systems and Thermodynamics, Getreidemarkt 9/BA, 1060 Vienna, Austria. 2020-10-27

[PIA-22] Piacquadio, S.; Schirp-Schoenen, M., et al.: Experimental analysis of the thermal energy storage potential of a phase change material embedded in additively manufactured lattice structures RWTH Aachen University, Institute for structural mechanics and lightweight design, Wüllnerstraße 7, 52062, Aachen, Germany. 2022-11-05

[POI-13] Pointner, H.; Steinmann, W.-D., et al.: Introduction of the PCM Flux Concept for Latent Heat Storage. Energy Procedia 57 (2014) 643 – 652, 2013 ISES Solar World Congress German Aerospace Center (DLR), Institute of Technical Thermodynamics, 70569 Stuttgart, Germany. 2014

[QUI-12] Quinn, G.; Hodgson, E., et al.: Phase Change Material Trade Study: A Comparison Between Wax and Water for Manned Spacecraft: AIAA-2011-5229. JSC-CN-23351, 41st International Conference on Environmental Systems Hamilton Sundstrand, Windsor Locks, CT 06096; NASA Johnson Space Center, Houston, TX, 77058. 2011-01-01

[QUI-15] Quinn, G.; Stieber, J., et al.: Phase Change Material Heat Sink for an International Space Station Flight Experiment: ICES_2015_167, 45th International Conference on Environmental Systems Hamilton Sundstrand Space Systems International, Inc., Windsor Locks, Connecticut, 06096; NASA Johnson Space Center, Houston, Texas, 77058. 2015-07-12

[QUI-18] Quinn, G. J.; Ahlstrom, T., et al.: Phase Change Material Heat Sink Flight Experiment Results: ICES-2017-016, 47th International Conference on Environmental Systems Hamilton Sundstrand Space Systems International, Inc., Windsor Locks, Connecticut, 06096; NASA Johnson Space Center, 2101 NASA Parkway, Houston, Texas, 77058. Charleston, South Carolina, 2017-07-16

[REI-19] Reiswich, M.; Brandt, H., et al.: Passive Thermal Control by Integration of Phase Change Material into Additively Manufactured Structures: IAC-19,E2,2,8,x55200, 70th International Astronautical Congress (IAC), Washington D.C Department of Aerospace Engineering, FH Aachen – University of Applied Sciences, Hohenstaufenallee 6, 52064. 2019-10-21

[RIG-19] Righetti, G.; Savio, G., et al.: Experimental study of phase change material (PCM) embedded in 3D periodic structures realized via additive manufacturing, International Journal of Thermal Sciences 153 (2020) 106376Department of Management and Engineering, University of Padova, Vicenza, 36100, Italy; Department of Civil, Environmental and Architectural Engineering, University of Padova, Padova, 35131, Italy. 2020-03-20

[RIG-20] Righetti, G.; Savio, G., et al.: Experimental investigation of phase change of medium/high temperature paraffin wax embedded in 3D periodic structure, International Journal ofThermofluids 56 (2020) 100035 Department ofManagement and Engineering, University ofPadova, Vicenza, 36100, Italy; Department ofCivil, Environmental and Architectural Engineering University ofPadova, Padova, 35131, Italy. 2020-05-25

[RIG-21] Righetti, G.; Savio, G., et al.: On the design of Phase Change Materials based thermal management systems for electronics cooling, Applied Thermal Engineering 196 (2021) 117276 Department of Management and Engineering, University of Padova, 36100, Italy; Department of Civil, Environmental and Architectural Engineering, University of Padova, 35100, Italy. 2021-06-27

[ROE-14] Roesler, F.: Modellierung und Simulation der Phasenwechselvorgänge in makroverkapselten latenten thermischen Speichern: Dissertation. Lehrstuhl für Technische Thermodynamik und Transportprozesse (LTTT) Fakultät für Ingenieurwissenschaften Universität Bayreuth. Universität Bayreuth, 2014-06-04

[RUA-17] RUAG Space GmbH: Standard COOLCAT Products: K-2030-SPL-00001-RSA Issue 1, RUAG Space Thermal Insulation Products RUAG Space Thermal Insulation Products. 2019

[SAN-20] Sánchez, P.; J. M., Ezquerro, et al.: The effect of thermocapillary convection on PCM melting in microgravity: results and expectations: IAC-20,A2,3,8,x58029. International Astronautical Congress, 71st International Astronautical Congress (IAC) – The CyberSpace Edition, 12-14 October 2020 71st International Astronautical Congress (IAC) – The CyberSpace Edition, 12-14 October 2020 Universidad Politécnica de Madrid, Plaza de Cardenal Cisneros 3, 28040 Madrid, Spain. 2020-10-12

[SCH-22] Schulz, L.; Rauscher, U., et al.: Demonstration of 3D printed Phase Change Material Heat Capacitors for Space Application: ICES-2022-138, 51st International Conference on Environmental Systems Airbus Defence and Space GmbH, Friedrichshafen, Germany. St. Paul, Minnesota, 2022-07-14

[SOL-16] Soler, G. G, Fernández, M. E.: MTG insturment: mechanical design solutions focused on the structure thermoelastic behaviour and the sensitivity on the optical performance: ECSSMET-2016. A56155GG Airbus DS, Avda. Aragón 404, 28022 Madrid. Toulouse, France, 2016-09-27

[STE-02] Stephan, R. A.; Ungar, E. K.: Thermal Control System for Exploration: ETDP - Advanced Thermal Project. presentation ETDP - Advanced Thermal Project. 2007

[STE-10] Stephan, Ryan A.: Overview of NASA's Thermal Control System Development for Exploration Project: AIAA 2011-5186, In: *41st International Conference on Environmental* (2011)

[SWE-19] Sweidan, A. H.; Heider, Y., et al.: Modeling of PCM-based enhanced latent heat storage systems using a phase-field-porous media approach, Continuum Mech. Thermodyn. (2020) 32:861–882 Institute of General Mechanics, RWTH Aachen University, 52062 Aachen, Germany; Department of Civil Engineering and Engineering Mechanics, Columbia University, New York, NY 10027, USA. 2019-03-28

[TAO-16] Tao, W.; Leu, M. C.: Design of lattice structure for additive manufacturing, Public Version: DOI 10.1109/ISFA.2016.7790182 ISFA 2016 Department of Mechanical and Aerospace Engineering, Missouri University of Science and Technology Technology Technology Rolla, MO, 65409. 2018-11-27

[TRI-04] Tritt, T. M.: Thermal conductivity: Theory, properties, and applications, Physics of solids and liquids. New York, 2004

[TRI-15] Triebig. C.; Ulfers, H., et al.: IRS Analysis Report IRS_D_O_05 MTG-KT-IR-RP-001 OHB System AG, München. 2015-12-22

[TUM-14] Tumilowicz, E.; Chan, C. L., et al.: An enthalpy formulation for thermocline with encapsulated PCM thermal storage and benchmark solution using the method of characteristics, International Journal of Heat and Mass Transfer 79 (2014) 362–377 Department of Aerospace and Mechanical Engineering, The University of Arizona, 1130 N. Mountain Ave., Tucson, AZ 85721, USA. 2014-08-06

[UZA-17] Uzan, A. Y.; Kozak, Y., et al.: A novel multi-dimensional model for solidification process with supercooling, International Journal of Heat and Mass Transfer 106 (2017) 91–102 Heat Transfer Laboratory, Department of Mechanical Engineering, Ben-Gurion University of the Negev, Beer-Sheva 84105, Israel; Consultant, Weingartenstr. 37, 97072 Würzburg, Germany. 2016-10-11

[VAN-19] van Gerner, H. J.; Marc de, S., et al.: Lightweight Two Phase Pumped Cooling System with Aluminium Components produced with Additive Manufacturing: ICES-2019-01. International Conference on Environmental Systems, 7-11 July 2019, 49th International Conference on Environmental Systems Netherlands Aerospace Centre NLR, Amsterdam, The Netherlands; Thales Avionics Electrical Systems SAS, Chatou, Fran. Boston, Massachusetts, 2011-07-07

[VEL-15] Vélez, C.; Khayet, M., et al.: Temperature-dependent thermal properties of solid/liquid phase change even-numbered n-alkanes: n-Hexadecane, n-octadecane and n-eicosane: DOI:10.1016/j.apenergy.2015.01.054, Applied Energy 143 (2015) 383–394 Department of Applied Physics I, Faculty of physics, University Complutense of Madrid, Avda. Complutense s/n, Madrid 28040, Spain. 2015-01-07

[VER-18] Verevkin, S. P.; Zaitsau, D. H., et al.: Handbook of Thermal Analysis and Calorimetry: ISBN: 978-0-444-64062-8, Elsevier Radarweg 29, PO Box 211, 1000 AE Amsterdam, Netherlands. 2018

[VOG-19] Vogel, J.: Influence of natural convection on melting of phase change materials: Dissertation. Von der Fakultät Energie-, Verfahrens- und Biotechnik der Universität Stuttgart Institut für Gebäudeenergetik, Thermotechnik und Energiespeicherung der Universität Stuttgart. Karlsruhe, 2018-12-11

[VOL-90] Voller, V. R.: Fast implicit finite-difference method for the analysis of phase change problems: DOI: 10.1080/10407799008961737, Numerical Heat Transfer Mineral Resources Research Center, Department ofCivil and Mineral Engineering, University ofMinnesota, Minneapolis, Minnesota 55455. 2007-05-21

[WAT-15] Watter, H.: Hydraulik und Pneumatik: Anwendungen und Simulation. DOI: 10.1007/978-3-658-07860-7, Springer Vieweg ISBN 978-3-658-07859-1. Wiesbaden, 2015

[WIL-20] Wild, D.; Schrezenmeier, J., et al.: Thermal Characterization of additive manufactured Integral Structures for Phase Change Applications: ICES-2020-183, International Conference on Environmental Systems FH Aachen – University of Applied Sciences, 52064 Aachen, Germany; Universität der Bundeswehr München, 85577 Neubiberg, Germany. July 2020

[WIL-21] Wild, D.; Czupalla, M., et al.: Modeling, Prediction and Test of Additive Manufactured Integral Structures with Embedded Lattice and Phase Change Material Applying Infused Thermal Solutions (ITS): ICES-2021-110, 50th International Conference on Environmental Systems FH Aachen – University of Applied Sciences, 52064 Aachen, Germany; Universität der Bundeswehr München, 85577 Neubiberg, Germany. 2021-07-12

[WIL-23] Wild, D.; Schrezenmeier, J.: Infused Thermal Solutions - Erfolgskontrollbericht: Erfolgskontrollbericht nach Anlage 2 der BNBest-BMBF 98. Forschungs-/Kooperationsprojekt 50RP1975 FH Aachen – University of Applied Sciences, 52064 Aachen, Germany. 2023-01-31

[YAM-14] Yamada, K.; Nagano, H., et al.: Heat Storage Panel Using a Phase change Material Encapsulated in a High thermal conductivity CFRP for Micro Satellites: ICES-2014-119, 44th International Conference on Environmental Systems Nagoya University, Nagoya, Aichi, 464-8603, Japan; University of Tokyo, Tokyo, 113-8656, Japan; Hokkaido University, Sapporo, Hokkaido, 060-8628, Japan. Tucson, Arizona, 2014-07-13

[ZHA-15] Zhang, P.; Meng, Z., et al.: Experimental and Numerical Study of Heat Transfer Characteristics of a Paraffin/Metal Foam Composite PCM, 7th International Conference on Applied Energy – ICAE 2015 Energy Procedia 75 (2015) 3091 – 3097. 2015-08-01

[ZHA-19] Zhang, Y.; Ma, G., et al.: Numerical and experimental study of phase-change temperature controller containing graded cellular material fabricated by additive manufacturing, Applied Thermal Engineering 150 (2019) 1297–1305 State Key Laboratory of Structural Analysis for Industrial Equipment, Dalian University of Technology, Dalian 116024, China. 2019-01-29

[ZHE-19] Zheng, J.; Yu, C., et al.: Optimization of the Melting Performance of a Thermal Energy Storage Unit with Fractal Net Fins MIIT Key Laboratory of Thermal Control of Electronic Equipment, School of Energy and Power Engineering Nanjing University of Science and Technology, Nanjing 210094, China. 2019-01-15

[ZOL-19] Zoltán, A.; Zoltán, S.: Thermal behaviour of materials in interrupted phase change, Journal of Thermal Analysis and Calorimetry (2019) 138:3915–3924 Department of Building Services and Process Engineering, Budapest University of Technology and Economics, Müegyetem rakpart 3-9, Budapest 1111, Hungary. 2019-07-19

10 APPENDIX

10.1 PCM Data Overview

The following Table 10.1 contains the relevant thermo-physical properties of the paraffins used in this work. The general use of latent heat storage materials is focused on organic PCMs, which are known as paraffins. The reason are that paraffins have a high mass specific latent heat of fusion, non-toxic and are available in a wide range with different melting temperatures to allow flexible thermal designs for passive thermal control.

Table 10.1: Overview of the relevant thermo-physical properties of the applied PCMs within the ITS research

PCM	Tetradecane	Hexadecane	Octadecane	Eicosane
CAS number	CAS 629-59-4	CAS 544-76-3	CAS 593-45-3	CAS 112-95-8
Formula	$C_{14}H_{30}$	$C_{16}H_{34}$	$C_{18}H_{38}$	$C_{20}H_{42}$
Transition temperature	6.1°C	18.2°C	29.3°C	36.1°C
Purity	99%	99%	99%	99%
Supplier	abcr GmbH	abcr GmbH	abcr GmbH	abcr GmbH
Specific heat capacity	2100.0 kJ/kgK	2110.0 kJ/kgK	2124.0 kJ/kgK	2136.0 kJ/kgK
Density	763 kg/m³	773 kg/m³	777 kg/m³	789 kg/m³
Latent heat of fusion	227.2 kJ/kg	237.1 kJ/kg	242.5 kJ/kg	247.3 kJ/kg
Reference data sheet	[PCM-01]	[PCM-02]	[PCM-03]	[PCM-04]

10.2 Thermo-Optical Measurement Results

Table 10.2: Results of the thermo-optical measurements of specific test plates, which are additively manufactured in different orientations, with machined and originally porous surface, with and without heat treatment [WIL-20]

Specimen	$\varepsilon_{20°} \approx \varepsilon_N$	$\varepsilon_{60°}$	ε_H	Measured ε_H	Error σ	α	Measured α	Error σ
Machined	0.024	0.044	0.029			0.284		
0°	0.030	0.041	0.037	0.034 ± 0.03	0.004	0.277	0.286 ± 0.03	0.010
Not heat treated	0.030	0.057	0.037			0.296		
Machined	0.023	0.036	0.027			0.231		
45°	0.028	0.038	0.034	0.033 ± 0.03	0.005	0.249	0.244 ± 0.03	0.011
Not heat treated	0.030	0.041	0.037			0.252		
Machined	0.024	0.037	0.030			0.201		
90°	0.026	0.037	0.031	0.032 ± 0.03	0.003	0.225	0.216 ± 0.03	0.013
Not heat treated	0.029	0.035	0.035			0.222		
Machined	0.031	0.081	0.038			0.336		
0°	0.039	0.047	0.048	0.043 ± 0.03	0.005	0.290	0.310 ± 0.03	0.023
Heat treated	0.036	0.041	0.043			0.306		
Machined	0.028	0.053	0.034			0.259		
45°	0.031	0.046	0.038	0.034 ± 0.03	0.004	0.253	0.267 ± 0.03	0.020
Heat treated	0.025	0.031	0.030			0.290		
Machined	0.023	0.028	0.028			0.261		
90°	0.029	0.034	0.036	0.033 ± 0.03	0.004	0.259	0.253 ± 0.03	0.013
Heat treated	0.028	0.031	0.034			0.238		
Porous	0.132	0.147	0.157			0.628		
0°	0.123	0.141	0.146	0.151 ± 0.03	0.006	0.636	0.632 ± 0.03	0.004
Not heat treated	0.125	0.145	0.149			0.632		
Porous	0.187	0.231	0.216			0.703		
45°	0.152	0.186	0.179	0.195 ± 0.03	0.019	0.698	0.698 ± 0.03	0.006
Not heat treated	0.163	0.179	0.191			0.691		
Porous	0.120	0.127	0.143			0.714		
90°	0.119	0.113	0.142	0.151 ± 0.03	0.015	0.648	0.686 ± 0.03	0.034
Not heat treated	0.142	0.163	0.168			0.695		
Porous	0.120	0.127	0.143			0.619		
0°	0.124	0.128	0.147	0.141 ± 0.03	0.008	0.623	0.619 ± 0.03	0.005
Heat treated	0.110	0.125	0.132			0.614		
Porous	0.184	0.198	0.213			0.702		
45°	0.170	0.206	0.199	0.201 ± 0.03	0.011	0.699	0.701 ± 0.03	0.002
Heat treated	0.164	0.197	0.192			0.700		
Porous	0.158	0.219	0.186			0.762		
90°	0.142	0.176	0.168	0.168 ± 0.03	0.018	0.644	0.704 ± 0.03	0.059
Heat treated	0.126	0.157	0.150			0.705		

10.3 Convection Specimen Hardware Overview

The following Table 10.3 contains all relevant data of the convection specimen, which is a vertically orientated flat plate mounted on the TVC cold plate.

Table 10.3: Parameters of the ITS PCM convection specimen, which was subject to thermal vacuum tests with the embedded paraffin hexadecane

Parameter PCM specimen	Characteristic values
Dimensions	200 x 190 x 11.5 mm
Wall thickness	ca. 0.75 mm
Dry mass (screws, seals and embedded lattice matrix)	504 g
PCM	Hexadecane ($C_{16}H_{34}$)
PCM mass	195 g
Total mass (screws, seals, embedded lattice matrix and PCM)	699 g
Lattice volume fraction	ca. 15.7%
Lattice cell size	6x6x6 mm
Strut diameter	0.75 mm
Mesh size	CQUAD4 with 5.0 mm
Inclination angles tested (0°: vertical orientation, Figure 6.11 left)	0°, 15°, 30°, 45°, 60°, 75°, 90°

10.4 Open Wall Window Specimen Hardware Overview

The Table 10.4 hereafter comprises the relevant data of the open wall window specimen, which is a vertically orientated flat plate. On one side there is no vertical wall fabricated so that one can look into the model and see the lattice and PCM-filled double-walled volume. A macrolon plate encapsulates the PCM chamber.

Table 10.4: Parameters of the ITS specimen flat plate in order to validate the thermal stability and to provide measurements for the sensitivity studies

Parameter PCM specimen	Characteristic values
Dimensions (HxWxD)	197 x 189 x 11.5 mm
Wall thickness	ca. 0.5 mm
Dry mass (screws, seals and embedded lattice matrix)	504 g
PCM	Hexadecane ($C_{16}H_{34}$)
PCM mass	166 g
Total mass (screws, seals, embedded lattice matrix and PCM)	670 g
Lattice volume fraction	ca. 15.7%
Lattice cell size	6x6x6 mm
Strut diameter	0.75 mm

10.5 Model Cycle Stability Specimen Hardware Overview

This chapter contains the technical data of the specimen used to test and further validate the model cycle stability of the ITS technology related on interrupted and completed phase change cycles.

Table 10.5: Parameters of the ITS open wall window specimen in order to verify the macroscopic PCM melting behaviour and the melting fronts by optical (visible and IR) recordings

Parameter PCM specimen	Characteristic values
Dimensions (HxWxD)	160 x 190 x 15 mm
Wall thickness	ca. 0.75 mm
Dry mass (screws, seals and embedded lattice matrix)	1200 g
PCM	Hexadecane ($C_{16}H_{34}$)
PCM mass	131.5 g
Volume PCM void space (entire macro-encapsulation)	120 x 150 x 10 mm
Total mass (screws, seals, embedded lattice matrix and PCM)	1331.5 g
Lattice volume fraction	ca. 17.6%
Lattice cell size	6x6x6 mm
Strut diameter	0.75 mm
Thickness macrolon plate	10 mm
Cold plat temperature for cooling	const. -5°C
Total heater power	const. 20 W

10.6 Measurement Results of the Model Cycle Stability Specimen

Table 10.6: Cyclical stability thermal test setup and test results of the large-scale specimen flat plate

Cyclical stability tests	Values
Cold plate temperature	const. 10°C
Heater power	const. 10 W
Heating time / cooling time	60 min / 60 min
Cycle period	120 min
Minimal temperature w/o PCM	12.3°C
Maximal temperature w/o PCM	30.7°C
Minimal temperature with PCM	17.3°C
Maximal temperature with PCM	27.3°C
Temperature span reduction due to PCM (peak-peak)	-45.6% / -8.4K
Cycle stability (maximal deviation)	± 0.3 K

Table 10.7: Thermal mapping results in order to derive the mesh size sensitivity of the ITS thermal models in relation of the PCM embedded

Mesh size [mm]	Mean temperature deviation [K]	Max. temperature deviation [K]
24	1.8	2.4
12	1.0	1.9
6	0.7	1.9
3	0.7	1.8

10.7 Multiple PCM Cylinder Specimen Hardware Overview

Table 10.8: Parameters of the ITS cylinder specimen in order to validate the thermal stability and the PCM subroutine capability to consider multiple PCMs within one component

Parameter PCM specimen	Characteristic values
Dimensions (HxWxD)	198 x 115 x 115 mm
Wall thickness	ca. 0.5 mm
Dry mass (screws, seals and embedded lattice matrix)	879 g
PCM	Hexadecane ($C_{16}H_{34}$)
Total PCM mass	326.5 g
PCM mass tetradecane ($C_{14}H_{30}$) / melting point: 6°C	78.5 g
PCM mass hexadecane ($C_{16}H_{34}$) / melting point: 18.2°C	82.0 g
PCM mass octadecane ($C_{18}H_{38}$) / melting point: 28.3°C	82.5 g
PCM mass eicosane ($C_{20}H_{42}$) / melting point: 36.5°C	83.5 g
Total mass (screws, seals, embedded lattice matrix and PCM)	1201 g
Lattice volume fraction	ca. 15.7%
Lattice cell size	6x6x6 mm
Strut diameter	0.75 mm
Cold plate temperature	const. -5°C

10.8 Temperature Dependent Material Properties Overview

Table 10.9: Temperature dependent properties, which are subject to sensitivity analyses, based on a review of Velez et al. [VEL-15]

Temperature dependent property	Sensitivity
Thermal conductivity	▪ Variation with temperature ▪ Shift between phase states
Latent heat of fusion	▪ Different values for solid and liquid state
Specific heat capacity	▪ Different values for solid and liquid state ▪ Overall temperature dependent formulation
Density variation	▪ Variation with temperature ▪ At increasing density the compressibility decreases

10.9 ITS Demonstrator Use Case Studies Overview

Table 10.10: Use case trade-off matrix with potential subsystem applications and use cases (vertical) in relation to weighted system specifications (horizontal), in order to derive the highest potential use case for the assessment of the final ITS demonstrator [WIL-23]

Potential use cases related on system specifications and properties	Increase in relative stiffness	Reduced energy consumption	Additional relative system mass	Additional relative installation space	Integration of functions and interfaces	Higher performance (thermal and mechanical)	Reduction of the integration effort	Complex geometry	Verification and validation effort	Cost reduction	Reduction of the delivery time	Impact on missions	Economic use	Further development of technology maturity	**Score total potential**
Radiator panel with integrated heat pipes	1	5	1	5	3	3	1	3	3	1	1	3	1	1	**32**
Active phased array antenna	1	3	1	3	1	1	1	3	3	1	1	3	3	1	**26**
Heat pipes	3	1	5	3	3	3	3	1	3	1	1	3	3	5	**38**
Optical bench	5	3	3	3	5	3	3	5	1	5	3	3	3	3	**48**
Optical baffle system	5	3	5	5	5	5	5	5	1	5	3	5	3	3	**58**
Laser communication terminal (LCT)	3	3	3	3	5	5	5	5	1	3	3	5	3	5	**52**
Electronic box, battery housing	3	3	3	5	5	5	3	5	3	3	3	5	5	5	**56**

The specifications are weighted by factors in dependence on the strongest impact respectively demand on the use case. The major arguments and decision drivers are the call of achievable thermal performance enhancement, mission impact and scientific added value of a potential component, by using the ITS technology.

The increase in stiffness of a component by ITS integral structures can be attributed to the high Steiner fraction, which is due to the double-wall design with the intermediate lattice.

In addition, it is assumed that the additional relative mass needed for the implementation of the ITS design is not high or even in combination with topology optimisations (which are not part of this work) or further modifications can lead to a reduction of the system mass compared to a conventional design.

Another important potential is the joining of interfaces by combining individual components and add-on parts to one additive manufactured monolithic structure from one cast, for reducing the integration effort of an ITS component in space systems.

On the other side, with the implementation of the ITS technology additional or extended verification and validation processes are required according to ECSS. This validation effort also includes ensuring and testing the additively manufactured structure for defects and structural integrity. In addition, the vacuum-tightness of the PCM chambers shall be confirmed beyond doubt. For this, it is necessary that the sealing of the PCM chambers can be permanently ensured with a high degree of reliability.

10.10 ITS Demonstrator Thermal Interfaces Definition

It can be seen from Figure 10.1, that the optics of the instrument are protected (as usually) by a baffle system, which is an external solar baffle against incident solar radiation. The optical bench is located underneath the IRS baffle structure. The mirrors are only positioned and attached to the optical bench at each end of the baffles, to deflect the beam. However, neither electronic components nor mirrors are taken into account for the redesign of the ITS demonstrator, but only the inner baffle assembly structure as depicted on the right side in Figure 7.1. [WIL-23]

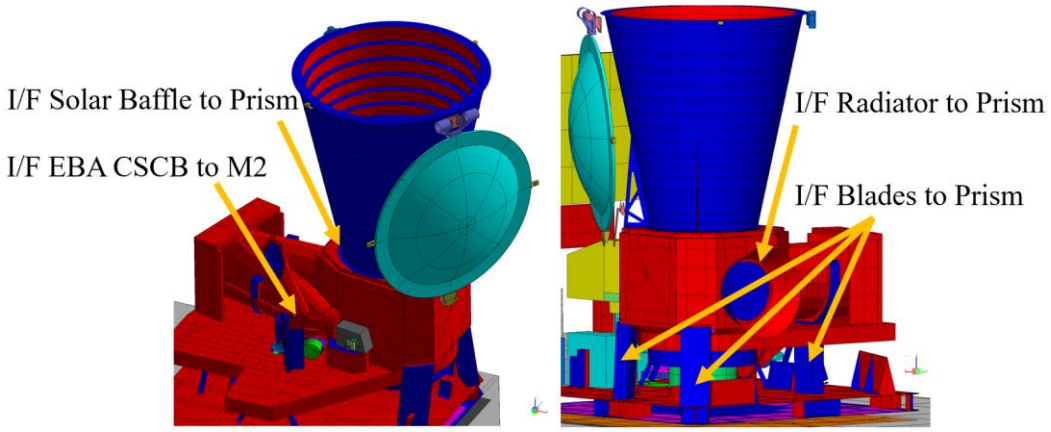

Figure 10.1: Thermal model view on the EBA and the IRS instrument, which is accommodated on the baseplate by plades, together with all relevant interfaces and assembled parts [OHB-19]

The interfaces to which the inner baffle assembly is interconnected are also defined in Figure 10.1. The basis for the definition of the test scenarios and cases are the EQ and D56 hot cases. The underlying data were taken from the thermal report [TRI-15]. The hot cases EQ and D56 are analysed to determine the solar load profile (total solar heat source QS) and the interface heat flows of the inner baffle assembly. The solar radiation of three consecutive orbits around D56 and EQ are therefore analysed from the MTG thermal model, those temperature profiles are shown in chapter 10.15. [TRI-15]

Ongoing, all results and findings from the ITS research project to date are incorporated into the implementation of the demonstrator thermal model design. Moreover, the large number of TVC thermal balance tests, cycling tests and material characterisation measurements of the specimen test series provide an initial baseline for thermal model validation and correlation of the demonstrator hardware.

As Gräbener et al. in [JOS-01] and [BER-19] already mentioned in a preliminary ITS study, the cumulative solar heat flow shall be determined by deriving the solar energy, which is absorbed by the surfaces of the EBA structure. Thinking further and more differentiated to capture the heat flows in the entirety of the baffle system, it is necessary to cut the MTG EBA submodel free at all interfaces.

The following Figure 10.2 visualizes the interfaces (yellow shells) where external parts are removed and the model has therefore been cut free, in order to extract only the inner baffle assembly structure. For a better understanding of the interface layout, recap to Figure 10.1, which depicts the original MTG instrument thermal model with all attachments and parts.

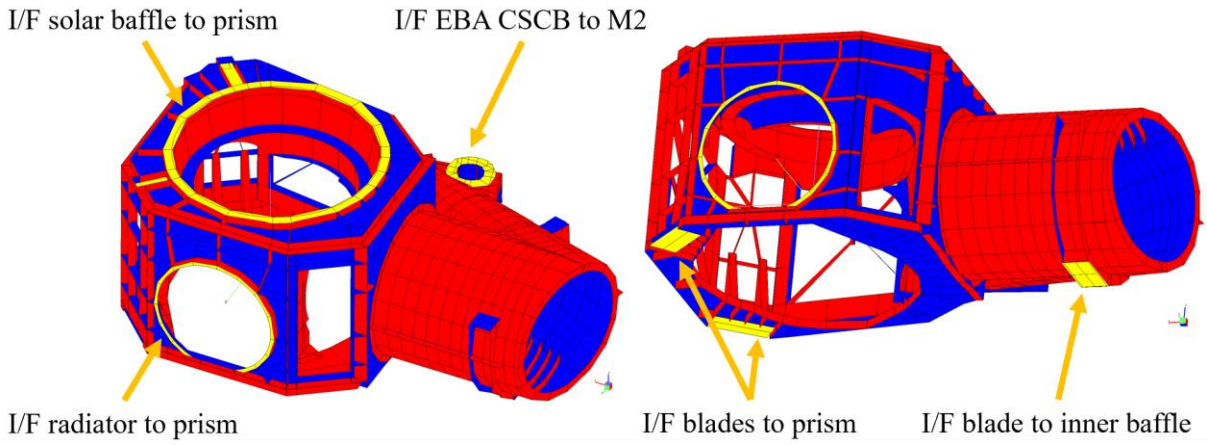

Figure 10.2: Free cut conductive interfaces (yellow shells) to account, additionally to the solar irradiation (QS), the complete heat flow paths between the assembly parts of the MTG EBA design

The thermal interfaces are prepared in more details in their balance limits in relation on the MTG model in the appendix located in chapter 10.18. In addition the resulting heat flow profiles, which pass through the interface paths are depicted in Figure 10.16 and Figure 10.17 for the orbit cases D56 and EQ.

The cooling behaviour between the MTG model and the unfilled ITS demonstrator (without PCM) fundamentally differ from each other, related on the conductive and radiative coupling of the ITS redesign compared to the MTG baffle assembly. All inner and outer sides of the MTG baffle assembly, except the optical path, are covered with MLI. The same MLI setup also applies to the ITS demonstrator.

The baffle structure of the MTG model is conductively coupled to the base plate via titanium plades in the satellite. The temperature of the base plate varies in the course of the orbit. The scaled and modified ITS demonstrator, on the other hand, is coupled to the TVC cold plate by highly conductive aluminium GSE adapters. The cold plate is kept at almost constant temperature.

Furthermore the assembly parts solar baffle, prism radiator and CSCB baffle of the MTG model (refer Figure 10.5) provide at certain orbit times cooling of the baffle structure (refer Figure 10.18 and Figure 10.19), as these parts partially radiate heat into space as secondary radiators. This behaviour is not possible with the ITS demonstrator in the TVC setup, as these components are not present in the ITS design. The only reasonable cooling path for the ITS demonstrator exists via the GSE adapters to the cold plate of the TVC. The TVC cold plate is cooled by circulation-pumped silicone oil.

10.11 ITS Demonstrator Redesign for Manufacturing, Assembly and Integration

The AIT process of the demonstrator is related to the volume constraints of the TVC. As Gräbener et al. in [JOS-01] and [BER-19] already mentioned in a preliminary ITS study, it is necessary to scale the demonstrator geometry in the first instance. To continue this process, it is necessary to define steps for model preparation, conversion, fabrication and post-processing on the way to the final ITS demonstrator. The following Figure 10.3 depicts the two parts prism and inner baffle, which when assembled result in the inner baffle assembly. In turn the inner baffle and prism parts of the original MTG model are each assembled by numbers of small parts and attachments. The Figure 10.4 depicts the ITS demonstrator redesign CAD model, which can be additively manufactured.

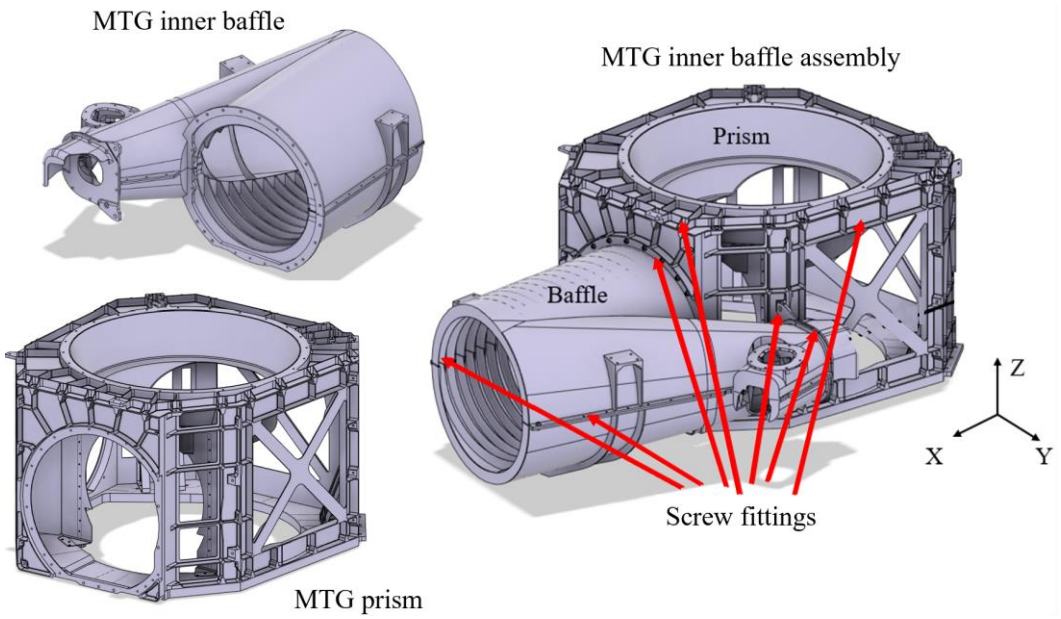

Figure 10.3: Original MTG IRS baffle assembly with the submodels inner baffle and prism. The submodels prism and inner baffle consist of various individual and small parts and are joined by screwed and riveted connections each [WIL-23]; [OHB-19]

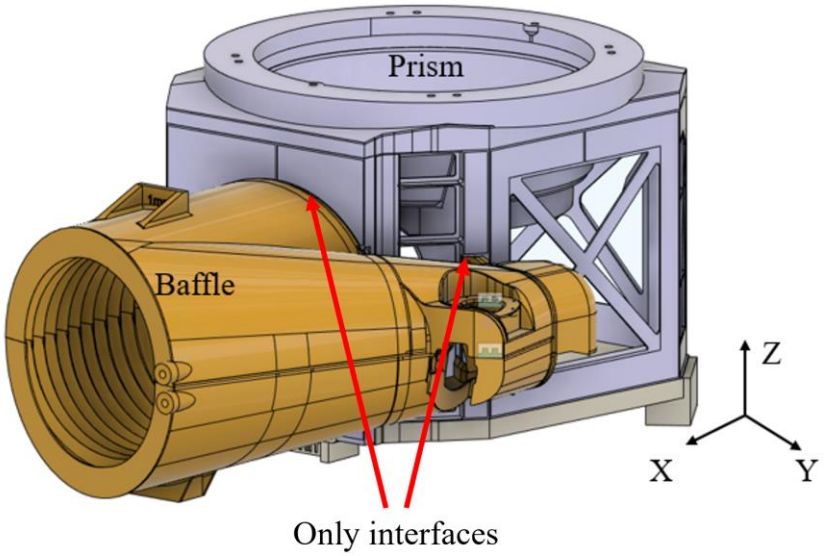

Figure 10.4: ITS demonstrator redesign CAD model, which is additive manufacturable [WIL-23]

10.12 Demonstrator Structure Geometry Scaling and Modification

The largest additive manufacturing system at the FH Aachen can provide a maximum effective construction space for monolithic built parts of ca. 720 x 320 x 450 mm. In order to meet the requirement for the maximum effective construction space, the inner baffle assembly had to be scaled down on a scale of 1:3, based on the ESATAN erg model data of [OHB-19]. The thermal model scaling, transformation and redesign process is schematically visualised in Figure 10.5.

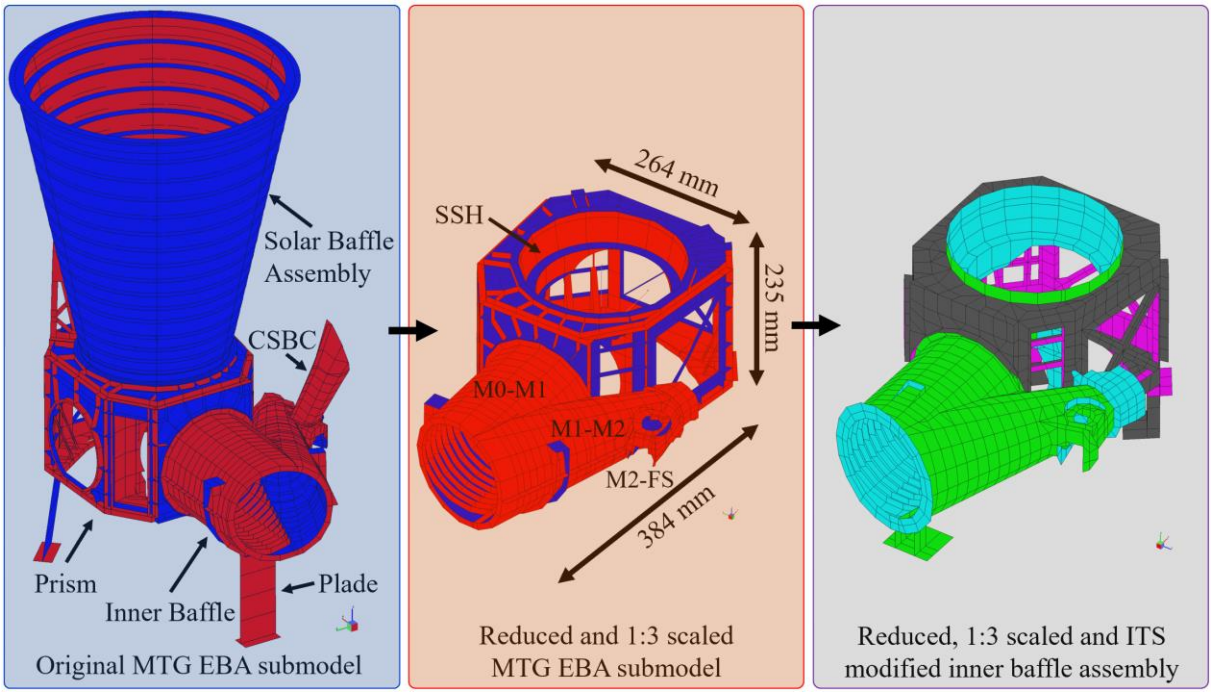

Figure 10.5: Thermal model scaling, transformation and redesign process of the ITS demonstrator. The bassline is provided by the original MTG EBA submodel (left), from which the reduced and 1:3 scaled IRS model (middle) is generated, which in turn has been the baseline of the modified ITS demonstrator (right)

According to Triebig et al. [TRI-15], Elguea et al. [ELG-16] and Soler et al. [SOL-16] the inner baffle submodel consists of three partial baffles joined together. These three partial baffles are named by the mirror designations at the interfaces: M0-M1, M1-M2 and M2-FS. The plades accommodate the baffle assembly to a honeycomb base plate, which is not shown in Figure 10.5. The sun shield (SSH) in the aperture area is a part of the prism and protects the instrument from direct sun intrusion by absorbing parts of the solar radiation. [WIL-23]

In the course of the ITS redesign, further adaptions were necessary for the scalability. The (a) inner baffle assembly supports plades, (b) the solar baffle assembly and (c) the CSBC baffle assembly were removed. This is because even when scaled down, the solar baffle assembly and the CSBC assembly are far too large for additive manufacturing and for the subsequent thermal testing in the available TVC.

For the model down scaling the centre of mass (COM) of the inner baffle assembly is derived considering all points, which define the FDM thermal node corner points. Ongoing the distances (vector lengths) of each point to the common COM are calculated. Finally, the shells of the inner baffle assembly are rearranged and thus scaled down along the direction vector by a factor of three.

10.13 Demonstrator Additive Manufacturing

As described in more details in chapter 5, all monolithic ITS integral specimens and the functionally adapted demonstrator are manufactured by additive manufacturing on the GE Concept Laser X-Line 2000R manufacturing system. The main advantage of this manufacturing system is that it had the largest available manufacturing space on the market at the time of the ITS project. This enables the simultaneous production of the demonstrator submodels inner baffle and prism on the same carrier plate. All ITS parts are made from the CL32AL DIN-EN-1706 AlSi10Mg alloy. The raw material of the aluminium alloy is available in powder form and is remelted during manufacturing through a LBPF process. [CON-02]

The following Figure 10.6 shows the demonstrator submodels as printed with the process relevant support structures, which will be removed in subsequent processing steps. The support structures are generated by using the software Magics. [WIL-23]

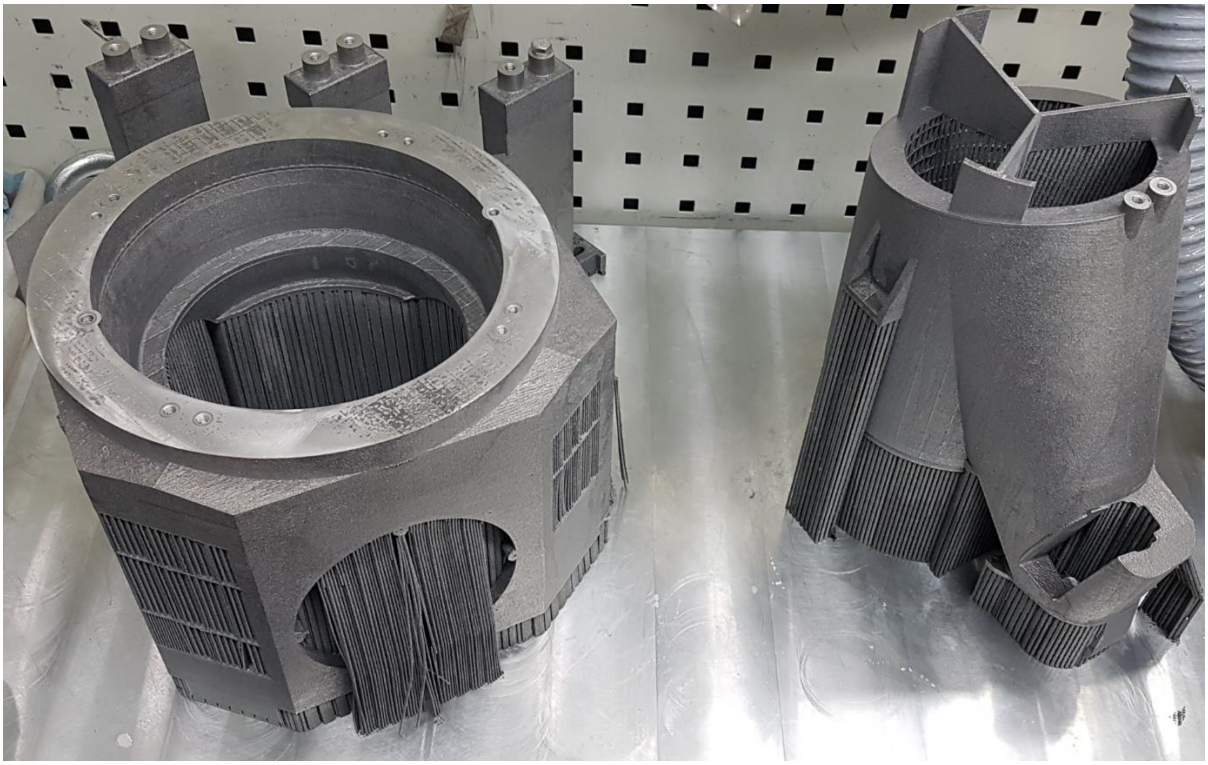

Figure 10.6: Additive manufactured ITS demonstrator submodels prism (left) and inner baffle (right) as-printed with the process relevant support structures, all still attached to the carrier plate [WIL-23]

In general, when positioning and aligning the components to be manufactured on the carrier plate in the CAD model, it is important to ensure that as few overhangs (mandatory > 45°) and support structures as possible must be used. This reduces the required time of the downstream post-processing and finishing steps considerably. As a general rule, support structures should ideally be placed in areas that require machining anyway. [WIL-23]

The mechanical interfaces and surface properties on the contact surfaces at the interface planes could only be achieved through precision machining. Additive manufacturing processes do not have the resolution and precision needed to produce the optical vanes and surfaces directly through additive manufacturing (as-printed) without the need for post-machining (as-finished). Mechanical post-processing of the interface surface is therefore essential, as this is the only way to ensure an adequate level of thermal conductance for proportional modelling. [WIL-23]

Concluding, in the following Figure 10.7 the reworked inner baffle and prism submodels of the ITS demonstrator are shown as finished. In direct comparison to the original MTG design in Figure 10.3, the differences of the ITS redesign are clearly recognizable. The assembly of the ITS demonstrator takes place via the prism MX panel flange interface and the inner baffle PX flange ring interface. The submodels are assembled by 17 x M3 (metric) stainless steel screws. The screws used for the accommodation of the thermal GSE adapters are M5x12 stainless steel screws. [WIL-23]

For the interface between the prism and the inner baffle assembly, a thermal filler had been used to counteract process deviations and roughness. This thermal filler is of type Laird TPLI 240 gap filler A10096-02 with an approximated conductance of 5000 W/m²K.

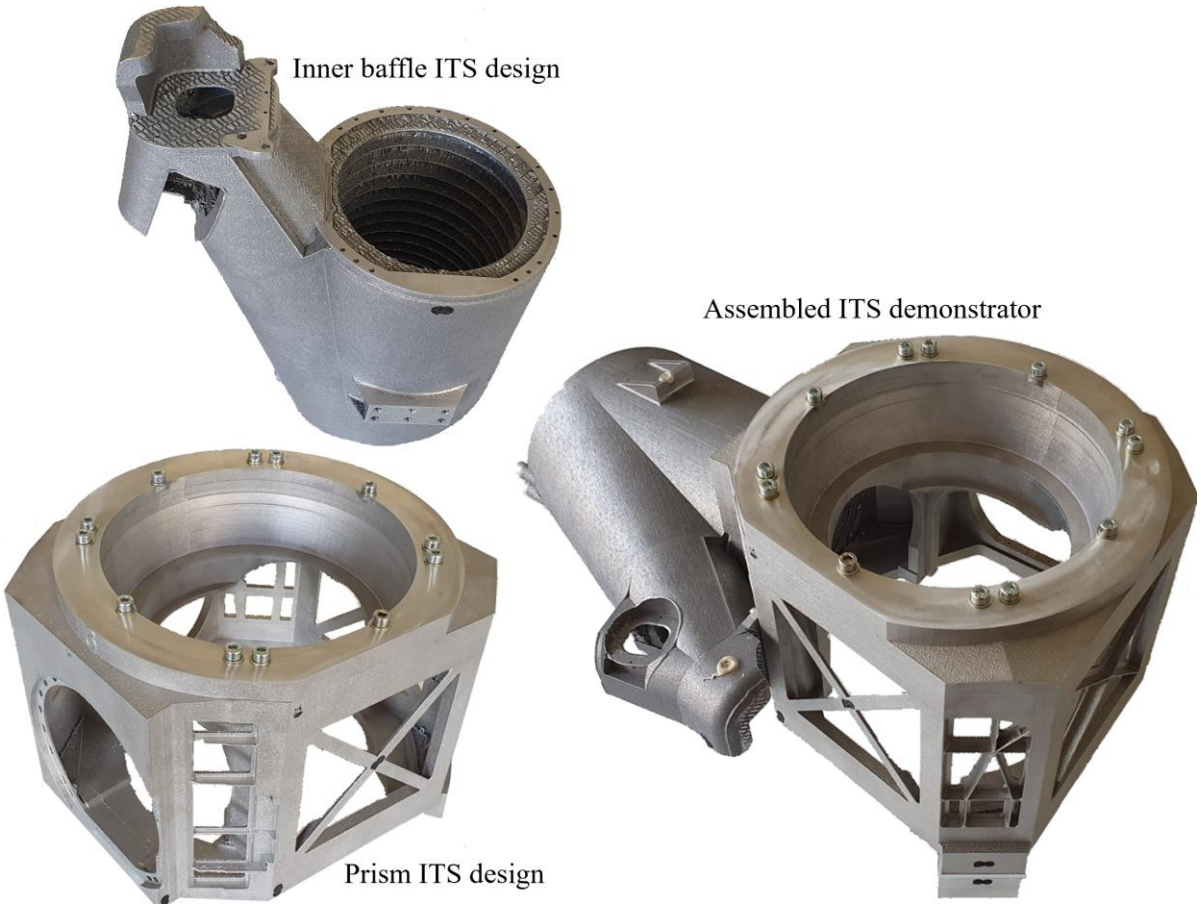

Figure 10.7: ITS demonstrator in scale 1:3 (right) with thermal GSE adapter, which is assembled by the monolithic additively manufactured integral parts prism (left, down) and the inner baffle (left, up) [WIL-23]

The lattice structures, which are embedded in the ITS demonstrator are generated with Autodesk Netfabb 2019. In the following Figure 10.8 and Figure 10.9, the PCM bodies are shown schematically on the left side. Respectively the right side depicts the generated lattice bodies. [WIL-23]

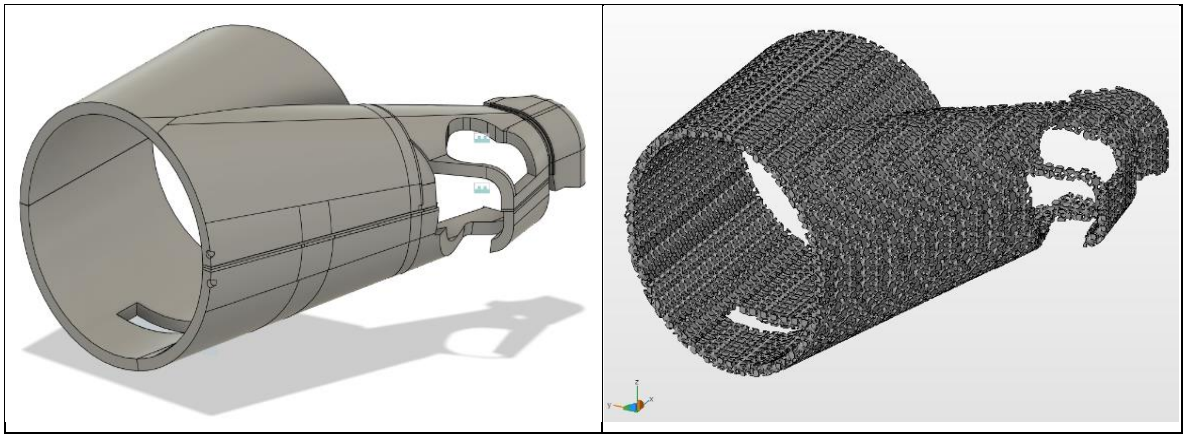

Figure 10.8: Schematic view of the monolithic CAD PCM body (left) and the lattice body (right) of the inner baffle submodel [WIL-23]

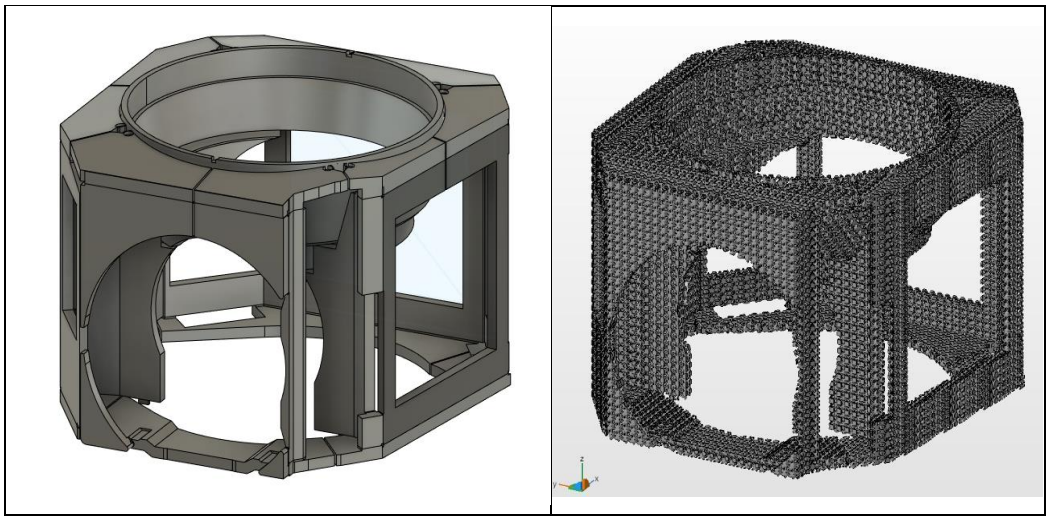

Figure 10.9: Schematic view of the CAD PCM body (left) and the lattice body (right) of the prism submodel [WIL-23]

The inner baffle was modelled in CAD from only one continuous PCM body. The prism submodel on the other hand was modelled of five separated PCM bodies. The reason is that the prism geometry exhibits sharp edges and steep transitions with strongly varying thicknesses, which do not allow a contiguous lattice body and is further not practicable fillable with PCM. In general one ITS design goal is to distribute the required PCM mass over large areas to lower the required PCM layer thickness in order to achieve a more rapid heat input into the PCM mass over a larger area. [WIL-23]

10.14 Overview of the Demonstrator Mass Distribution

The inner baffle part has one single continuous PCM body, while the PCM body of the prism part consists of five encapsulated partial volumes entirely, which are highlighted in different colours. The complex geometry of the prism in combination with sharp edges and multiple transitions prevent to implement only one continuous PCM body, which can then be reliably filled through one specific inlet.

PCM distribution and chamber of submodel inner baffle	Inner baffle part
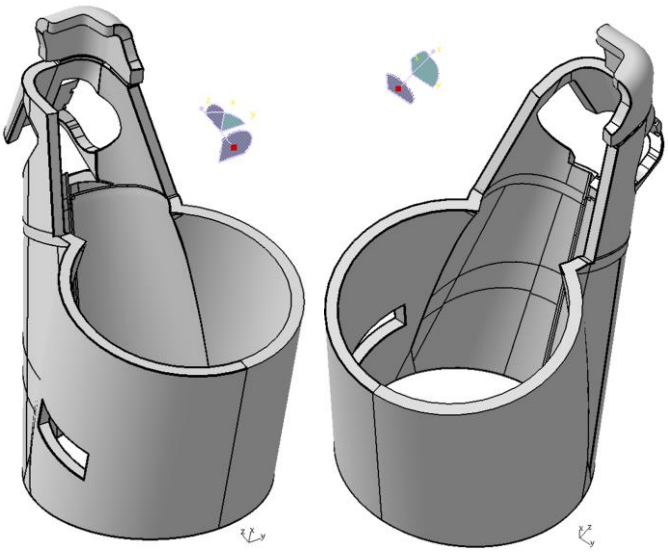	

Figure 10.10: Overview of the geometry sections (right) and the corresponding large contiguous PCM body (left) of the submodel inner baffle

PCM distribution and chambers of submodel prism	Prism part
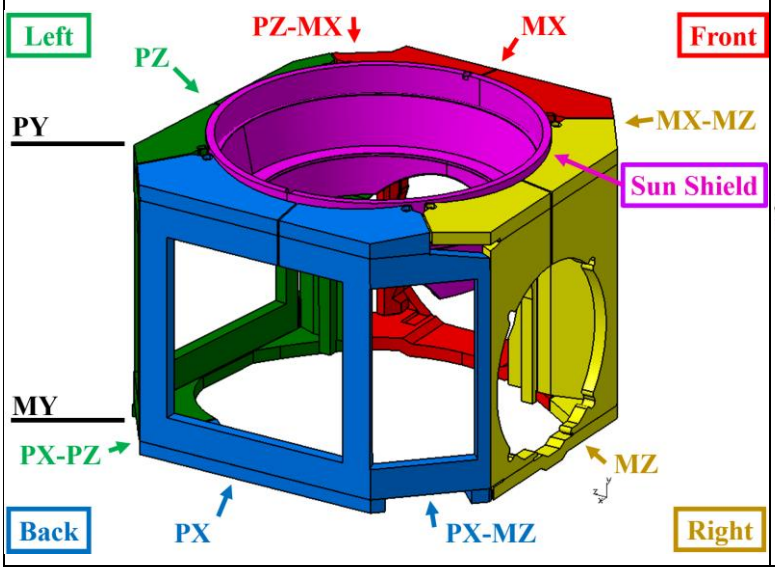	

Figure 10.11: Overview of the geometry sections (right) and the corresponding coloured five PCM bodies (left) of the submodel prism, which are encapsulated from each other due to the complexity of the prism geometry

10.15 MTG Temperature Profiles

This chapter contains the cumulative plots of the original MTG inner baffle assembly temperature profiles for the hot cases EQ and D56 over the relevant orbits.

10.15.1 D56 Hot Case

It can be seen in the Figure 10.12 below, as described in chapter 7.3, that the hot case D56 is the case with the highest extreme temperatures.

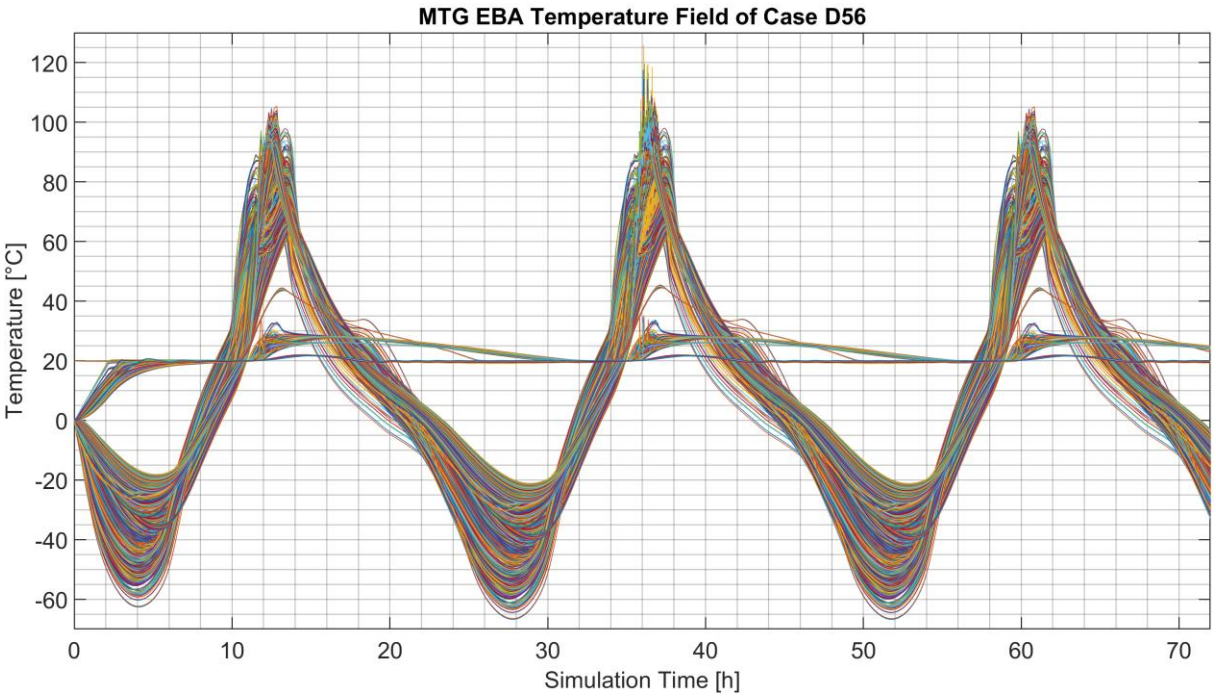

Figure 10.12: Overall overview of the temperature curves including all thermal nodes and those temperature curves of the EBA structure of case D56 [TRI-15]; [OHB-19]

10.15.2 EQ Hot Case

In contrast to the hot case D56, the second hot case EQ has the highest temperature instabilities (gradients). The following Figure 10.13 depicts the cumulative temperature profiles of the inner baffle assembly structure in case EQ.

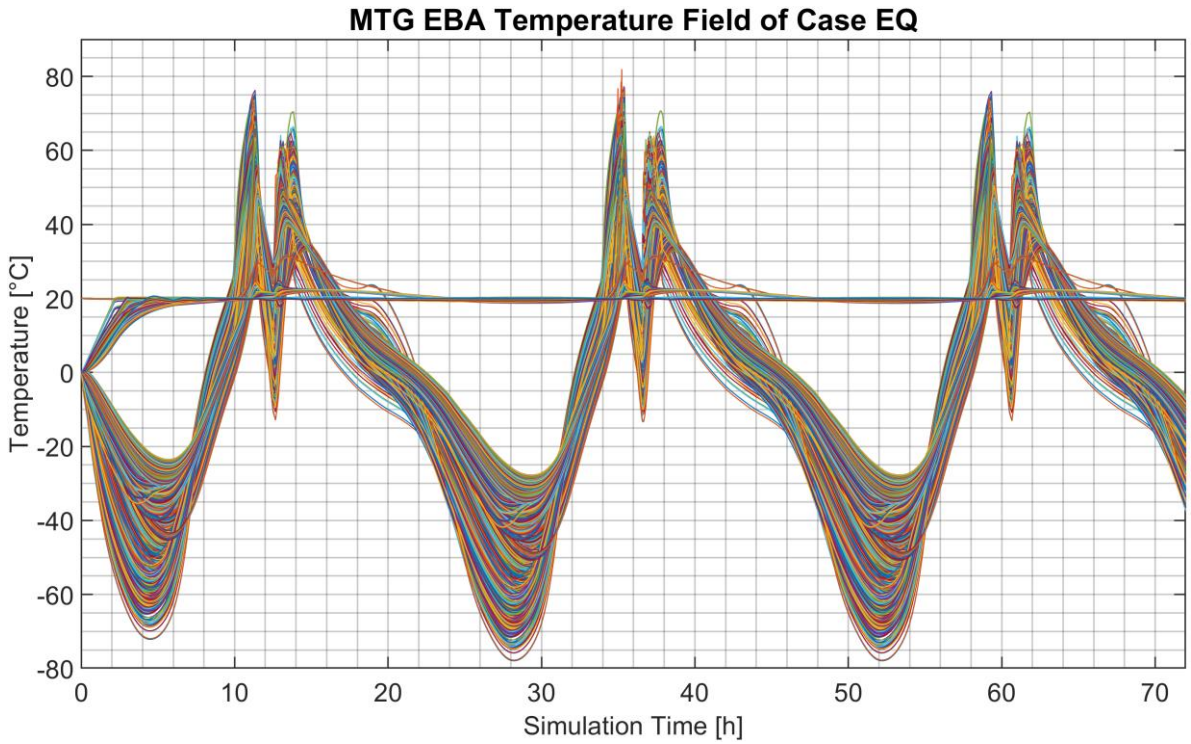

Figure 10.13: Overall overview of the temperature profiles including all thermal nodes and those temperature curves of the EBA structure for the case EQ [TRI-15]; [OHB-19]

10.16 ITS Demonstrator Hardware Overview

The following tables summarise the relevant data of the as-finished demonstrator submodels, which are used for the thermal simulations and tests of the final ITS validation campaigns.

Table 10.11: Parameters of the ITS demonstrator inner baffle submodel, in order to validate the achievable thermal stability and performance due to the ITS technology

Parameter inner baffle submodel	Characteristic values
Dimensions (HxWxD)	244 x 190 x 218 mm
Wall thickness	ca. 1.0 mm
Dry mass (without screws and adapter, with embedded lattice matrix)	1189 g
PCM	Hexadecane ($C_{16}H_{34}$)
PCM mass	182 g
Total mass (screws, seals, embedded lattice matrix and PCM)	1376 g
Lattice volume fraction	ca. 29.4%
Lattice cell size	6x6x6 mm
Strut diameter	1.0 mm

Table 10.12: Parameters of the ITS demonstrator prism submodel, in order to validate the achievable thermal stability and performance due to the ITS technology

Parameter prism submodel	Characteristic values
Dimensions (HxWxD)	235 x 225 x 211 mm
Wall thickness	ca. 1.0 mm
Dry mass (without screws and adapter, with embedded lattice matrix)	2234 g
PCM	Hexadecane ($C_{16}H_{34}$)
PCM mass	484.2 g
Total mass (screws, seals, embedded lattice matrix and PCM)	2778.5 g
Lattice volume fraction	ca. 17.9%
Lattice cell size	6x6x6 mm
Strut diameter	0.75 mm

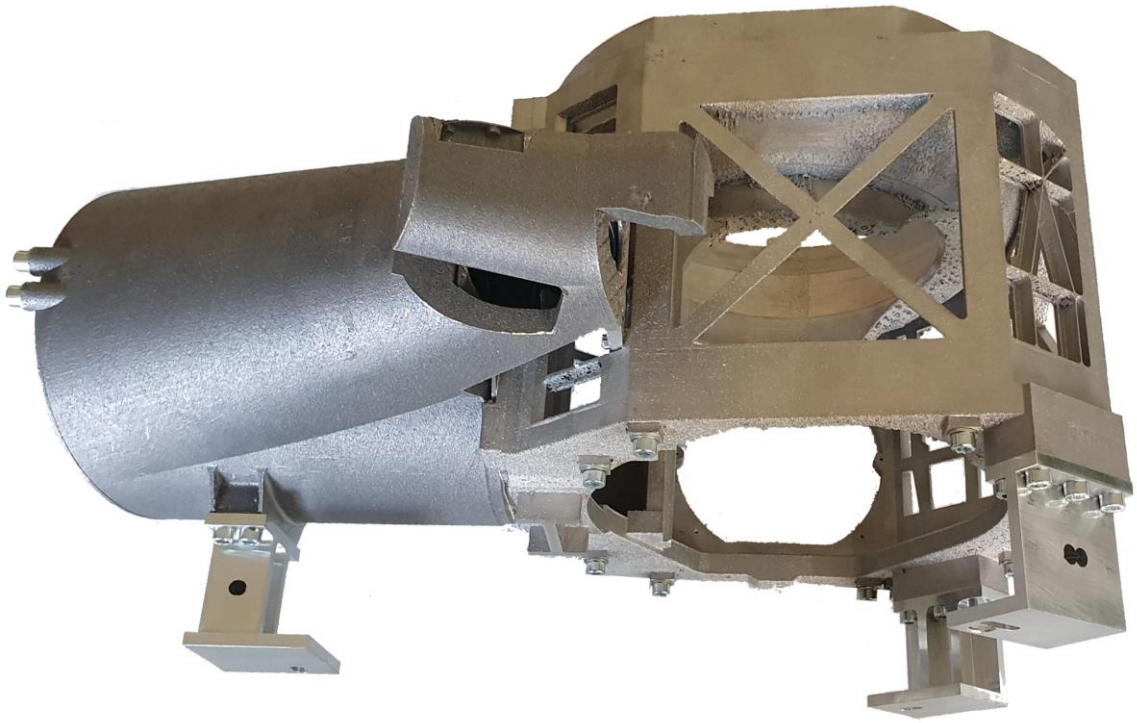

Figure 10.14: ITS demonstrator assembly, which consists of the inner baffle and the prism submodels, with mounted thermal aluminium GSE adapters for nominal test operations in the TVC [WIL-23]

Table 10.13: Parameters of the ITS demonstrator assembly in order to validate the thermal stability and performance

Parameter of the ITS demonstrator assembly	Characteristic values
Dimensions (LxWxH) without GSE adapters	384 x 264 x 235 mm
Dry mass (with screws, with interface screws, without GSE adapter)	3497.5 g
PCM	Hexadecane ($C_{16}H_{34}$)
Total PCM mass	667.5 g
Theoretical total lattice mass	842.9 g
Total mass (with lattice, with PCM, with screws, with GSE adapter)	4427.5 g

10.17 ITS Demonstrator Thermal Model Overview

This chapter contains the data and thermal model overview of the ITS demonstrator. As mentioned, the ITS demonstrator thermal model consists of the submodels prism and inner baffle.

10.17.1 Demonstrator Submodels

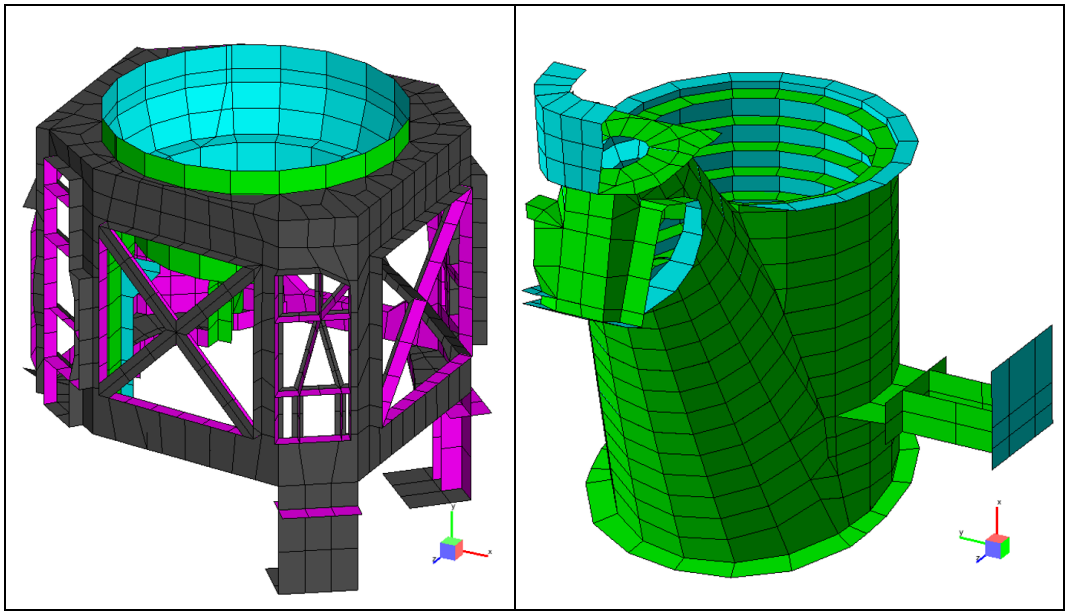

Figure 10.15: Overview of the thermal submodels prism (left) and inner baffle (right) of the ITS demonstrator thermal model [WIL-23]

10.17.2 Bulk and Thermo-Optical Material Properties Summary

The following Table 10.14 and Table 10.15 summarise the materials applied for the TVC environment and the ITS demonstrator. The material data include the bulk and thermo-optical properties.

Table 10.14: Overview of the applied materials and the corresponding bulk properties at ca. 20°C, used for the TVC as well as for the ITS demonstrator structure and GSE [WIL-23]

Material	Part/function	Density [kg/m³]	Specific heat capacity [J/kgK]	Thermal conductivity [W/mK]
AW-6082	GSE adapter	2710.0	900.0	167.0
MLI	Radiative cover	0.0	0.0	0.01
AlSi10Mg	With heat treatment	2698.0	902.0	165.0
AlSi10Mg	w/o heat treatment	2698.0	897.0	150.0
PCM C16	Thermal control	772.9	2110.0	0.15
Aluminium	TVC cold plate	2712.0	910.0	237.0
Stainless steel	TVC recipient	7850.0	477.0	50.0
Glass	TVC sight glass	3000.0	800.0	1.5

Table 10.15: Overview of the applied materials and the corresponding thermo-optical properties, used for the TVC tests as well as for the ITS demonstrator structure and GSE [WIL-23]

Optical property [-]	Material					
	AW-6082	MLI	AlSi10Mg	Aluminium	Stainless steel	Glass
IR emissivity	0.86	0.78	0.127	0.11	0.2	0.91
IR reflectivity	0.14	0.22	0.873	0.89	0.8	0.09
IR transmissivity	0.0	0.0	0.0	0.0	0.0	0.0
Solar absorbance	0.9	0.46	0.632	0.4	0.4	0.13
Solar reflectance	0.1	0.54	0.368	0.6	0.368	0.0
Solar transmissivity	0.0	0.0	0.0	0.0	0.0	0.85
IR spectral reflectivity	0.0	0.0	0.0	0.0	0.0	0.0
Solar spectral reflectivity	0.0	0.0	0.0	0.0	0.0	0.2

10.17.3 Demonstrator Thermal Model Nodes Summary

The following Table 10.16 summarises and lists the submodel dependent total number of thermal nodes used to generate the ITS demonstrator thermal model, including the corresponding PCM nodes of the submodels.

Table 10.16: Overview and summary of the total number of thermal nodes for both submodels prism and inner baffle including all PCM nodes, which all consist in the ITS demonstrator thermal model

Submodels	Total number thermal nodes	Of which PCM nodes
TVC	35	0
Prism	2847	656
Inner baffle	2004	439
Total	4886	1103

10.18 ITS Demonstrator Thermal Interfaces Detailed Overview

10.18.1 Definition of Conductive Interfaces and Radiative Shielding

Figure 10.16 shows the heat flow paths of the conductive interfaces cut free, which result from the omission of the solar baffle, CSCB baffle and the base plate parts. Also the radiative shielding of the MLI is shown. Only the aluminium adapters are not wrapped in MLI.

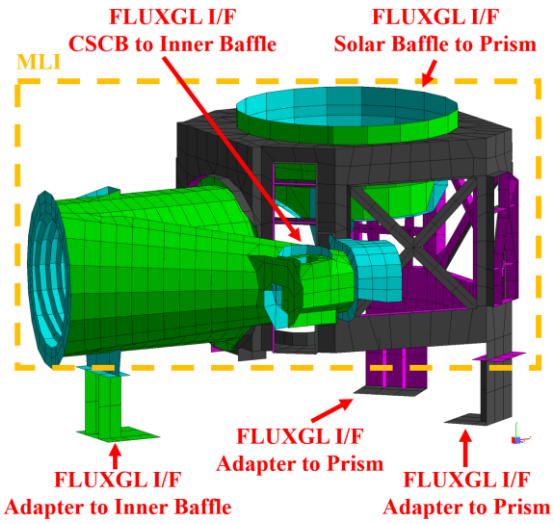

Figure 10.16: Definition of the thermal conductive interfaces from free cutting, in order to derive among others the conductive (FLUXGL) heat flow paths applied to the ITS redesign

Figure 10.17 on the other hand, contains an overall view of the cumulative conductive (*FLUXGL*), radiative (*FLUXGR*) and total (*FLUXGT*) heat flow paths related on the ITS demonstrator assembly. These boundaries are essential for the scaling to derive the capacitance ratio and further the PCM mass.

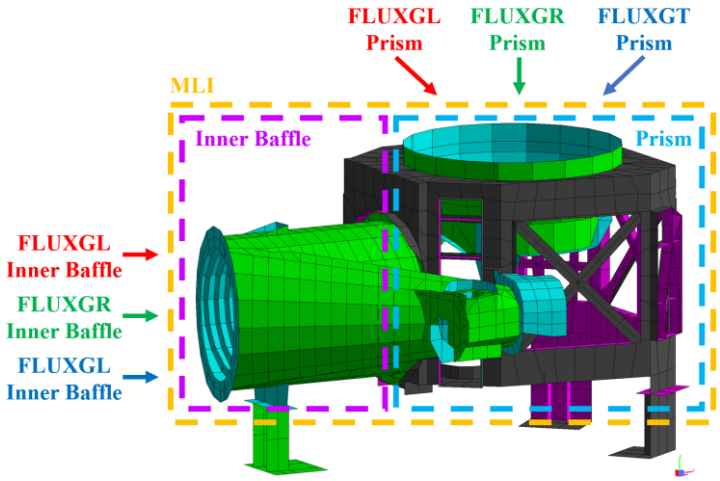

Figure 10.17: Definition of the thermal boundaries, in order to derive the cumulative conductive (FLUXGL), radiative (FLUXGR) and total (FLUXGT) heat flow paths on the submodel level prism and inner baffle

The occurring radiative and conductive heat flows of the MTG model in the relevant hot cases D56 and EQ are analysed to obtain an equivalent scaled heat load profile for the ITS demonstrator.

10.18.2 Overview of the Interfacial Heat Flow Profiles

The heat flow profiles depicted in the figures below are related on the interfacial definitions from Figure 10.17. This determines the proportional heat flow path and the cumulative net heat flow, which enters the interface zones and thus the relevant submodels prism and inner baffle in order to balancing the net heat. The results of the conductive (*FLUXGL*), radiative (*FLUXGR*) and total (*FLUXGT*) heat flow analyses from the MTG thermal model D56 hot case are summarised in the Figure 10.18. Whereas the heat flow analyses results of the hot case EQ are depicted in Figure 10.19.

By definition in ESATAN, a positive heat flow is considered to be incoming and thus heating the thermal node group. A negative heat flow cools the thermal node within the thermal boundaries.

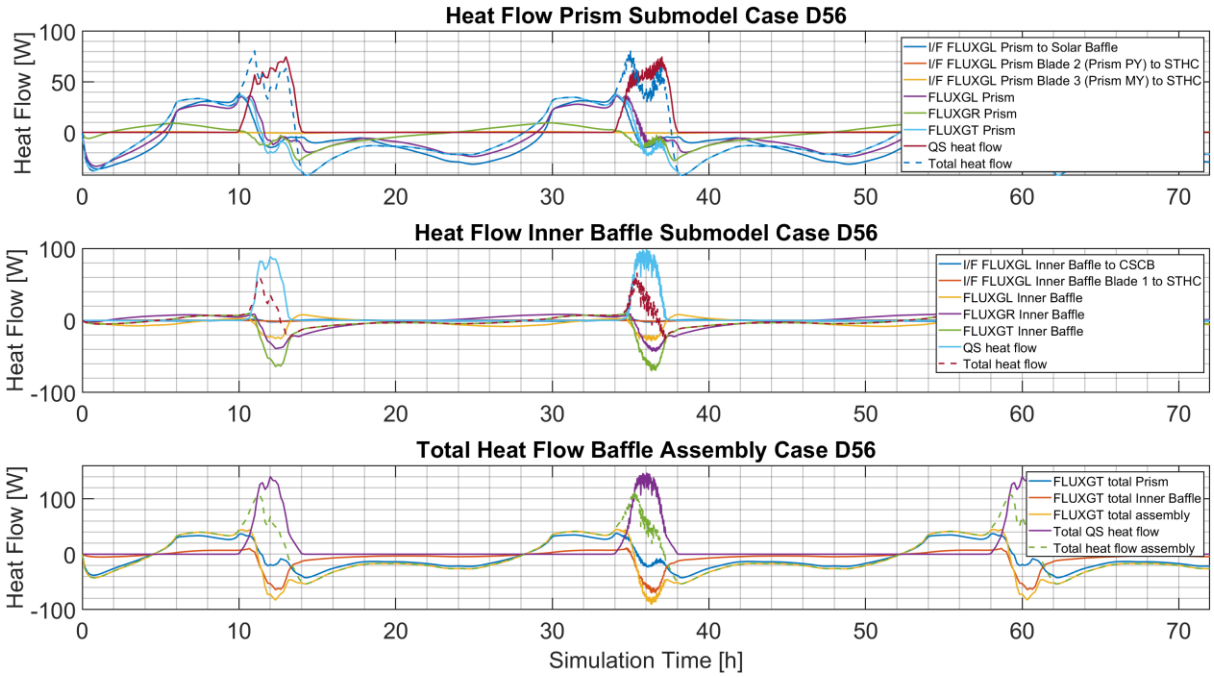

Figure 10.18: Energy balance of the original MTG EBA submodel with cut interfaces for the determination of the time-dependent heating or cooling power profiles acting on the structure for the case D56

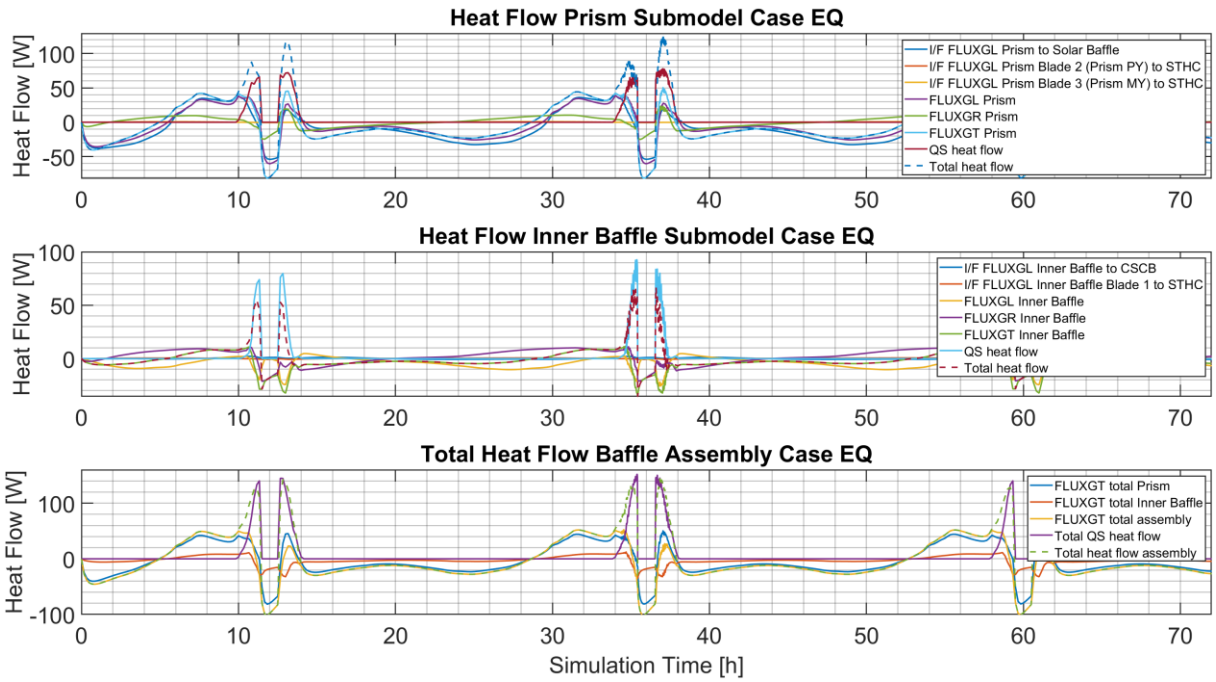

Figure 10.19: Energy balance of the original MTG EBA submodel with cut interfaces for the determination of the time-dependent heating or cooling power profiles acting on the structure for the case EQ

10.19 Relevant Mean Temperature Intervals to Assess the Demonstrator PCM Mass

The following Figure 10.20 and Figure 10.21 depict the total heat flows over all demonstrator sections averaged, together with the overall mean temperature curves for the cases D56 and EQ in order to identify the PCM active intervals. The interval limits are framed in black accordingly.

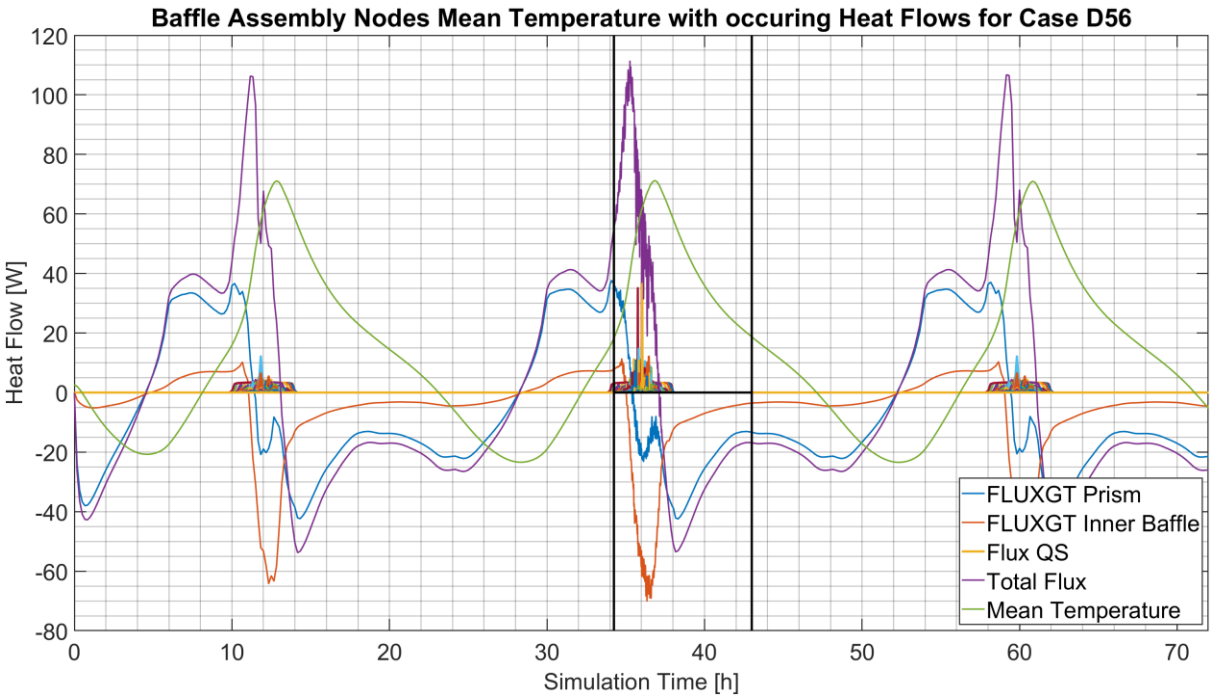

Figure 10.20: Overview of the overall heat flow behaviour of the MTG EBA structure thermal nodes, in order to derive the interval limits (black lines) in which the PCM can be effectively used, for case D56

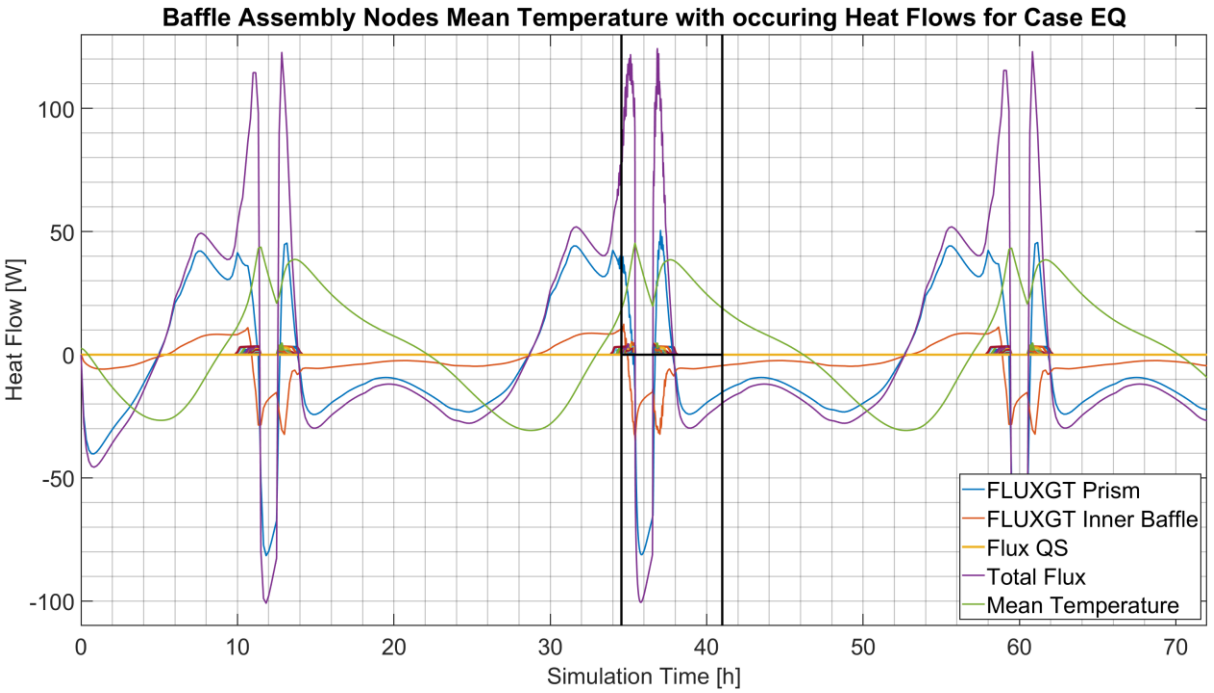

Figure 10.21: Overview of the overall heat flow behaviour of the MTG EBA structure thermal nodes, in order to derive the interval limits (black lines) in which the PCM can be effectively used, for case EQ

10.20 Heater Setup and Heating Profiles Assessment

The resulting MTG thermal model heating profiles of the inner baffle assembly structure are visualised in Figure 10.22 for case D56 and in Figure 10.23 for case EQ.

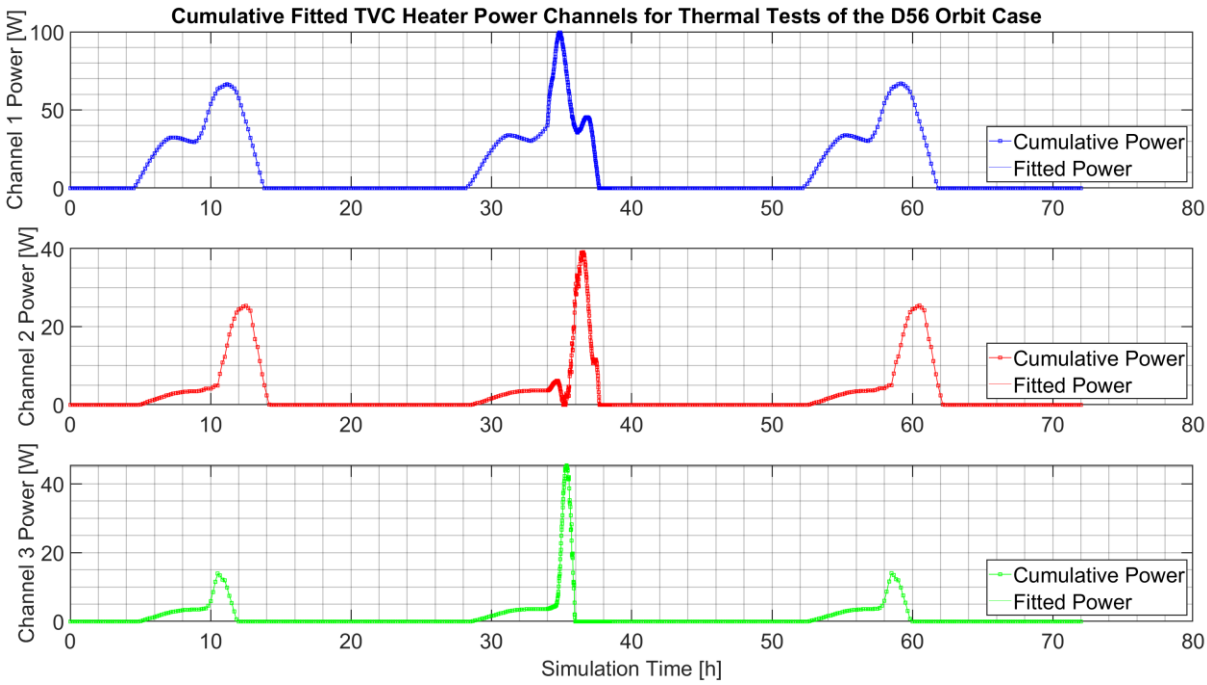

Figure 10.22: Cumulative MTG heat profiles $Q(t)_{Heat\ MTG}$ of the asymmetric heater channels, based on the MTG thermal model, in order to reproduce the heating profile for TVC tests of the D56 orbit case

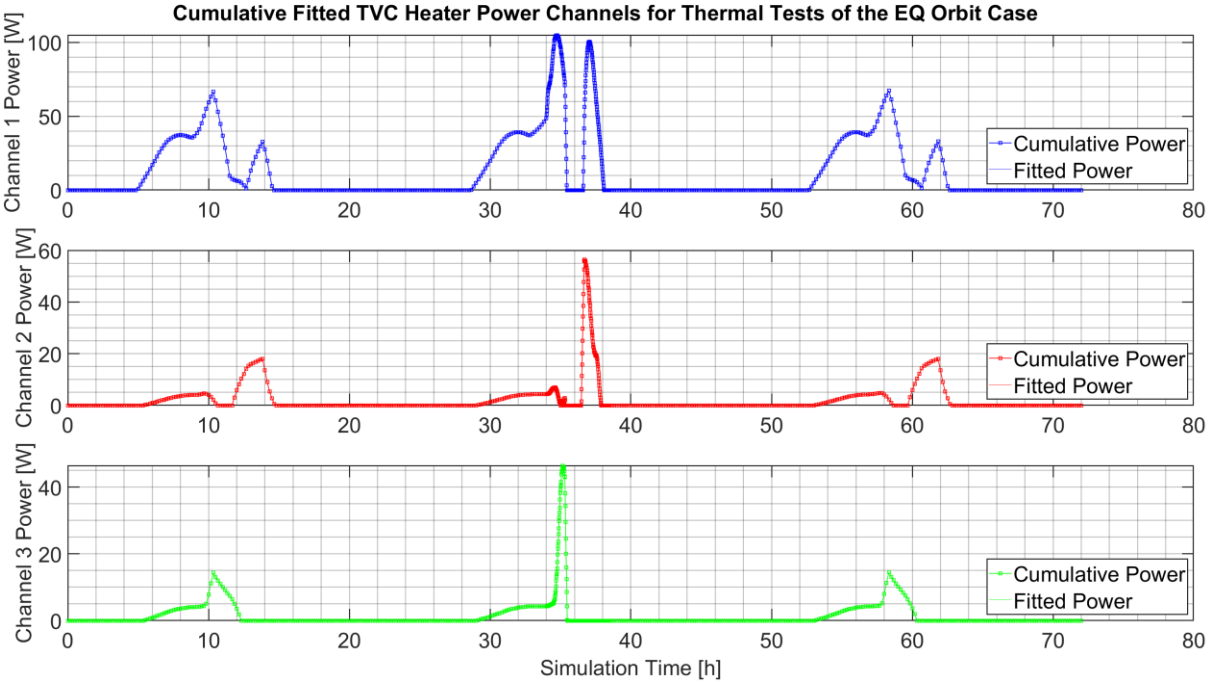

Figure 10.23: Cumulative MTG heat profiles $Q(t)_{Heat\ MTG}$ of the asymmetric heater channels, based on the MTG thermal model, in order to reproduce the heating profile for TVC tests of the EQ orbit case

The following Table 10.17 and Table 10.18 shall give an additional overview of the sunlit times and intervals of the MTG orbits.

Table 10.17: D56 orbit interval data with the orbit dependent maximal temperatures, largest occurring temperature gradients and the solar irradiation (QS) mean power

D56 orbits	Start [s]	End [s]	Max. T [°C]	Max. ΔT [K/s]	Mean QS [W]
D56 orbit 1	0	86400	105.4	0.07	22.2
D56 orbit 2	86400	172800	110.7	0.61	22.7
D56 orbit 3	172800	259200	105.3	0.07	22.2

Table 10.18: EQ orbit interval data with the orbit dependent maximal temperatures, largest occurring temperature gradients and the solar irradiation (QS) mean power

EQ orbits	Start [s]	End [s]	Max. T [°C]	Max. ΔT [K/s]	Mean QS [W]
EQ orbit 1	0	86400	76.3	0.08	13.3
EQ orbit 2	86400	172800	82.0	0.49	13.5
EQ orbit 3	172800	259200	76.0	0.08	13.3

10.20.1 Heater Setup Accommodation

The heater zones are defined by thermal analysis results, which have clarified the points of highest temperatures (hot spots). The occurring hot spots on the demonstrator hardware skin are then chosen as possible reference points for heater attachment positions. That was already the approach in the work of Gräbener et al. [JOS-01] and is also applied in this thesis.

Various heaters can comply with a heater cluster. The positions of the heater clusters are visualised and numbered in the Figure 10.24 to Figure 10.26. The different heater clusters are further assigned to three superordinate heater channels. These total heater channels are typically operated with different and varying power profiles. By knowing the total resistance of each heater channel, a channel-by-channel heater control can be implemented using a MATLAB program. The three channels can be controlled independently of each other in their outputs. The heater control program therefore adjusts the current and voltage output of each channel. To avoid over-temperature of the kapton heaters, at least one pilot temperature sensor is used for each of the three channels to monitor the kapton heater surface temperature.

From various TVC steady-state measurements with constant heater power values at diverse specimens, an averaged end-to-end efficiency of converting electrical heater power to heat on the aluminium skin at the heater locations was determined by correlations to approx. 0.92.

This value also serves as a basis for the validation and correlation of the thermal predictions. Possible causes to interpret the determined overall efficiency are (a) the contact resistance between the kapton heater adhesive and the metallic skin, (b) radiative losses through the MLI, (c) electrical contact resistance due to plug connections and (d) heat loss due to the conductive coupling of the electrical lines for heater supply with the TVC environment (chamber and cold plate).

The following Figure 10.24 to Figure 10.26 show the already mentioned heater setup with all heaters attached to the ITS demonstrator outer skin. In addition, the temperature sensor setup and accommodation is also shown.

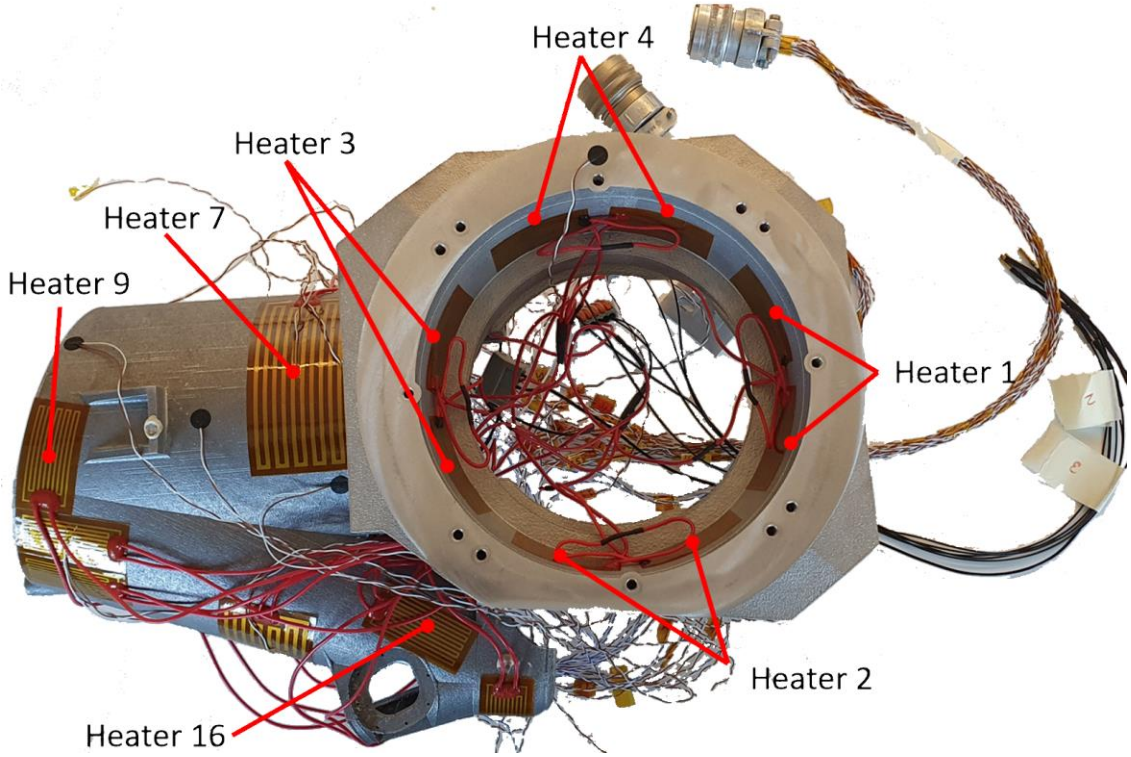

Figure 10.24: Heater positions, orientations and numbering of the ITS demonstrator setup upper side

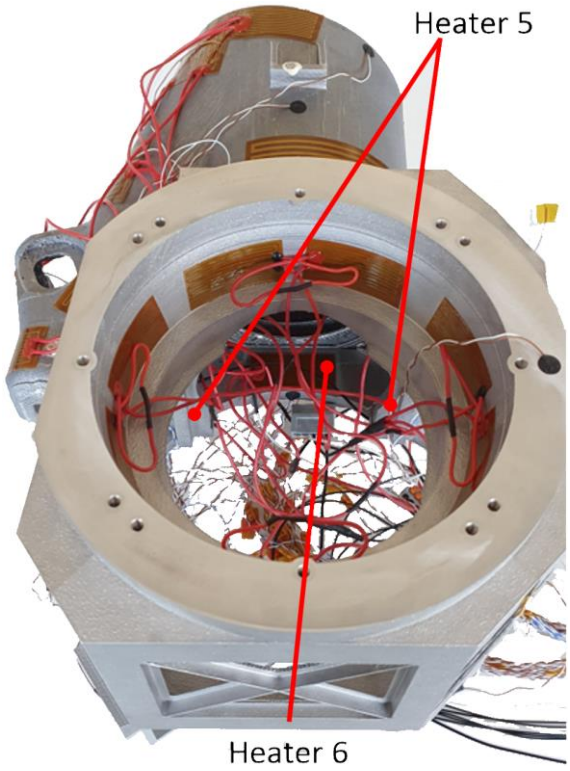

Figure 10.25: Heater positions, orientations and numbering of the ITS demonstrator setup interior

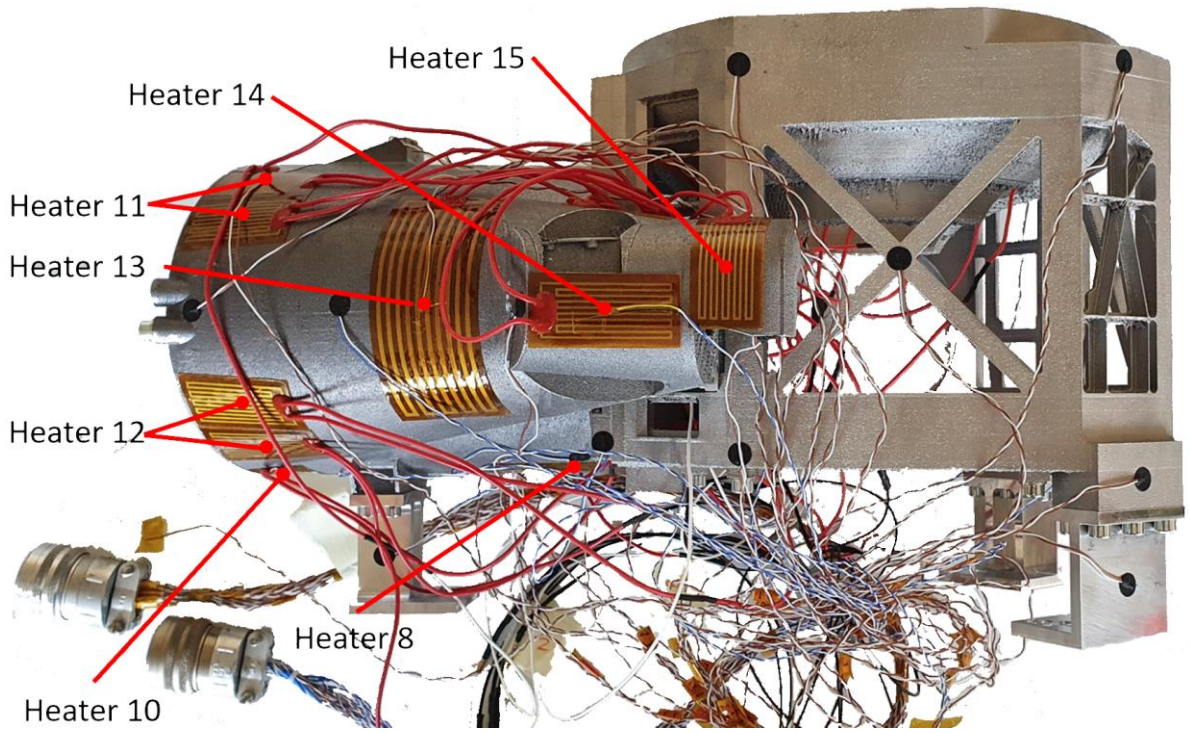

Figure 10.26: Heater positions, orientations and numbering of the ITS demonstrator setup left and lower side

Another necessary validation step for the verification of the heater and sensor setup is to verify the quality of the adhesive bonding of the heaters and carbon tabs to the ITS demonstrator outer skin. Incorrect or completely bonded heater patches could quickly and severely overheat and cause damage to the heater setup due to the lack of proper thermal coupling to the ITS demonstrator structure.

10.20.2 Heater Setup Pre-Test

In this chapter pre-tests have been carried out for the validation of the reliable and proper adhesive bonding of the heater patches to the aluminium skin of the demonstrator, in order to rule out possible heater detachments and electrical malfunctions in the various heater lines.

This is done by recording IR images of the demonstrator in the heating state without MLI. For an initial heater qualification, the diverse kapton heaters had been operated at a power greater than 2.0 W/cm² to validate the reliability of the heaters even at steep temperature gradients. The infrared images are taken in the laboratory environment in ambience conditions. The temperature sensor setup is described in Table 6.1 and used type-T thermocouples. The results of the IR recordings can be seen in Figure 10.27 with the visualised false-colour temperature range of ca. 25°C (black) to ca. 105°C (white).

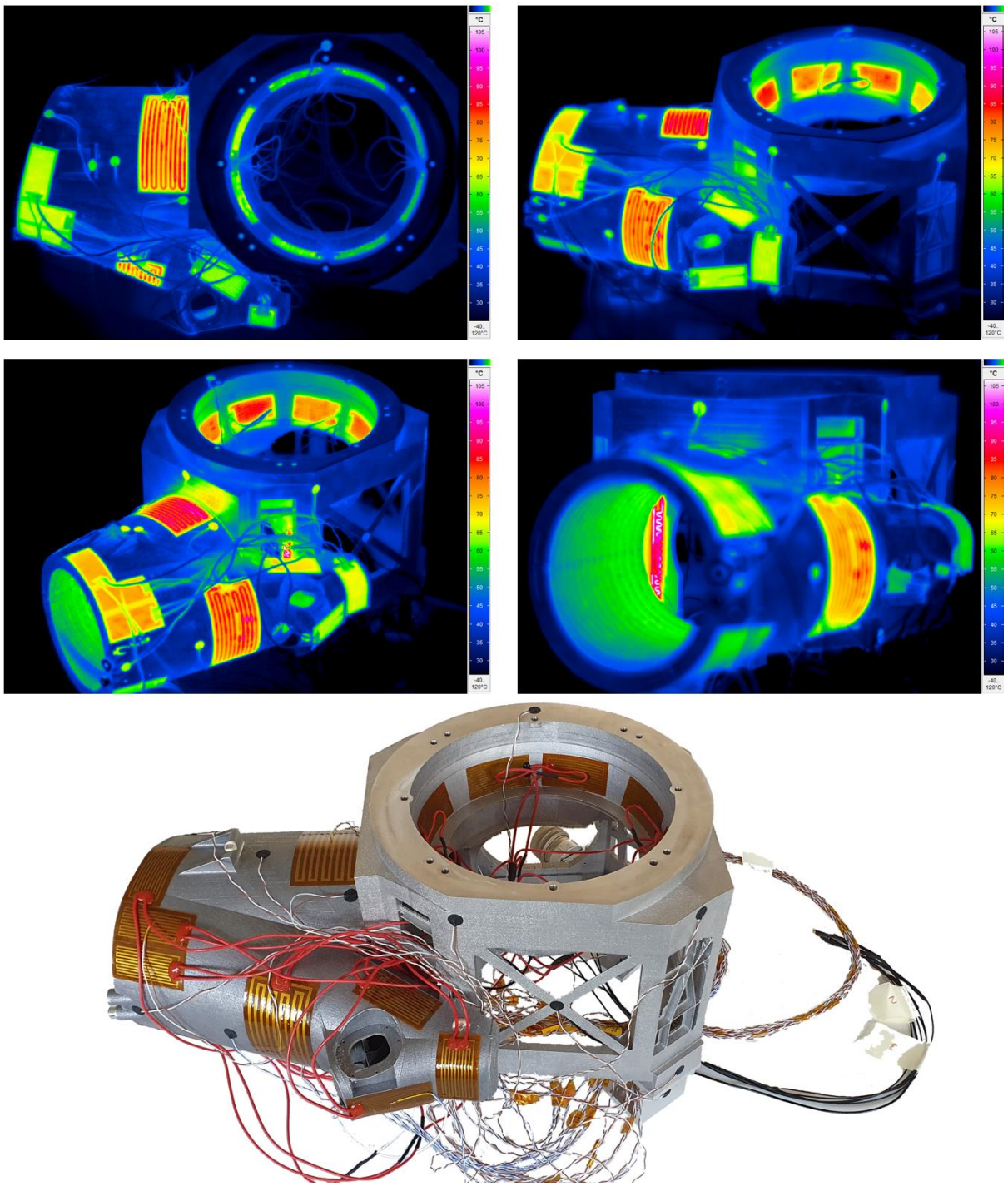

Figure 10.27: ITS demonstrator heater power lines and thermocouple setup, depicted by IR imaging in order to verify the proper adhesive bonding of the kapton heaters to the demonstrator skin

The evaluation of the IR recordings showed that none of the heaters detached over the test period. For the validation of the heater concept the fully connected heater circuits of the three channels were operated with the respective maximum power values. In addition, the individual heaters were tested for a period of 10 minutes with a minimum power of > 2.0 W/cm² to simulate thermal shocks.

10.21 Temperature Sensor Setup and Accommodation

The temperature sensors are attached to the demonstrator skin by heat-conductive EM-Tec CT9 double sided adhesive carbon tabs from the company Micro to Nano with product number 15-000409.

The tabs together with the attached sensors can be seen among others in Figure 10.24 to Figure 10.26. Due to the integrated mesh, which is embedded in the carbon adhesive tabs the tabs also adhere to non-machined and rough surfaces such as those found on additively manufactured metallic components in combination with a complex geometry with radii.

The sensor network was defined based on the following design drivers to be validated. This includes sharp edges, thin-walled aluminium struts, PCM chambers with large surface area but moderate thickness, massive and solid aluminium structures (solar baffle interface flange) and geometrically complex large-volume conic shaped PCM chambers (PCM ring chamber of the SSH).

One reference sensor (thermocouple) is permanently attached to the cold plate to track possible temperature fluctuations of the cold plate (heat sink) in order to monitor a reduction in cooling capacity.

The following Figure 10.28 to Figure 10.31 depict the thermocouple sensor setup with the corresponding numbering of the temperature sensors from different perspectives related on the thermal model assembly.

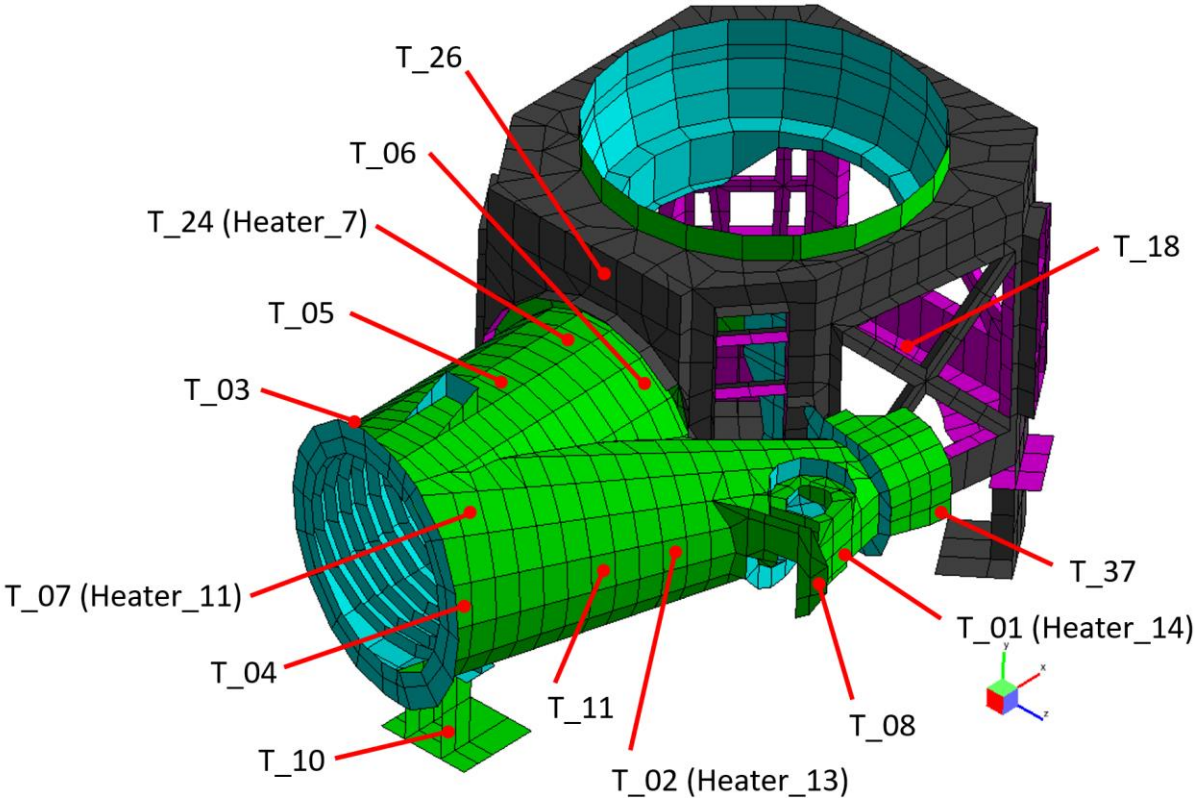

Figure 10.28: Temperature sensor setup, positions and numbering of the inner baffle upside shells

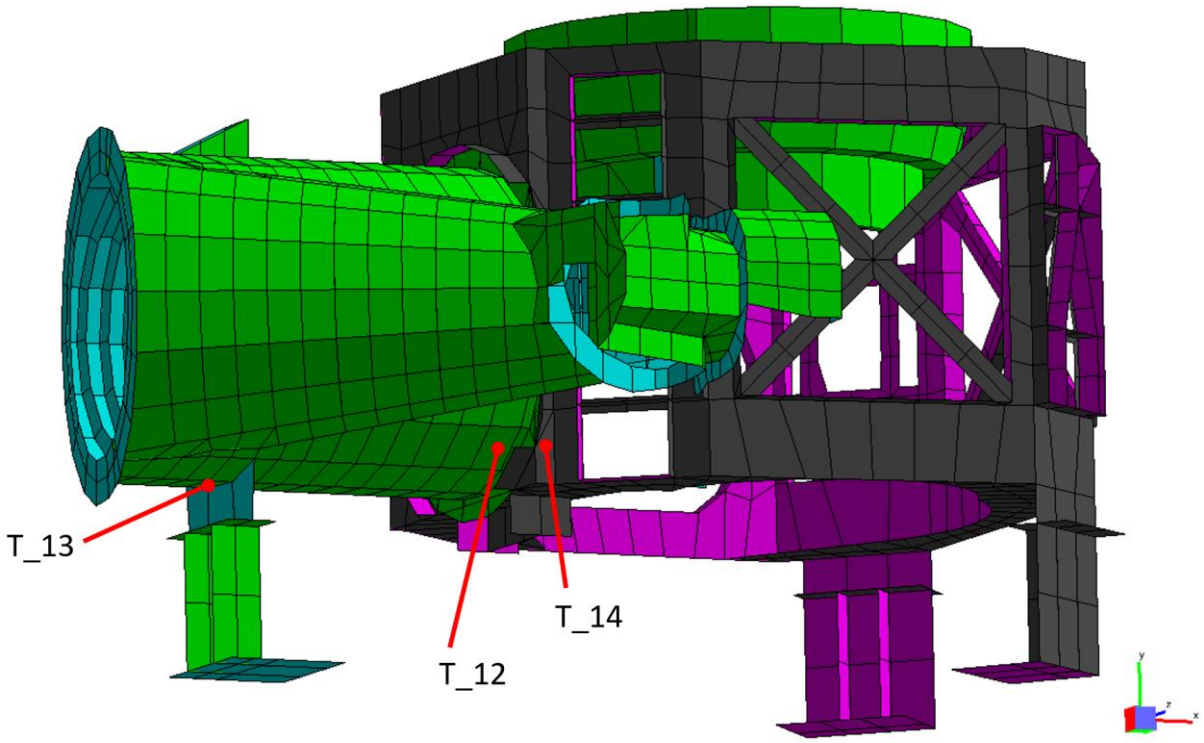

Figure 10.29: Temperature sensor setup, positions and numbering of the inner baffle downside shells

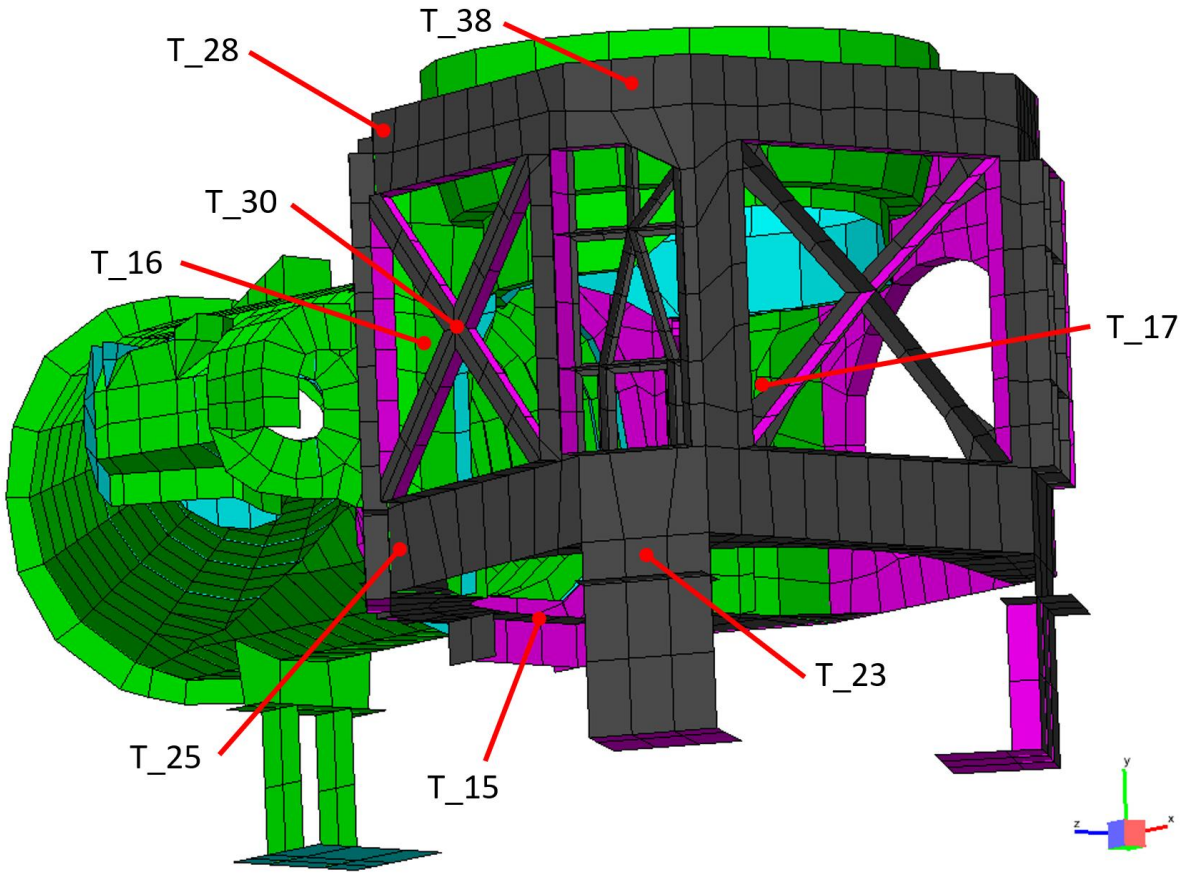

Figure 10.30: Temperature sensor setup, positions and numbering of the prism left side shells

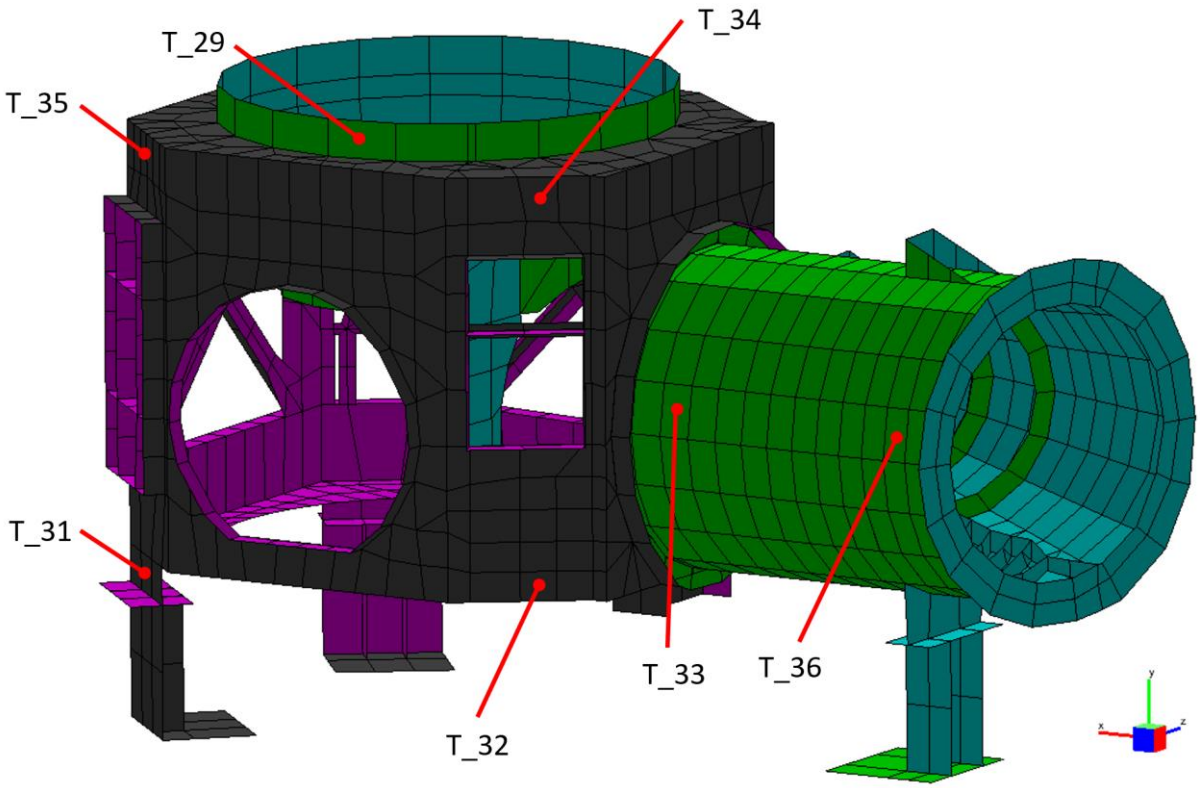

Figure 10.31: Temperature sensor setup, positions and numbering of the prism and inner baffle right side shells

10.22 Overview of the Heater Power Profiles Determination

The following Figure 10.32 and Figure 10.33 depict the derived heater power curves of the three PI controlled channels, for the cases D56 and EQ. The PI controller is operated with the settings of a proportional gain of $P = 5.0$ and an integral gain of $I = 1.0$.

Table 10.19: Definition of the experimental PI controller test setup, in order to derive the heater power profiles to mimic the thermal behaviour of the MTG orbit model for the cases D56 and EQ

Channel	Pilot sensor	Reference MTG	Referenced heater	Heater monitoring
1	T38	N390203	Heater 4	T29
2	T08	N633400	Heater 14	T01
3	T06	N601139	Heater 7	T24

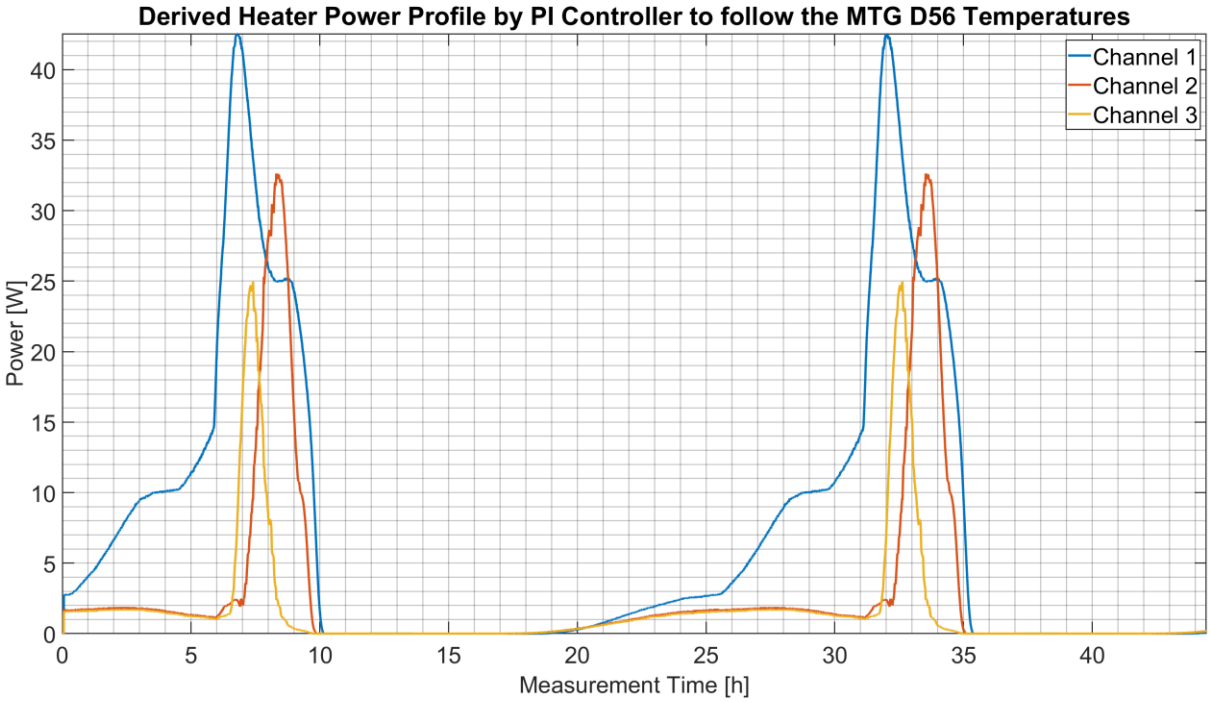

Figure 10.32: Derived heater power profiles by heater PI control to follow the MTG D56 orbit temperatures of the thermal model, applied on the ITS demonstrator hardware in the TVC

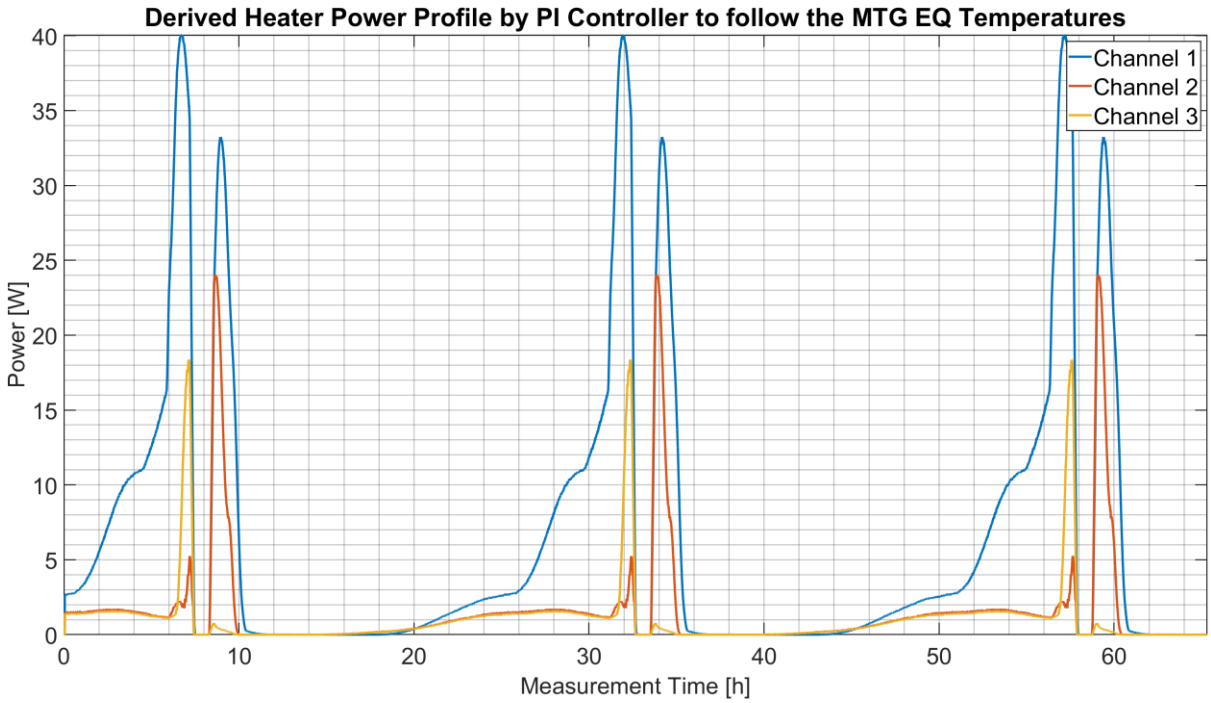

Figure 10.33: Derived heater power profiles by heater PI control to follow the MTG EQ orbit temperatures of the thermal model, applied on the ITS demonstrator hardware in the TVC

10.23 Demonstrator Thermal Vacuum Chamber Test Conditions and Parameters

The following Table 10.20 contains a comprehensive listing of the TVC test conditions and parameters, which are applied and determined in order to provide the demonstrator TVC measurement sequences.

Table 10.20: Overview of the experimental test parameters, environmental conditions and measurement equipment performance envelope

Test parameters and setting	Value
Absolute pressure in TVC during tests	$< 10^{-5}$ mbar
Degree of surface cleanliness	surfaces are cleaned with isopropanol
Relative temperature accuracy of the thermocouples	± 0.2°C (section 6.1)
Temperature logging rate of the measurement equipment	ca. 1 seconds
Power output accuracy of the power supply units	± 0.5%
Power output logging rate	ca. 2 seconds
End-to-end efficiency of the heater system	0.92
Accuracy of the positioning of the temperature sensors	± 3.0 mm
Ambience temperature	ca. 22 ± 5°C
Relative humidity	50 ± 10%

10.24 Summary of the Demonstrator Conductive Interfaces Validation Tests

The Figure 10.34 and Table 10.21 below summarise the measurement results of the validation tests in order to analyse and correlate the assumed values of the effective thermal contact conductance of the interfaces in the demonstrator thermal models.

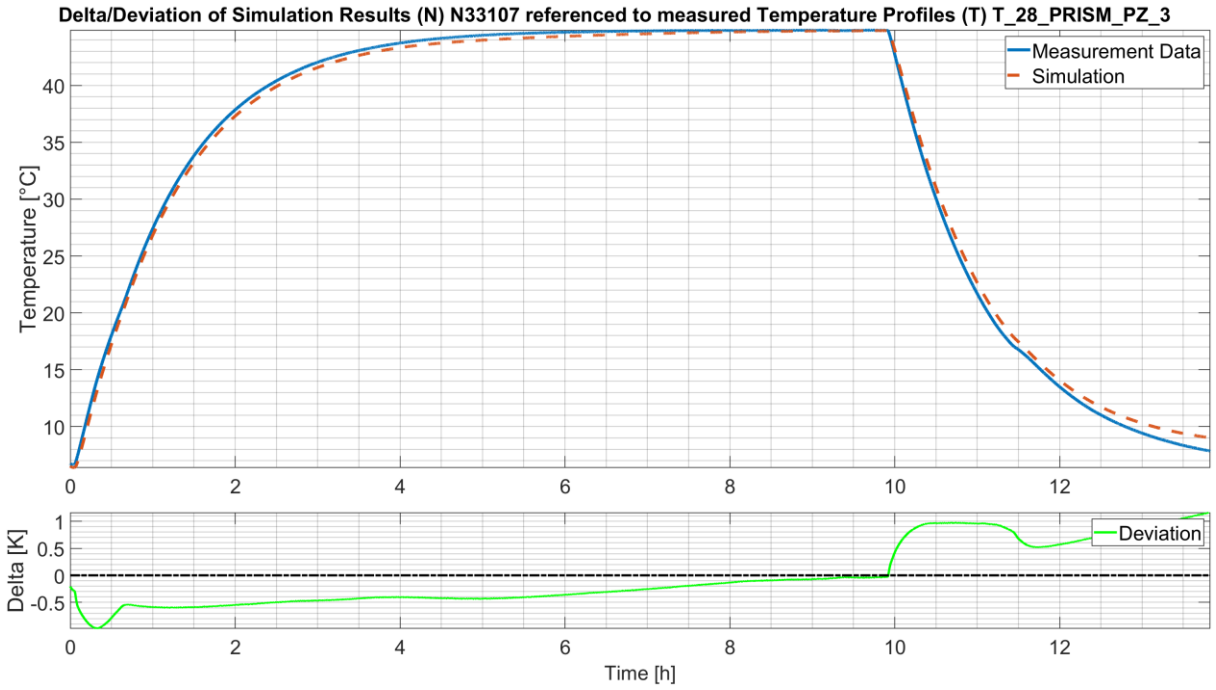

Figure 10.34: ITS thermal model prediction results of a representative test sequence without PCM (empty model) compared to demonstrator steady-state measurement, in order to validate and further correlate the thermal model GSE adapter interfaces and the intermediate interface at the inner baffle and prism flange contact zone

Table 10.21: Comparison of the ITS demonstrator thermal model prediction results to the steady-state measurements of a representative test sequence without PCM (empty model)

ITS demonstrator steady-state TVC tests	Values
Heater power	const. 30 W
Temperature relaxation criterion	< 0.5K/h
Cold plate temperature	5 ± 0.6°C
Maximal temperature	ca. 52°C
Mean temperature deviation of the prediction compared to test	-0.35K
Maximal temperature deviation	1.1K

10.25 Demonstrator Correlation Results for the Hot Case EQ

On the basis of the correlated demonstrator thermal model, related on the conductive interfaces and the effective heater power input, the following figures depict the results of the cyclic TVC tests of the ITS demonstrator without and with embedded PCM for the hot case EQ.

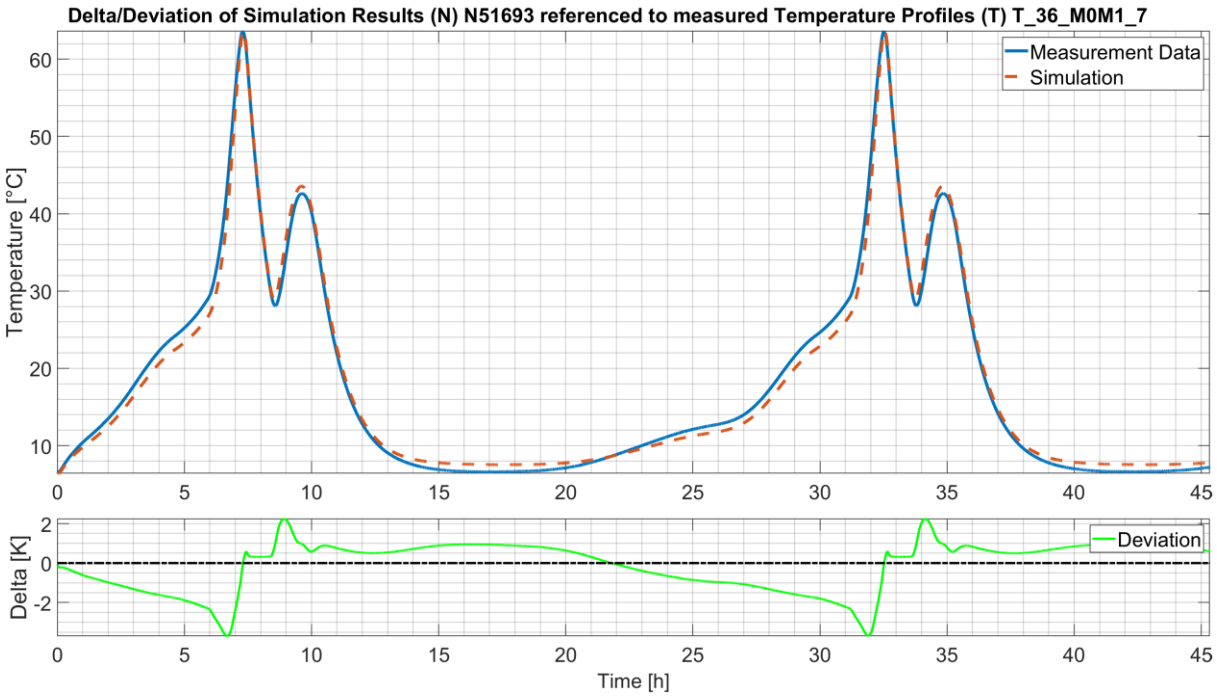

Figure 10.35: Correlation of the thermal predictions of the ITS demonstrator in empty state (no PCM embedded), using the sensor T36, compared to the measured data from the TVC tests based on the orbit profile EQ [WIL-23]

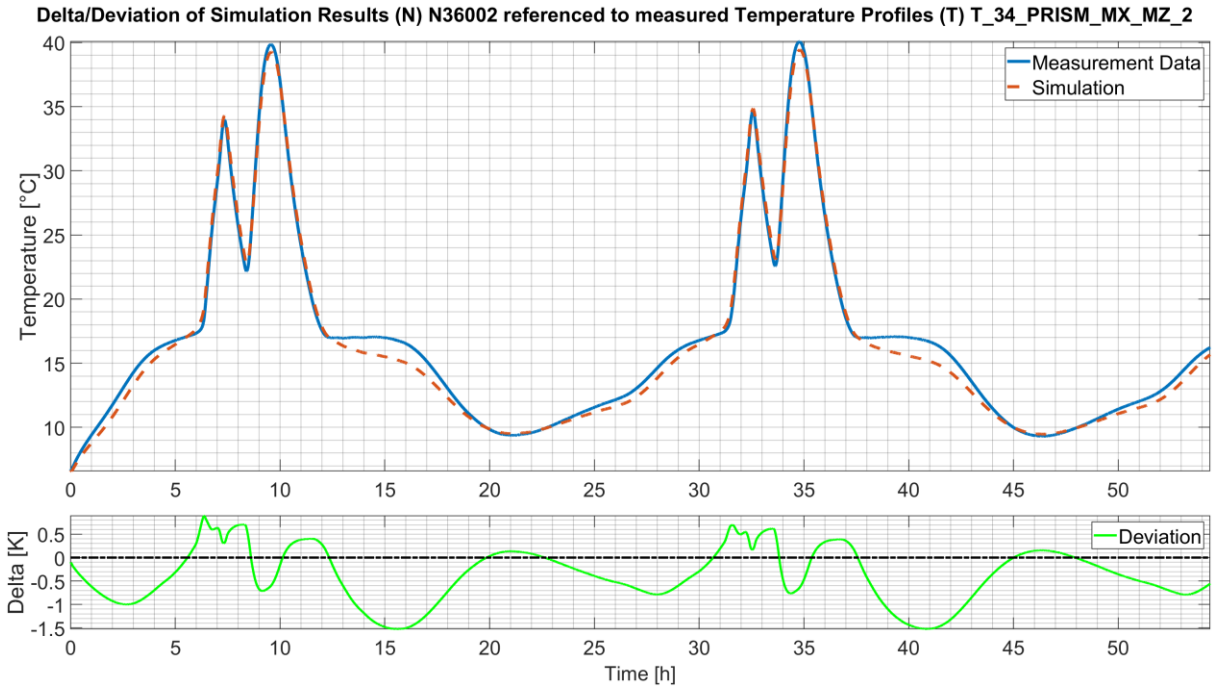

Figure 10.36: Correlation of the thermal predictions of the ITS demonstrator in the filled state (embedded PCM), using the sensor T34, compared to the measured data from the TVC tests based on the orbit profile EQ [WIL-23]

10.26 Demonstrator Correlation Results for the Hot Case D56

The figures below depict the results of the cyclic TVC tests of the ITS demonstrator without and with embedded PCM for the hot case D56.

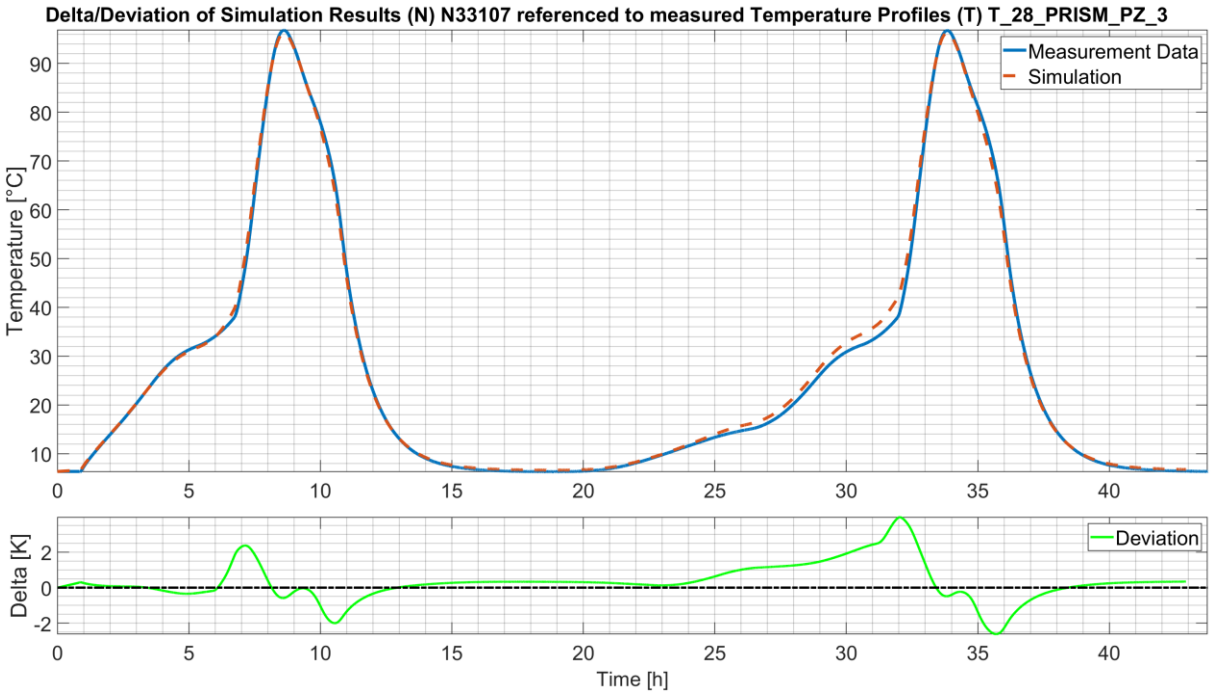

Figure 10.37: Correlation of the thermal predictions of the ITS demonstrator in empty state (no PCM embedded), using sensor T28, compared to the measured data from the TVC tests based on the orbit profile D56 [WIL-23]

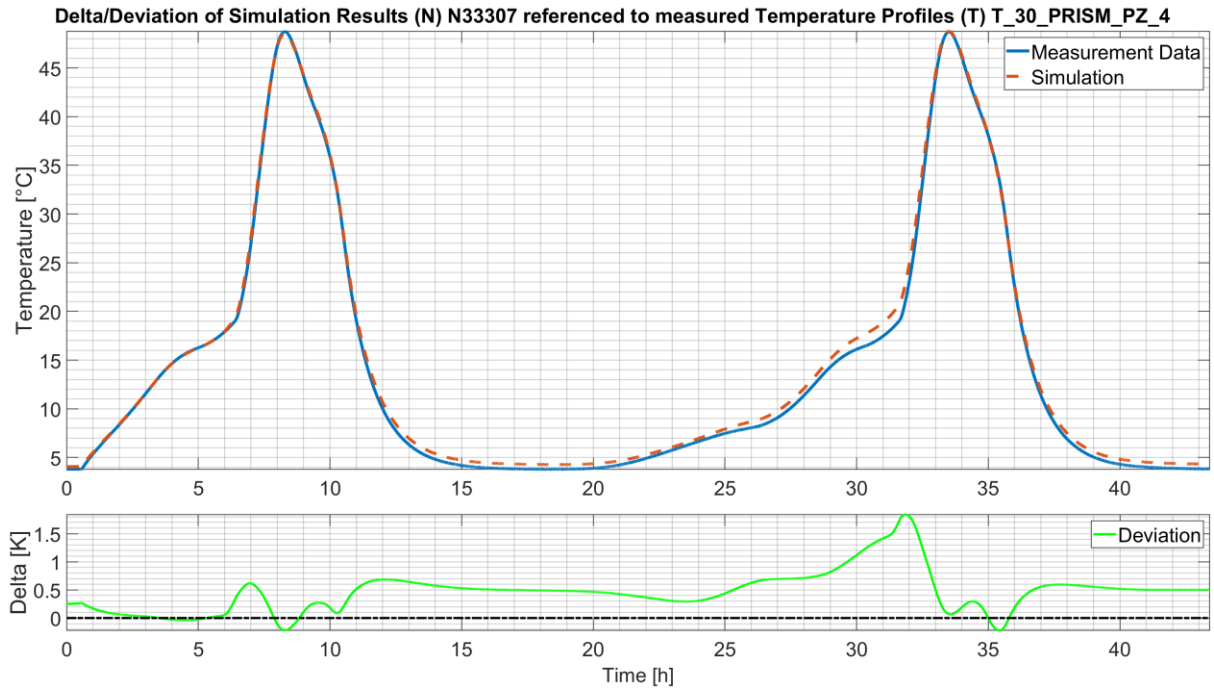

Figure 10.38: Correlation of the thermal predictions of the ITS demonstrator in the filled state (embedded PCM), using the sensor T30, compared to the measured data of the TVC tests based on the orbit profile D56 [WIL-23]

10.27 Demonstrator PCM Nodes Heat Flow Curves

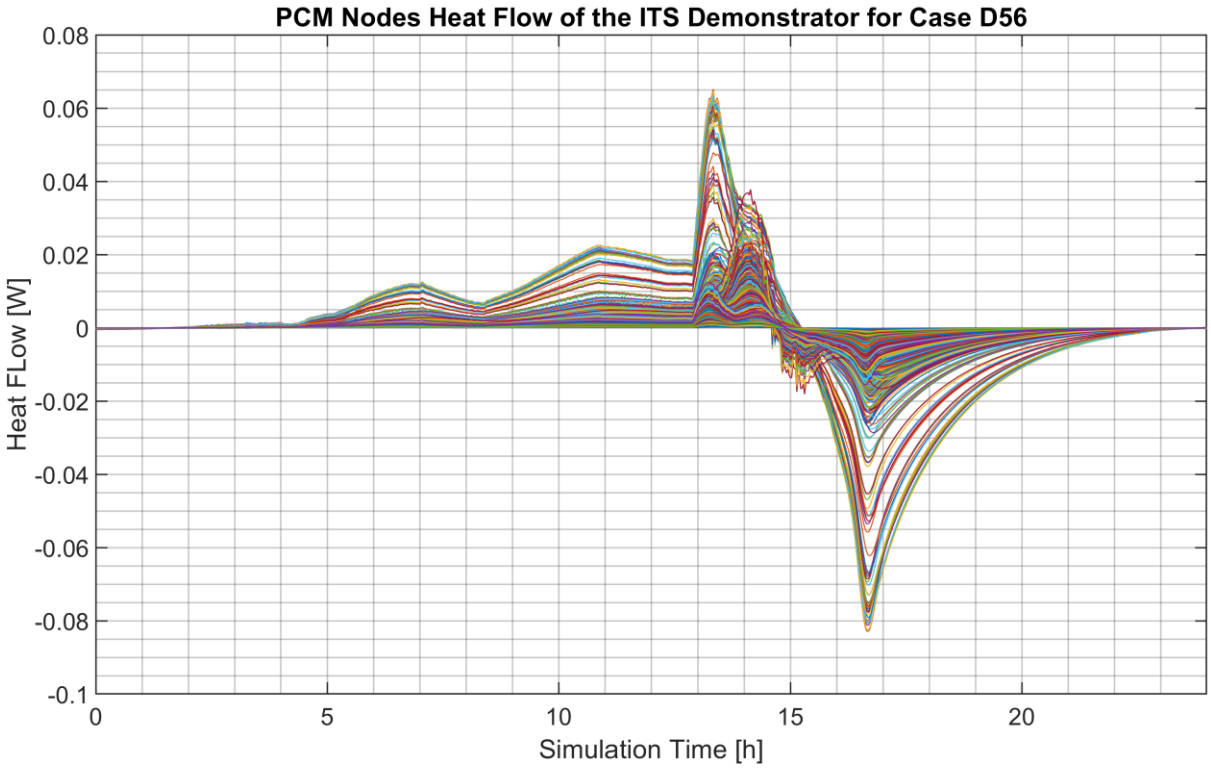

Figure 10.39: Cumulative heat flow curves of the ITS demonstrator thermal model for the case D56 for one complete simulated orbit

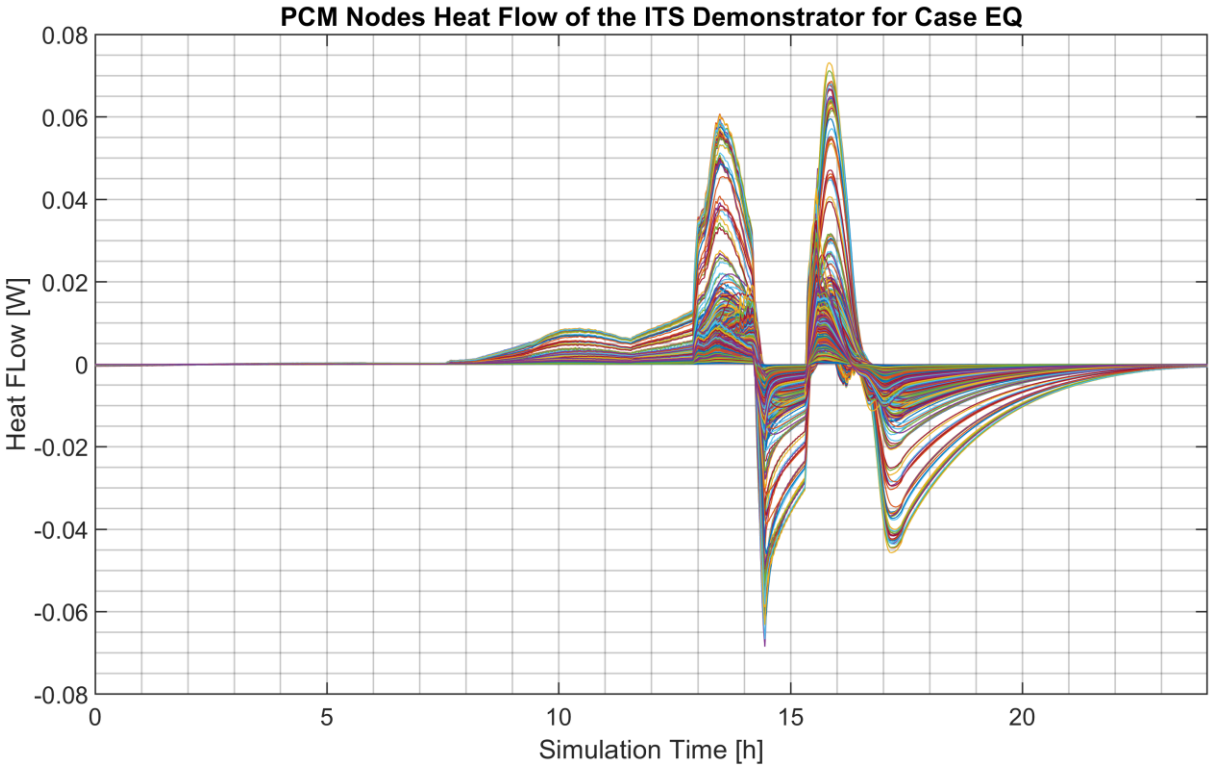

Figure 10.40: Cumulative heat flow curves of the ITS demonstrator thermal model for the case D56 for one complete simulated orbit

10.28 Demonstrator Temperature Stability

This section summarises the appended graphs of the calculated temperature stabilities of the hot cases EQ and D56, related on the ITS demonstrator hardware for the thermal nodes N22229 and N51609. These specified nodes exhibit the largest temperature instabilities in the unfilled state (without PCM) of the demonstrator during the proceeded TVC tests. The temperature stabilities are calculated for 600 s, 900 s and 3600 s. The detailed evaluation of the temperature stability improvements can be found in chapter 0.

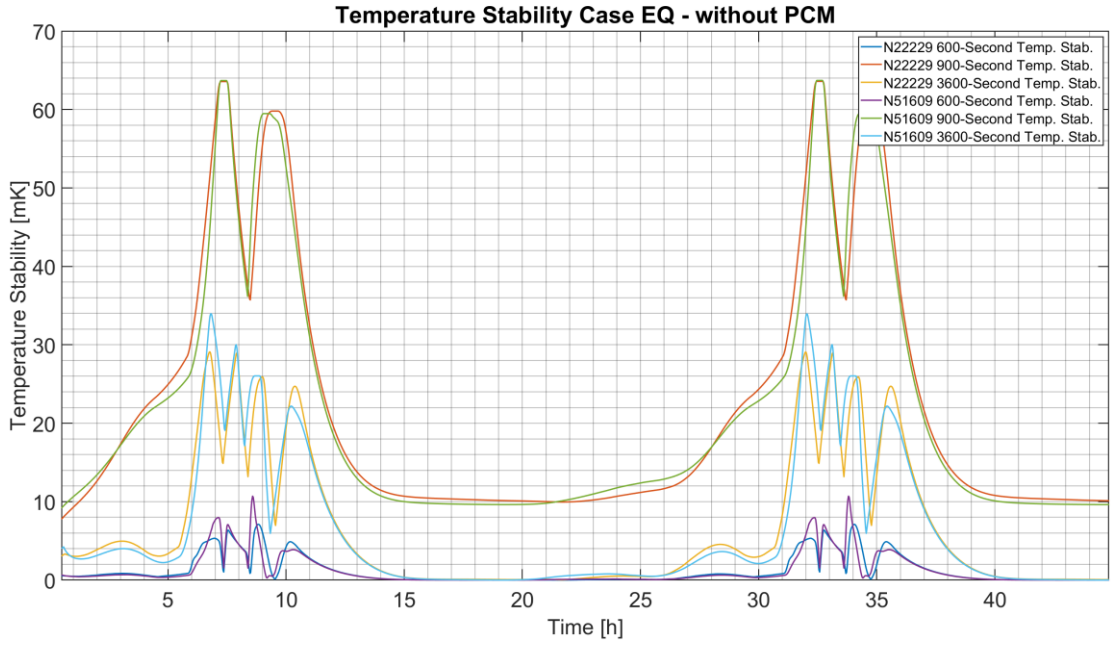

Figure 10.41: Temperature stabilities of the ITS demonstrator without embedded PCM at characteristic nodes with the highest instabilities, for the case EQ

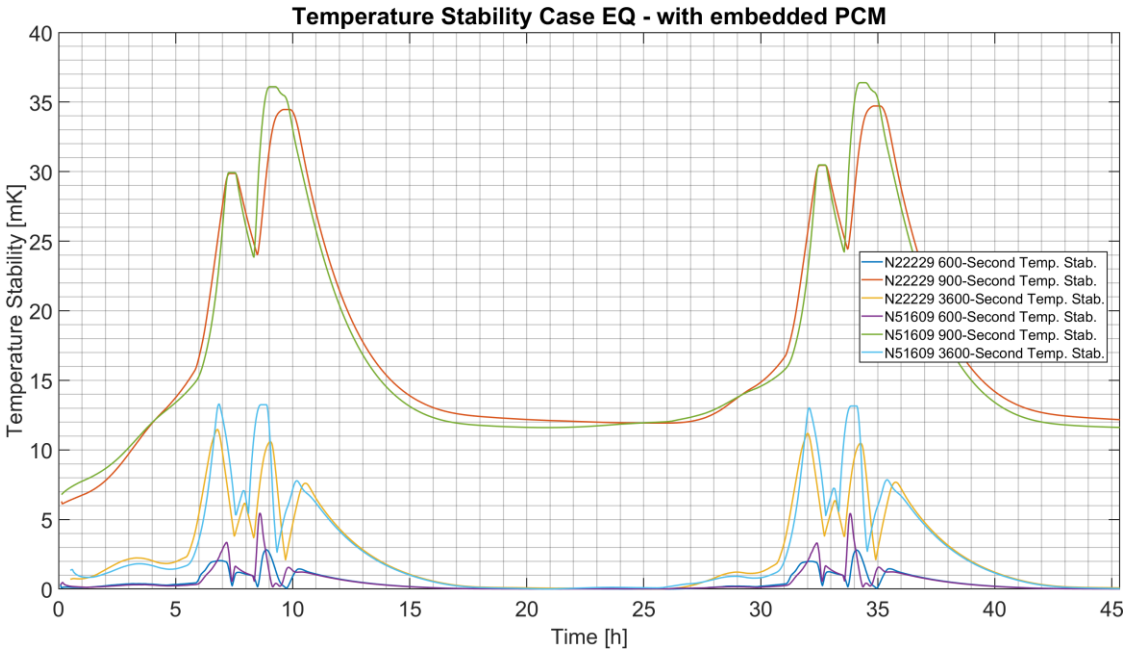

Figure 10.42: Temperature stabilities of the ITS demonstrator with embedded PCM at characteristic nodes with the highest instabilities, for the case EQ

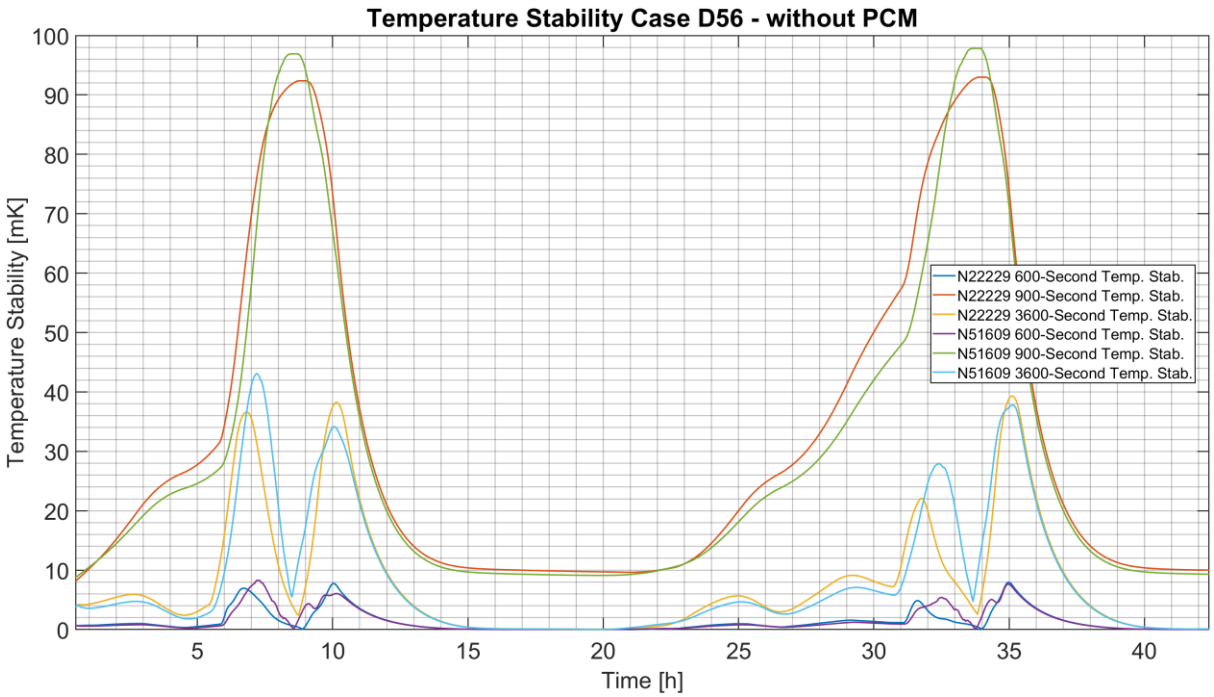

Figure 10.43: Temperature stabilities of the ITS demonstrator without embedded PCM at characteristic nodes with the highest instabilities, for the case D56

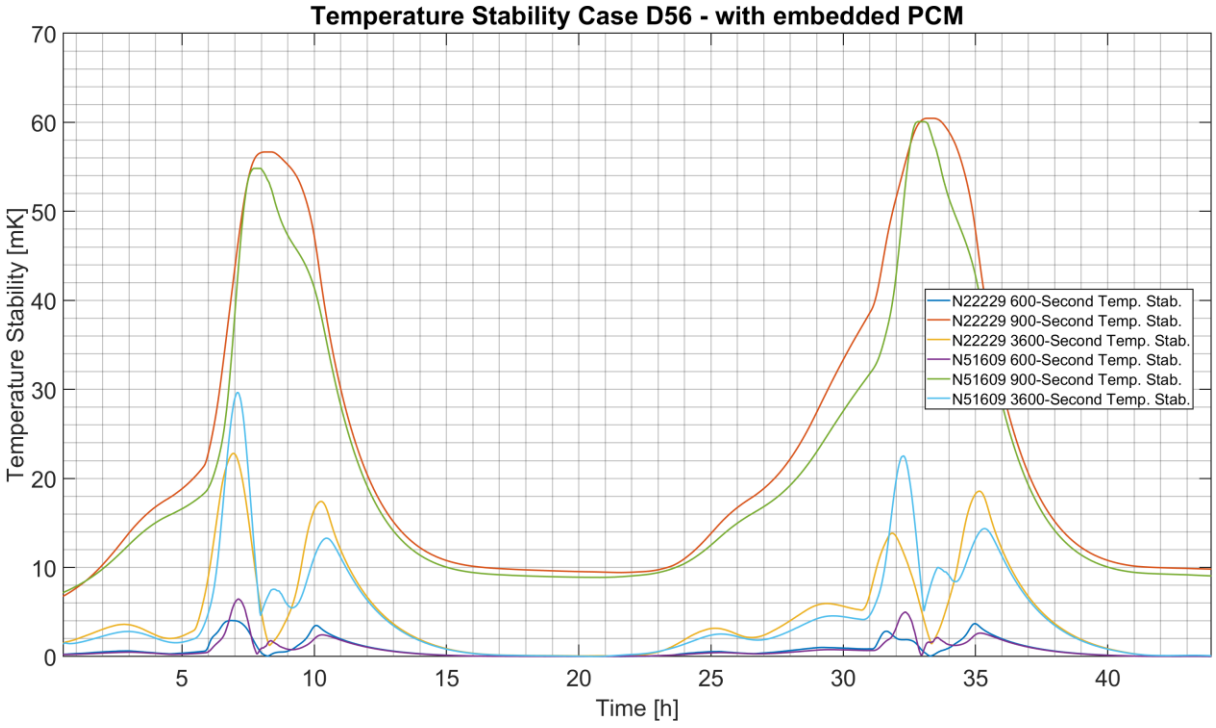

Figure 10.44: Temperature stabilities of the ITS demonstrator with embedded PCM at characteristic nodes with the highest instabilities, for the case D56